UNIVERSITY OF CALIFORNIA,
IRVINE

Model Scale Tests of Laterally Loaded Piles in Sand

DISSERTATION

submitted in partial satisfaction of the requirements
for the degree of

DOCTOR OF PHILOSOPHY

in Civil and Environmental Engineering

by

Camilla Favaretti

Dissertation Committee:
Professor Anne Lemnitzer, Chair
Professor Lizhi Sun
Professor Farzin Zareian

2018

TABLE OF CONTENTS

LIST OF FIGURES

Page

LIST OF TABLES

ACKNOWLEDGMENTS

This research project was sponsored by Pacific Earthquake Engineering Research Center's (PEER's), Deep Foundation Institute (DFI), and the International Association of Drilling Foundations (ADSC). Any opinions, findings, and conclusions or recommendations expressed in this material are those of the author and do not necessarily reflect those of the sponsors.

I would like to thank my advisor, Professor Anne Lemnitzer, as well as Professors Farzin Zareian and Lizhi Sun for serving in my committee. Thanks to the many colleagues and staff members, I had the pleasure to meet and work with.

I am especially grateful to the many people that assisted me in these years. In particular, Dr. Sergio Carnalla, whose invaluable advices helped me going through my lab days; Dr. Eric Ahlberg, who more than once saved my day; my colleagues Dr. Luis Herrera and Lohrasb Keykhosropour, for being always on my side; and all the undergraduate students I had the pleasure to work with. Thank you Adib, Adriana, Amber, Daniel, Julia, Nicole, and Octavio!

Finally, thanks to my family, Nick and all my wonderful friends for supporting me throughout this journey.

CURRICULUM VITAE

Camilla Favaretti

EDUCATION

Doctor of Philosophy in Civil and Environmental Engineering **2018**
University of California, Irvine *Irvine, California*

Master of Science in Civil Engineering **2013**
University of California, Irvine *Irvine, California*

Master of Science in Civil Engineering **2012**
Universita' degli Studi di Padova *Padova, Italy*

Bachelor of Science in Architectural Engineering **2010**
Universita' degli Studi di Padova *Padova, Italy*

RESEARCH EXPERIENCE

Graduate Research Assistant **2013–2018**
University of California, Irvine *Irvine, California*

TEACHING EXPERIENCE

Teaching Assistant for CEE30 Statics **2015**
University of California, Irvine *Irvine, California*

Teaching Assistant for CEE130 Soil Mechanics and Laboratory **2013-2015**
University of California, Irvine *Irvine, California*

WORK EXPERIENCE

Intern **2016**
Arup *New York, New York*

CONFERENCE PUBLICATIONS AND PRESENTATIONS

Lemnitzer A. and Favaretti C., Project Overview: Towards next generation p-y curves Part 1: State of the art and state of practice". **Jan 2018**
PEER Annual Meeting, Berkeley, CA.

Favaretti, C., Lemnitzer, A., Turner, J., and Stuedlein, A. "Recent Advances in *p-y* formulations for lateral load transfer of deep foundations based on experimental studies". **Mar 2015**
International Foundations Congress and Equipment Exposition (IFCEE), San Antonio, Texas.

Favaretti, C. and Lemnitzer, A. "Development of a Database for Laterally Loaded Piles: A review and Collection of Experimental studies and data". **Oct 2014**
DFI Annual Conference, Atlanta, GA.

Favaretti, C and Lemnitzer A. (2014). "Recent advances in *p-y* formulations based on experimental research work". **Aug 2014**
15^{th} European Conference on Earthquake Engineering and Seismology, Istanbul, Turkey.

Favaretti, C. and Lemnitzer, A. "Development of a Database for Laterally Loaded Piles". **Sept 2013**
DFI Annual Conference, Phoenix, AZ.

ABSTRACT OF THE DISSERTATION

Model Scale Tests of Laterally Loaded Piles in Sand

By

Camilla Favaretti

Doctor of Philosophy in Civil and Environmental Engineering

University of California, Irvine, 2018

Professor Anne Lemnitzer, Chair

Deep foundations are one of the most common foundation systems used in engineering practice. Prediction of pile response requires a good understanding of the mechanism that governs interaction between the pile and the soil. In order to obtain efficient and economical pile designs, geotechnical engineers utilize experimental studies combined with traditional analytical models. Most formulations used today are based on elastic solutions or Winkler formulations (e.g. p-y curves) that were derived and calibrated with limited amounts of existing test data. Controversies exist with respect to the influence of various parameters, such as head fixity, pile installation techniques, soil profiling, and axial- lateral load. Moreover, the interpretation of the data from pile instrumentation is not straightforward, given the numerical errors that incur in the double differentiation of the bending moment profile. Specifically, this research pursues the following objectives:

1. Selected p-y curves limitations, including the influence of different concrete, reinforcement, and tip restraint, are addressed through combined experimental and numerical studies on model-scale test specimens.

2. Advanced construction materials, such as high-strength polymer concrete and innovative polymeric reinforcement materials, are also examined to assess their suitability for commercial introduction into routine foundation design practice.

3. An innovative strain gauge based instrumentation will help 1D instrumentation (i.e. longitudinal strain measurements).

4. The results obtained from the model-scale lateral loaded tests on concrete piles are evaluated to provide insights in the soil-pile interaction behavior. An optimization technique implemented in a genetic algorithm framework is proposed to facilitate data interpretation and to derive p-y curves even in presence of disturbed data readings and pile nonlinearity. The proposed genetic algorithm targets directly p-y curves and evaluates them through the minimization of a fitness function, represented by the explained variance (EV) between raw p-y values and fitted p-y function. Moreover, this approach allows the generation of p-y curves from an ensemble of different statistical methods.

The ultimate intention of this study is to incrementally eliminate uncertainties associated with pile analysis and provide new understanding for design in practice.

Chapter 1

Introduction

1.1 Laterally Loaded Piles

Pile foundations are one of the most common foundation systems in engineering practice. In cases where the bearing capacity of near-surface soils is insufficient to carry superstructure loading via shallow foundation elements, such as footings and rafts, piles are used to safely transfer loads to deeper and more suitable layers. Although deep foundations are primarily used to transfer vertical loading, lateral force resistance becomes critical in areas with seismic activities, in sloping ground, and when subjected to impact loading and wind, as shown in Fig. 1.1.

1.1.1 Static Load Transfer Mechanism

Upon application of lateral loading, piles deform and displace horizontally into the surrounding soil. Fig. 1.2a shows a solid pile of circular cross-section subjected to lateral loading. Fig. 1.2b describes the distribution of the horizontal stresses acting on the face of the pile

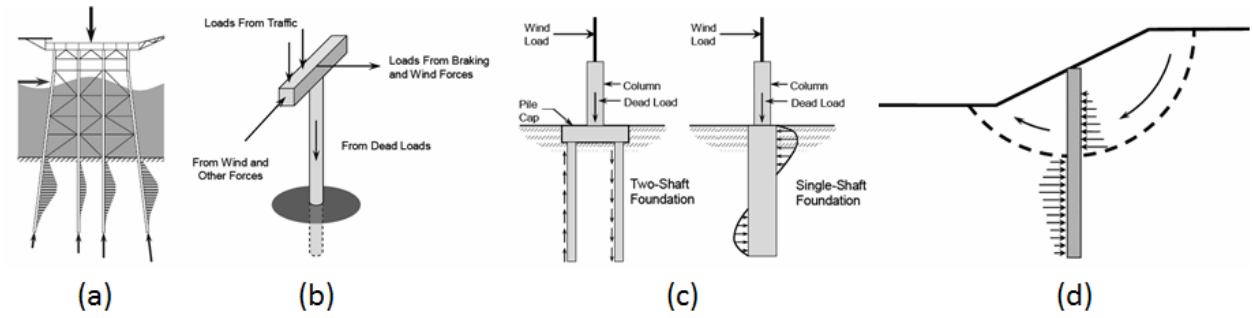

Figure 1.1: Deep foundations applications: (a) Offshore applications, (b) Single pile support for a bridge, (c) Pile supported overhead sign, (d) Piles to stabilize slopes. Source: Reese et al. [91].

before and after the application of the load.

Stresses will decrease on the back side of the pile (active pressure) and increase on the front side (passive pressure). Stresses in transition regions will have both, a normal and a shearing component. Integration of these unit stresses yields the horizontal soil reaction to pile displacement, p_t (load per unit pile length), which acts in opposite direction to the lateral pile displacement, y_t.

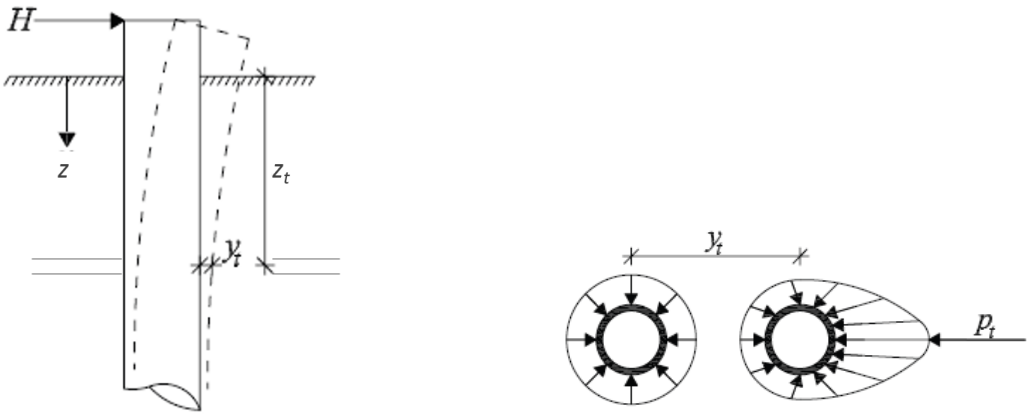

(a) Pile deflection due to lateral loading

(b) Horizontal stresses on pile before and after loading

Figure 1.2: Static load transfer mechanism. Source: Reese and Van Impe [89].

1.1.2 Failure Mechanism

The failure evolution of a laterally loaded pile is complex and depends on the pile's dimensionless length factor, ηL. This factor is a function of the pile diameter, length, and elastic modulus, as well as the type of soil it is embedded in (Broms [18] and [19]). When $\eta L \geq 4$, the pile is considered a long flexible pile, and when $\eta L \leq 2$, the pile is considered a short rigid pile. The failure of a short rigid pile occurs when the lateral resistance of the soil has been exceeded. In this case the pile will experience rotation and/or translation. The failure mechanisms of a short rigid pile for the free headed and fixed head condition are shown in Fig. 1.3(a and b). In the case of long flexible piles, failure is associated with the exceedance of moment capacity at one or more points along the pile length. The pile will bend and form a plastic hinge approximately 2-3 pile diameters below ground surface. The failure modes for long flexible pile are shown in Fig. 1.3(c and d). When piles can be easily categorized in short or long piles, subsequent analysis and design can be eased through the availability of solutions in the literature. In most practical applications, piles behave flexible and the prediction of their response is a soil-structure interaction (SSI) problem. A more challenging task is the analysis of intermediate piles which experience a combination of both failure mechanism as described above.

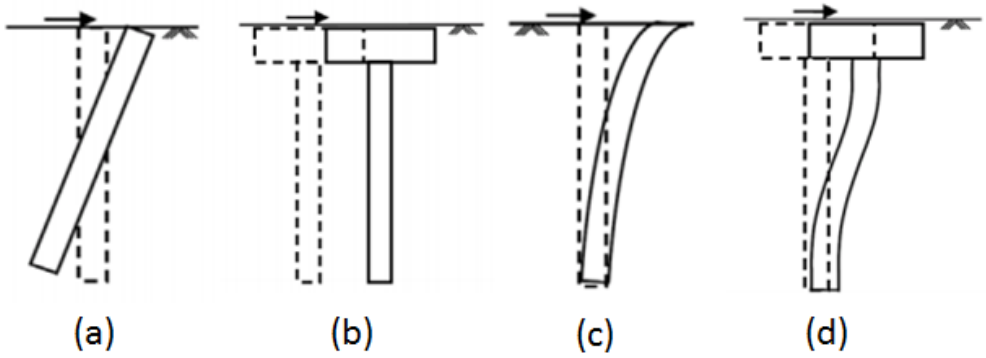

Figure 1.3: Typical failure modes in short rigid piles ((a) Rotation, and (b) Translation) and long flexible piles ((c) Free bending, and (d) Bending constrained at the top).

1.2 Design Methodologies for Laterally Loaded Piles

A good understanding of the governing interaction mechanisms between the pile and the surrounding soil is required to reasonably predict the anticipated pile response. In order to obtain efficient and economical pile designs, geotechnical engineers combine knowledge gained from experimental studies with traditional analytical and numerical models to estimate the foundation performance under the expected magnitude of lateral and axial loading. Pilot testing programs of full-scale pile specimens in the field remain the most reliable and direct method for determining the lateral response of a pile. Hereby, installation methods, loading rates, and site-specific soil variability are automatically accounted for in the pile response. However, well instrumented full-scale pile tests are expensive and experimental costs can rarely be justified for small construction projects. Hence, engineers rely heavily on knowledge gained from model and large scale experiments documented in literature.

Commonly employed pile design methodologies, range from simple analytical models that represent the soil through a series of independent nonlinear springs, to rigorous three-dimensional numerical solutions, which directly employ constitutive material relationships to predict the pile response. The most commonly used analysis methods for laterally loaded piles can be divided into five main categories:

- limit state models (e.g. Blum [12]; Hansen and Christensen [36]; Broms [18] and [19]);
- subgrade reaction methods, which include the characteristic load method (e.g. Duncan et al. [27]), the non dimensional load method (e.g. Reese and Matlock [87]), and $p-y$ method (e.g. Reese et al. [86] and [90]; Matlock [60]);
- elasticity method (Poulos [81] and [82]; Poulos et al. [83]; Butterfield and Banerjee [9]);
- finite element method (e.g. Abdel-Rahman and Achmus [2]; Abaqus [1]; Plaxis [17];

GPILE-3D [48]); and

- finite difference method (e.g. FLAC [43]).

Since the above-mentioned methods use a large spectrum of assumptions with respect to soil homogeneity, soil stiffness variation, and ultimate lateral resistance, large discrepancies exist between the results obtained through the respective approaches. When combining the need for simplicity, reduced computational effort, and accuracy, only few methods remain beneficial and economical in routine engineering practice. Among such, the subgrade reaction method (e.g. Winkler model and p-y method) is at the forefront of analytical tools to predict the response of laterally loaded piles. In the subgrade reaction approach, the pile is modeled as an elastic beam and the soil is represented by a series of nonlinear springs with a stiffness, K $[F/L]$. These springs are conventionally referred to as p-y springs and describe the relationship between the soil resistance, p, and the pile deflection y at a given depth. Recent studies (e.g. Lemnitzer [51]) have shown that the p-y method of analysis remains the primary choice of analytical tools among practicing engineers. In surveys conducted by PI Lemnitzer, over 90% of the respondents indicated that the p-y type of analysis is the first choice for lateral pile design, followed by 16% of the respondents who indicated that they also use Finite Difference methods or rigid and limit state methods to supplement or double check their lateral pile analyses.

The following chapters will focus on the use of subgrade reaction formulations and examine the various relationships proposed in literature. To clarify the different terminologies used for soil-structure interaction parameters, Table 1.1 is used to define the spectrum of terms pertinent to the subgrade reaction theory (e.g. coefficient of subgrade reaction, k_s, modulus of subgrade reaction or Winkler modulus, k, and stiffness of subgrade reaction spring, K). The definition of these parameters is often confused in literature. Hence, care needs to be exercised in properly applying the mathematical parameters.

Table 1.1: Summary of definition used in subgrade reaction theory.

Symbol	Description	Dimension	Definition
z	Depth to point being considered	L	
y	Pile deflection	L	
D	Pile diameter	L	
s	Spring spacing	L	
F	Spring force	F	$p * s$
p	Soil resistance per unit length	F/L	
P	Soil pressure	F/L^2	p/D
K	Lumped spring constant	F/L	F/y; $k * s$
k	Modulus of subgrade reaction	F/L^2	p/y; $k_s * D$
k_0	Initial modulus of subgrade reaction	F/L^2	$dp/dy, y = 0$
k_s	Coefficient of subgrade reaction	F/L^3	P/y; K/D
$k_{s,0}$	Initial coefficient of subgrade reaction	F/L^3	$dP/dy, y = 0$
n_h	Constant of horizontal subgrade reaction	F/L^3	$k_s * D/z$

1.3 A Detailed Review of the Winkler Approach

Winkler [117] was among the first researchers to analyze the response of elastic beams on elastic foundations. This general concept was initially introduced for the analysis of rigid plates, but extended in subsequent decades to flexible foundations with different spring properties to account for different types of soil (e.g. Filonenko-Borodich [32], Hetenyi [37], Pasternak [80], Reissner [92]). As shown in Fig. 1.4, the soil is modelled by a bed of linear-elastic uncoupled springs. The spring stiffness is called modulus of subgrade reaction, k, and is expressed in units of force per length squared $[F/L^2]$.

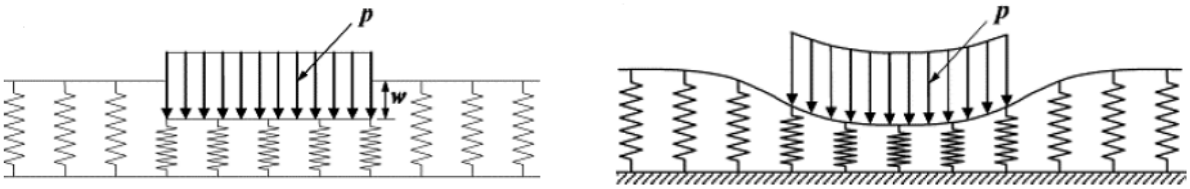

(a) Rigid foundation (b) Flexible foundation

Figure 1.4: Winkler Model.

This fundamental approach was adopted by **Hetenyi** [37] to simulate the behavior of a single pile. The mathematical relationship for the elastic beam supported on an elastic foundation

is shown in Eq. 1.7. If an infinitely small element, dz, is cut out of the beam (Fig. 1.5), the equilibrium of moments (ignoring second-order terms) leads to the equation:

$$(M + dM) - M + Ndy - Qdz = 0 \tag{1.1}$$

or

$$\frac{dM}{dz} + N\frac{dy}{dz} - Q = 0 \tag{1.2}$$

Differentiating Eq. 1.2 with respect to z, the following equation is obtained:

$$\frac{d^2M}{dz^2} + N\frac{d^2y}{dz^2} - \frac{dQ}{dz} = 0 \tag{1.3}$$

Moment M, shear force Q and horizontal soil reaction p are given from the following well-known expressions:

$$\frac{d^2M}{dz^2} = E_pI_p\frac{d^4y}{dz^4} \tag{1.4}$$

$$\frac{dQ}{dz} = p \tag{1.5}$$

$$p = ky \tag{1.6}$$

where E_p is the modulus of elasticity of the pile and I_p is the cross sectional moment of inertia. Substituting Eqs. 1.4, 1.5, and 1.6 in Eq. 1.3, the governing equation of a pile subjected to lateral loads is obtained:

$$E_pI_p\frac{d^4y}{dz^4} + N\frac{d^2y}{dz^2} + ky = 0 \tag{1.7}$$

Neglecting the axial load N, Eq. 1.7 becomes:

$$E_pI_p\frac{d^4y}{dz^4} + ky = 0 \tag{1.8}$$

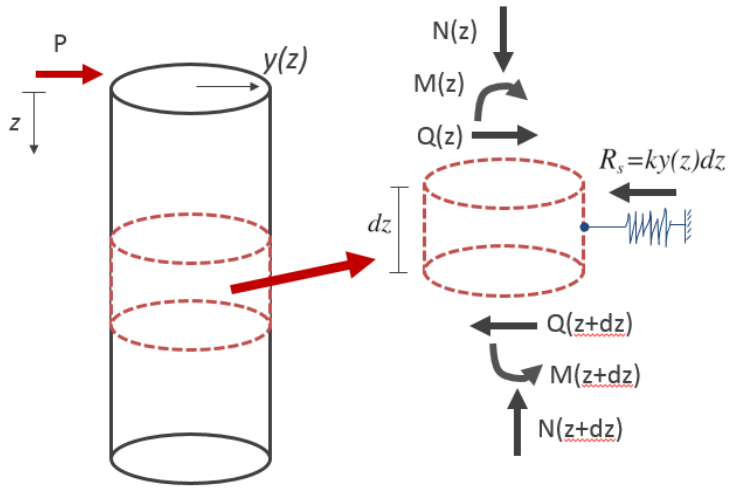

Figure 1.5: Forces on an infinitesimal beam element.

The general solution of Eq. 1.8 can be written as:

$$y(z) = \quad e^{\lambda z}\left[A\sin\lambda z + B\cos\lambda z\right] + e^{-\lambda z}\left[C\sin\lambda z + D\cos\lambda z\right] \tag{1.9}$$

where A, B, C, and D depend on the top and bottom boundary conditions at the pile tip and head, and λ is a Winkler parameter, given by the following expression:

$$\lambda = \sqrt[4]{\frac{k}{4E_pI_p}} \tag{1.10}$$

The original subgrade method assumed the soil to be linearly elastic and the soil modulus to vary with depth in a predetermined manner [65]. **McClelland and Focht** [62] implemented the finite difference technique in the Winkler formulation to solve the nonlinear problem of a laterally loaded pile. They introduced the concept of the soil resistance deflection curve, known as $p-y$ curve, which can be used to obtain values of the soil modulus with depth. These curves are nonlinear and can vary with depth. The elastic modulus is function of depth and deflection.

Due to its simplicity, the subgrade reaction method is widely employed in practice, and has gained increased popularity in recent years with the availability of software tools such as

COM624 [88], and its commercial version, called LPILE [91].

A brief summary of the $p-y$ method of analysis is presented in the following section.

1.4 General Introduction to *p-y* Curves

The $p-y$ method is a modification of the basic Winkler model, where p is the soil pressure per unit length of pile, and y is the pile deflection. Since the soil behavior is nonlinear, the soil resistance along the pile is modelled through independent non-linear springs with stiffness K $[F/L]$, as shown in Fig. 1.6. K is given by a series of nonlinear $p-y$ curves that are depth dependent. This formulation can easily treat a pile in layered soil deposit. Note that if the springs were spaced a unit distance ($s = 1$), the spring stiffness K would coincide with the Winkler modulus k.

The spring parameters can be described as follows:

- The subgrade reaction modulus, k, at a given depth, is defined as the secant modulus p/y. k depends on pile deflection, y, and depth, z, as well as the physical properties and load conditions, and it is not a soil property. k may be considered constant for small deflections (elastic, k_0) for a particular depth, but decreases with increasing deflection (Fig. 1.7b) [89].
- The ultimate soil resistance, p_u, represents the upper bound. The horizontal line (i.e. ultimate capacity) implies that the soil has an ideal plastic behavior and no additional loss of shear strength occurs with increasing strain.

The method is semi-empirical because the shape of the $p-y$ curves is determined from field load tests. **Cox et al.** [24] reported experiments from 1966 on fully instrumented test piles in sand and clay installed at Mustang Island. Based on the Mustang Island tests,

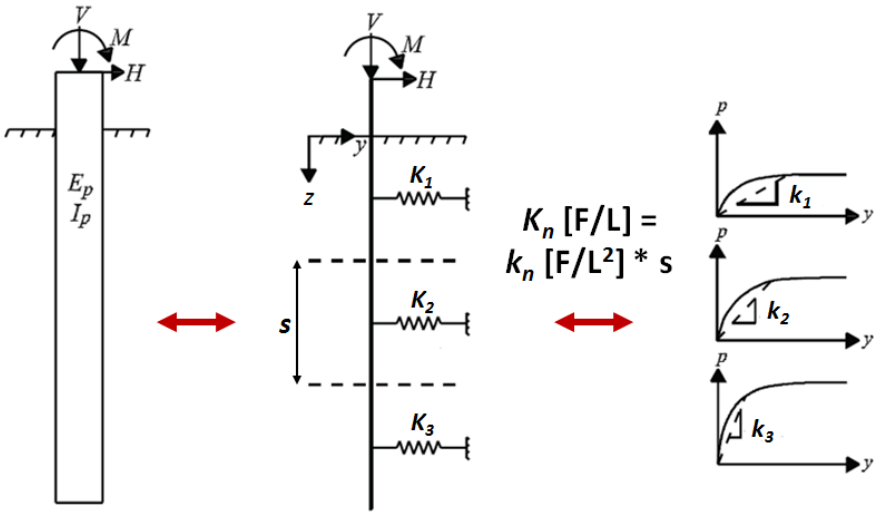

Figure 1.6: $p - y$ curve discretization.

Reese et al. [86] and **Reese et al.** [90] derived semi-empirical $p - y$ curve expressions for cohesionless and cohesive soils, respectively. These expressions became the state-of-the-art in the following years. **Murchison and O' Neill** [70] compared Reese et al.' s [86] $p - y$ curves with other simplified expressions (also based on the Mustang Island tests) by evaluating them against a database of lateral pile load tests. A hyperbolic form was found to offer better results compared to the original parabolic expressions [86]. This method was adopted by the American Petroleum Institute (API) for sands [8]. In 1970, **Matlock** [60] derived a $p - y$ formulation for clays based on the tests conducted in Lake Austin and reported by **Matlock et al.** [61].

The pile deflections, rotations, and bending moments are calculated by solving the 4^{th} order bending equation of the beam (Eq. 1.8) using finite difference or finite element numerical techniques. The pile is divided into a number of small segments and $p - y$ curves are used to represent soil resistance. The mathematical derivation for the various response profiles of the pile (e.g. deflection y, slope S, curvature ϕ, moment M, shear V, and soil pressure p)

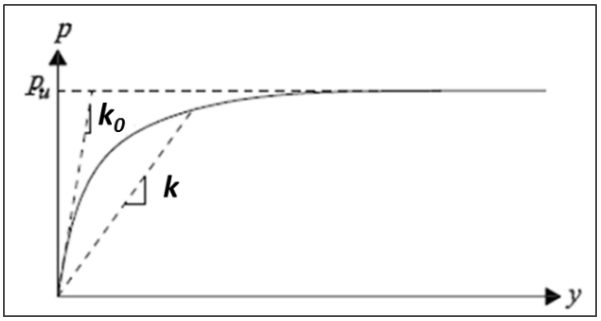

(a) Typical $p-y$ curve

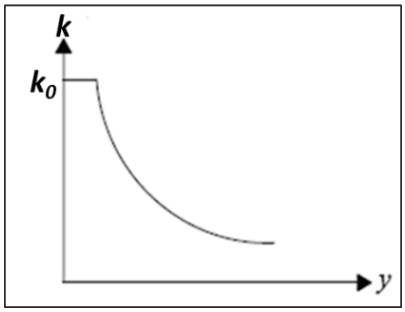

(b) Variation of k at a given point along the pile

Figure 1.7: General $p-y$ curve shape and variation of the stiffness with lateral displacement [89].

are presented in Eqs. 1.11 and Fig. 1.8 for the case of zero axial loading.

$$S = \frac{dy}{dz} \tag{1.11a}$$

$$\phi = \frac{d^2y}{dz^2} \tag{1.11b}$$

$$M = EI\frac{dS}{dz} = EI\frac{d^2y}{dz^2} \tag{1.11c}$$

$$V = \frac{dM}{dz} = EI\frac{d^3y}{dz^3} \tag{1.11d}$$

$$p = \frac{dV}{dz} = EI\frac{d^4y}{dz^4} \tag{1.11e}$$

The classical derivation procedure of experimental $p-y$ relationships follows a double-integration and double-differentiation process, starting with the internal pile curvature readings. After internal curvature measurements are obtained from strain gauges installed inside the pile, rotations and deflections, as well as bending moments, shear and lateral soil reactions in and around the pile are calculated.

Recent research has also proposed using in-situ measurements such as CPT or dilatometer test results to predict the p-y curves (e.g. Novello [77]; Robertson et al. [95] and [93]). But the applicability of the methods is very site dependent (Li et al. [53]).

The widely used API $p-y$ curves for predicting the static response of piles in cohesive and

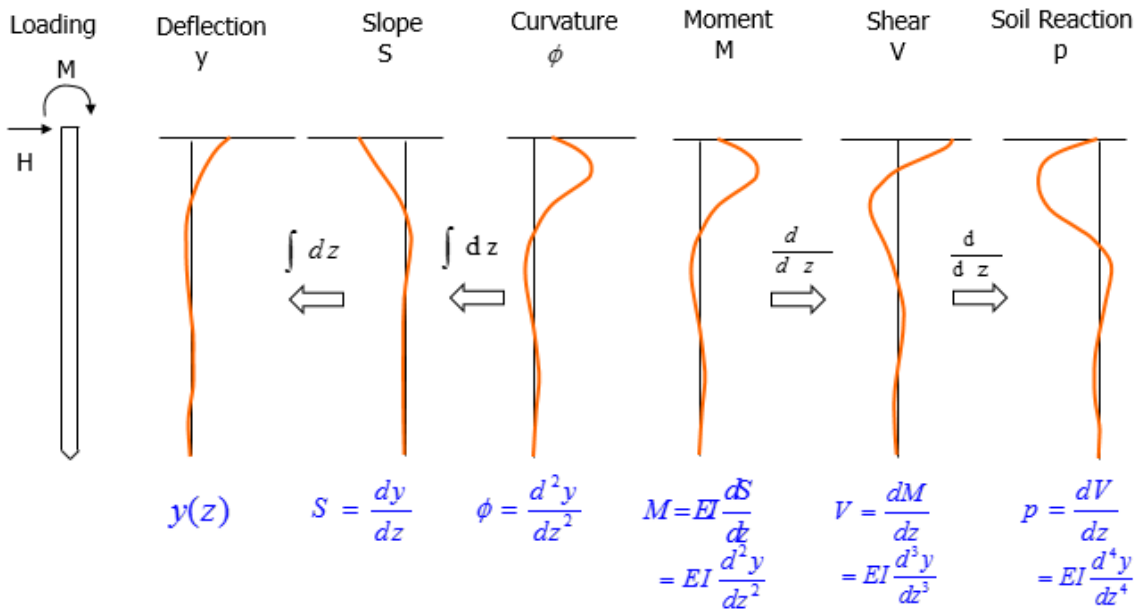

Figure 1.8: Schematic of p-y curves generation trough double derivation and double integration.

cohesionless soils are briefly presented below.

1.5 Review of Traditional *p-y* Relationships (i.e. API *p-y* Curves)

1.5.1 *p-y* Curves for Clays

Matlock [60] investigated the behavior of laterally loaded piles in soft clays with presence of free water. He proposed a parabolic $p - y$ curve (Eqs. 1.12, 1.13), characterized by a theoretical initial tangent modulus that is infinite at zero deflection (Fig. 1.9).

$$p = 0.5 p_u \left(\frac{y}{y_{50}}\right)^{1/3}, y < 8y_{50} \tag{1.12}$$

$$p = p_u, \quad y > 8y_{50} \tag{1.13}$$

The initial tangent stiffness relies on the deflection at 50% ultimate soil resistance of the $p-y$ curve (y_{50}), given by Eq. 1.14:

$$y_{50} = 2.5\varepsilon_{50}D \tag{1.14}$$

where D is the pile diameter and ε_{50} is the value of the strain corresponding to one-half of the maximum principal stress difference.

The ultimate resistance per unit length of the pile, p_u, can be calculated as the minimum of the two values obtained from the following equation:

$$p_u = min\left[\left(3 + \frac{\gamma z}{c} + \frac{J}{D}z\right)cD, \quad 9cD\right] \tag{1.15}$$

where γ is the unit weight of the soil, z the depth below the surface, c the undrained shear strength of the soil, D the pile diameter, and J is an empirical constant (0.50 for soft clays, 0.25 for medium clays).

The first failure mode accounts for the variation of the soil resistance within the upper zone close to the pile head and it is composed by three terms. The first value (3) is associated with the resistance at the surface, the second term ($\frac{\gamma z}{c}$) gives the increase with depth due to the overburden pressure, and the third term ($\frac{J}{D}z$) may be viewed as the geometrically related restraint that even a weightless soil around a pile would provide against upward flow of the soil. The second equation ($9cD$) yields the soil resistance at greater depths around a cylindrical pile.

Reese et al. [90] proposed a $p-y$ formulation to describe the response of stiff clays in the presence of free water, based on a pile load test on a 24-inch diameter pipe pile. The soil resistance at depth z for the value of p_u was calculated as the smaller of the two values defined in Eqs. 1.16 and 1.17. The quantities p_{c1} and p_{c2} are denoted as the ultimate resistance at

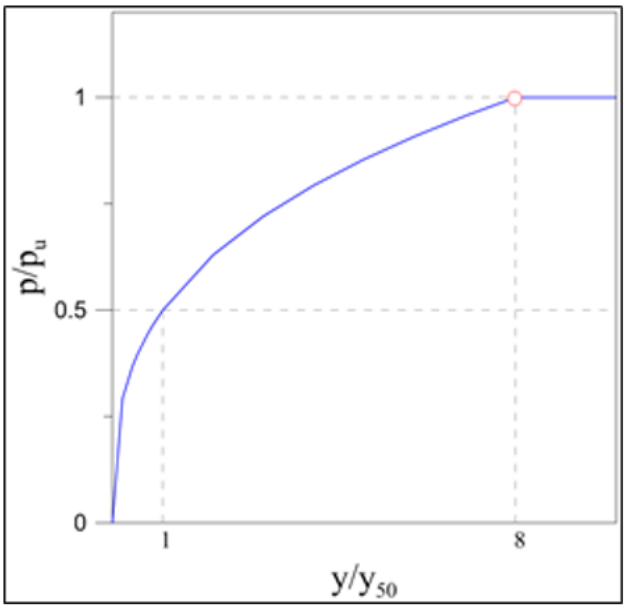

Figure 1.9: $p-y$ curve after Matlock [60].

shallow and deep depths, respectively.

$$p_{c1} = 2c_a D + \gamma' D z + 2.832 c_a z \tag{1.16}$$

$$p_{c2} = 11 c_u D \tag{1.17}$$

However, computed ultimate soil resistance p_c was found considerably higher than the experimental values $(p_u)_s$. Hence, ultimate resistance values were empirically adjusted by dividing the observed ultimate resistance $(p_u)_s$ by the computed soil resistance p_c, as follows:

$$A_s = \frac{(p_u)_s}{p_c} \tag{1.18}$$

The experimentally determined values of coefficient A_s (static loading) are a function of the normalized depth (z/D). The $p-y$ curve is composed by five parts (Fig. 1.10), obtained by the following equations.

1. Initial straight line, p_1:

$$p_1 = (k_{s,0} z)\, y \tag{1.19}$$

where $k_{s,0}$ can be taken from Table 1.2.

2. First parabolic portion, p_2 (Intersection with Eq. 1.19 $\leq$ y $\leq A_s y_{50}$):

$$p_2 = 0.5 p_u \left(\frac{y}{y_{50}}\right)^{1/2} \tag{1.20}$$

3. Second parabolic portion, p_3 ($A_s y_{50} \leq$ y $\leq 6 A_s y_{50}$):

$$p_3 = 0.5 p_u \left(\frac{y}{y_{50}}\right)^{1/2} - 0.055 p_u \left(\frac{y - A_s y_{50}}{A_s y_{50}}\right)^{5/4} \tag{1.21}$$

4. Second straight-line portion, p_4 ($6 A_s y_{50} \leq$ y $\leq 18 A_s y_{50}$):

$$p_4 = p_u \left[1.225 \left(A_s\right)^{1/2} - 0.75 A_s - 0.411\right] \tag{1.22}$$

5. Final straight-line portion, p_5 ($18 A_s y_{50} \leq$ y):

$$p_5 = p_u \tag{1.23}$$

Table 1.2: Initial coefficient of subgrade reaction, $k_{s,0}$, according to Reese et al. [90].

	Average undrained shear strength, c_a [kPa]		
	50-100	200-300	300-400
$k_{s,0}$(static) [MN/m3]	135	270	540
$k_{s,0}$(cyclic) [MN/m3]	55	110	540

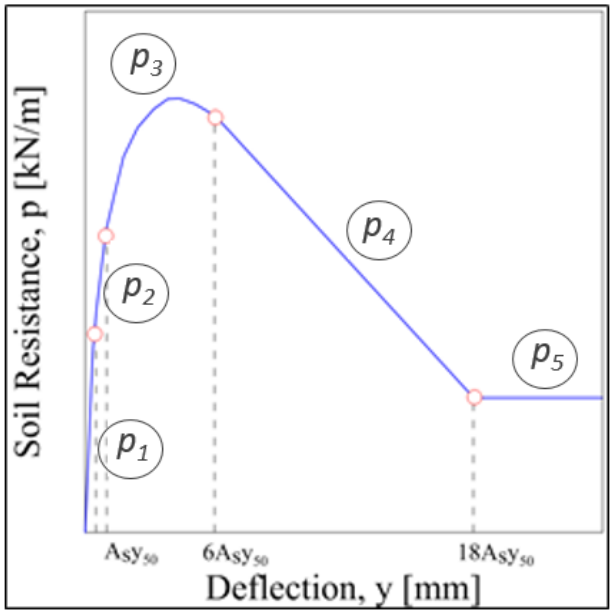

Figure 1.10: Schematic representation of $p - y$ curve after Reese [90].

1.5.2 *p-y* Curves for Sands

The $p - y$ method for sands was originally developed by Reese et al. [86]. Parallel to the study conducted by O' Neill and Gazioglu [78] for clays, API sponsored a study for sands conducted by O' Neill and Murchison [79] with the aim to simplify the original procedure by Reese et al. [86] without introducing significant fundamental changes to the approach. The proposed modification consisted of changing the mathematical curve shape of the $p - y$ relationship from a parabolic curve, as originally used in Reese et al. [86], into a hyperbolic shape.

Reese et al. [86] proposed a $p - y$ relationship that takes the different conditions above and below the water table into account. The $p - y$ formulation consists of three components as shown in Fig. 1.11: an initial straight line (p_1), a parabola (p_2), and a second set of straight lines (p_3 and p_4), assembled to one continuous curve.

The second to last straight segment ranging from (y_m, p_m) to (y_u, p_u), is bounded by an upper limit, which represents the ultimate soil resistance per unit length of the pile, p_u.

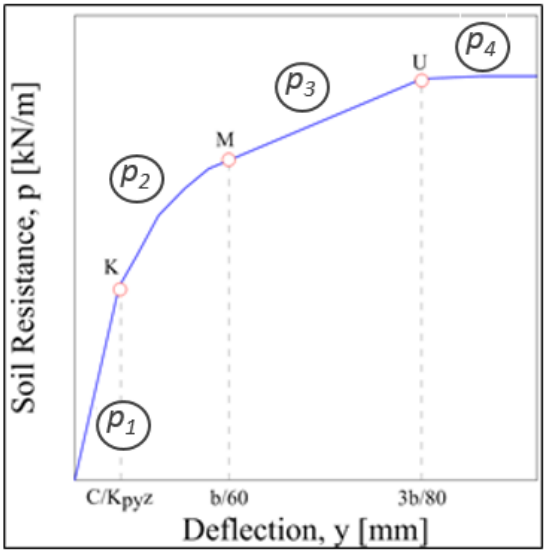

Figure 1.11: Schematic representation of $p-y$ curve after Reese et al. [86].

This ultimate resistance can be calculated at different depths according to the two following formulations:

$$p_{ct} = \gamma z[\frac{K_0 z \tan\varphi \sin\beta}{\tan(\beta-\varphi)\cos\alpha} + \frac{\tan\beta}{\tan(\beta-\varphi)}(D + z\tan\beta\tan\alpha) + K_0 z\tan\beta(\tan\varphi\sin\beta - \tan\alpha) - K_a D] \tag{1.24}$$

$$p_{cd} = K_a D\gamma z\left(\tan^8\beta - 1\right) + K_0 D\gamma z\tan\varphi\tan^4\beta \tag{1.25}$$

where p_{ct} (Eq. 1.24) is valid at shallow depths and p_{cd} (Eq. 1.25) applies to deep depths. The factors α and β, measured in degrees, can be estimated using the following relations:

$$\alpha = \frac{\varphi}{2} \tag{1.26}$$

$$\beta = 45° + \frac{\varphi}{2} \tag{1.27}$$

The angle β is estimated according to Rankine's theory, which is valid if the pile surface is assumed to be smooth. The factor α depends on the friction angle φ and load type. K_a and K_0 are the coefficients of active horizontal earth pressure and horizontal earth pressure at

rest, respectively:

$$K_a = \tan^2\left(45° - \frac{\varphi_{tr}}{2}\right) \tag{1.28}$$

$$K_0 = 0.4 \tag{1.29}$$

By comparing the theoretical ultimate resistance p_c (Eqs. 1.24 and 1.25) with the full-scale tests at Mustang Island [24], a poor agreement was found. Therefore, a coefficient A was introduced when calculating the actual ultimate resistance, p_u:

$$p_u = Ap_c \tag{1.30}$$

where the nondimensional coefficient A, for the ultimate soil resistance, is depending on the nondimensional depth z/D, as found in graph by Reese et al. [86] for both static and cyclic case.

The deformation corresponding to the ultimate resistance, p_u, is defined as $y_u = 3D/80$.

The soil resistance per unit length, p_m, at $y_m = D/60$ can be calculated as:

$$p_{ms} = B_s p_u \tag{1.31}$$

where B is a coefficient depending on the nondimensional depth z/D, as found in graph by Reese et al. [86] for both static and cyclic case.

The slope of the initial straight line, p_1, is defined by the initial coefficient of subgrade reaction $k_{s,0}$ $[F/L^3]$. It was suggested that k_s is zero at the ground surface and increases linearly with depth:

$$k_s = n_h \frac{z}{D} \tag{1.32}$$

This suggestion was based on experiments, which had shown that the initial slope of a lab-

oratory stress-strain curve for sand is a linear function of the confining pressure. Terzaghi [111] suggested values for the constant of horizontal subgrade reaction n_h $[F/L^3]$, as a function of the unit weight and the relative density of the sand. The values of n_h recommended by Terzaghi [111] are shown in Table 1.3. The values n_h obtained from the Mustang Island test [24] for the static case were 2.5 times the highest value reported by Terzaghi [111]. The values for the cyclic case were 3.9 times the highest value given by Terzaghi [111]. The values in Table 1.4 are recommended for static and cyclic loading.

Table 1.3: Values of n_h $[lb/in^3]$ for sands [111].

Relative Density	Loose	Medium	Dense
Above ground water table	8	24	65
Below ground water table	5	16	39

Table 1.4: Values of n_h $[lb/in^3]$ for sands [86].

Relative Density	Loose	Medium	Dense
Above ground water table	20	60	125
Below ground water table	25	90	225

The initial straight line ranging from 0 to p_1 is given by:

$$p_1 = k_0 y = n_h z y \tag{1.33}$$

The equation for the parabola, p_2, is described by:

$$p_2 = C y^{1/n} \tag{1.34}$$

where C and n are constants. The constants and the parabola' s start point (y_k, p_k) are

determined by the following criteria:

$$C = \frac{p_m}{y_m^{1/n}} \tag{1.35}$$

$$n = \frac{p_m}{m y_m} \tag{1.36}$$

$$m = \frac{p_u - p_m}{y_u - y_m} \tag{1.37}$$

$$y_k = \left(\frac{C}{n_h z}\right)^{n/n-1} \tag{1.38}$$

O' Neill and Murchison [79] proposed a $p - y$ curve formulation for sand above and below the water table (Fig. 1.12). This method resulted in the currently described sand $p - y$ criterion in API RP2A [8]. The hyperbolic expression is based on the testing of two identical instrumented piles installed at Mustang Island [24]. A total of seven load tests were performed on the piles consisting of two static tests and five cyclic tests. Both piles had a diameter of 24 in, a slenderness ratio of 34.4 and were installed in similar soil conditions. Expression for the proposed $p - y$ curve is presented in Eq. 1.39.

$$p = A p_u \tanh\left(\frac{n_h z}{A p_u} y\right) \tag{1.39}$$

where

$$p_u = min\left[\left(C_1 z + C_2 D\right)\gamma z, C_3 \gamma z\right] \tag{1.40}$$

C_1, C_2, C_3 are the coefficients determined according to internal friction angle (φ'), as found in graph by O' Neill and Murchison [79], and D and z are the pile diameter and depth, respectively.

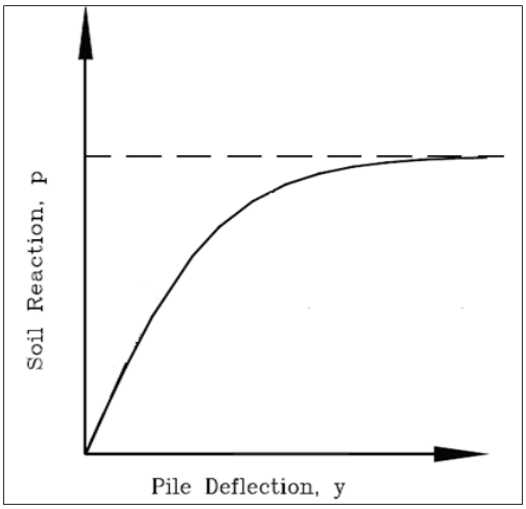

Figure 1.12: Schematic representation of $p - y$ curve for static loading after O' Neill and Murchinson [79].

1.6 Recent Research on *p-y* Curves: Selected Studies

The earliest recommendations on $p - y$ behavior date back to the 1950s and refer to work by Skempton [106] and Terzaghi [111]. Some of the pioneering experimental studies, as described above started in the early 60s and 70s, and include the work of Matlock [60], and Reese and Welch [90]. The biggest limitation in using $p - y$ formulations presented in Chapter 1.5 is the reliance on test results that stem from single, small-diameter driven piles or drilled shafts for specific types of soils. New types of pile foundations such as pile groups, micro piles, large-diameter drilled, driven and battered piles, or drilled displacement piles have been constructed since, and need more accurate design recommendations than currently available.

Significant progress in studying $p-y$ formulations has been made since 1980 and thereafter. The following sections will provide a brief discussion on selected studies that researched various geometric and demand aspects that influence the lateral load behavior of the pile, such as the influence of pile dimension, head fixity, type of load application, and group configurations.

1.6.1 Pile Diameter

The majority of early pile tests in literature were conducted on shafts with small diameters ranging from 0.3 m to 0.6 m. In turn, many recent studies focus on larger diameter piles and shafts to provide more appropriate design recommendations for geometries that differ from the small diameter pile research (e.g. Dunnavant et al. [28], Naramore and Feng [72], Ng et al. [75], Janoyan et al. [45], Hokmabadi et al. [38], Khalili-Tehrani et al. [47]). Larger diameter piles are capable of mobilizing more side friction and tip resistance and therefore early formulations are prone to under-predict the available capacities of recent pile geometries.

Stewart et al. [109] conducted field studies on reinforced concrete free-headed specimens with diameters of 0.6 m and 1.8 m, and found the specimen with a diameter of 1.8 m to mobilize a soil resistance (p) about 5 times greater than the smaller shaft. This increase stems predominantly from the contribution of ultimate soil resistance, p_u to the overall pile response [47]. Within the same testing program, Janoyan et al. [45] compared the experimentally derived p-y relationships for the 1.8 m diameter pile with recommendations by the American Petrolium Institute. Experimental formulations were found to have 60% larger capacity than the recommended API curves. For the smaller diameter pile (0.6 m), API and measured p-y curves were closer to each other; however, experimental p-y curves had approximately 20% less capacity than the API based estimate.

Juirnarongrit and Ashford [110] performed four tests on free-headed RC piles with diameters of 0.40, 0.60, 0.90 and 1.20 m, and conducted a comparison between experimental and standard curves. The API p–y curves for sands underestimated the measured soil resistance for the small diameter pile, whereas better agreement was found with larger piles. This finding is somewhat contradicting to the diameter-based increase recognized by Stewart et al. [109].

1.6.2 Pile Head Fixity

The rotational restraint at the pile head represents a critical boundary condition that influences the pile deflection and curvature profiles. An increase in rotational restraint (with the extreme case being a completely fixed pile head) leads to a reduction in lateral deflections, the introduction of two potential plastic hinge locations along the pile length, and the introduction of shear deformations in RC piles. Approximately 85% of the tests analyzed in the current literature review studied free-headed piles (e.g. Brown et al. [21] and [20], Kramer et al. [49], Ruesta and Townsend [100], Juirnarongrit and Ashford [110], Rollins et al. [96] and [99], Ismael et al. [41]). The remaining 15% of the tests were performed on hinged (e.g. Meimon et al. [64], Ng et al. [75]) or fixed head piles (e.g. Mokwa [66], Rollins and Sparks [98], Huang et al. [40], Walsh et al. [115], Lemnitzer et al. [52]).

Khalili-Tehrani et al. [47] compared test results from RC fixed and free headed pile researched by Stewart et al. [109] and Lemnitzer et al. [52]. It was observed that p-y curves derived from tests on free-head piles were up to 1.5 times stiffer than p-y curves derived from load tests on fixed head shafts. However, the ultimate fixed-head soil reaction p was up to 50% greater than the free-head pile soil reaction for a given lateral displacement and identical pile depths. Experimental curves were also compared with the API formulations for stiff clay, which revealed that the measured fixed-head pile had 100% larger capacity than the recomended API curves. The API model in turn overestimated the actual initial stiffness at small deflections (less than 50mm) by up to 30%. The authors propose a new set of p-y relationships for fixed head pile specimens in clay.

1.6.3 Effect of Cyclic Loading

In addition to strong cycling loading through seismic events or impact loading, wind, waves and thermal factors can produce more than 10^4 loading cycles during the typical design life of

a pile. While cyclic degradation was early known among foundation researchers (e.g. Sandeman [101]), Feagin [31] was the first researcher to document the observed loss of resistance in contractive soils under drained condition. He noticed a slight increase in displacement under repeated lateral load cycles, but a stabilization of displacements after 5 to 25 cycles. Matlock [60], Lee and Gilbert [50], Alizadeh [5], and Robertson et al. [94] tested piles in contractive soils in undrained conditions and noticed displacement increases of 10% between the first and repeated cycles at low load levels. For large load levels, displacement increases of up to 100% were observed, after which they tended to stabilize.

Turner et al. [113] summarized more than 82 load test case histories in an EPRI EL 5375 report that compares deep foundations for electrical transmission line structures subjected to static and repeated loading. Trends in drilled shafts were found to be very similar compared to driven pile studies mentioned above. Cyclic loading along with the draining condition has a different effect on cohesionless and cohesive soils.

Brown et al. [20] tested steel pipes in sand and noticed load differenced of 4% between the first and the 100^{th} cycle.

Rollins et al. [99] detected that the peak load was reduced by about 15% after only 15 cycles for a pile group in clay. Gaps play a significant role in reducing the resistance for small deflections. During the first cycle of loading, the shallower soils quickly mobilize their full strength in response to pile displacement due to their relatively low ultimate resistance, whereas deeper soils usually have a greater ultimate resistance and smaller pile displacement.

Other experimental studies that developed cyclic p-y curves were performed by Little and Briaud [54] with a typical number of 20 lateral loading cycles, and those by Long and Vanneste [55], whose experimental study included up to 500 cycles in some tests.

1.6.4 Group Configurations

Piles are frequently used in groups of closely spaced elements in bridges, dams, waterfront facilities and offshore constructions owing to the structural inefficiencies associated with high bending moments in connecting caps. Piles in closely-spaced groups behave differently than single, isolated piles because of pile-soil-pile interactions that take place within the group. The unequal distribution of load among piles within a group is caused by shadowing, gapping, and overlapping wedge effects, which results in a reduction of soil resistance (e.g. Brown et al. [20], Rollins et al. [97]). Model tests and full-scale tests indicate that piles are not influenced by group effects when center-to-center pile spacing exceeds 6 pile diameters ($6D$) in a direction parallel to the load, and when they exceed 3D measured in a direction perpendicular to the load (Mokwa [66]). Moreover, the resistance in the group piles is not uniform. Many researchers (e.g. Holloway et al. [39], Brown et al. [20]) observed that piles in trailing rows have significantly less resistance to a lateral loads than piles in the leading row, and therefore exhibit greater deflections. A common approach to incorporate group interaction effects, is the *p-multiplier* concept. *P-multipliers* are empirical reduction factors applied to the *p-y* curves for a single isolated pile and was originally suggested by Brown et al. [20]. This method accounts for the loss of soil resistance due to all pile-soil-pile interaction effects. Different values of *p-multipliers* are assigned to each row of the group. A review of the literature has shown that group interactions are driven by the following factors:

1. *Spacing*: Group interaction effects become progressively important in reducing lateral soil resistance as pile spacing decreases.

2. *Type of Soil*: Sand generally has a higher friction angle than clay and a wider passive wedge. As a result, more group interaction would be expected in sands than in clays (Rollins et al. [96]). Hereby the effects of rate of loading need to be considered.

3. *Pile Dimensions*: Mostafa et al. [68] showed that longer and larger piles would have

less pile-soil interactions. As the pile length increases, the relative contribution of the soil layers along the pile are more homogenous and the pile soil interactions along the shaft length decrease.

4. *Installation Effects*: The driving process is expected to increase the soil density by making the soil stiffer. Huang et al. [40] reported that bored pile group construction appeared to loosen the soil surrounding the piles, whereas the driven pile construction caused a densifying effects.

5. *Deflections*: Group interactions have been found to vary with the group deflection. The bigger group deflection, the smaller the *p-multiplier* (e.g. Huang et al. [40], Rollins et al. [96]).

6. *Head Fixity*: Head fixity influences the amount of measured deflections, as shown in two similar studies conducted on a 3*3 pile group with a 3-D spacing in sand by Huang et al. [40] and Rollins et al. [96]. For the fixed headed concrete pile group, Huang et al. [40] observed deflections of approximately $0.02D$, whereas Rollins et al. [96] measured deflections 10 times larger with free headed steel pile configuration. The fixed headed pile group was shown to exhibit significantly smaller reductions in soil reaction (i.e. the *p-multipliers* were larger) than for the free-headed pile group.

1.7 Limitations of *p-y* Curves

The readily available implementation of traditional $p-y$ relationships in commonly used design software makes the subgrade reaction method an attractive and economical tool within the geotechnical community. Yet its principal limitations include the lack of a strong theoretical basis for $p-y$ curves and the limited verification through instrumented load tests [112]. Even though recent research, as described in Chapter 1.6, has provided substantial

knowledge, and advanced our understanding of nonlinear performance behavior under specific boundary conditions, $p-y$ formulations have not received significant revisions since their original formulation in the 1960s and 1970s [23].

A key research objective of this research study is to fill vital data gaps and generate enhanced understanding for the design of laterally loaded pile foundations through an integrated experimental-numerical research exercise. Selected limitations with existing modelling approaches will first be reviewed to identify the experimental research needs and to supplement the new test data:

1. Conventional experimentally derived $p-y$ curves were based on a limited number of sampling points along the pile length (typically, < 10 points), resulting in unreliable data fitting especially for long piles. Pioneering work performed by various researchers utilized single sets of instrumentation (e.g. Matlock [60], Reese et al. [90]), while recent studies recognized the importance of redundancy of internal sensors (e.g. Wallace et al. [114]). The need for more precise measurements is highlighted by the degree of uncertainty amplified by double integrating and double differentiating the strain readings (i.e. pile curvature readings) for y and p, respectively.

2. Since 1999, various researchers (e.g, Wallace et al. [114], Anderson et al. [7], Coutinho [108]) have implemented nonlinear material models to account for the variation of bending stiffness (EI) along the pile length. However, most commonly used formulations such as API RP 2A [8] do not account for pile nonlinearity. In addition, double integration and double derivation techniques implicitly assume that planar pile cross-sections remain plane, but this assumption has received little investigation in the literature [22]. Conversely, recent studies have shown a significant influence of nonlinear structural shear deformations at the cross-sectional plane; these influences have not yet been implemented in any derivation procedures [59].

3. Boundary Conditions: Experimentally derived $p-y$ curves are significantly affected by head fixity conditions, primarily due to the different curvature profiles developed for the same level of pile-head displacement. Research on pile head fixity has revealed that $p-y$ curves derived for free-head conditions are stiffer than those obtained for head-restrained (i.e. fixed-head) conditions (e.g. Khalili-Tehrani et al. [47]), which has been attributed to the mobilized vertical shearing resistance t during free-head pile rotation. Current design guidelines do not incorporate the influence of mobilized vertical shearing resistance. This effect is less pronounced for fixed-head piles and is suppressed below the depth of the passive soil failure wedge (i.e. $3D$, where D is the pile diameter), where soil resistance is only due to compression. With minor exceptions, this effect has not yet been investigated theoretically nor have these frictional stresses been measured in experimental studies (e.g. Mylonakis [71]). Additionally, internal shear-flexure-interaction is not captured in any existing analytical methods, but known to contribute substantially to lateral pile head displacements of fixed head piles [59]. Similarly, fixity conditions at the pile base (e.g. tip fixity through rock-socketing) pose complex soil-rock-structure interaction demands on the design. Major inhibitors are lack of validated $p-y$ formulations for rock-type materials, and complicated interaction mechanisms at the soil-rock interface as a result impedance contrast between soft soil and strong rock layers.

4. Current parabolic $p-y$ formulations (i.e. $p-y$ curves with displacement formulations $=\sqrt{y/y_{50}}$) cannot inherently capture the elastic stiffness at small displacement levels. Differentiation of the displacements yields negative exponents, which exhibit an asymptotic behavior (i.e. infinite stiffness). Overestimation of the initial stiffness, as found in the API RP 2A recommendations, has been extensively verified through experimental studies (e.g. Khalili-Tehrani et al. [47]).

5. As described by Briaud et al. [16], the influence of horizontal side friction on $p-y$

curves (known as the "pile diameter effect") is assumed linear in current formulations. The contribution of side friction to the overall soil reaction has been estimated by subtracting the direct soil pressure recorded with conventional pressure sensors from soil resistance (p) [16]. This assumption is only applicable to loose, dry sands (i.e. no gapping). No experimental data exist, where side friction and direct pressure are accurately separated. Dimensional analysis indicates that the initial $p - y$ stiffness increases linearly with pile diameter for soils with linearly increasing soil stiffness E_s (e.g. Gibson soil). However, for soils with homogeneous or parabolic stiffness profiles, the $p - y$ relationship is either independent of pile diameter or dependent by a factor equal to $D^{0.5}$ [69]. In addition, modern foundation construction practice often involves foundation diameters that significantly exceed diameters tested in earlier studies ($\geq$ 4 ft), leading to costly over-conservatism (Ahlberg [4]). An excellent example is the design of large diameter monotube foundations for wind turbines using $p - y$ curves derived from lateral load tests on small diameter piles.

6. Incomplete knowledge of pile installation effects: Pile driving results in an increase in lateral soil stress and generates significant strain at the pile-soil interface, which yields an offset when subjected to additional lateral loading. This offset is not considered in traditional $p - y$ formulations. Installation effects are strongly pronounced in clays, where thixotropic effects and pore pressure generation cause temporary loss of strength during pile driving (McVay et al. [63]; Dyson and Randolph [29]). Similarly, bored pile construction may result in a decrease in lateral soil stress and generates strain at the pile-soil interface.

7. Limited information exists about how to properly integrate dynamic and cyclic behavior and quantify stiffness degradation, strength deterioration, and the effects of unloading and reloading (Makris et al. [57]; Boulanger et al. [13]; Choi et al. [23]). This information is crucial for bridges and buildings, but also for offshore and energy

structures (e.g., wind towers, transmission line structures).

8. The lack of exact limit-analysis solutions poses significant challenges in predicting the ultimate soil resistance for piles in sands (Loukidis and Vavourakis [56]). Exact limit-analysis solutions are available, though, for piles in clays (Randolph and Houlsby [84]).

9. The coupled effect of $p-y$ and $t-z$ relationships (i.e. biaxial bending and bending under different axial loading levels) is not properly quantified. 3D plasticity formulations are required to account simultaneously for the effects of multiaxial loading (Novak et al. [76]); however, this effect cannot be addressed accurately given the lack of available experimental data under combined loading.

The research studies pursued in this PhD thesis seek to help address selected limitations as outlined above by specifically focusing on limitations (1) – (4) through combined experimental and numerical studies. The ultimate objective of this exercise is to incrementally eliminate uncertainties associated with pile analysis and provide knew understanding for design in practice.

Chapter 2

Research Motivations and Objectives

Subgrade reaction methods, as implemented through the *p-y* curve analysis algorithm, remain the most globally utilized analytical tool to characterize the response of deep foundations. The method offers practical advantages such as the prediction of fully nonlinear lateral load-deflection response, the ability to incorporate multi-layered soil profiles, the integration of nonlinear stiffness (*M-EI*) behavior, and a completed description of structural demand parameters (shear, moment, displacement, and rotation).

As identified before, its implementation in commonly used design software makes it an attractive and economical tool within the geotechnical community. Yet its principal limitations include the lack of a strong theoretical basis for *p-y* curves and the limited verification through instrumented load tests (Turner [112]). As a result, current deep foundation engineering is driven by uncertainty that results in outrageous overdesign, often by factors of three or four, ultimately costing taxpayers hundreds of thousands of dollars.

Performance- based frameworks, grounded in deformation and displacement driven response evaluation, and ubiquitous in other areas of geotechnical engineering (e.g. geotechnical earthquake engineering), can provide the foundation engineering field with integrated experimental-

numerical, and risk-informed approaches that are verified through statistical simulations and are capable of providing next-generation response functions for infrastructure foundation systems. These frameworks could offer more accurate and parsimonious design solutions (avoiding overdesign and therefore requiring less material), spurring the introduction and implementation of novel instrumentation technologies and sustainable materials that reduce the carbon footprint, such as green concrete. In addition, a performance-based design approach will accelerate the transition to use of high-performance materials (e.g. self-healing concrete, high-strength steel) with permanently integrated integrity assessment capabilities (e.g. hollow rebar cross-hole sonic logging (CSL), temperature integrity testing (TIP)) by providing a validated design platform to accurately characterize a foundation's response behavior.

With the objective of increasing our knowledge in current areas of p-y limitations as identified in Chapter 1.7, and to assess potentially new technologies to help establish a performance-based design framework for foundation design over the next decade, a key research objective of this study is to fill vital data gaps and generate enhanced understanding of and new formulations for the design of laterally loaded pile foundations through an integrated experimental-numerical research program.

2.1 Research Objectives

Specifically, the following objectives are pursued as part of this PhD research:

1. Provide new data for deep foundations with geo-structurally complex boundary conditions, (i.e. various levels of fixity at the pile base) through coordinated experimental and numerical studies on model-scale test specimens. This will remedy the current shortage of experimental data and pilot interaction curves investigating SSI effects of

intermediate pile geometries.

2. Explore physical damage evolution, deformation patterns and failure mechanisms, associated with the complex response mechanism observed in free-tip and fixed-tip piles, and provide fundamental understanding of the complex internal behavior and SSI mechanisms affecting pile foundation systems.

3. Examine the use of advanced construction materials, such as high-strength polymer concrete and innovative polymeric reinforcement materials to assess its suitability for commercial introduction into routine foundation design practice.

4. Introduce innovative experimental tools to improve our fundamental understanding of complex three-dimensional (3D) soil-structure interaction (SSI) by extracting volumetric measurements in deep foundation systems that could not be obtained in geotechnical engineering with any known method or device to date. The proposed instrumentation is groundbreaking in that it will be the first attempt to measure 3D strains experimentally in foundation engineering using embedded sensor technology. Successful completion will eliminate uncertainties, by facilitating direct measurements superior to inverse data analyses.

5. Utilize advanced computational techniques such as machine learning approaches and hyper parametric optimization algorithms to explore a better description of curvature and moment data for the derivation of nonlinear resistance functions.

6. Develop validated nonlinear models to verify the overall response behavior and parametrically study the demand and response relationship by strategically varying critical model input parameters to provide a complete physical understanding of deep foundation behavior and a more accurate (and safer while more economical) foundation design framework for a broad range of applications.

7. Provide a performance assessment of the experimentally-numerically derived design

formulations of laterally loaded pile foundations in loose sands through comparison with traditional analytical and numerical analysis procedures.

2.2 Structure of this Dissertation

Following the general introduction to laterally loaded foundation elements provided in the current and previous Chapters (Chapters 1 and 2), Chapter 3 presents the core of this dissertation research and provides a detailed description of the experimental research program. Four model scale pile specimens are placed into a soil container, filled with medium to loose sand and subject to lateral loading until complete pile failure is obtained. The chapter will describe the test setup, the material properties, the construction sequence, the test specimen geometry and reinforcement, the test instrumentation, the test observation including a description of damage progression and failure evolutions and conclude with fundamental test results. Test results will comprise of a complete description of pile head load deformation relationships, and the documentation of representative sensors response histories, such as strain gauges, displacement transducer, and soil pressure sensors. Preliminary processed test data, such as curvature profiles, will be included as well.

Chapter 4 will built on Chapter 3 by providing a more thorough analysis and discussion of the test results. It will include a quantitative comparison among the model scale specimens and describe the performance with different specimen materials. In addition, Chapter4 will focus on the derivation of shear data, including internal shear strains using the tetrahedral instrumentation developed in Chapter 4, and external strains using traditionally installed strain gauge instrumentation at the pile perimeter. This data is important for the comparison between analytical engineering demand parameters and experimental observations.

Chapter 5 is dedicated to the derivation of soil resistance functions during lateral loading.

Chapter 5 will first discuss the fundamental mathematical procedure associated with the derivation of p-y relationships from experimental curvature measurements, and then describe the traditional and alternative fitting procedures employed during the data analyses. Chapter 5 will contain a major contribution in providing new resistance function for intermediate piles with different structural boundary conditions in loose sands, and compare newly obtained formulations with code based recommendations. This chapter will also include a detailed description of the machine learning techniques employed to fit curvature and moment data for consecutive double integration and derivation procedures. A comparison of the overall pile performance and the predicted performance using analytical formulations will also be provided.

Chapter 6 will close with conclusions drawn from the experimental and numerical studies and provide suggestions for future studies, including the further development of instrumentation, and recommended additional testing for specific pile –soil boundary conditions to address more limitations as identified in Chapter 1.

Appendix A describes the proof of concept testing associated with an innovative instrumentation methodology, based on a tetrahedral strain gauge carrier to capture internal 3D strains. The Appendix will first explain the selection of materials, followed by the construction of small scale test specimens, the assembly of the instrumentation carriers, the attachment of the sensor and the analysis of the test results. A comparison between the numerical results using 3D FEM software and the results of the small scale testing program will be made.

Chapter 3

Model Scale Experiments

A series of model-scale single pile experiments was conducted to study the nonlinear pile soil interactions between four pile specimens placed in sand with different geometries, reinforcement, and boundary conditions. Table 3.1 presents a general overview of all four test specimens. The test setup and soil material were identical for all four test specimens and are described in detail in subchapter 3.1. Hereafter, Chapter 3 continues to provide details pertaining to each individual pile specimen, i.e., the specimen instrumentation, specimen reinforcement, loading and test results.

The four pile specimens are briefly summarized:

1. *8 in Polymer Concrete Pile with Steel Reinforcement* - Polymer concrete and steel reinforcement were used for this pile specimen. Tetrahedral strain gauge carriers and longitudinal strain gauges were used as internal instrumentation; external sensors consisted of surface strain gauges in rosette configuration, LVDTs and string potentiometers. The laminar soil box was restrained through external bracing, but limited lateral movement occurred at the top of the box at larger horizontal displacement levels.

2. *8 in Regular Concrete Pile with Geotextile Reinforcement* -Regular 4 ksi concrete was used in combination with innovative stiff polymer grids (square aperture size = 1.0 in) in place of traditional steel reinforcement. This pile was instrumented with internal strain gauges placed on two opposite sides of the pile and attached to the reinforcement grid. The laminar soil box was fully braced and restrained from moving.

3. *8 in Polymer Concrete Pile with Geotextile Reinforcement* - This specimen was constructed with polymer concrete similar to Pile *1*. The reinforcement had the same mechanical properties of the one used in Pile *2*, but the aperture size was increased (square aperture size = 1.6 in). Internal strain gauges were installed on two opposite longitudinal sides. The laminar soil box was fully restrained from moving.

4. *10 in Polymer Concrete Pile with Steel Reinforcement in Bedrock* - This pile specimen was constructed with a larger pile diameter, but similar construction materials. Concrete and reinforcement, as well as longitudinal and transversal ratios, stayed the same as in Pile *1*. This test investigates the pile response under tip fixity condition. The pile tip is embedded in a 42 inch rock-socket, simulated through concrete. Pile instrumentation consisted of tetrahedral gauge carriers, external and internal strain gauges, and LVDTS and string pots. The laminar soil box was fully restrained against lateral movement.

Table 3.1: Model scale experiments overview.

Specimen	**Pile 1**	**Pile 2**	**Pile 3**	**Pile 4**
Diameter [in]	8	8	8	10
Length [in]	120	120	120	125
Concrete Material	Polymer Concrete	Regular Concrete	Polymer Concrete	Polymer Concrete
Reinforcement Material	Steel: 6-#3 long. bars (ρ_l= 1.3%); 5-in diam #3 ties at 8 in (ρ_s= As/Ag= 0.8%)	Geogrid100: Aperture Size =1 in x 1 in	Geogrid150: Aperture Size= 1.6 in x 1.6 in	Steel: 2-#3, 4-#4 long. bars (ρ_l= 1.3%); 7-in diam. #4 ties at 8 in (ρ_s= As/Ag= 0.8%)
Head Boundary Condition	Free	Free	Free	Free
Tip Boundary Condition	Embedded	Embedded	Embedded	Fixed
Soil Material	Sand (D_r=50%)	Sand (D_r=50%)	Sand (D_r=50%)	Sand (D_r=50%)

3.1 Test Setup

3.1.1 Soil Container

All piles were installed in a laminar soil box (LSB) with inside dimensions of 39 in in width (W), 73 in in length (L) and 93 in in height (H). The laminar box consists of 19 four-inch thick aluminum frames. The laminar frames are separated by steel rollers with a diameter 43/8 in. During testing, the box was restrained using a rigid bracing systems, consisting of concrete reaction blocks, wooden braces and steel girders as shown in Fig. 3.1. In addition, the bottom of the laminar soil box was rigidly attached to the laboratory's strong floor,

and horizontally restrained through steel beams placed between the laboratory's strong wall or adjacent concrete reaction blocks and the box bottom. It is important to mention that lateral movement was observed and measured during the test of Specimen *1*. A maximum horizontal displacement of 0.5 inch at the top of the laminar box in the push direction (i.e. West side) was recorded. Hereafter, and in order to avoid further movements for consecutive pile tests, the soil box restraints were reinforced through high-strength dywidag rods and a set of steel chains anchored into the strong wall. Figures 3.1a and 3.1b show the initial and upgraded bracing system, respectively. Figure 3.2 presents the elevation and the plan view of the fully restrained laminar soil box, with details on the vertical and horizontal restrains.

The instrumented piles were installed in the center of the laminar soil box and secured through temporary bracing during sand placement. This construction process sought to replicate the lateral stress condition around drilled shaft foundations. Temporary bracing was progressively removed as the soil layers reached higher elevations. The top of the pile was held in place through chains secured on the reaction wall. Figure 3.3 shows photographs during pile installation and sand placement.

(a) Initial wooden bracing.

(b) Reinforced wooden bracing.

Figure 3.1: Laminar soil box' s bracing.

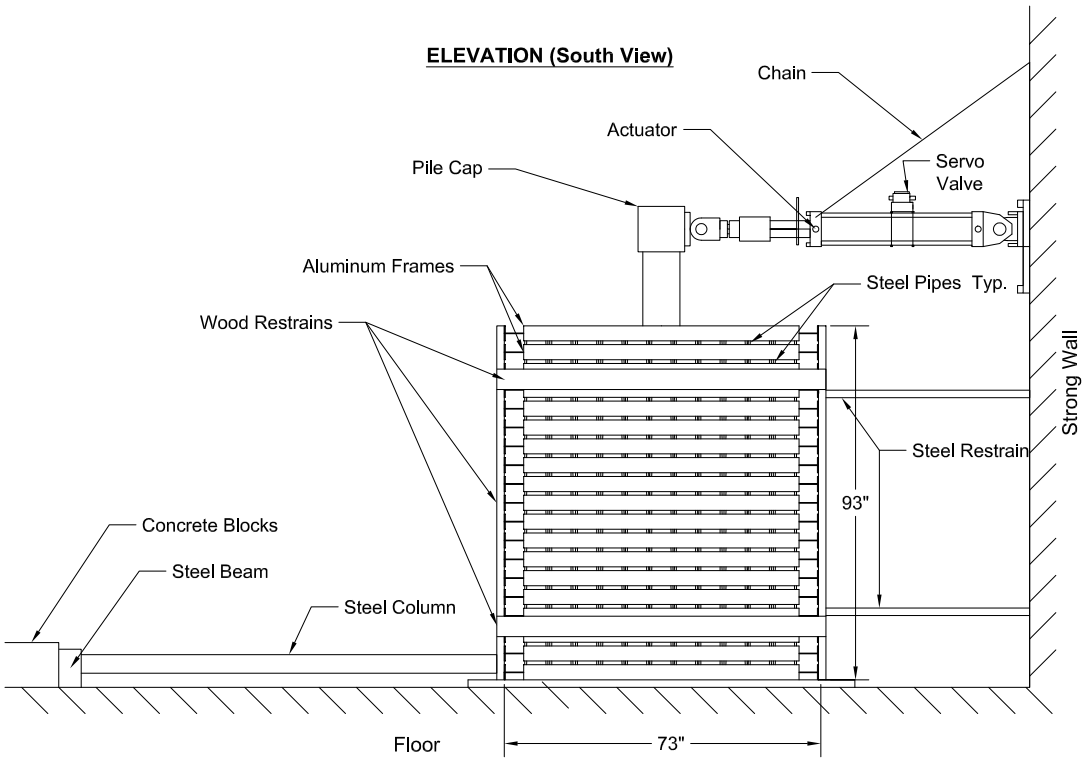

(a) Elevation view.

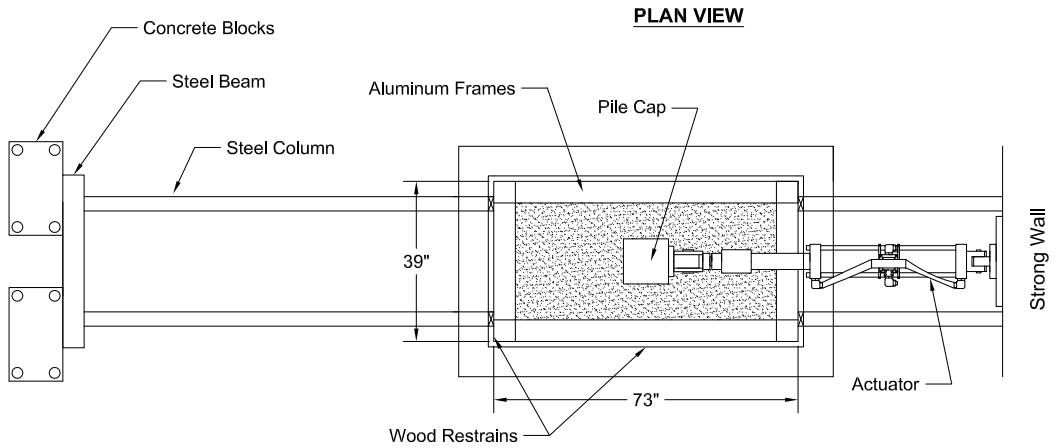

(b) Plan view.

Figure 3.2: Laminar soil box' s setup.

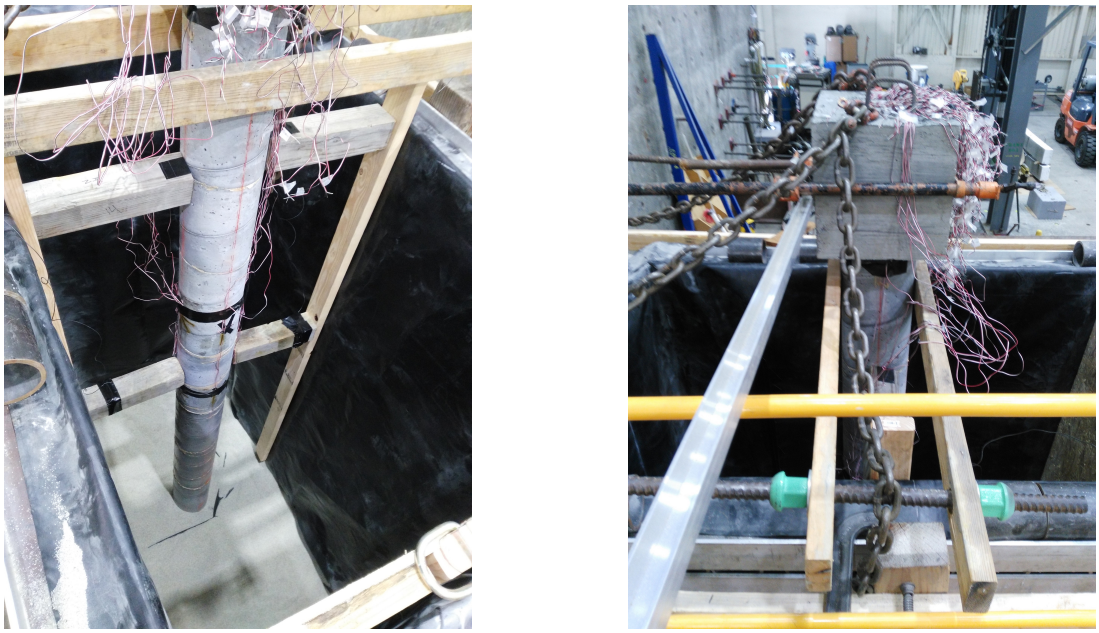

(a) (b)

Figure 3.3: Pile temporary bracing.

3.1.2 Soil Material Properties and Soil Placement

The fill material consisted of commercially available sand known in the construction community as #16 Industrial Sand. The material was acquired through a local supplier (P.W. Gillibrand). The selection of sand was motivated by the ease of earthwork constructability (i.e. placement through pluviation), as well as the limited availability of lateral load test data sufficiently instrumented to derive p-y relationships for reinforced concrete piles in sand [56]. The soil characterization program consisted of laboratory testing including soil classification, unit weight, and compaction. Dilatometer testing was performed at the end of pile testing.

Laboratory Tests

Soil Description and Index Properties The #16 sand is a clean, washed, and fine sand. The plot of the grain size distribution curve, in general accordance with ASTM D422, is shown in Fig. 3.4. About 0.44% of the sand passes the No. 40 sieve and 0.02% passes the No. 200 sieve. The coefficient of uniformity is 1.78, the coefficient of curvature is 1.05, and the Unified Classification is SP. The specific gravity of solids, determined in general accordance with ASTM D854, is 2.63. The sand is poorly graded.

Standard Density Relationships The moisture-density relationship was determined for the #16 Industrial Sand using the modified Proctor procedure (ASTM D1557). The maximum dry unit weight was found to be 120 pcf at an optimum water content of 11%. The maximum and minimum densities, in general accordance with ASTM D1157 and ASTM D4254, are 120 and 90 pcf, respectively. Fig. 3.5 shows the compaction curve and the zero-air-voids curve.

Shear Strength Shear strength of the #16 Industrial Sand was determined via direct shear testing, in accordance with ASTM D3080. As shown in Fig. 3.6, three confining pressures were applied to the specimen. The selected pressures were representative of the average overburden pressure of the soil at the depths of 23.6 in, 47.2 in, and 70.9 in. The friction angle was found to be 44° and the average cohesion value of 0.7 psi.

Table 3.2 summarizes the soil properties determined through the laboratory investigation.

Table 3.2: #16 Industrial Sand physical properties.

Sand Properties	
Percentile Sand Grain Diameters D_{10}, D_{30}, D_{60} $[mm]$	0.73, 1, 1.3
Uniformity Coefficient, C_u	1.78
Coefficient of Curvature, C_c	1.05
Particle Density, G_s	2.63
Maximum Dry Unit Weigth, γ_d^{max} $[lb/ft^3]$	120
Minimum Dry Unit Weigth, γ_d^{min} $[lb/ft^3]$	90
Minimum Void Ratio, e_{min}	0.37
Maximum Void Ratio, e_{max}	0.8
Friction Angle,φ [°]	43.5
Cohesion, c [psi]	0.7

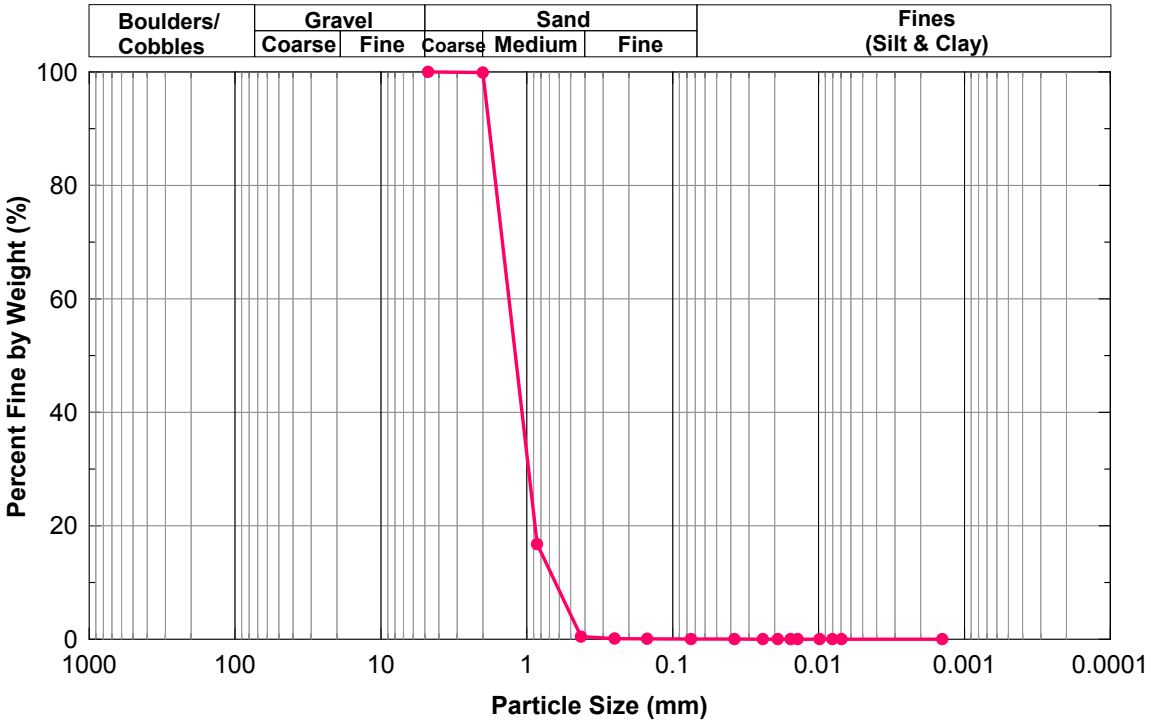

Figure 3.4: #16 Industrial Sand gradation curve.

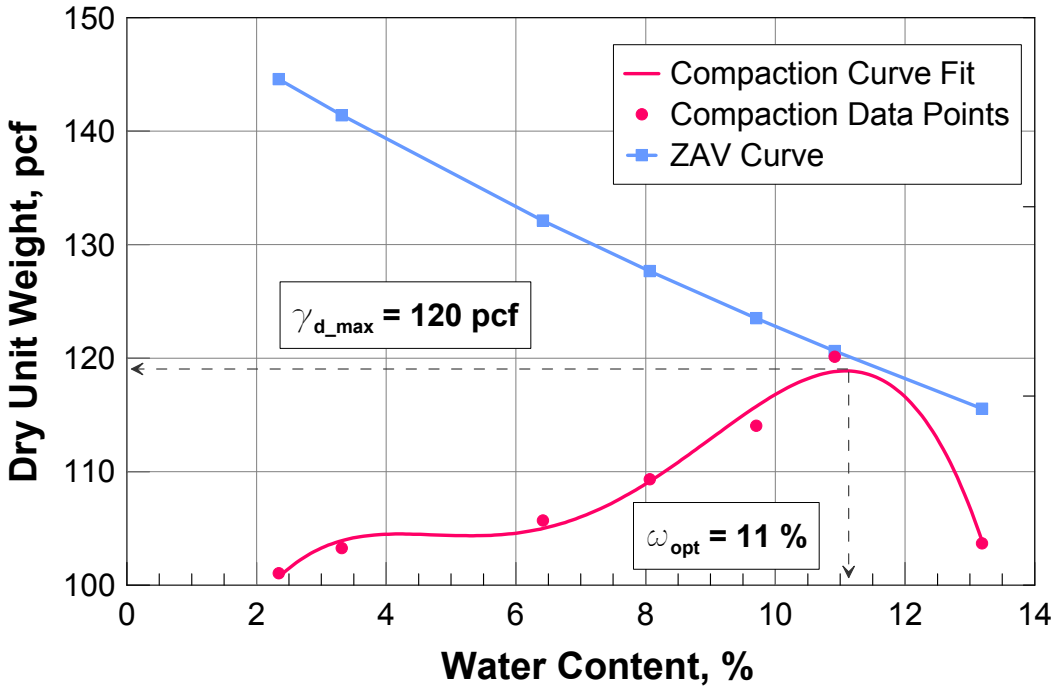

Figure 3.5: #16 Industrial Sand compaction curve.

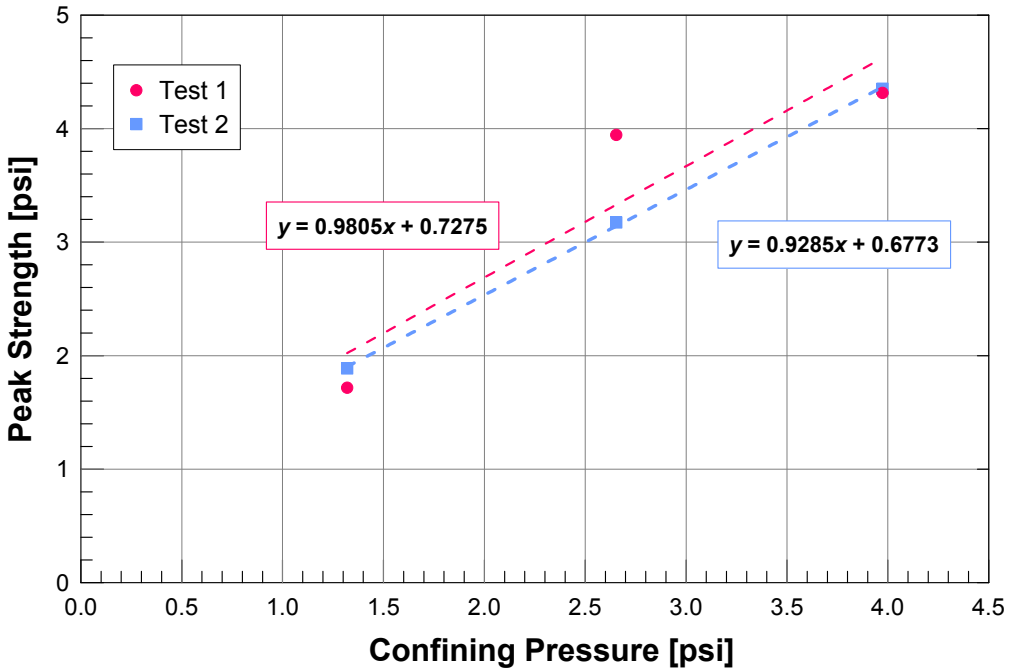

Figure 3.6: #16 Industrial Sand direct shear test.

In-Situ Tests

Dilatometer testing (DMT) was performed in the laminar soil box at the end of Piles *1* and *2* tests. DMT measurements were taken at approximately 20-inch intervals to a maximum depth of about 85 in. To the extent possible, the DMT tests were performed in accordance with the information and recommendations given in Schertmann [102] and Marchetti et al. [58]. The DMT soundings were primarily used as qualitative means of identifying changes in the soil stratigraphy.

Soil Placement

An important requirement for the experiments was the ability to generate a soil profile that was uniform and repeatable for all pile tests. The dry pluviation technique was used to place the sand into the laminar soil box. The target relative density was selected as medium-dense corresponding to $D_r = 40\%$ and 60%.

A pluviator was designed, constructed and calibrated. The system is shown in Fig. 3.7. The pluviator consisted of a wooden hopper (W= 29.5 in, L= 43.0 in, and H= 34 in), with a 8 in hole in the center. A No. 6 sieve was attached to the opening to regulate the material flow. In addition, the mass flux was controlled by a valve, which could be opened and closed. The device was moved during the pluviation process by a three-axis crane in order to cover the entire surface of the laminar soil box (Fig. 3.8a).

In order to achieve a relative density between 40% and 60%, a calibration procedure was conducted in which the pluviator was positioned above the laminar soil box and three Proctor molds with known volume and weights were positioned at different elevations within the laminar soil box. Upon filling the proctor molds with dry sand (Fig. 3.9a), the weight-volume relationships were used to back-calculate the sand densities. The mold has dimensions of 4

in in diameter and 4.56 in of height; the thickness of the mold base is 0.59 in.

The pluviator was tested with a full aperture, which corresponds to a flow rate of 4 in^3/sec. Five different falling heights were evaluated: 20, 40, 60, 80, and 100 in. The reference distance was measured between the lower side of the sieve and the surface where the collection mold was placed. In order to narrow the measurement results' confidence intervals, at least three measurements per drop height were performed. Table 3.3 shows the average relative density, D_r, values obtained from the samples used in the calibration phase. The tests showed that the relative density for this particular type of sand was not significantly influenced by the increase of drop height with in the considered range, as shown in Fig. 3.9b. The relative density was determined from:

$$D_r = \frac{\gamma_d - \gamma_d^{min}}{\gamma_d^{max} - \gamma_d^{min}} * \frac{\gamma_d^{max}}{\gamma_d} * 100 \tag{3.1}$$

where γ_d is the specific weight of the specimen, γ_d^{max} and γ_d^{min} are the maximum and minimum specific weights for the sand, obtained trough the ASTM D 1557 and ASTM D 4254-16 procedures, respectively. These values are included in Table 3.2.

(a)

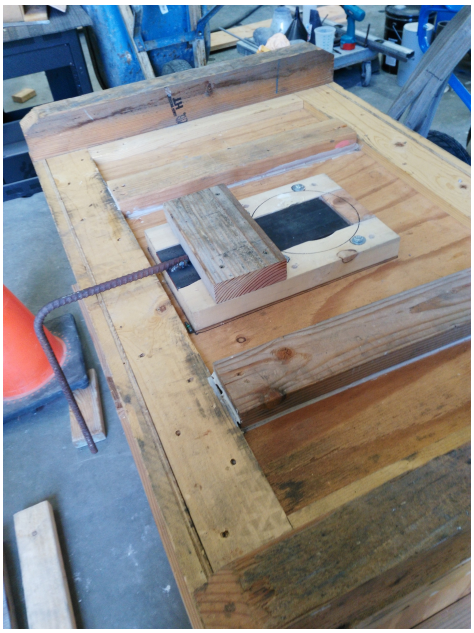

(b)

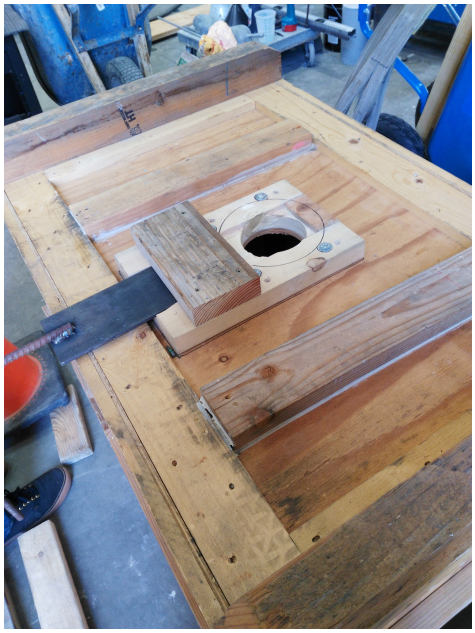

(c)

(d)

Figure 3.7: Wooden pluviator used to achieve medium-dense density (40%- 60%).

Table 3.3: Soil density results obtained from pluviator calibration.

Sample #	**Design Falling Height** $[in]$	**Weight of Sand in Mold** $[lb]$	**Average Dry Unit Weight** $[lb/ft^3]$	**Average Relative Density** [%]
1	20	3.4865	105.1	55
2	40	3.496	105.4	51
3	60	3.5195	106.1	53
4	80	3.4965	105.4	53
5	100	3.481	105.0	56
6	110	3.5135	106.0	52

A similar monitoring procedure was conducted while pluviating the sand material during specimen construction. Several soil samples were taken at different falling heights. To facilitate an easier sampling, the proctor mold was replaced with a light-weight plastic mold with dimensions of 5 in in diameter and 6.5 in in height. The plastic mold's volume corresponds to 0.069 in^2 (Fig. 3.8b). The mold was placed in a wooden box that was lowered to a known elevation within the LSB. The falling height was measured between lower side of the pluviator sieve and the surface where the collection mold was placed. After the mold was filled with sand, the box was raised, and the mold weighted. This process was repeated until the LSB was completely filled with sand.

Table 3.4 presents the soil sampling results during the pluviation process for all four test specimens. Figs. 3.10 show the soil sampling locations during the dry pluviation for each test.

(a) Pluviator attached to the crane

(b) Mold

Figure 3.8: Dry Pluviation of sand in LSB.

(a) Proctor molds used during the calibration

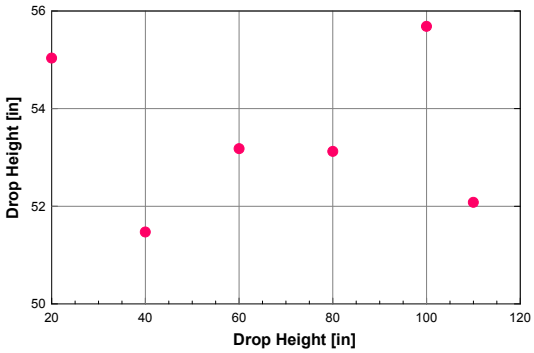

(b) Relative density vs. drop height

Figure 3.9: Pluviator' s calibration with constant flow rate (4 in^3/sec).

Table 3.4: Soil sampling during the sand pluviation of each test.

Pile Test #	**Sample** #	**Falling Height** $[in]$	**Weight of Sand** $[lb]$	**Dry unit weight** $[lb/ft^3]$	**Relative Density** [%]
1	1	110	7.176	104.4	54.8
	2	100	7.058	102.7	49.0
	3	91	7.076	102.9	49.9
	4	85	7.104	103.3	51.3
	5	75	7.061	102.7	49.2
	6	78	7.062	102.7	49.2
	7	72	7.078	103.0	50
	8	63	7.115	103.5	51.8
	9	53	7.134	103.8	52.8
	10	47	6.989	101.7	45.5
	11	37	7.013	102.0	46.8
2	1	110	7.176	104.4	54.8
	2	100	7.058	102.7	49.0
	3	91	7.076	102.9	49.9
	4	85	7.104	103.3	51.3
	5	75	7.061	102.7	49.2
	6	78	7.062	102.7	49.2
	7	72	7.078	103.0	50
	8	63	7.115	103.5	51.8
	9	53	7.134	103.8	52.8
	10	47	6.989	101.7	45.5
	11	37	7.013	102.0	46.8
3	1	117	7.080	103.0	50.1
	2	108	7.106	103.4	51.4
	3	99	7.061	102.7	49.2
	4	87	7.060	102.7	49.1
	5	82	7.117	103.5	51.9
	6	69	7.084	103.1	50.3
	7	62	7.042	102.4	48.2
	8	57	7.061	102.7	49.2
	9	47	7.053	102.6	48.8
	10	43	7.061	102.7	49.2
	11	36	7.031	102.3	47.7
4	1	77	7.069	103	49.6
	2	70	7.062	103	49.2
	3	64	7.136	104	52.9
	4	51	7.093	103	50.8
	5	39	7.091	103	50.7
	6	32	7.072	103	49.8

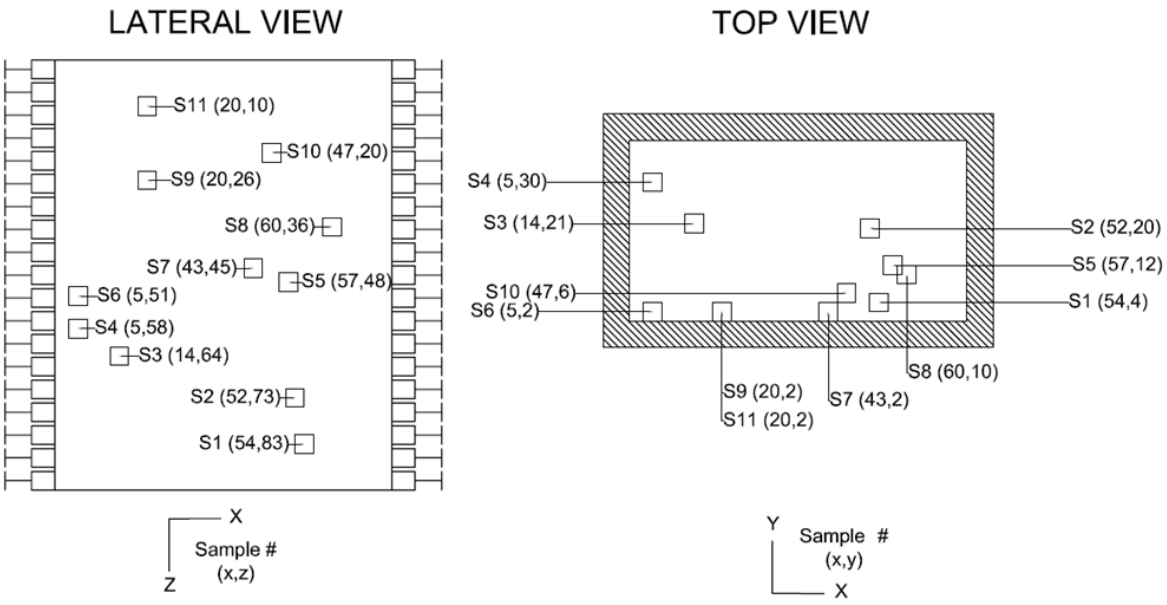

(a) 8 in polymer concrete pile with steel reinforcement

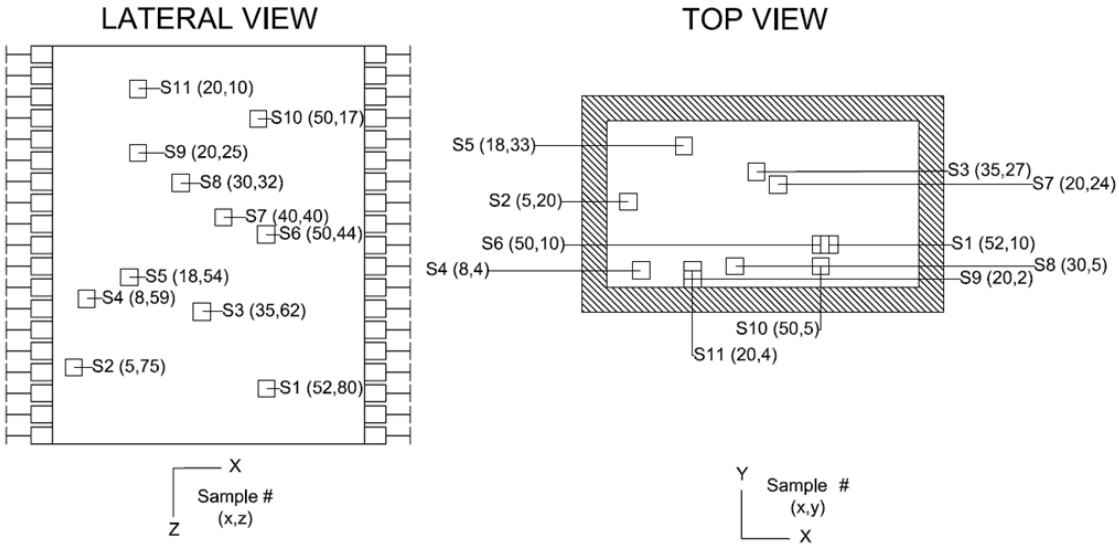

(b) 8 in regular concrete pile with geotextile reinforcement

Figure 3.10: Soil sampling locations (Units: inches).

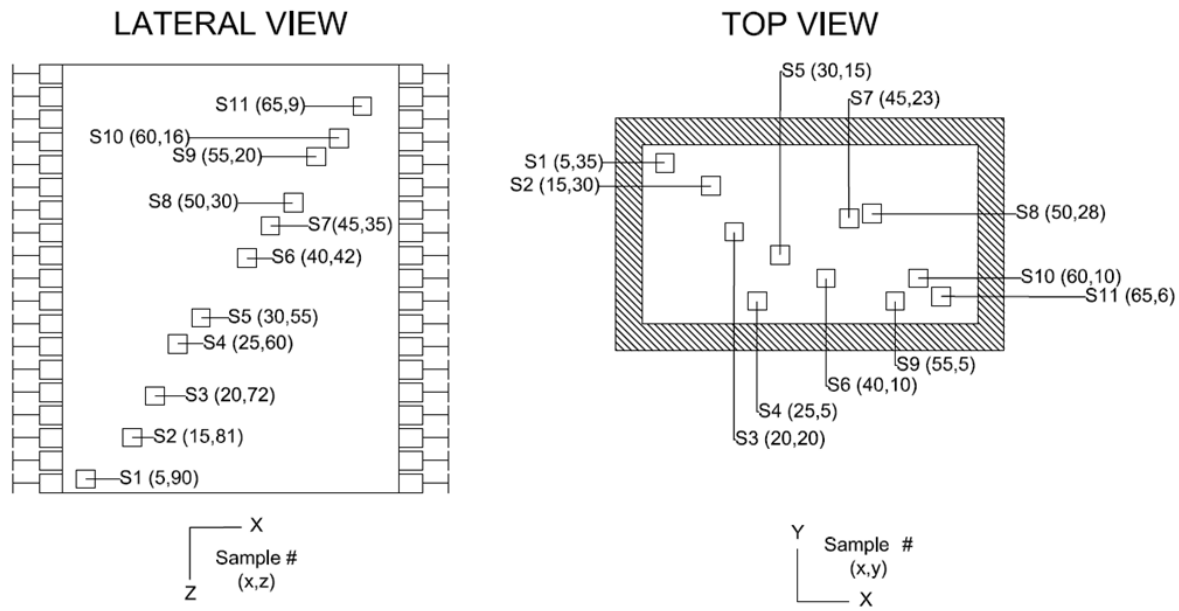

(c) 8 in polymer concrete pile with geotextile reinforcement

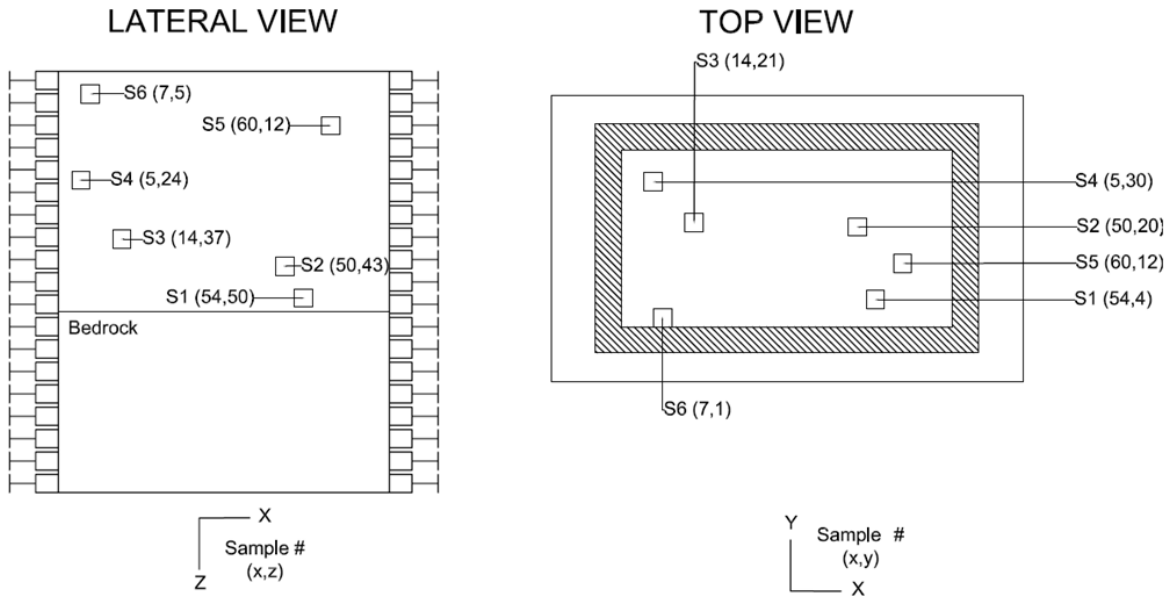

(d) 10 in polymer concrete pile with steel reinforcement

Figure 3.10: Soil sampling locations (Units: inches) (cont.).

3.1.3 Test Specimens

Table 3.5 presents a general overview of the geometric and material characteristics of each pile specimen. The following section will describe the specimen details, material testing and specimen construction.

Table 3.5: Overview of test specimens.

Pile Test #	**1**	**2**	**3**	**4**
Test Date 2017	Aug-4	Aug-18	Oct-13	Nov-21
Diameter [in]	8	8	8	10
Length [in]	120	120	120	125
Concrete Type: Pile	Polymer	Regular	Polymer	Polymer
Concrete Type: Bedrock	-	-	-	Regular
f'_c **[ksi]**	10	5	8	8 (Bedrock: 4 ksi)
f'_{sp} **[psi]**	617	413	-	550
Reinforcement Type	Steel: 6-#3 long. bars (ρ_l= 1.3%); 5-in diam #3 ties at 8 in (ρ_s= As/Ag= 0.8%)	Geogrid100: Aperture Size =1 in x 1 in	Geogrid150: Aperture Size= 1.6 in x 1.6 in	Steel: 2-#3, 4-#4 long. bars (ρ_l= 1.3%); 7-in diam. #4 ties at 8 in (ρ_s= As/Ag= 0.8%)
Rebar Yield [ksi]	60	Ultimate tensile Strength = 8.1 kip/ft at 3 in	Ultimate tensile Strength = 8.1 kip/ft at 3 in	60
Soil	Sand: see Table 3.2			
Boundary Conditions	Partially Restrained LSB	Fixed LSB	Fixed LSB	Fixed LSB

Pile 1: 8 in Polymer Concrete Pile with Steel Reinforcement

Specimen *1* had a pile diameter of 8 in and a total length of 120 in. 92 inches of pile length were embedded in the soil and 28 inches extended above the ground surface. The pile reinforcement consisted of Grade 60 A706 rebar. The longitudinal pile reinforcement consisted of 6-#3 bars ($\rho_l = A_s/A_g = 1.3\%$), and transverse reinforcement consisted of #3 circular ties (5-inch diameter) at 6.0 inch pitch across the entire pile length ($\rho_s = A_s/A_g = 0.5\ \%$). No additional rebar testing was conducted. The yield strength was taken as 60 ksi.

The concrete material consisted of a polymer concrete mix, commercially available as Sikacrete 211 SCC Plus, with a compressive strength of 6.5 ksi. Standard 6 x 12 in concrete cylinders were sampled during concrete placement and tested according to ASTM C39. Measured compressive strengths (f'_c) indicated an average value of 10 ksi and an average elastic modulus, E, of 4318 ksi. Splitting tensile tests were performed by Twining Laboratories according to ASTM C496/C496M. The average splitting tensile strength (f'_{sp}) was determined to be 617 psi. A summary of the compressive and tensile tests are presented in Table 3.6.

Table 3.6: Pile *1*. Summary table of concrete cylinders test results by UCI and Twining Laboratories.

Test #	**Testing Lab**	**Date 2017**	**Compressive Strength [ksi]**	**Split Tensile Strength [psi]**	**Elastic Modulus [ksi]**
1	UCI	Jun-15	-	-	4716.2
2	UCI	Jun-15	-	-	3919.9
3	Twining Lab.	Aug-2	10.33	-	4560.7
4	Twining Lab.	Aug-2	10.41	-	4667.6
5	Twining Lab.	Aug-2	9.83	-	-
6	Twining Lab.	Aug-2	-	572	-
7	Twining Lab.	Aug-2	-	662	-

The construction of Pile *1* was completed on May, 6th 2017 and its installation inside the laminar soil box in June, 2017. Pictures of the specimen construction are shown in Fig. 3.11.

(a)

(b)

(c)

(d)

Figure 3.11: Pile *1*. Construction phases.

Pile 2: 8 in Regular Concrete Pile with Geotextile Reinforcement

Specimen *2* had a pile diameter of 8 in and a total length of 120 in. 92 inches of pile length were embedded in the soil and 28 inches extended above the ground surface. Regular concrete was used with average values of 5 ksi as f'_c, 3258 ksi as E, and 413 psi as f'_{sp}, as shown in Table 3.7, which presents the concrete cylinders test results conducted by UCI and Twining Laboratories.

This test explores a new type of reinforcement, known as *ConForce Grid* manufactured by Titan. This product is composed of stiff polymer grids, which are non-corrodible. The material provides a durable alternative to steel reinforcement. Applications include structural pavement reinforcement and subgrade strengthening. The product has entered the commercial market in 2017 and has been evaluated within several research efforts since. The primary objective of a grid-type of reinforcement is a broader distribution of tensile stresses and the reduction of localized cracking. The ConForce Grid is intended to increase flexural stiffness of regular concrete, provide a larger shear strength, and improve post crack ductility of the concrete structure. This type of reinforcement has never been used for pile and column-type of applications. Hence test results will yield the potential and limitations of this particular application as well as recommendations for potential improvements of the product.

The ConForce Grid (model TE-SCR100) had an aperture size of 1 in x 1 in. Tensile testing according to ASTM D 6637 in machine direction and cross directions were performed by SGI Testing Services, LLC. Results are presented in Tables 3.7 and 3.8, respectively. As shown in Fig. 3.12a, an average ultimate tensile strength of 8.27 kip/ft at an ultimate strain of 2.8 in was obtained in machine direction. In cross direction, an average ultimate tensile strength of 7.95 kip/ft at an ultimate strain of 3.0 in was obtained (Fig. 3.12b).

Table 3.7: Pile *2*. Summary table of concrete cylinders test results by UCI and Twining Laboratories.

Test #	**Testing Lab**	**Date 2017**	**Compressive Strength [ksi]**	**Split Tensile Strength [psi]**	**Elastic Modulus [ksi]**
1	Twining Lab.	Aug-23	5.156	-	-
2	Twining Lab.	Aug-23	5.110	-	-
3	Twining Lab.	Aug-23	4.922	-	-
4	Twining Lab.	Aug-23	-	404	-
5	Twining Lab.	Aug-23	-	423	-
6	UCI	Sept-12	-	-	3258.3

Table 3.8: Summary table of geogrid tensile tests conducted in Machine Direction by SGI Testing Services, LLC.

Test #	**Tension at Selected Strains [kips/ft]**			**Ultimate Strength [kips/ft]**	**Strain at Ultimate [%]**
	0.5%	**1**%	**2**%		
1	0.90	2.20	5.73	8.58	2.9
2	1.05	2.19	5.80	7.97	2.7
3	1.01	2.41	5.98	8.04	2.7
4	0.91	2.49	5.78	8.48	2.8
5	1.06	2.42	5.92	8.30	2.8
Mean	0.99	2.34	5.84	8.27	2.8

Table 3.9: Summary able of geogrid tensile tests conducted in Cross Direction by SGI Testing Services, LLC.

Test #	**Tension at Selected Strains [kips/ft]**			**Ultimate Strength [kips/ft]**	**Strain at Ultimate [%]**
	0.5%	**1%**	**2%**		
1	1.40	2.79	5.58	7.80	3.0
2	1.45	2.86	5.73	7.88	3.0
3	1.42	2.95	5.53	8.22	3.2
4	1.27	2.78	5.76	8.02	2.9
5	1.19	2.84	5.75	7.86	2.8
Mean	1.35	2.84	5.67	7.95	3.0

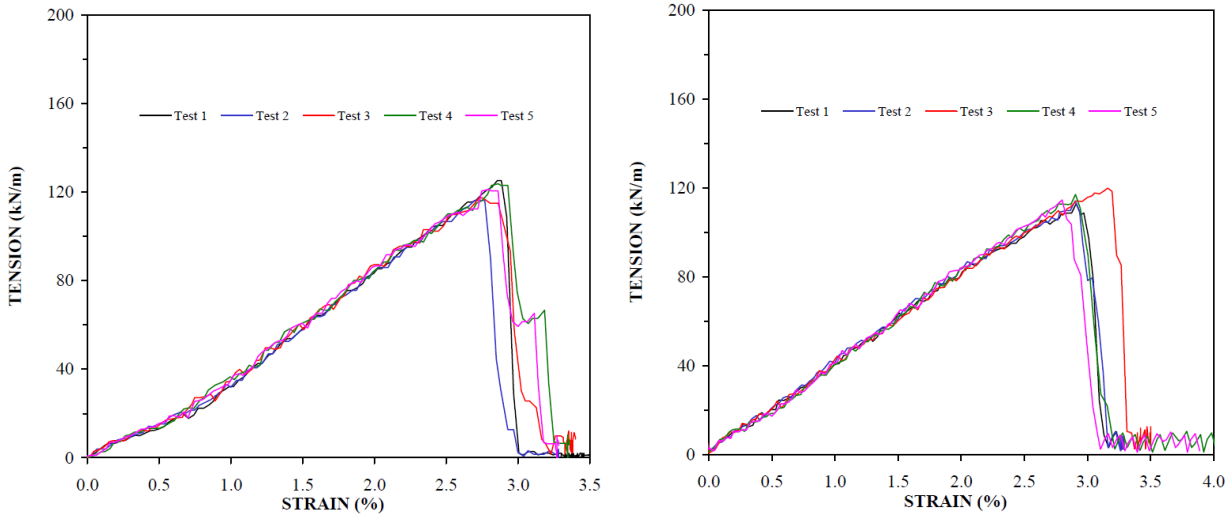

(a) Machine Direction.

(b) Cross Direction.

Figure 3.12: Titan TE-SCR100 tensile properties obtained by SGI Testing, LLC.

The construction of Pile *2* was completed on June, 9th 2017 and its installation inside the laminar soil box in August, 2017. Pictures of the specimen construction are shown in Fig. 3.13.

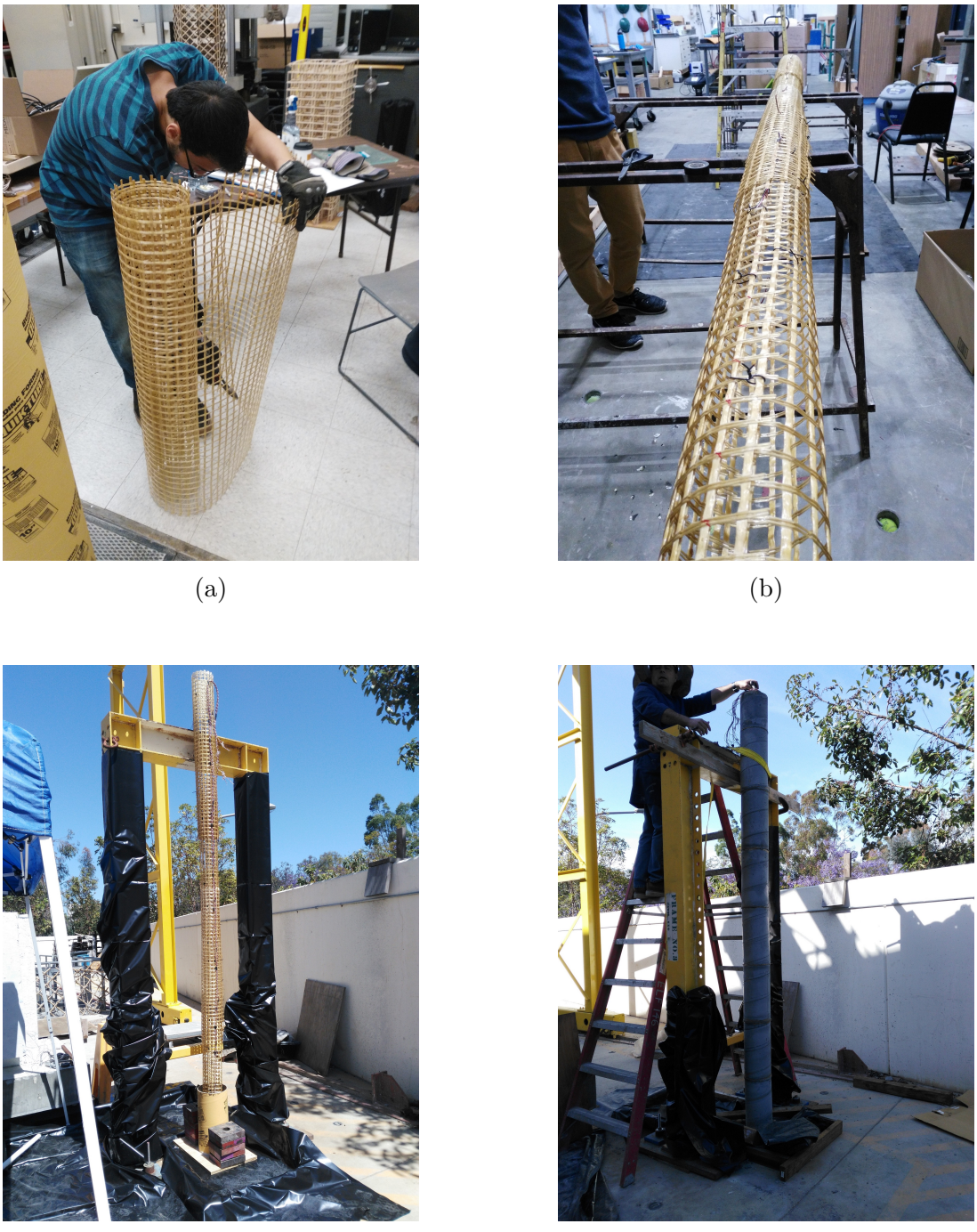

(a) (b)

(c) (d)

Figure 3.13: Pile *2*. Construction phases.

Pile 3: 8 in Polymer Concrete Pile with Geotextile Reinforcement

Specimen *3* had a pile diameter of 8 in and a total length of 120 in. 92 inches of pile length were embedded in the soil and 28 inches extended above the ground surface. The concrete used was *Sikacrete 211 SCC Plus*, polymer concrete also used in the first pile.

The pile reinforcement was *ConForce Grid TE-SCR150* by Titan. The main difference from the previously used reinforcement was the aperture size, which was increased of 0.6 in to make the pouring process easier. The mechanical properties are presented in Fig. 3.12 and Table 3.9.

The construction of Pile *3* was completed on September, 6th 2017 and installed inside the laminar soil box in September, 2017. Pictures of the specimen construction are shown in Fig. 3.14.

(a)

(b)

(c)

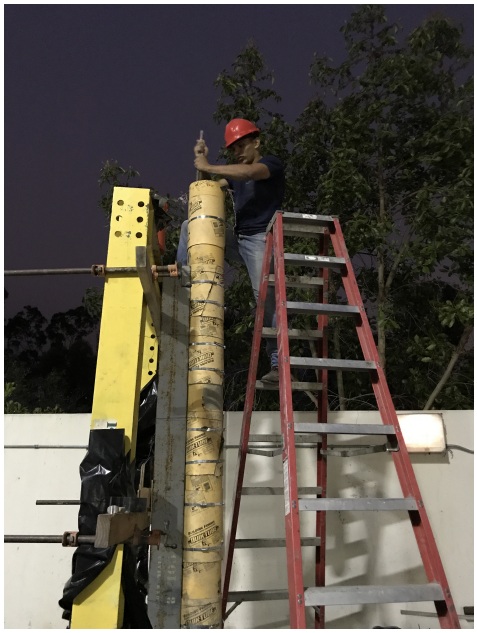

(d)

Figure 3.14: Pile *3*. Construction phases.

Pile 4: 10 in Polymer Concrete Pile with Steel Reinforcement

Specimen *4* had a pile diameter of 10 inches and a total length of 125 in. The pile was placed in a two-layer soil stratigraphy. The pile was fixed at the bottom by embedding the lower 40 inch of pile length in concrete. This concrete layer simulates a rock-socket condition in the field.

The pile reinforcement consisted of 2-#3 and 4-#4 longitudinal bars ($\rho_l = A_s/A_g = 1.3\%$), and #4 circular ties (7-inch diameter) at a 6 in pitch over the pile length ($\rho_s = A_s/A_g = 0.8\%$). Nominal A706 Grade 60 reinforcement was used, with coupon tests provided by the supplier indicating a yield stress of approximately 60 ksi.

Results from 6 x 12 in concrete cylinder tests, conducted according to ASTM C39, are shown in Table 3.10. Testing of these samples indicated an average concrete compressive strength, f'_c, of 8.16 ksi, an elastic modulus, E, of 4318.4 ksi, and a split tensile strength, f'_{sp}, of 549.5 psi. The measured bedrock f'_c is 4 ksi.

The construction of Pile *4* was completed on June, 9th 2017 and its installation inside the laminar soil box in November, 2017. Pictures of the specimen construction are shown in Fig. 3.15.

Table 3.10: Pile *4*. Summary table of concrete cylinders test results by UCI and Twining Laboratories.

Test #	**Testing Lab**	**Date 2017**	**Compressive Strength [ksi]**	**Split Tensile Strength [psi]**	**Elastic Modulus [ksi]**
1	Twining Lab.	Aug-23	7.993	-	-
2	Twining Lab.	Aug-23	9.573	-	-
3	Twining Lab.	Aug-23	6.930	-	-
4	Twining Lab.	Aug-23	-	461	-
5	Twining Lab.	Aug-23	-	638	-
6	UCI	Sept-12	-	-	4096.4
7	UCI	Sept-12	-	-	4540.4
8 (Bedrock)	UCI	Dec-5	3.7	-	-
9 (Bedrock)	UCI	Dec-5	4.3	-	-
10 (Bedrock)	UCI	Dec-5	4.0	-	-

(a)

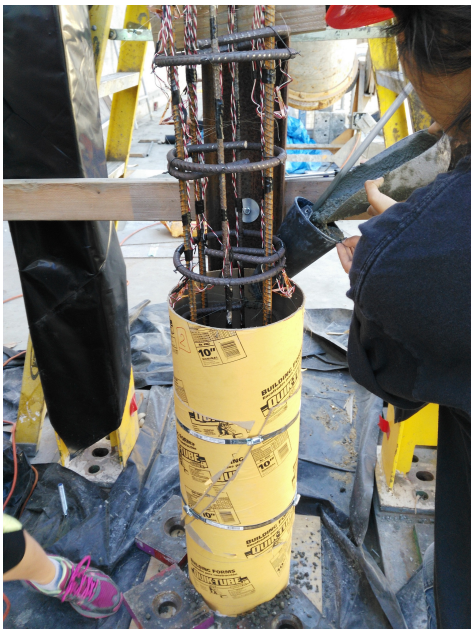

(b)

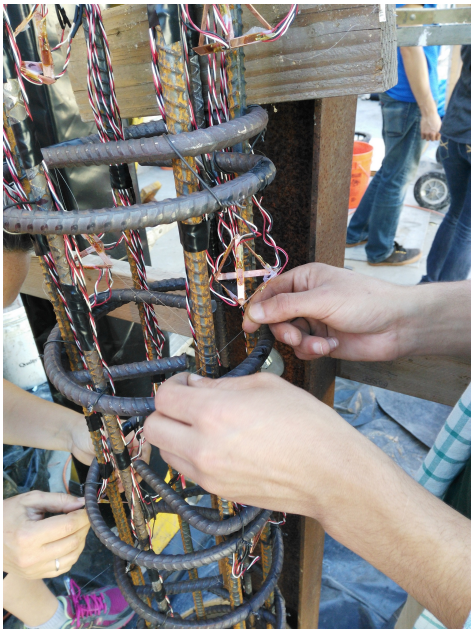

(c)

(d)

Figure 3.15: Pile *4*. Construction phases.

3.2 Instrumentation

The soil-pile specimens were instrumented to record load, pressure, strain, and displacements during the test execution. Two cameras were installed to monitor the soil surface behavior, as well as pile and laminar soil box movements during the loading cycles. One camera was mounted above the specimen to provide recordings in plan view. A second camera was positioned on the north side of the container to provide a side view of the test setup. These cameras collected photos at a 5 fps.

An overview of the external sensors and soils pressure sensors used in this series of tests is presented in Fig. 3.16. External sensors consisted primarily of string potentiometers and LVDTs. Soil pressure sensors were placed inside the specimen at the interface with the container wall. Table 3.11 summarizes the type and the number of channels of data acquisition that were used in each test. The hydraulic actuator had a long-stroke AC LVDT to capture redundant displacement measurements of the pile cap. All sensors were connected to a National Instrument data acquisition system. A detailed description of the instrumentation implemented in the four tests is presented hereafter.

Table 3.11: Instrumentation plan summary.

Test #	**Strain Gauges**			**String Pots**		**LVDTs**	**Soil Pressure Sensors**
	Rebars	Tetrahedra	External	LSB	Pile		
1	22	120	16	4	2	1	7
2	18	-	-	5	2	2	7
3	20	-	-	5	2	2	7
4	22	156	4	5	2	2	3

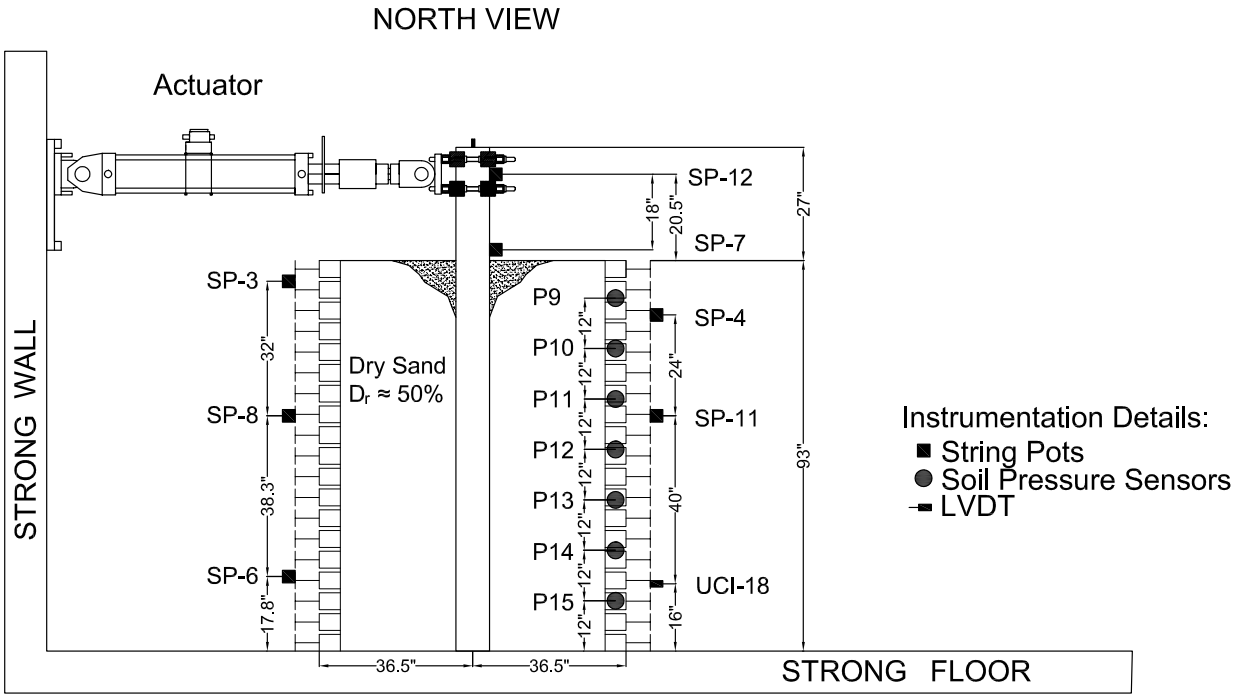

Figure 3.16: External instrumentaion' s layout.

3.2.1 External Instrumentation of Laminar Soil Box

The laminar soil box was externally instrumented with five string potentiometers and one LVDT to measure potential lateral movements during each test. The string pot configuration used for all four specimens can be seen in Fig. 3.16. Note that the SP-6 string pot and the UCI-18 LVDT were added after the first test in order to allow for additional monitoring of box movements after lateral displacements were observed while testing Specimen *1*.

3.2.2 Soil Pressure Sensors

A rigid sheet with seven soil pressure sensors was installed along the west side of the laminar soil box and secured along the box wall. The sensors are distributed across the vertical height and were spaced 12 in on center from each other (Fig. 3.17a). The amount of soil pressure sensors was reduced for Specimen *4* (Fig. 3.17b). No pressure sensors were embedded in the rock layer.

(a) Original soil pressure sensors' disposition.

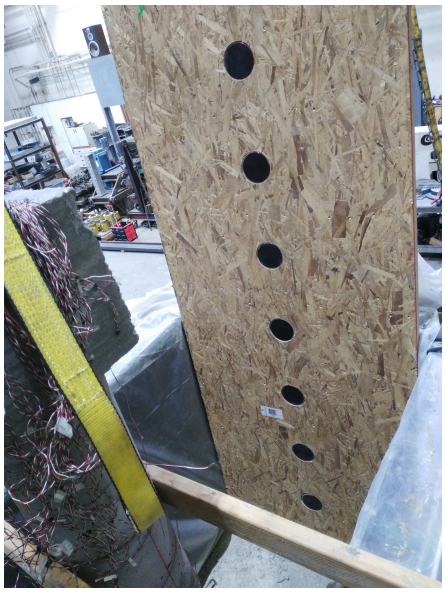

(b) Soil pressure sensors on top of the bedrock.

Figure 3.17: Soil pressure sensors' layout.

3.2.3 Pile Instrumentation

Pile instrumentation consisted of internal longitudinal strain gauges placed along the longitudinal rebars and strain gauges attached to the tetrahedral carriers, placed near the pile circumference. External pile instrumentation consisted of surface strain gauges placed in longitudinal and rosette configuration along the outside pile perimeter. Two string-pot displacement transducers were attached to the cap (SP-12) and to the pile near the ground surface (SP-7) to measure the displacements of the pile relative to a fixed external reference

point (Fig. 3.16). The reference column was placed 28 in away from the laminar soil box' s West side. The fixed point for the box' s East side was represented by the strong wall. These measurements will minimize curvature fitting errors and increase the accuracy of the double integration process employed in computing pile deflection (y).

Traditional Instrumentation

Pile specimens were primarily instrumented with internal strain gauges. Strain gauges were attached on two longitudinal opposite rebars, or geogrids, at intervals of approximately 6 inches. Strain readings from gauges located on opposite sides were used to back-calculate pile curvatures.

External surface gauges placed in form of rosettes were used to back-calculate axial and shear strains and the pile interface.

In accordance with its location, three different types of strain gauges were used. For the internal, longitudinal reinforcement (rebar and geogrid) the strain gauges consisted of Micro-Measurements model CEA-06-250UW-120 (matrix width= 0.27 in; matrix length= 0.55 in). For the tetrahedra (Chapter 3.2.4), smaller gauges, i.e., CEA-06-240UZ-120 (matrix width= 0.24 in; matrix length= 5.12 in) were used. External strain gauges placed at the pile surface consisted of model number C2A-06-20CLW-120 (matrix width= 0.235 in; matrix length= 2.235 in). Figure 3.18 depicts the various types of strain gauges. And the location they are installed in.

The procedure used to install strain gauges was generally the same for the four types of surfaces (steel, copper, geogrid, and concrete) with few differences. The general procedure includes phasis like degreasing, abrading and conditioning. In the case of the geogrid, the surface preparation consisted in only abrading it with sand paper. No further treatments were used in order not to degrade the material. In the case of the strain gauges installed

on the pile, the surface preparation was more complex since it included and additional phase of pore filling with M-Bond AE-10. The gauges were then affixed to all the different surfaces using M-Bond 200 adhesive and coated with M-Coat A, M-Coat B, from Vishay Micromeasurements, for protection.

More details about the strain gauges installed on each pile are included in the following paragraphs.

(a) Strain gauges on steel rebars.

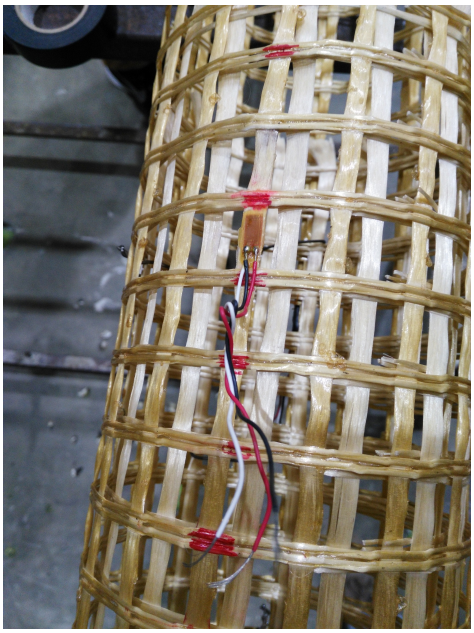

(b) Strain gauges on geogrid.

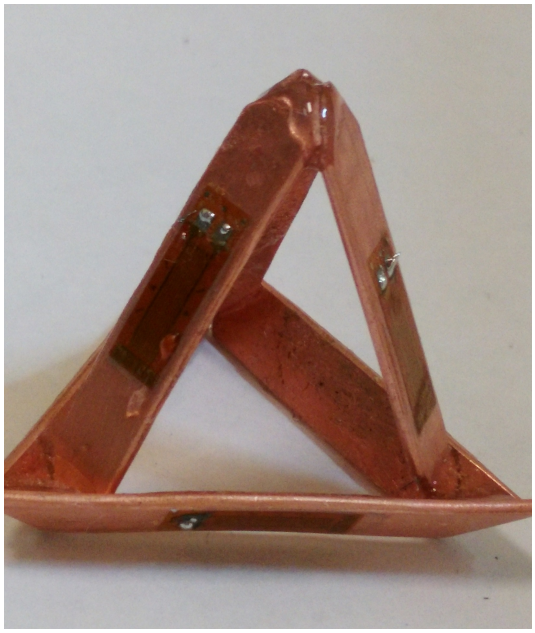

(c) Strain gauges on copper bars.

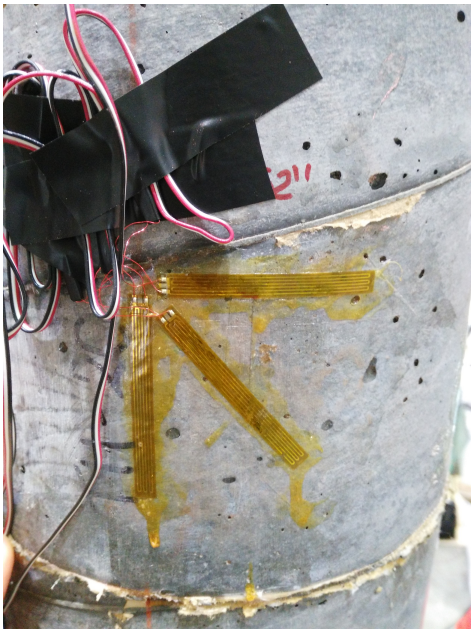

(d) Strain gauges on concrete.

Figure 3.18: Strain gauges installed on four different surfaces.

8 in Polymer Concrete Pile with Steel Reinforcement This specimen was instrumented with 22 strain gauges installed on two opposite longitudinal rebars (Fig. 3.22). Moreover, there were 16 external strain gauges distributed among the bending (East and West pile) and shear (North and South pile) sides of the pile (Fig. 3.23).

8 in Regular Concrete Pile with Geotextile Reinforcement This specimen was instrumented with 18 strain gauges installed on two opposite longitudinal sides of the geotextile reinforcement (Fig. 3.24).

8 in Polymer Concrete Pile with Geotextile Reinforcement This specimen was instrumented with 20 strain gauges installed on two opposite longitudinal sides of the geotextile reinforcement (Fig. 3.25).

10 in Polymer Concrete Pile with Steel Reinforcement This specimen was instrumented with 22 strain gauges installed on two longitudinal rebars (Fig. 3.26). Moreover, there were 4 external strain gauges distributed among the bending (East and West) and shear (North and South) sides of the pile (Fig. 3.27).

3.2.4 Tetrahedral Strain Gauge Carrier

Slowik et al. [107] successfully demonstrated the measurement of 3D core stresses developed in fiber reinforced concrete sections using a single FOS strand wrapped around a tetrahedral wire carrier. The instrumented tetrahedron served as 3D FOS carrier structure, as shown in Fig. 3.19. This mechanism allowed for the test material to be poured around the wire carrier, and the cross-sectional difference between the carrier and the test material were minimized.

Upon extensively evaluating the various 3D strain measurement concepts employed in lit-

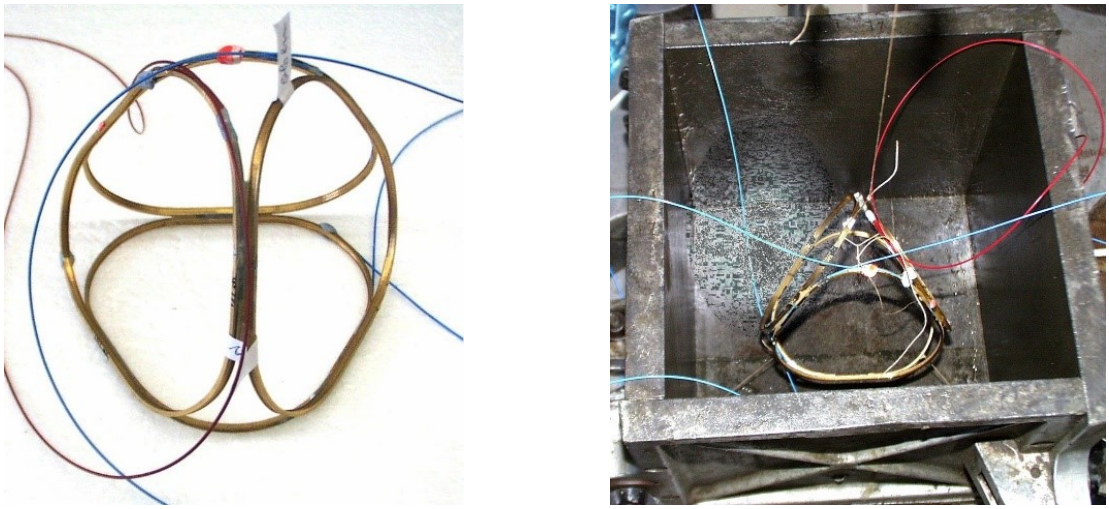

(a) (b)

Figure 3.19: Tetrahedron model embedded in a fiber reinforced concrete column after Slowik et al. [107].

erature, the one proposed by Slowik' s [107] appeared to be most useful for the envisioned application. This concept shall be modified to ease construction and implementation, as well as to provide a more cost-efficient methodology. The FOS technology would be suitable for the proposed model scale tests due to their high accuracy, robustness and resistance to corrosion. However, the high sensor cost and time-intensive construction procedure represent a strong limitation.

The proposed instrumentation create an instrumented tetrahedron that serves as three dimensional strain gauge carrier (Fig. 3.20a). Each tetrahedral leg will be furnished with a uniaxial strain gauge. To fully describe the 3D strain resultant at the volumetric centroid of the tetrahedron, three normal strain and six shearing strain components must be known. The fully instrumented tetrahedron can be situated at any desired location in the test specimen mold, which will then be filled with a cast-able material. The enclosed tetrahedron will deform with the specimen material and could provide individual strain measurements needed to derive the 3D state of stress at the specified location. The tetrahedron device should be complemented with traditional instrumentation in order to obtain redundant measurements

and validate individual strain components. Moreover, two tetrahedra will be located at the same depth in order to enable data redundancy. To enable the estimation of pile-soil interface stresses, internal stresses in the vicinity of the pile periphery can be translated into pile-soil interface stresses by using a surface traction vector (T).

Data Reduction and Analysis

In order to derive the 3D state of stress at the center of the tetrahedron and to translate these stresses into interface stresses or traction forces at the pile surface, the following data conversion algorithm is proposed. The data reduction consists of converting the internal strain measurements to the traction forces acting on the pile perimeter. Six strain gauges ($a-f$) are located on the edges six sides of the wired tetrahedron, as shown in Fig. 3.20. As presented in Table 3.12 details, the orientation of each strain gauge is given by using three angles in reference to the coordinate system: α, with the $x-$axis, β, with the $y-$axis and γ, with the $z-$axis. To accurately and fully describe the 3D strain resultant acting at the volumetric centroid of a tetrahedron, three normal strain components (ε_i) and six shearing strain components (γ_{ij}) must be known. Six independent normal strain components are thus required to fully define the strain state, satisfied by six uniaxial strain gauges attached to the flat wire tetrahedron legs.

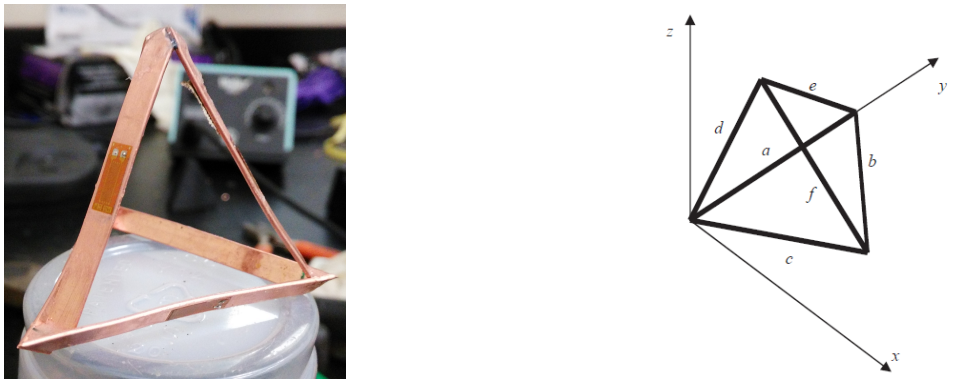

(a) Tetrahedron (b) Sensors' labeling

Figure 3.20: Sensor disposition in the tetrahedron.

Table 3.12: List of sensors angles [°] with respect of x, y, z axis.

Sensor	α	β	γ
a	90	0	90
b	150	60	90
c	30	60	90
d	73.22	60	35.26
e	73.22	120	35.26
f	125.26	90	35.26

The mathematical derivation procedure is explained hereafter. Considering the six gauges $(a-f)$ located at the angles α, β, and γ (Table 3.12), the $a-$, $b-$, $c-$, $d-$, $e-$, $f-$ directed normal strains are:

$$\varepsilon_a = \varepsilon_x \cos^2\alpha_a + \varepsilon_y \cos^2\beta_a + \varepsilon_z \cos^2\gamma_a + \gamma_{xy} \cos\alpha_a \cos\beta_a + \gamma_{yz} \cos\beta_a \cos\gamma_a + \gamma_{zx} \cos\gamma_a \cos\alpha_a \tag{3.2}$$

When translated into a matrix format, Eq. 3.2 becomes:

$$\begin{bmatrix} \varepsilon_a \\ \varepsilon_b \\ \varepsilon_c \\ \varepsilon_d \\ \varepsilon_e \\ \varepsilon_f \end{bmatrix} = [T] \begin{bmatrix} \varepsilon_x \\ \varepsilon_y \\ \varepsilon_z \\ \gamma_{xy} \\ \gamma_{yz} \\ \gamma_{zx} \end{bmatrix} \tag{3.3}$$

where $[T]$ is the transformation matrix as function of the orientation angles of the strain

gauges. $[T]$ can be expressed as:

$$[T] = \begin{bmatrix} \cos^2\alpha_a & \cos^2\beta_a & \cos^2\gamma_a & \cos\alpha_a\cos\beta_a & \cos\beta_a\cos\gamma_a & \cos\gamma_a\cos\alpha_a \\ \cos^2\alpha_b & \cos^2\beta_b & \cos^2\gamma_b & \cos\alpha_b\cos\beta_b & \cos\beta_b\cos\gamma_b & \cos\gamma_b\cos\alpha_b \\ \cos^2\alpha_c & \cos^2\beta_c & \cos^2\gamma_c & \cos\alpha_c\cos\beta_c & \cos\beta_c\cos\gamma_c & \cos\gamma_c\cos\alpha_c \\ \cos^2\alpha_d & \cos^2\beta_d & \cos^2\gamma_d & \cos\alpha_d\cos\beta_d & \cos\beta_d\cos\gamma_d & \cos\gamma_d\cos\alpha_d \\ \cos^2\alpha_e & \cos^2\beta_e & \cos^2\gamma_e & \cos\alpha_e\cos\beta_e & \cos\beta_e\cos\gamma_e & \cos\gamma_e\cos\alpha_e \\ \cos^2\alpha_f & \cos^2\beta_f & \cos^2\gamma_f & \cos\alpha_f\cos\beta_f & \cos\beta_f\cos\gamma_f & \cos\gamma_f\cos\alpha_f \end{bmatrix} \tag{3.4}$$

For a three- dimensional state of stress, each of the six stress components can be expressed as a linear function of the six components of strain within the linear elastic range using Hooke' s law:

$$\sigma_x = \frac{E}{(1+\upsilon)(1-2\upsilon)}\left[(1-\upsilon)\varepsilon_x + \upsilon(\varepsilon_y + \varepsilon_z)\right] \tag{3.5a}$$

$$\sigma_y = \frac{E}{(1+\upsilon)(1-2\upsilon)}\left[(1-\upsilon)\varepsilon_y + \upsilon(\varepsilon_z + \varepsilon_x)\right] \tag{3.5b}$$

$$\sigma_z = \frac{E}{(1+\upsilon)(1-2\upsilon)}\left[(1-\upsilon)\varepsilon_z + \upsilon(\varepsilon_x + \varepsilon_y)\right] \tag{3.5c}$$

$$\tau_{xy} = G\gamma_{xy} \tag{3.5d}$$

$$\tau_{yz} = G\gamma_{yz} \tag{3.5e}$$

$$\tau_{xz} = G\gamma_{xz} \tag{3.5f}$$

with $G = \frac{E}{2(1+\upsilon)}$.

In matrix notation, Eqs. 3.5 become:

$$\begin{bmatrix} \sigma_x \\ \sigma_y \\ \sigma_z \\ \tau_{xy} \\ \tau_{yz} \\ \tau_{zx} \end{bmatrix} = \frac{E}{(1+\upsilon)(1-2\nu)} \begin{bmatrix} (1-\nu) & \nu & \nu & 0 & 0 & 0 \\ \nu & (1-\nu) & \nu & 0 & 0 & 0 \\ \nu & \nu & (1-\nu) & 0 & 0 & 0 \\ 0 & 0 & 0 & \frac{(1-2\nu)}{2} & 0 & 0 \\ 0 & 0 & 0 & 0 & \frac{(1-2\nu)}{2} & 0 \\ 0 & 0 & 0 & 0 & 0 & \frac{(1-2\nu)}{2} \end{bmatrix} \begin{bmatrix} \varepsilon_x \\ \varepsilon_y \\ \varepsilon_z \\ \gamma_{xy} \\ \gamma_{yz} \\ \gamma_{zx} \end{bmatrix} \tag{3.6}$$

The surface of a solid can be subjected to distributed forces, such as t_x, t_y, and t_z, in the x, y, and z directions, respectively. The state of stress at a point on the surface of the body can be expressed by the traction vector $[t]$, as follows:

$$[t] = \begin{bmatrix} t_x \\ t_y \\ t_z \end{bmatrix} \tag{3.7}$$

$$t_x = \sigma_x \cos\theta + \tau_{xy} \sin\theta \tag{3.8a}$$

$$t_y = \sigma_y \sin\theta + \tau_{yx} \cos\theta \tag{3.8b}$$

$$t_z = \tau_{zx} \cos\theta + \tau_{zy} \sin\theta \tag{3.8c}$$

where the direction cosines of the vector that is normal to the surface, vector $[n]$, are n_x, n_y, and n_z. The following equation expresses the normal vector $[n]$ in 3D:

$$n = \begin{bmatrix} n_x \\ n_y \\ n_z \end{bmatrix} \tag{3.9}$$

By replacing the instrumented tetrahedron at a point close to the pile periphery (Fig. 3.21), and obtaining the 3D strains at the centroid of the tetrahedron (close to the pile-soil interface), the 3D stresses and the external traction vector can be determined.

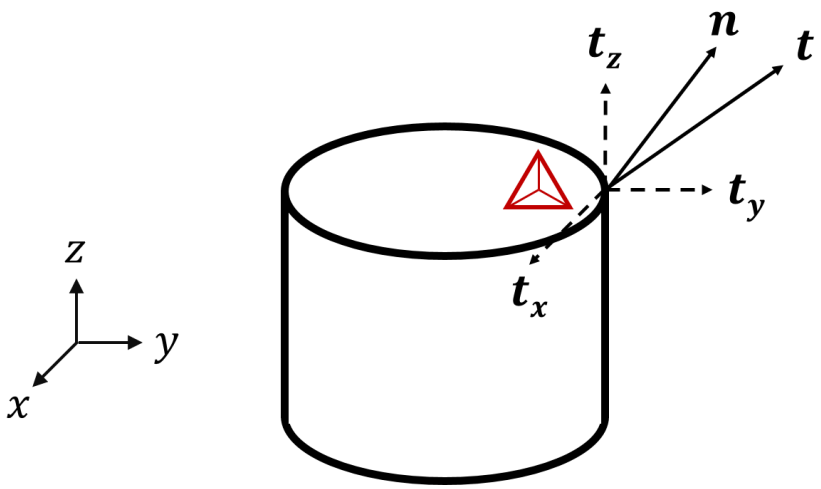

Figure 3.21: Traction boundary condition of a plane solid in 3D space.

8 in Polymer Concrete Pile with Steel Reinforcement This specimen was instrumented with 120 strain gauges installed on copper tetrahedra (Fig. 3.22).

10 in Polymer Concrete Pile with Steel Reinforcement This specimen was instrumented with 156 strain gauges installed on copper tetrahedra (Fig. 3.26).

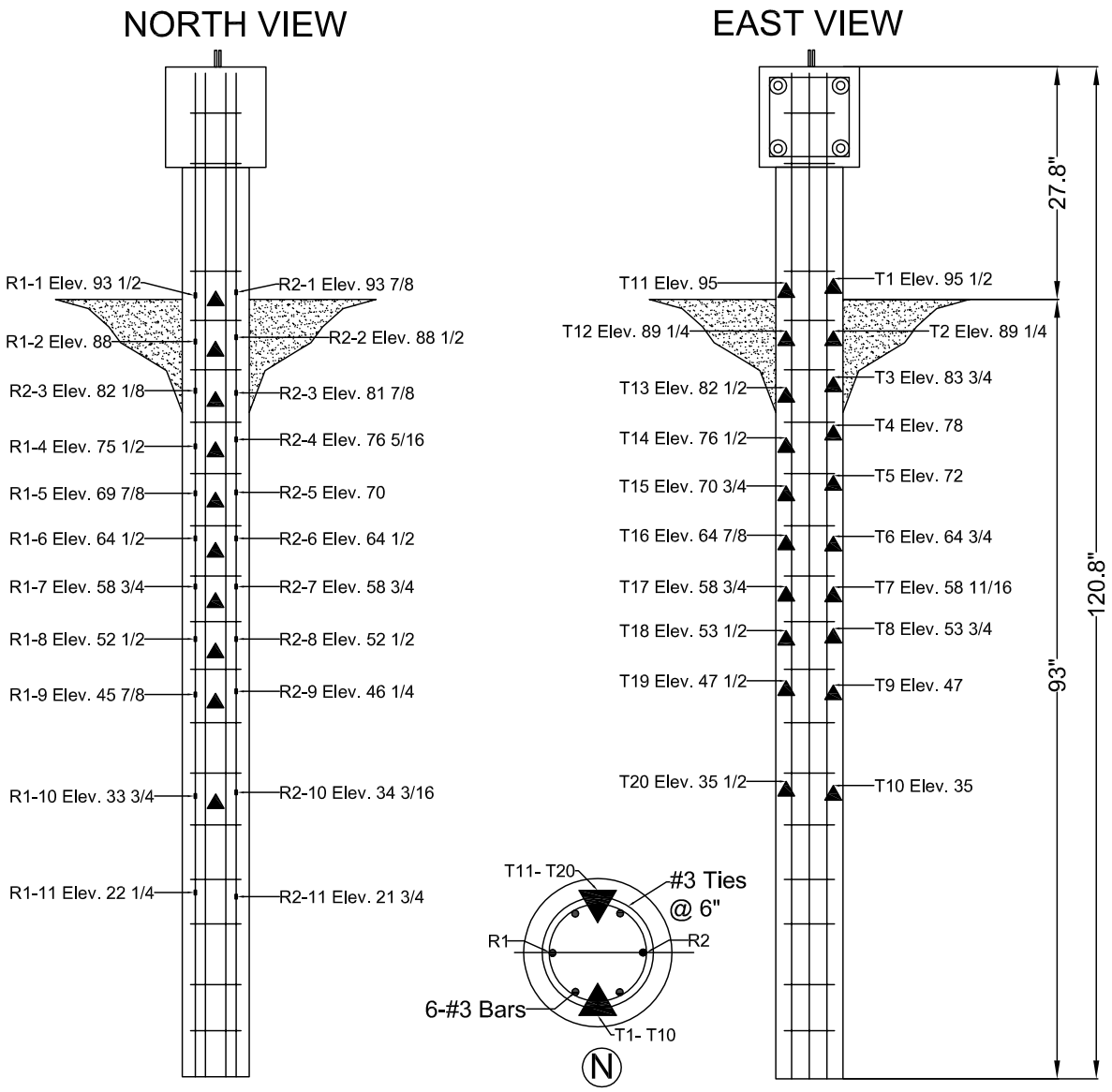

Figure 3.22: Pile 1. Schematic of the location of the strain gauges installed on two longitudinal rebars (North View), tetrahedra (East View), and pile cross section.

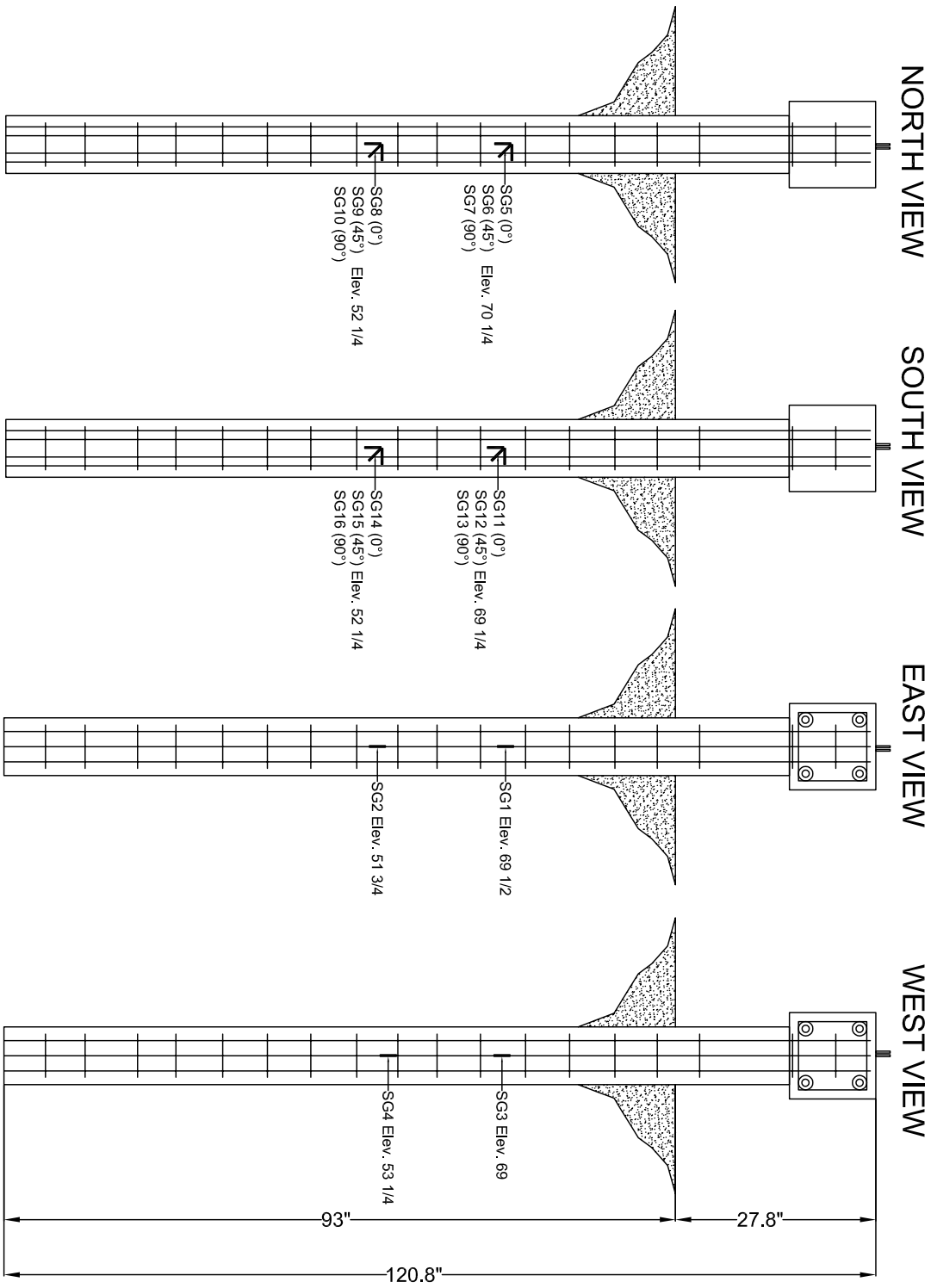

Figure 3.23: Pile 1. Schematic of the location of the external strain gauges located on the two shear sides (North and South Views), and bending sides of the pile (East and West Views).

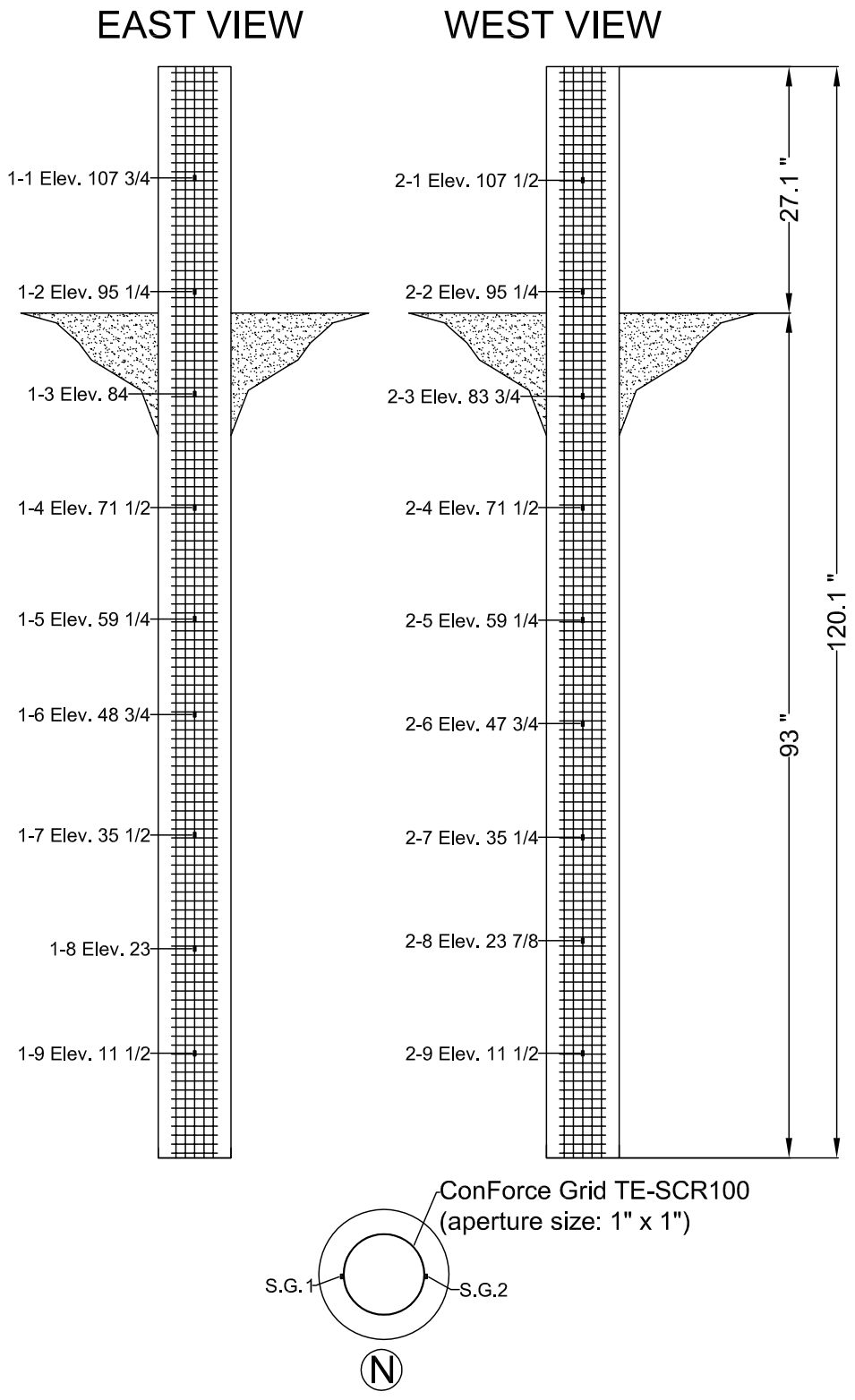

Figure 3.24: Pile 2. Schematic of the location of the strain gauges installed on the geogrid reinforcement and pile cross section.

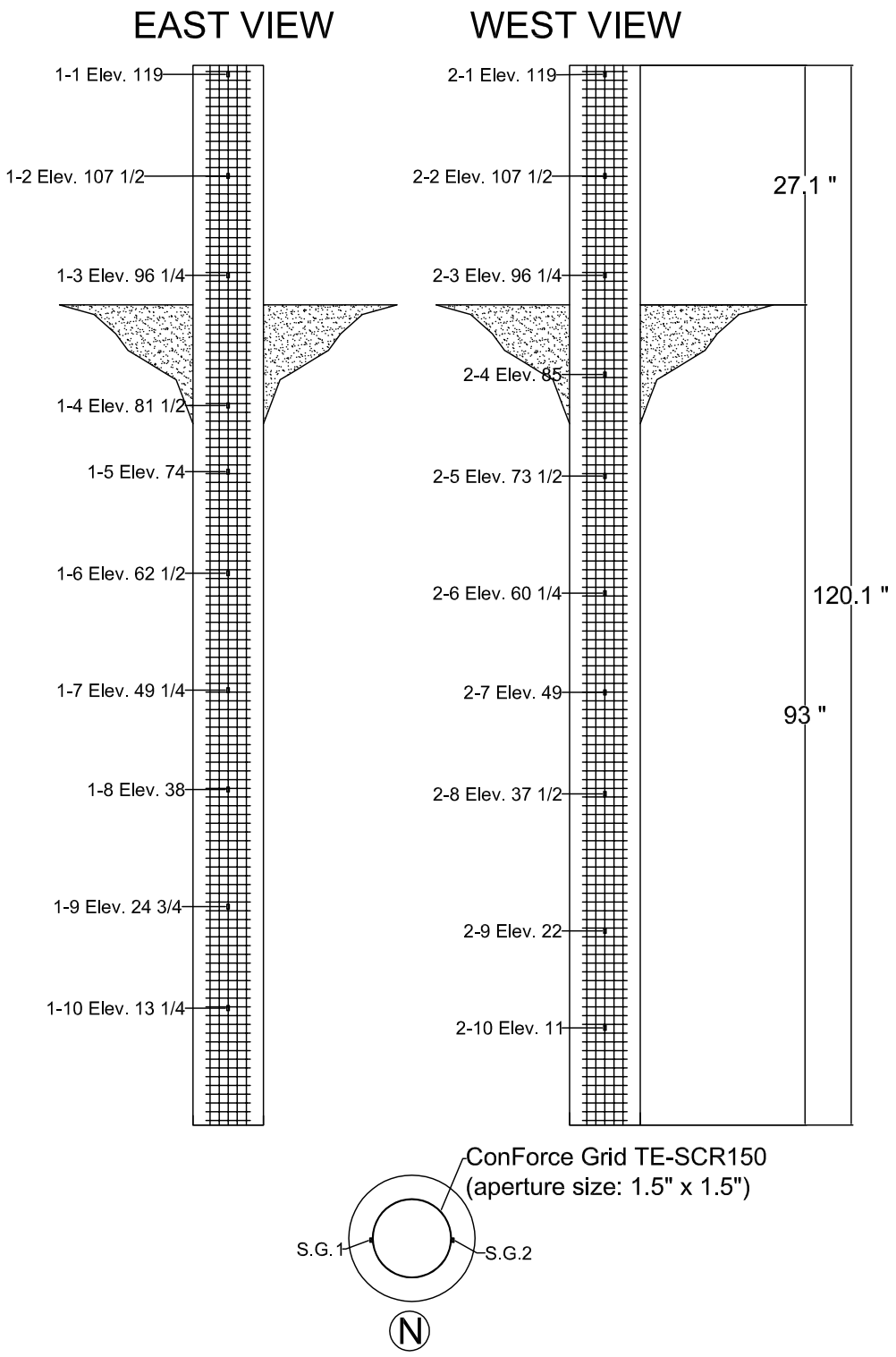

Figure 3.25: Pile 3. Schematic of the location of the strain gauges installed on the geogrid reinforcement and pile cross section.

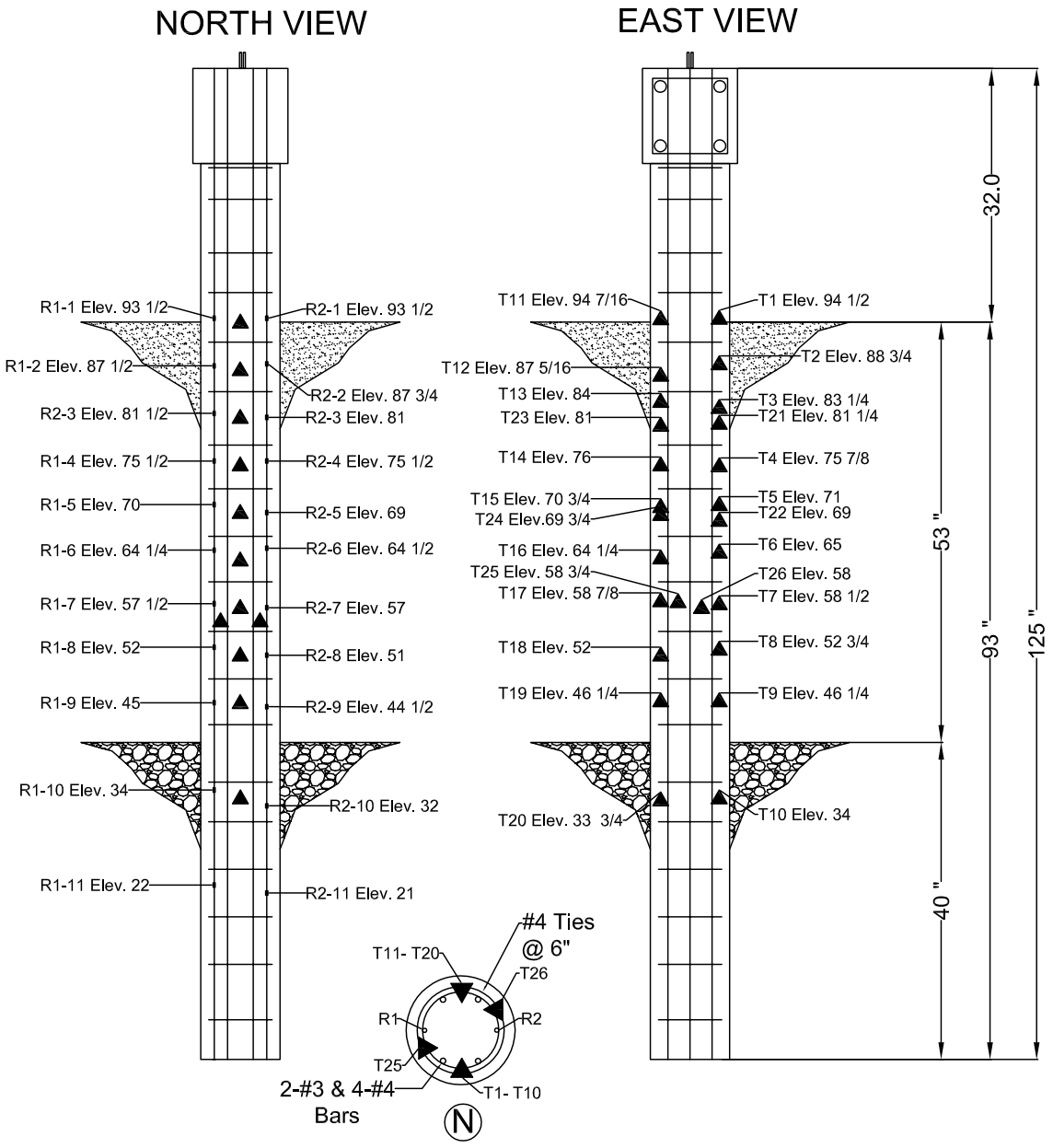

Figure 3.26: Pile 4. Schematic of the location of the strain gauges installed on two longitudinal rebars (North View), tetrahedra (East View), and pile cross section.

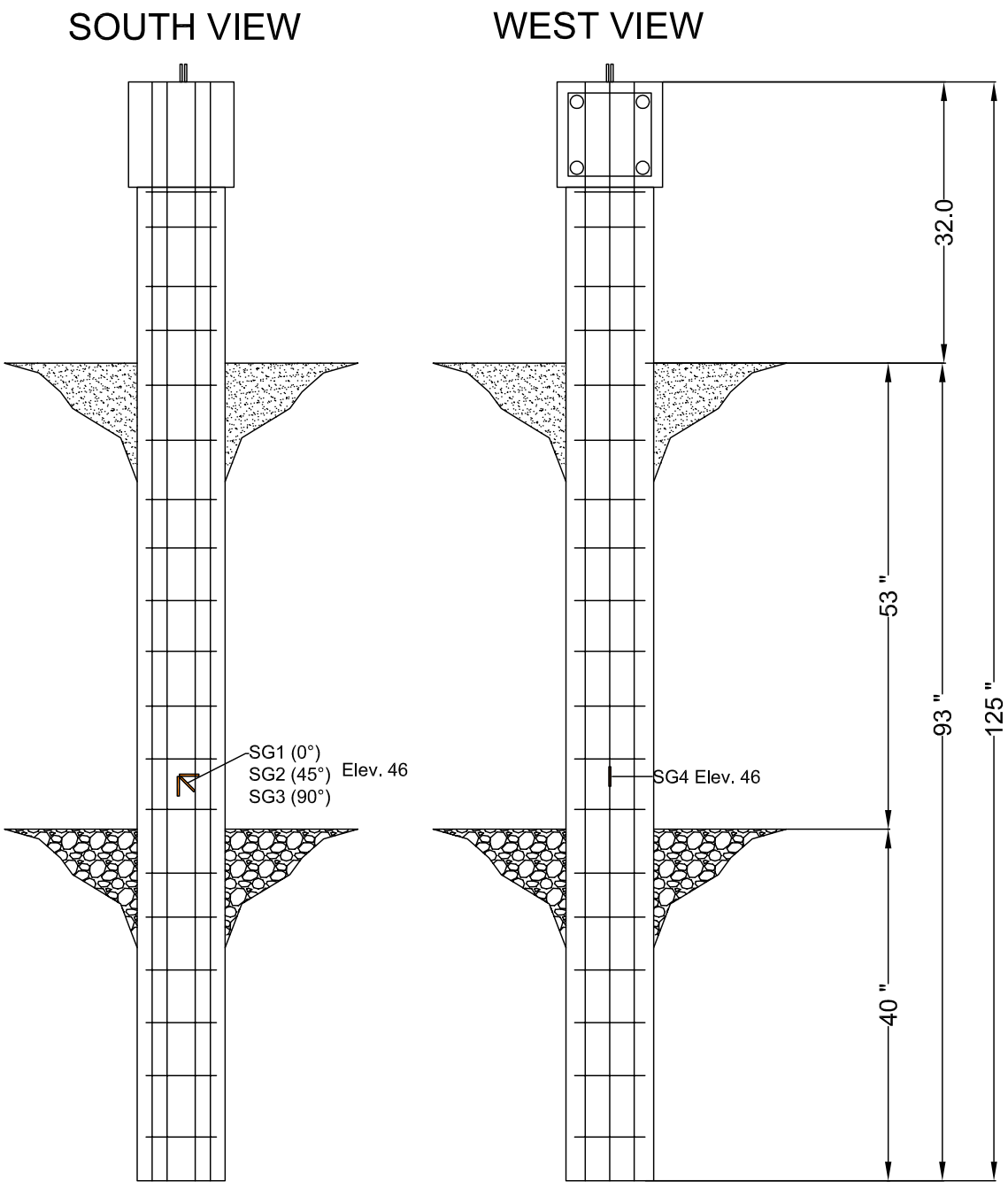

Figure 3.27: Pile 4. Schematic of the location of the external strain gauges located on one bending side and one shear side of the pile.

3.3 Test Protocol

Quasi static reverse cyclic lateral loading was applied with one hydraulic actuator.

The actuator was attached on one end to the strong wall at a height of 114.8 in, and on the other to the pile top (Fig. 3.16). Two different types of pile caps were adopted. The piles with steel reinforcement had a concrete cap (12 x 12 x 12 in) with four 1.5 in diameter holes located at a center - to - center distance of 7.5 in from each others, to match the actuator plate holes pattern (Fig. 3.28a). In the case of the geotextile piles, a combination of wood and steel plates were used to embrace the pile top and attach it to the actuator plate. The details of this attachment are shown in Fig. 3.28b.

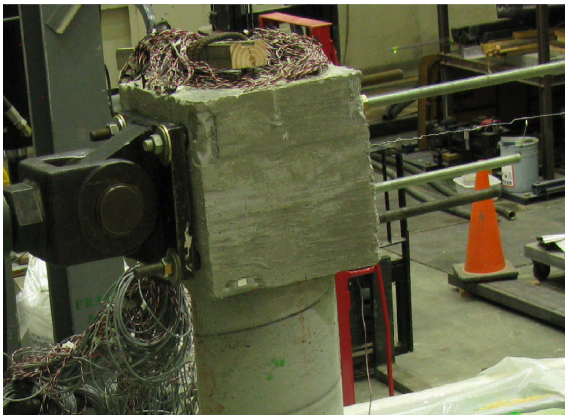

(a) Pile-actuator attachment detail for Pile 1 and 4.

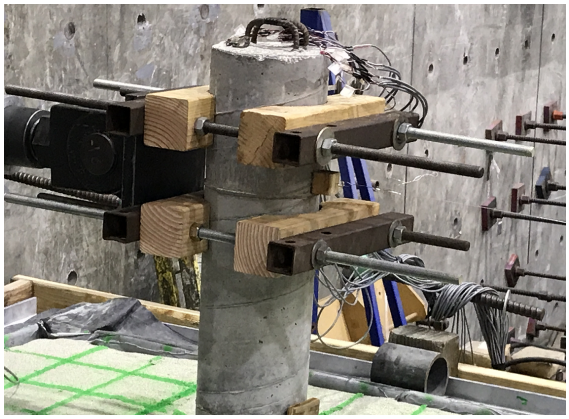

(b) Pile-actuator attachment detail for Pile 2 and 3.

Figure 3.28: Pile - actuator attachment details.

Testing protocol was guided by results obtained from the pre-test analytical studies with the software LPILE. In accordance with ASCE 41-06 S1, three loading cycles were applied at each displacement level. The testing protocol was followed with only minor deviations for all specimens. Adjustments were made towards the end of the test (e.g. after yield and encountering excessive plastic deformations) or at intermediate loading levels. Tables 3.13a through 3.13d show the actual load displacement sequence followed during the test along with Fig. 3.18a, which show the displacement time histories of each specimen, along with

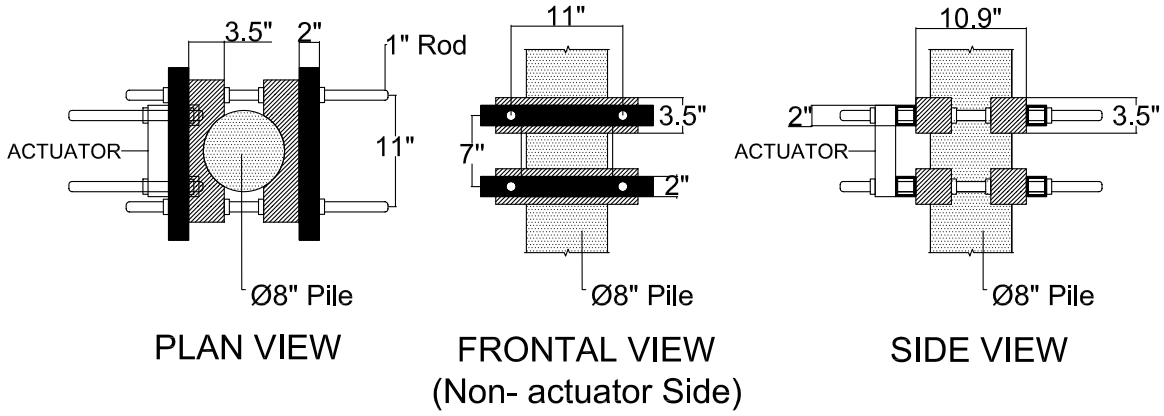

Figure 3.29: Details of the attachment used for the two 8 in piles with geotextile as reinforcement.

the respective load time histories.

3.4 Test Results

This section presents experimental results directly derived from the test data. Sensors that did not fully zero were adjusted during the post testing data processing. Sensors that produced disturbed signals were filtered using a low pass filter.

This section includes the full cyclic force-displacement relationship with an integrated backbone curve, representative sensor response histories (e.g. strain gauges located on longitudinal rebars, string pots, soil pressure sensors), curvature profiles with respect to pile elevation for significant pile deflections, and experimental moment- curvature relationships. An analysis of the cracks observed on the pile after it was taken out of the laminar soil box is also presented.

The sign conventions were set to the global coordinate system; horizontal motion (y direction) is positive from east to west, the vertical motion (z direction) is positive upward, and lateral

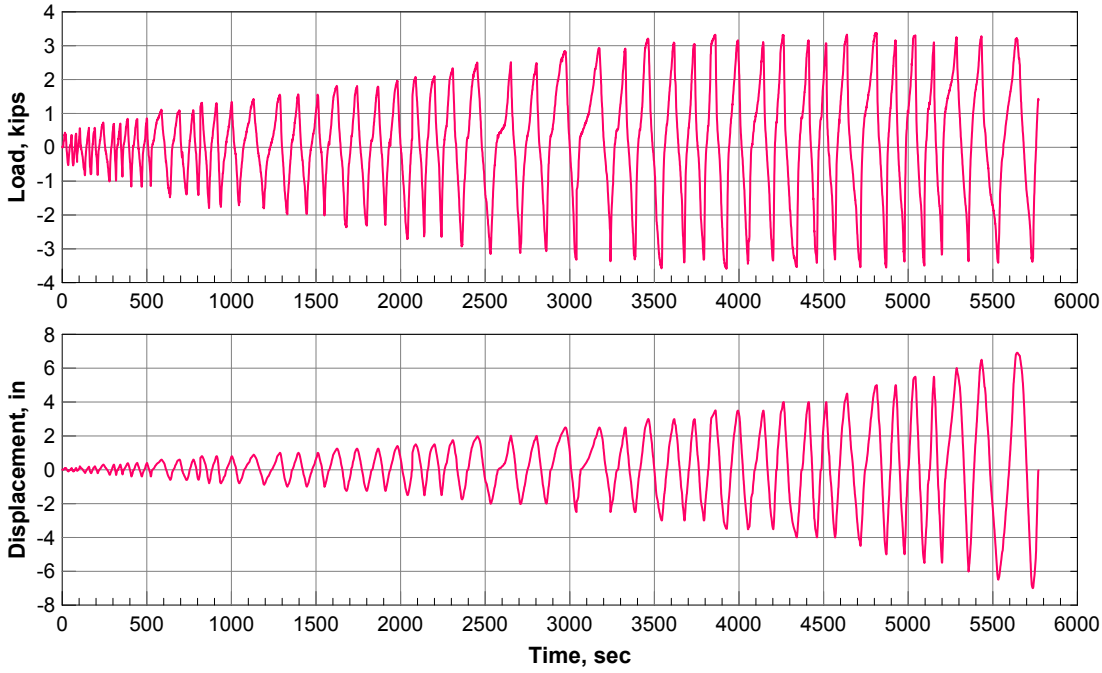

(a) Pile 1: 8 in polymer concrete pile with steel reinforcement.

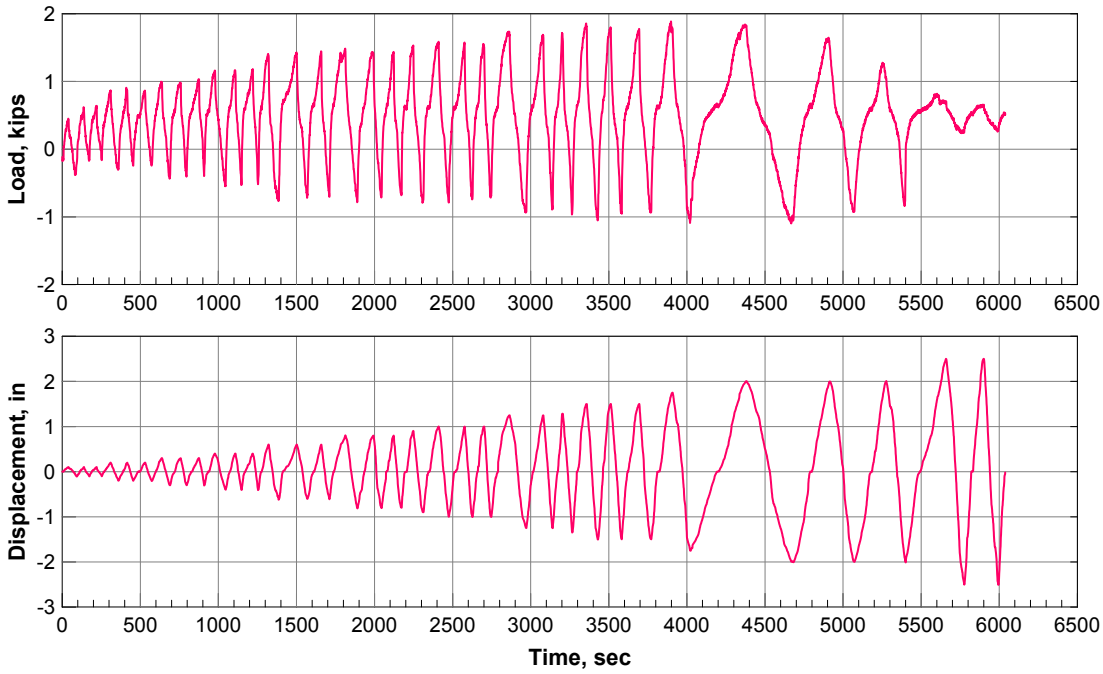

(b) Pile 2: 8 in Regular Concrete Pile with geotextile reinforcement.

Figure 3.30: Top load and top displacement time histories.

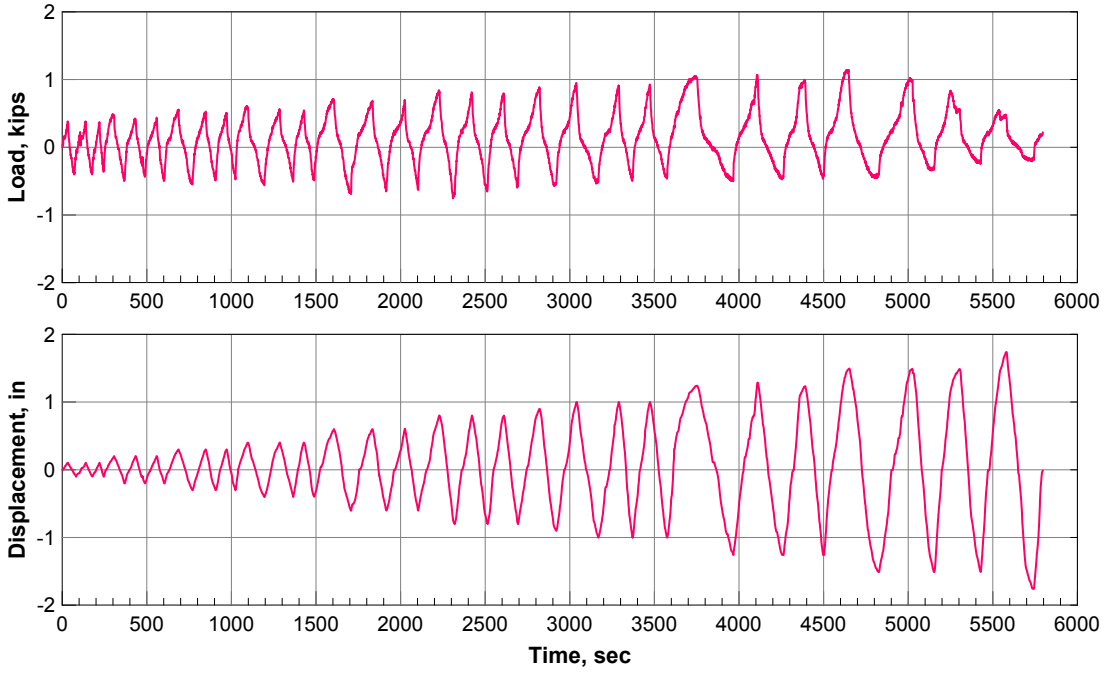

(c) Pile 3: 8 in Polymer Concrete Pile with geotextile reinforcement.

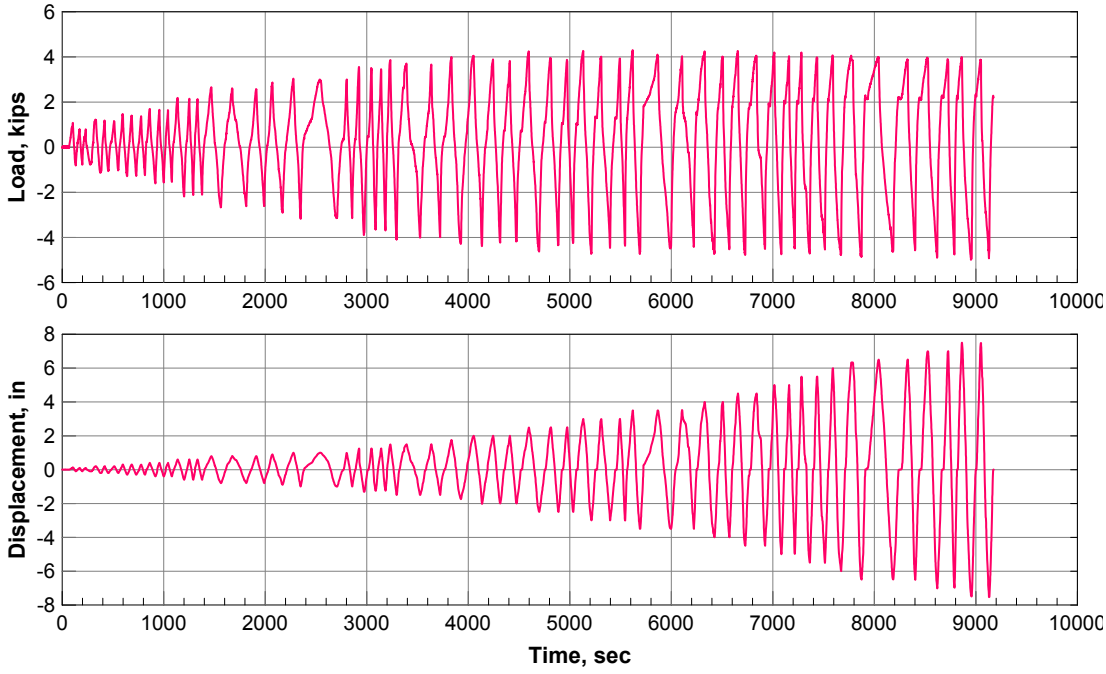

(d) Pile 4: 10 in polymer concrete pile with steel reinforcement.

Figure 3.30: Top load and top displacement time histories (cont.).

δ_y **Multiplier**	**Displacement [in]**	**Cycles**
1/8	0.1	3
1/4	0.2	3
2/5	0.3	3
1/2	0.4	3
3/4	0.6	3
1	0.8	3
1 1/4	0.9	1
1 1/3	1.0	3
1 1/2	1.25	3
2	1.5	3
2 1/3	1.75	1
2 2/3	2.0	3
3 1/3	2.5	3
4	3.0	3
4 2/3	3.5	3
5 1/3	4.0	3
6	4.5	1
6 2/3	5.0	2
7 1/3	5.5	2
8	6.0	1
8 2/3	6.5	1
9 1/3	7.0	1

(a) Pile 1.

δ_y **Multiplier**	**Displacement [in]**	**Cycles**
1/8	0.1	3
1/4	0.2	3
2/5	0.3	3
1/2	0.4	3
3/4	0.6	3
1	0.8	3
1 1/4	0.9	1
1 1/3	1.0	3
1 1/2	1.25	3
2	1.5	3
2 1/3	1.75	1
2 2/3	2.0	3
3 1/3	2.5	2

(b) Pile 2.

Table 3.13: Displacement levels for four specimens (Predicted Yield Displacement, δ_y=0.75 in).

δ_y **Multiplier**	**Displacement [in]**	**Cycles**
1/8	0.1	3
1/4	0.2	3
2/5	0.3	3
1/2	0.4	3
3/4	0.6	3
1	0.8	3
1 1/4	0.9	1
1 1/3	1.0	3
1 1/2	1.25	3
2	1.5	3
2 1/3	1.75	1

(c) Pile 3.

δ_y **Multiplier**	**Displacement [in]**	**Cycles**
1/8	0.1	3
1/4	0.2	3
2/5	0.3	3
1/2	0.4	3
3/4	0.6	3
1	0.8	3
1 1/4	0.9	1
1 1/3	1.0	3
1 1/2	1.25	3
2	1.5	3
2 1/3	1.75	1
2 2/3	2.0	3
3 1/3	2.5	3
4	3.0	3
4 2/3	3.5	3
5 1/3	4.0	3
6	4.5	1
6 2/3	5.0	2
7 1/3	5.5	2
8	6.0	1
8 2/3	6.5	3
9 1/3	7.0	2
10	7.5	2

(d) Pile 4.

Table 3.13: Displacement levels for four specimens (Predicted Yield Displacement, δ_y=0.75 in) (cont.).

motion (x direction) is positive from south to north (Fig. 3.31).

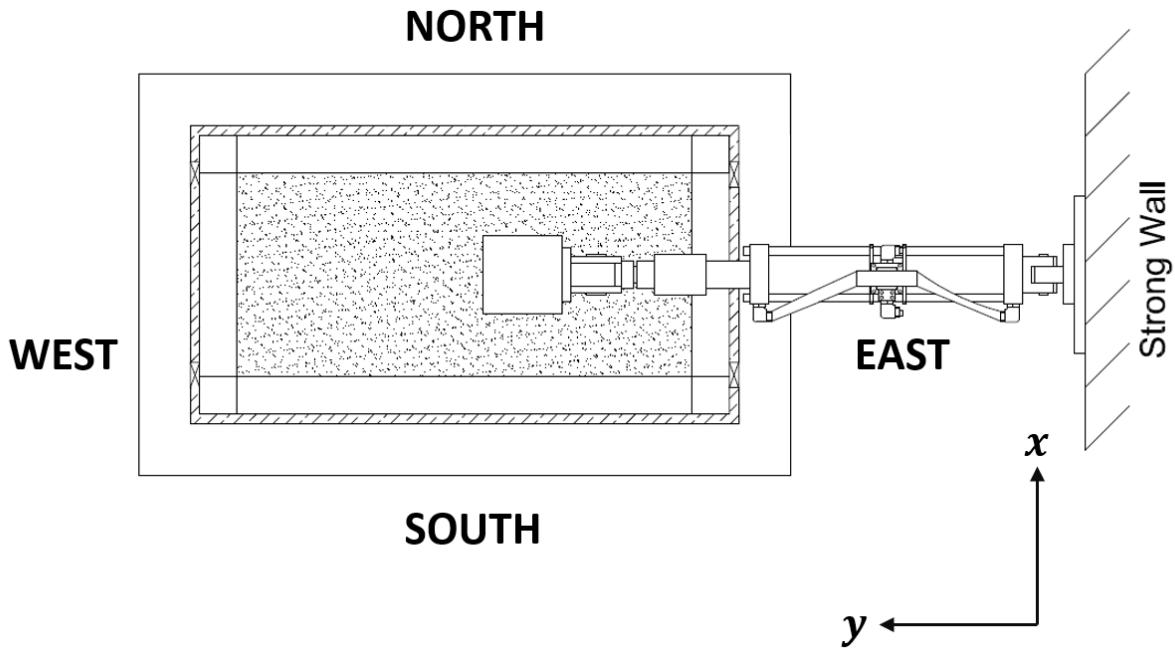

Figure 3.31: Global coordinates of the laminar soil box.

Table 3.14 provides a summary of the test results for the four specimens indicating measured loads at significant displacements.

3.4.1 8 in Polymer Concrete with Steel Reinforcement

The test started on July, 31st and was completed on August, 4th 2017. Selected photographs of the specimen during and after the test are shown in Figs. 3.32 and 3.33.

Large horizontal cracks formed around the pile at an elevation of 70- 75 in, which means 2-3 pile diameters below the soil surface. Although the cracks developed all around the pile circumference, the most damaged sides were the ones in the bending direction, with a width of 1- 2 in for the biggest cracks. Smaller cracks (less than 1/2 in) can be found in all four pile sides between 55 in and 80 in of elevation.

Table 3.14: Tests results overview.

Pile Specimens	**1**		**2**		**3**		**4**	
Load Direction	Push	Pull	Push	Pull	Push	Pull	Push	Pull
Actuator Peak Reaction Force [kips]	3.4	3.6	1.8	1.0	1.0	0.7	4.2	4.9
Displacement at peak force [in]	5	3.5	2	1.5	1.25	0.8	3	7.5
Max Displacement [in]	6.9	7	2.5	2.5	1.74	1.76	7.5	7.5
Actuator Reaction Force at max displacement [kips]	3.2	3.3	0.7	0.2	0.4	0.2	3.9	4.9
Yield Load [kips]	2.9	3	0.5	0.7	1.1	0.7	3.6	3.9
Yield Displacement [in]	2.5	1.7	0.6	1.4	1.5	0.75	1.2	1.3

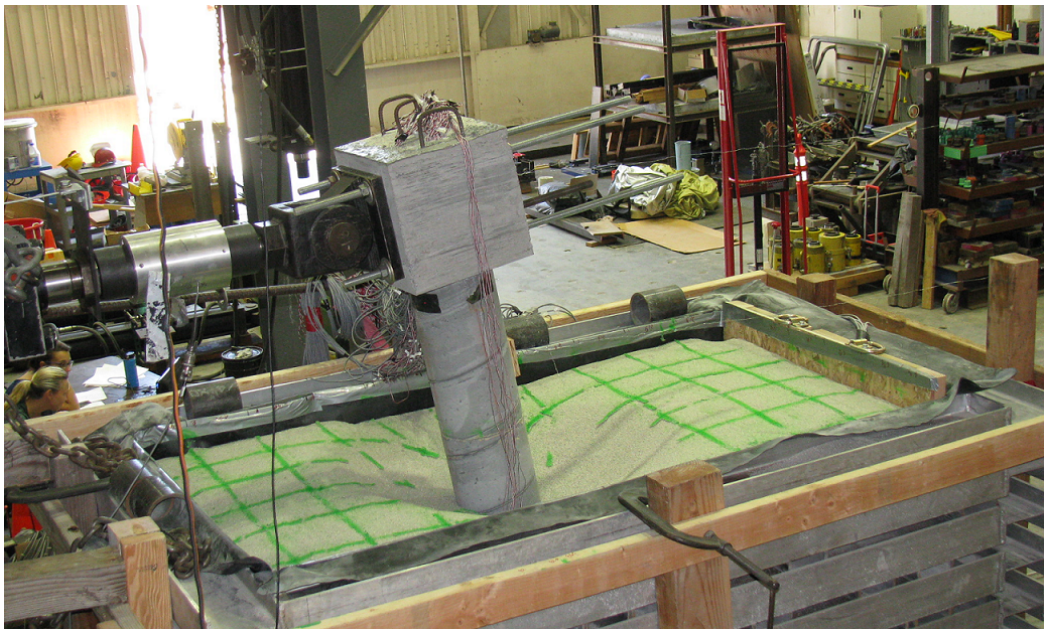

Figure 3.32: Pile 1: Maximum pile head deflection (7 in) and movements of the soil surface.

(a) North view.

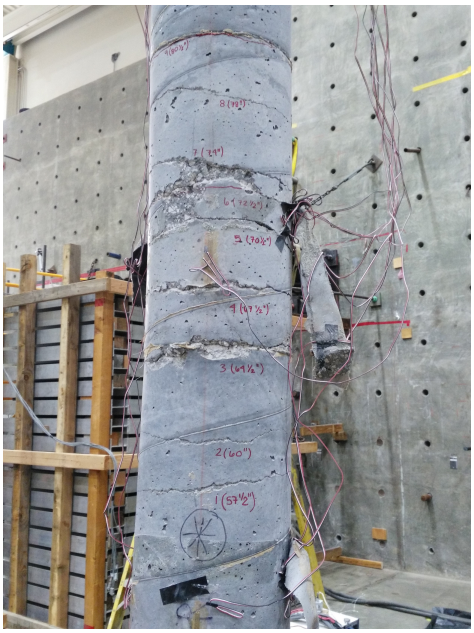

(b) East view.

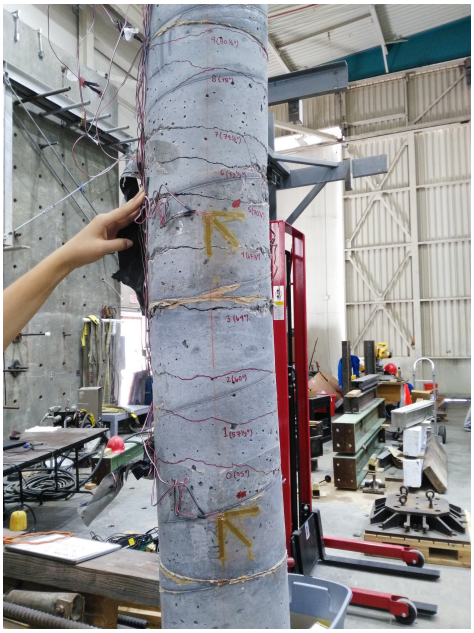

(c) South view.

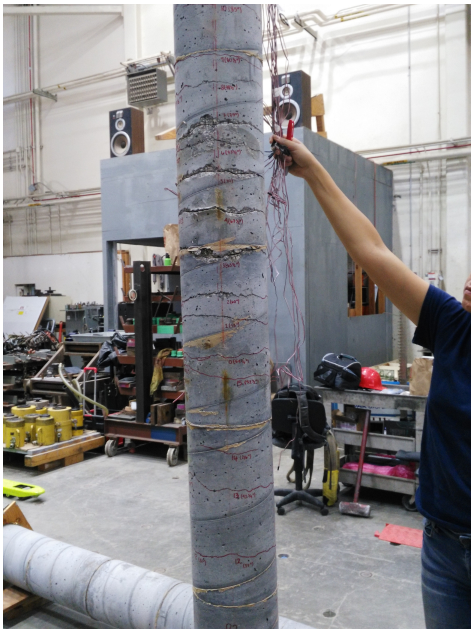

(d) West view.

Figure 3.33: Pile 1: Cracks.

Load vs Deflection

The measured cyclic response of the pile is shown in Fig. 3.34, and backbone load vs. deflection curves are shown in Fig. 3.35. The backbone curve was created using peak values for each cycle in push (positive) and pull (negative) direction. The maximum load observed in the push loading direction was 3.4 kips at 5 in of displacement, whereas the maximum load observed in the pull direction was 3.6 kips at 3.5 in of displacement. The yield force in push direction was 0.4 kips at a horizontal displacement of 0.1 in. In the pull direction the yield force measured 0.8 kips at a displacement of 0.2 in. The maximum displacement of Pile 1 was 6.9 in in the push direction, and 7.0 in the opposite direction.

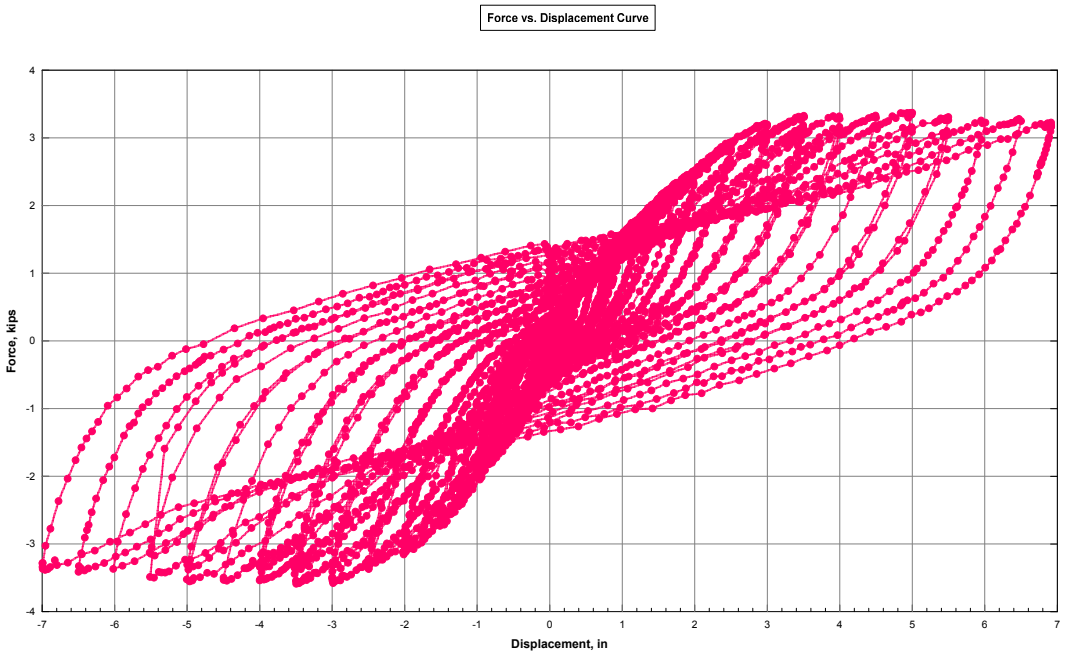

Figure 3.34: Pile 1: Cyclic response of the pile to the 7 in displacement level.

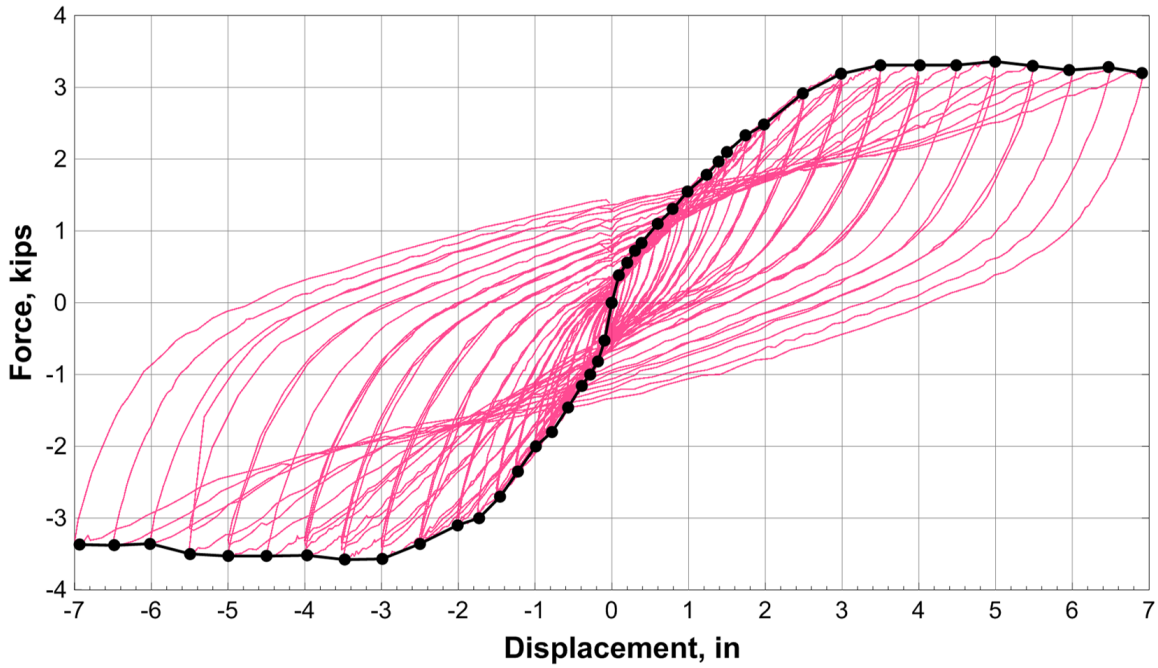

Figure 3.35: Pile 1: Backbone curve.

Representative Sensor Response Histories

The following paragraphs show the output of the strain gauges, string pots, and soil pressure sensors as a function of time. Once the sensors begin to fail and give unrealistic results, the readings are discarded from that point on for future analyses.

Strain Gauges Figs. 3.36 and 3.37 show response histories of 22 strain gauges affixed along the longitudinal rebars located opposite to each other on the pile cross section (Fig. 3.22). *R1* are located on the east side (in tension during pushing), while *R2* sensors are in the west side (in tension during pulling).

The strain gauges recorded approximately a maximum tensile strain of 0.011, corresponding to a +4.0 in displacement, at an elevation of 58 3/4 in ($R1-7$). The maximum compressive strain was found to be approximately 0.012, and it was found at an elevation of 88.5 in for

a -4.5 in deflection ($R2-2$)

After $+/-3$ in of pile head deflections, many sensors begin to give unrealistic results and progressively fail.

Tetrahedron 20 tetrahedra were installed inside the pile, for a total of 120 strain gauges (Fig. 3.22). Fig. 3.38 shows the response history of six strain gauges installed in the tetrahedron labeled as *T2* and located at the elevation of 89 1/4 in.

The strain gauges recorded approximately a maximum tensile strain of 0.04, corresponding to a +3 in displacement, at an elevation of 53 3/4 in. At the same location, the maximum compressive strain was also found. The recorded value was approximately 0.02, corresponding to a pile head deflection of -6 in.

External Strain Gauges 16 strain gauges were installed on the pile outside surface. In particular, four longitudinal strain gauges were installed in the pile bending direction (East and West sides), and 12 were attached on the pile shear direction (North and South sides), in a rectangular rosette configuration. More details about the external strain gauges' arrangements are included in Fig. 3.23.

Figs. 3.39, 3.40, and 3.41 show the response histories of the 16 external strain gauges.

The strain gauges on the shear side recorded approximately a maximum tensile strain of 0.021, corresponding to a +4 in displacement, at an elevation of 29 1/4 in from the bedrock. On the bending side, a maximum tensile strain was found to be 0.0012 for a deflection level of -2 in, at the elevation of 13 1/4 in from the bedrock. The maximum compressive strain was found to be approximately 0.01 on the shear side at an elevation of 30 1/4 in, for a +4 in deflection. The maximum compressive strain was found to be 0.01 as well, corresponding to a +2.50 in pile deflection and to an elevation of 13 1/4 in from the bedrock.

String Pots Four string pots were attached to two sides of the laminar soil box (see Fig. 3.16) to monitor its movements during the test. Other two string pots were attached to the pile top. Fig. 3.42 shows the time histories of the string pots used in this test and the pile top displacement history as reference.

The laminar soil box was allowed to small movements, registering a maximum displacement of approximately 1/2 in during the pushing of the pile. For details about the laminar soil movements in relation to the pile head displacement, refer to Figs. 3.43 and 3.44.

The string pot on the pile cap (*SP6*) well matches the movements of the actuator, showed in the LVDT graph (bottom graph in Fig. 3.42).

Soil Pressure Sensors Fig. 3.45 shows the output of the soil pressure sensors as a function of time. The units of measurement were pound per square inch (psi). The maximum pressure value registered was approximately 45 psi at depth of 33 in below the soil surface.

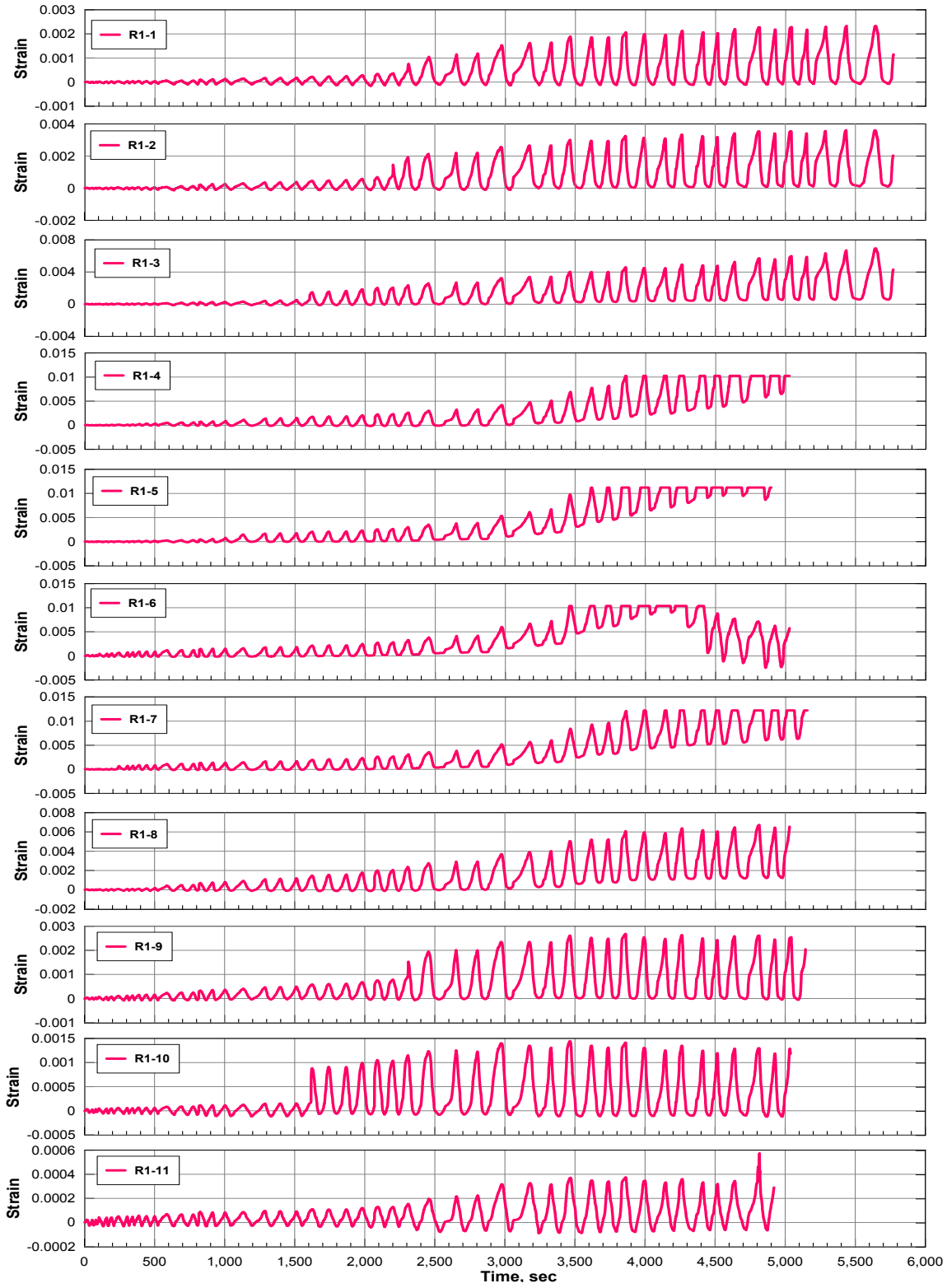

Figure 3.36: Pile 1: Strain gauges histories on longitudinal rebar *R1* (East side) for different pile elevations.

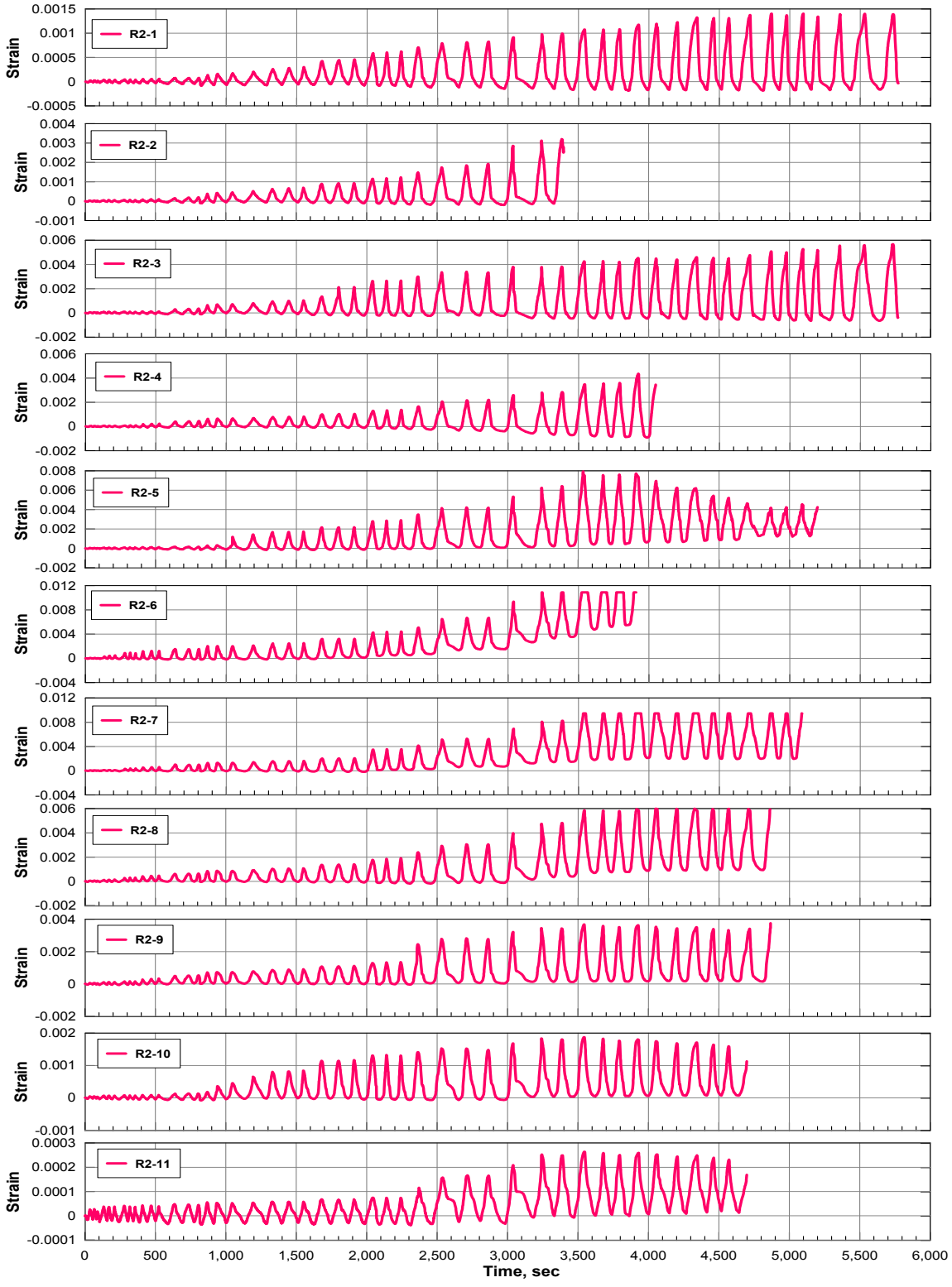

Figure 3.37: Pile 1: Strain gauges histories on longitudinal rebar *R2* (West side) for different pile elevations.

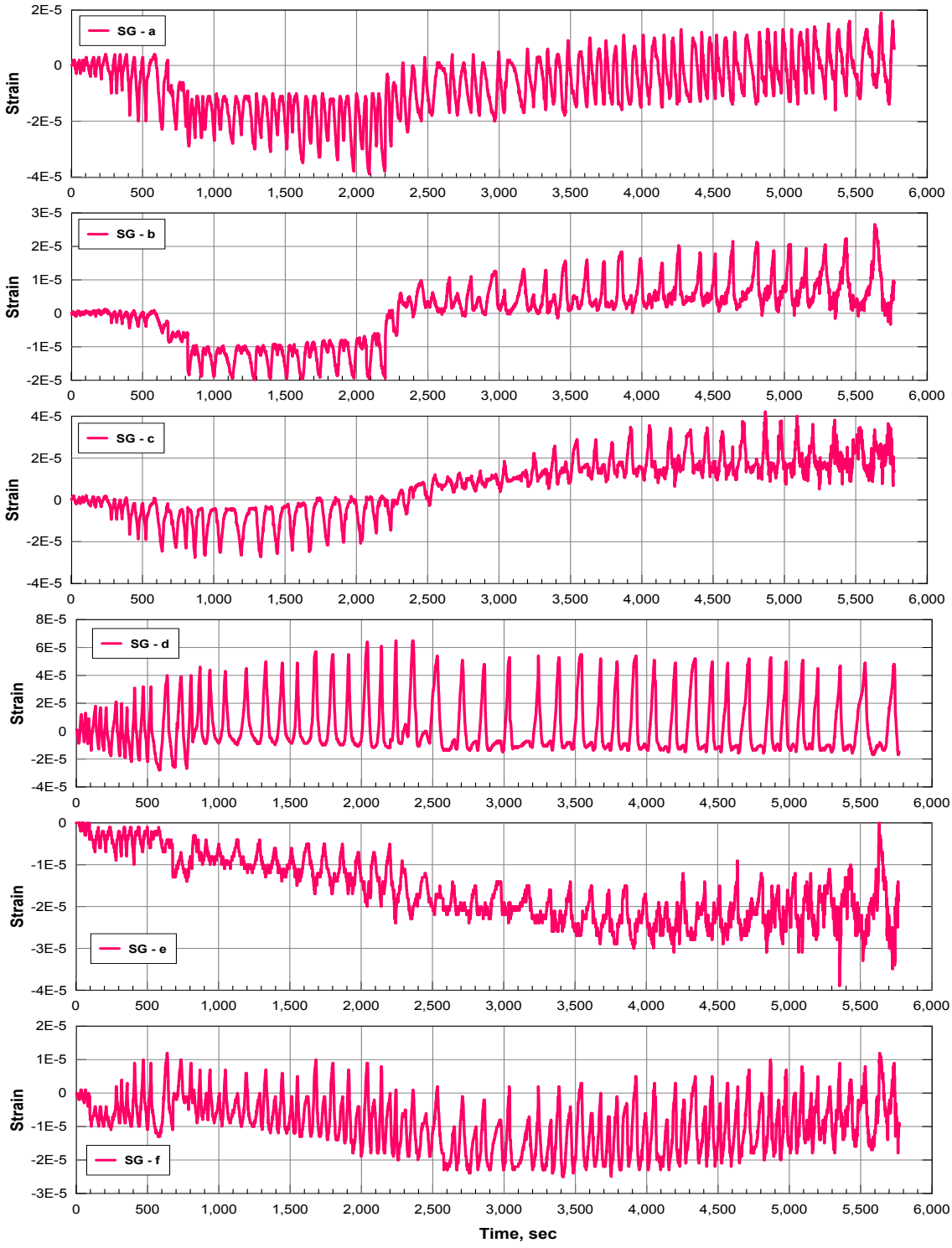

Figure 3.38: Pile 1: Strain gauges histories on *T2* tetrahedron located on the North side of the pile at an elevation of 89 1/4 in.

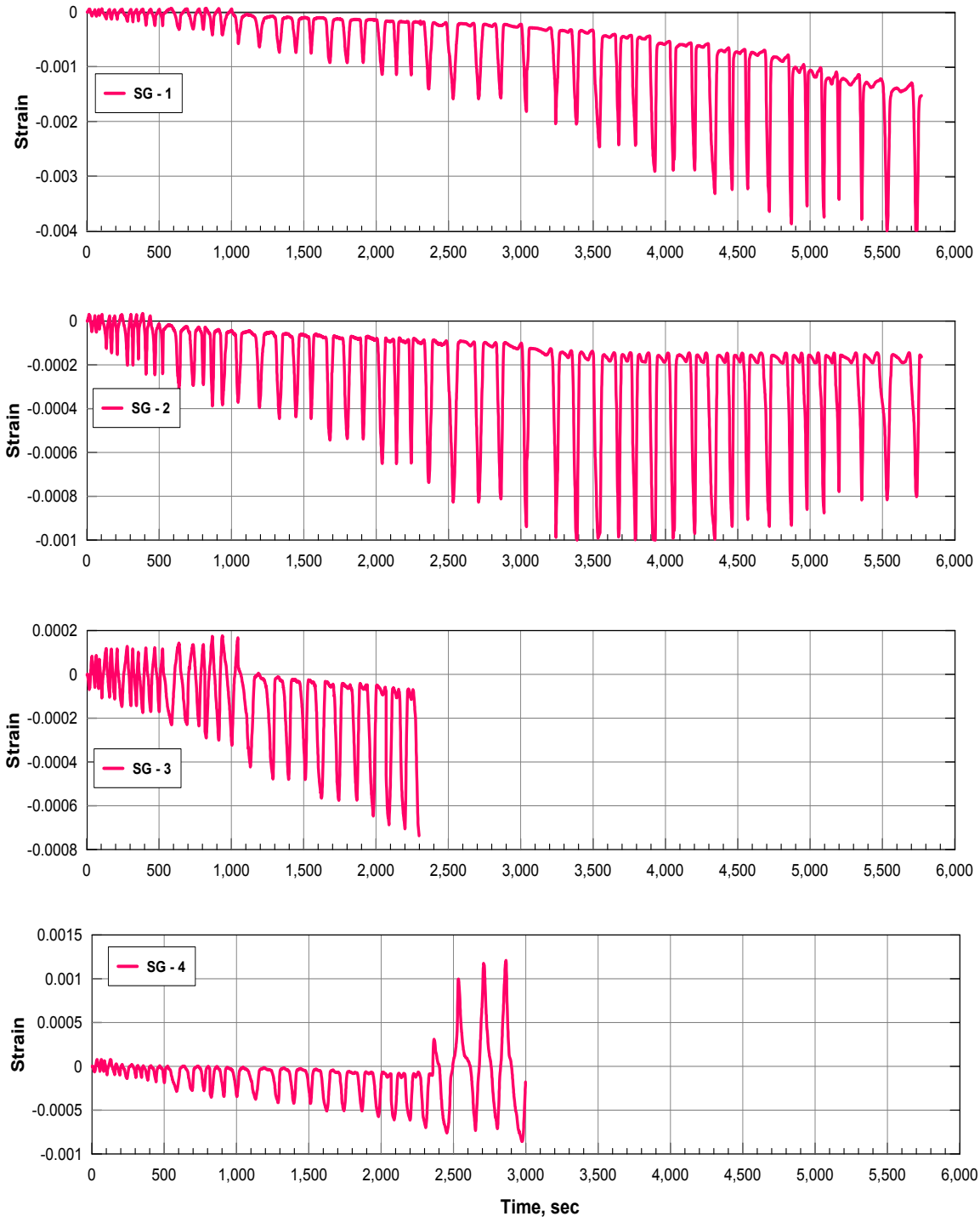

Figure 3.39: Pile 1: Time histories of external strain gauges located on the East and West sides (bending direction).

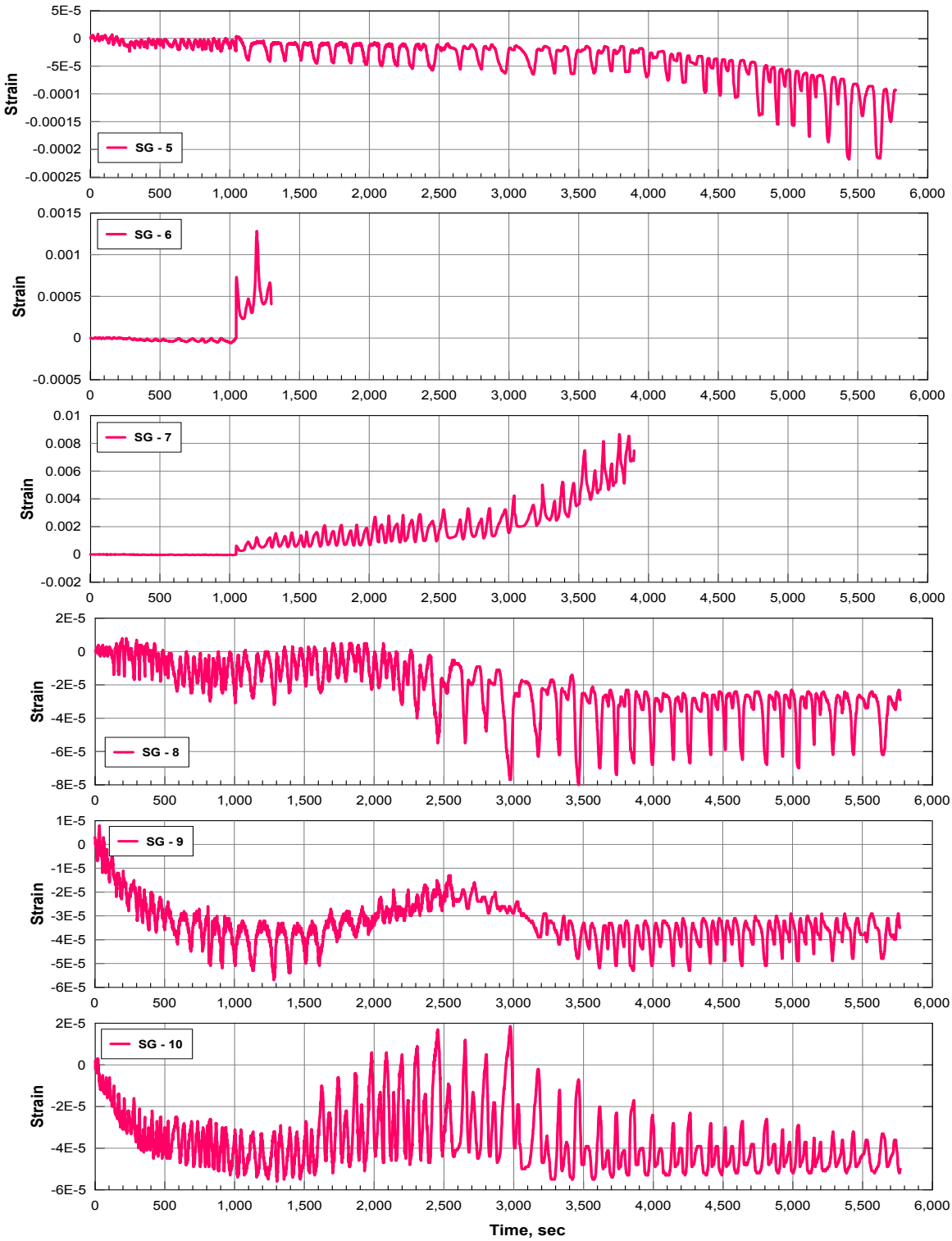

Figure 3.40: Pile 1: Time histories of external strain gauges located on the North side (shear direction).

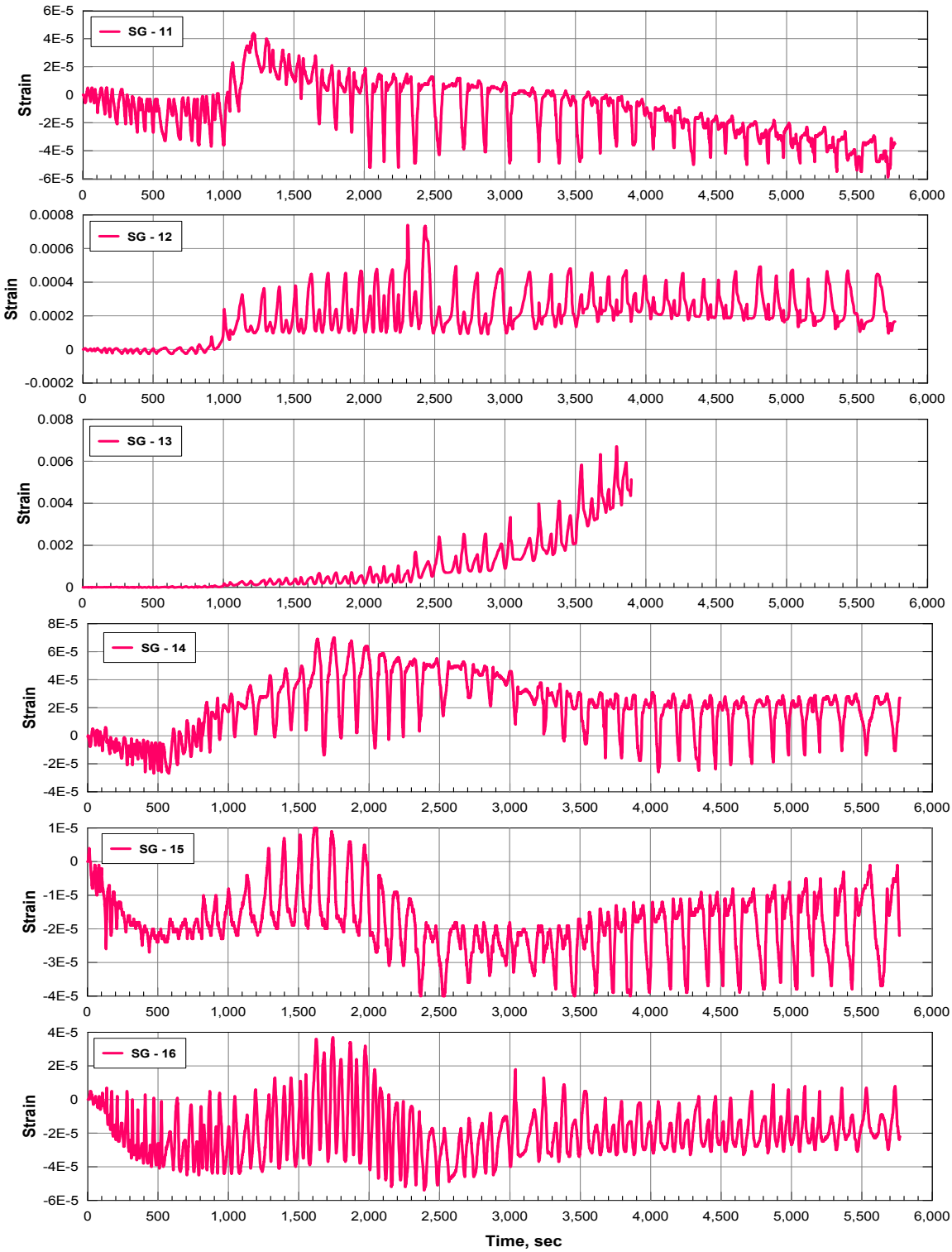

Figure 3.41: Pile 1: Time histories of external strain gauges located on the South side (shear direction).

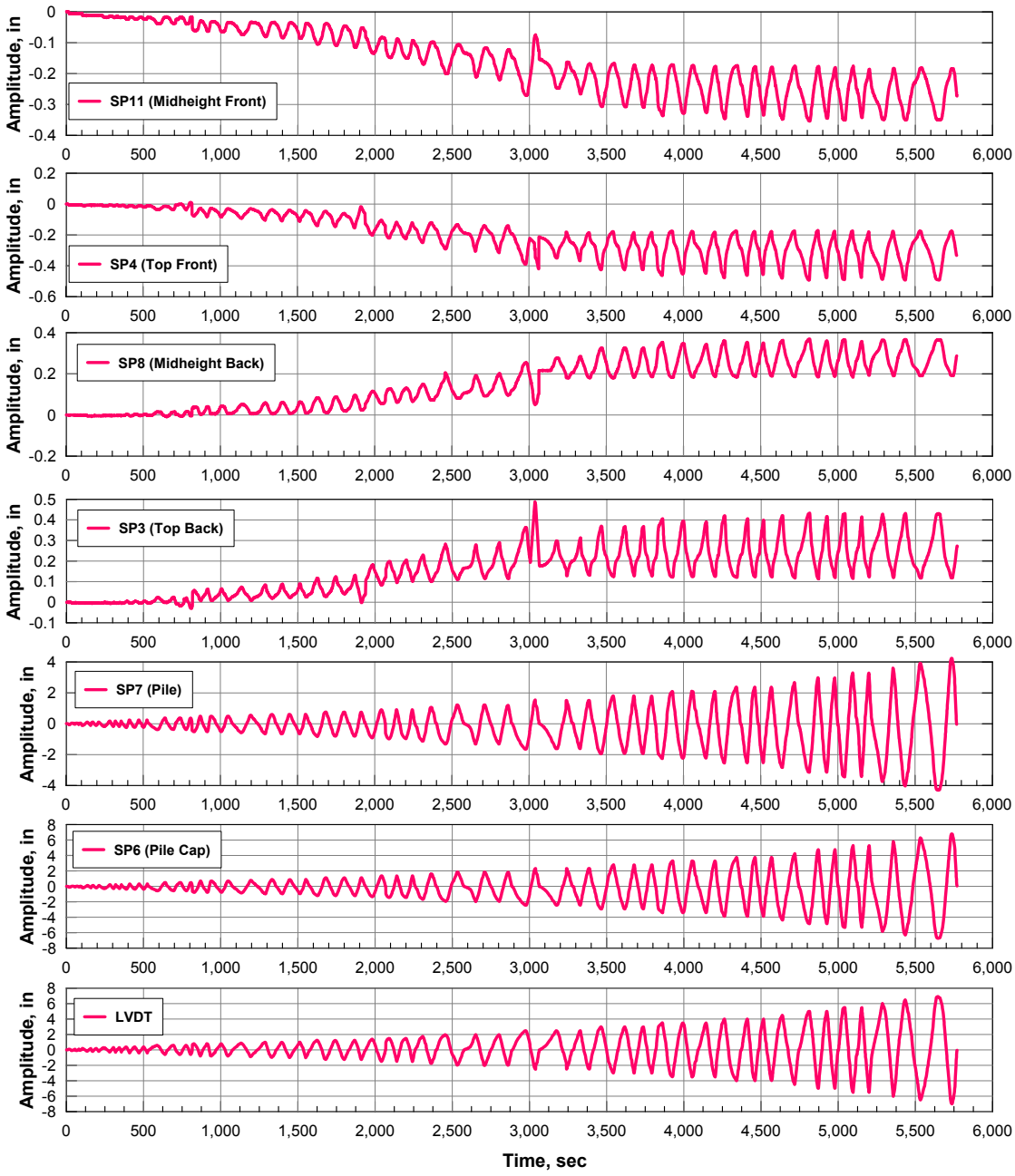

Figure 3.42: Pile 1: String pots histories.

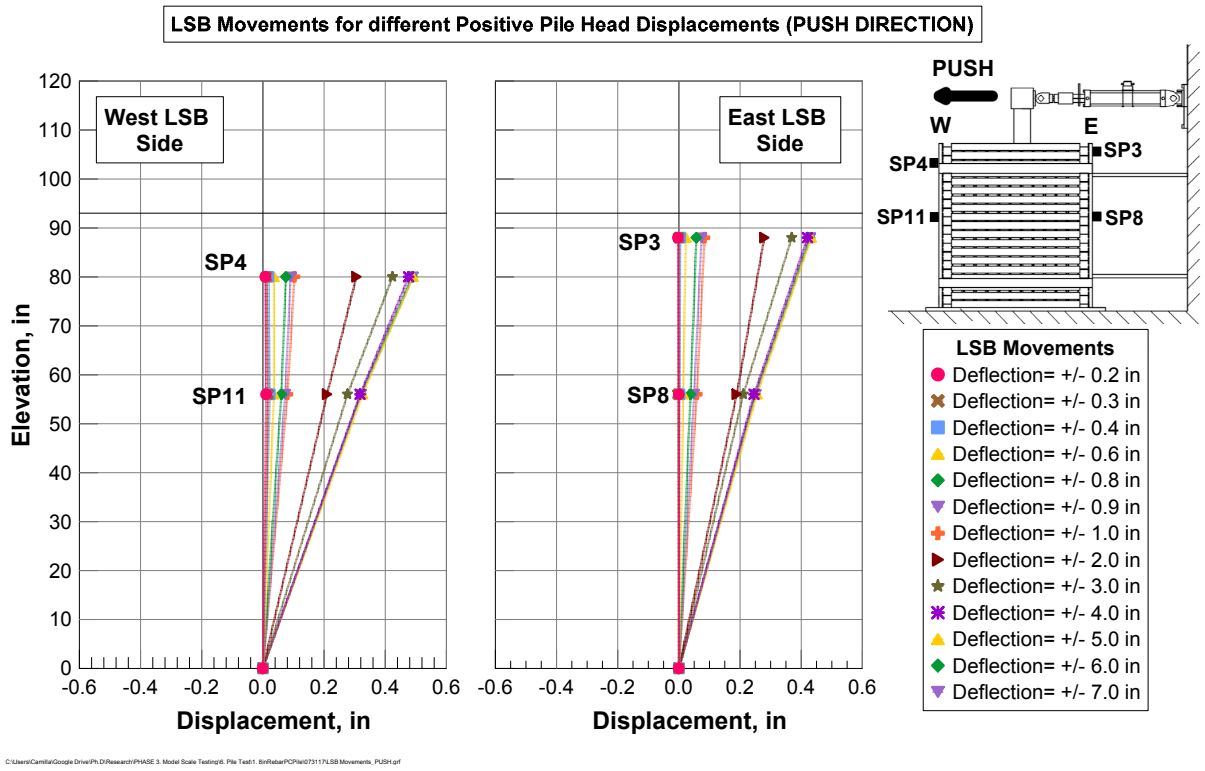

Figure 3.43: Pile 1: LSB movements in the push direction.

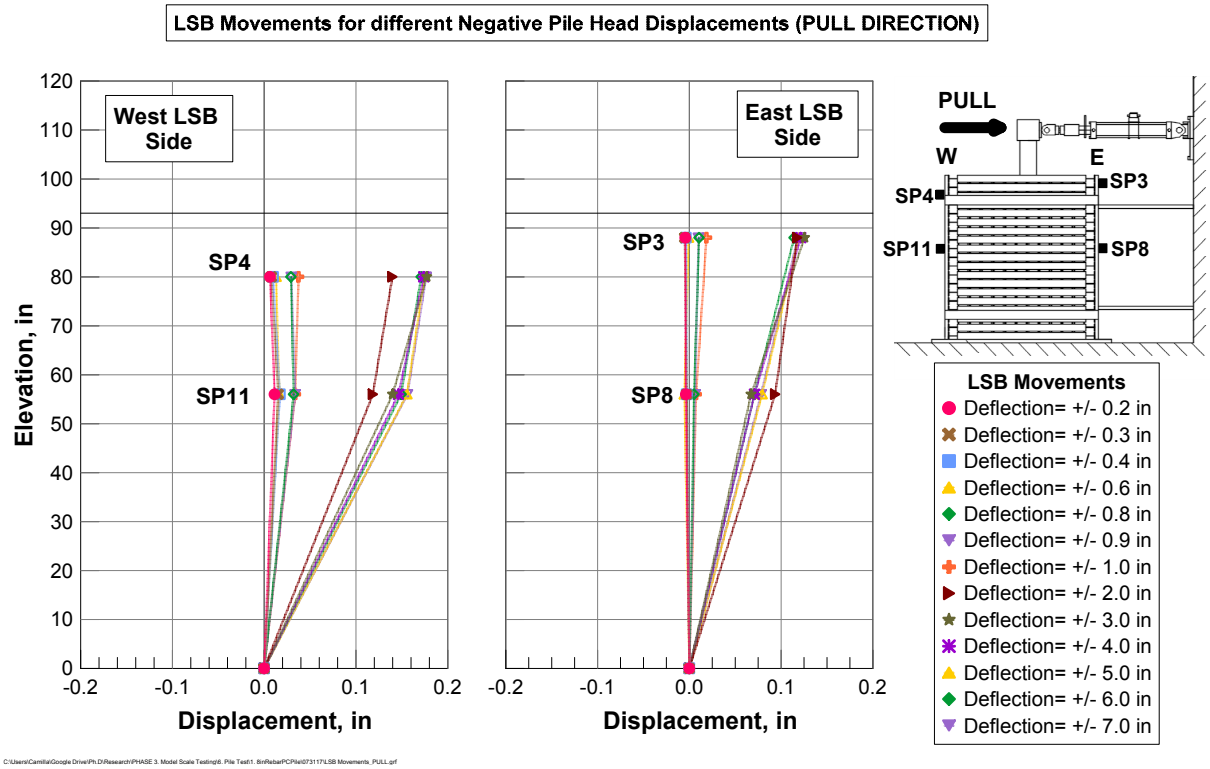

Figure 3.44: Pile 1: LSB movements in the pull direction.

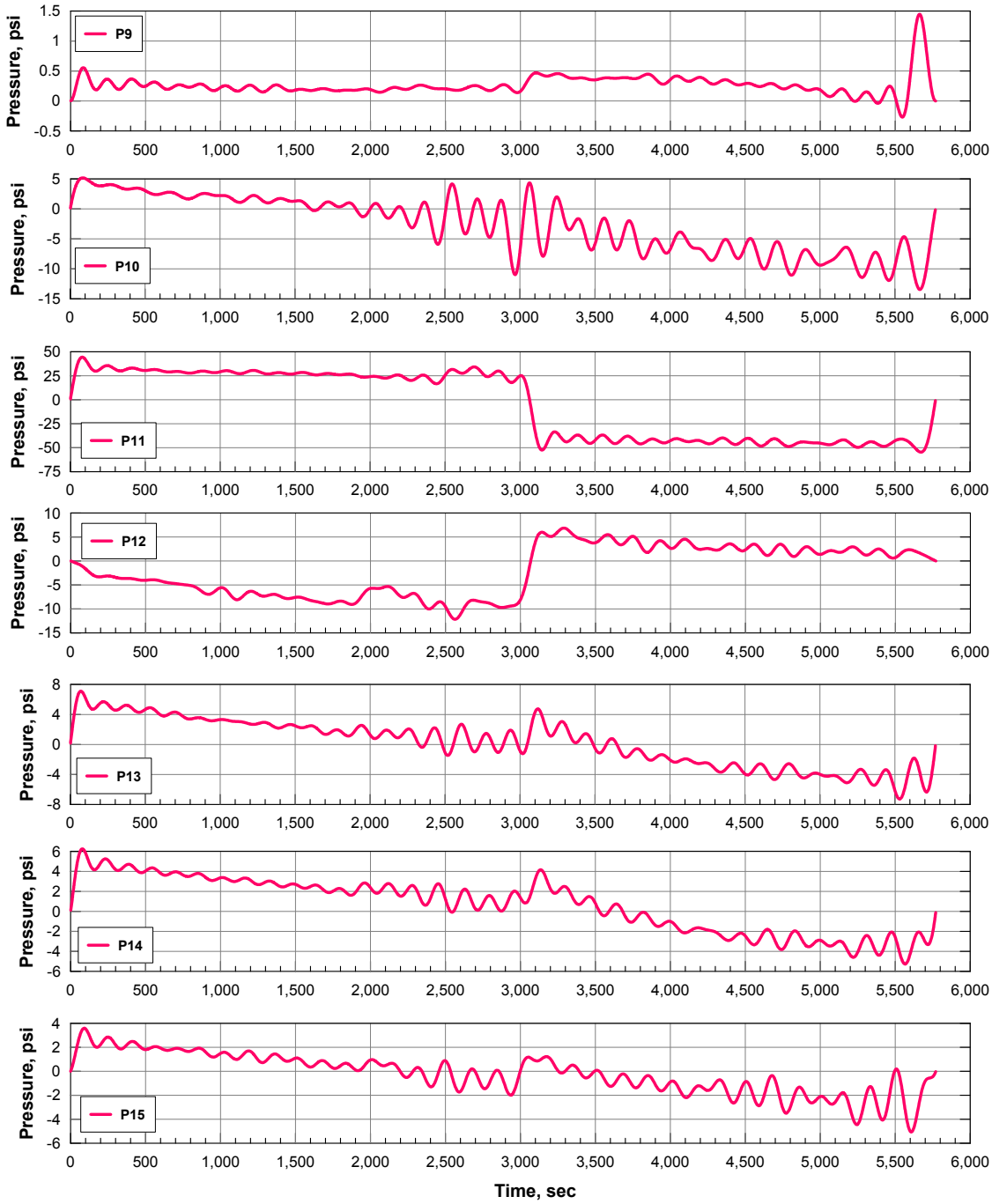

Figure 3.45: Pile 1: Soil pressure sensors' histories.

Curvature Profile

Calculated curvature values with respect to the pile elevation are shown in Fig. 3.46. Sensor depths and head displacements are noted on the plots. Curvature profiles for the model piles are calculated from pairs of strain gauges located at the same elevation. The curvature at each depth is generated using axial strain measurements as follows:

$$\phi(z) = \frac{d^2y}{dz^2} = \frac{\epsilon_1(z) - \epsilon_2(z)}{d} \tag{3.10}$$

where ε_1 and ε_2 are the axial strain measurements on opposites sides of the piles at elevation z, and d is the horizontal separation distance between sensors.

The largest curvature values were recorded within the yielding region (plastic hinge region) that formed at approximately 3 ft (3.5 pile diameters) below ground surface.

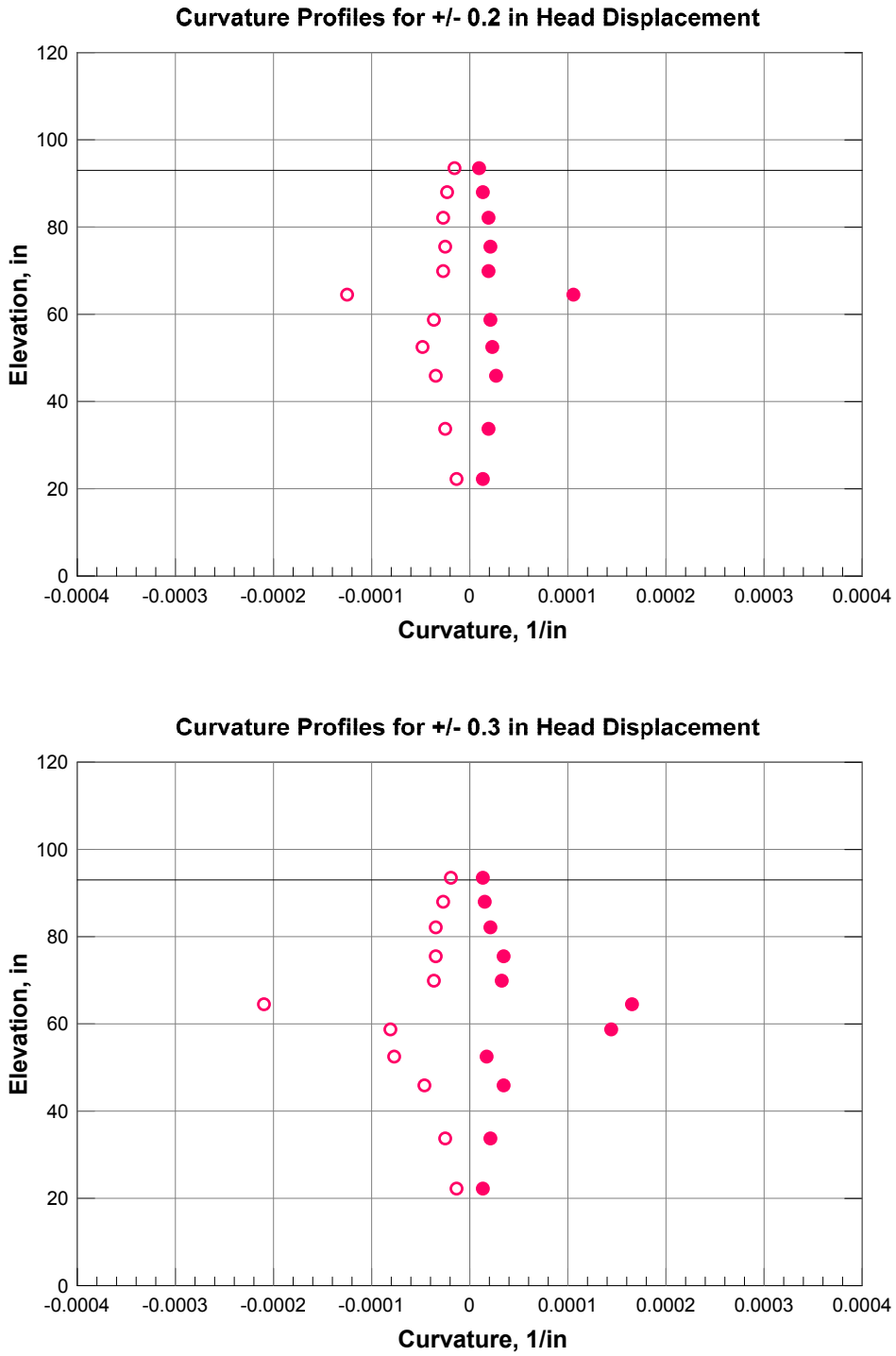

Figure 3.46: Pile *1*: Curvature profiles from 0.2 in to 3.5 in displacement levels. + and - indicate curvature values for positive and negative deflections, respectively.

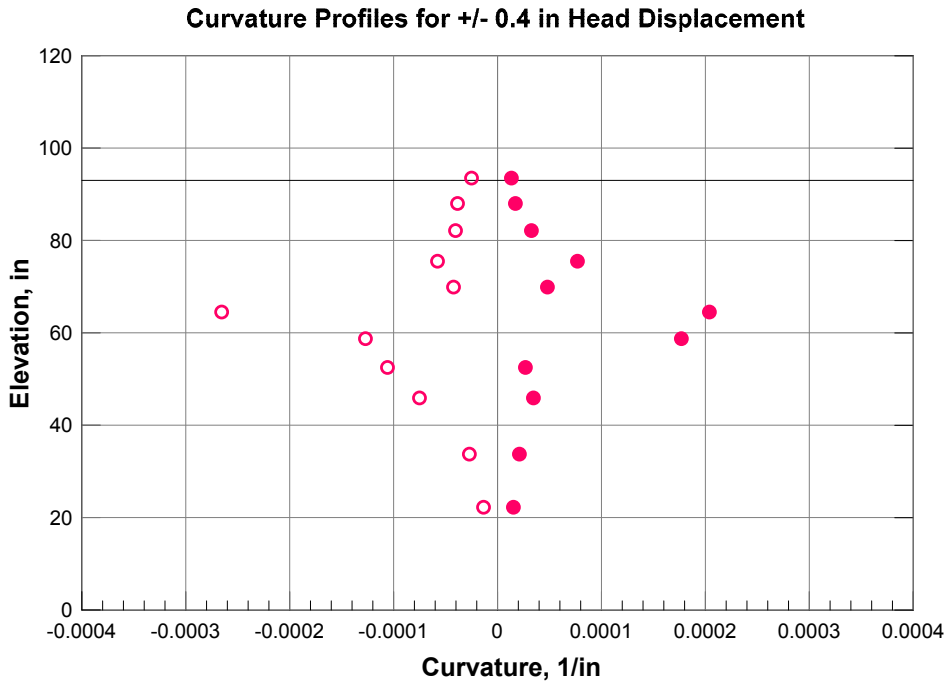

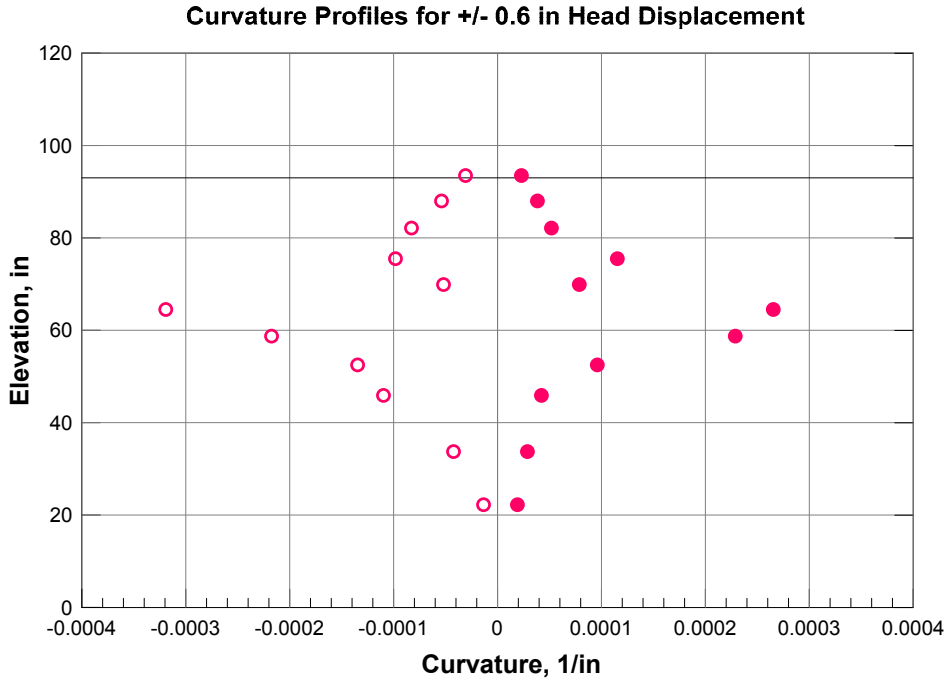

Figure 3.46: Pile *1*: Curvature profiles from 0.2 in to 3.5 in displacement levels. + and - indicate curvature values for positive and negative deflections, respectively (cont.).

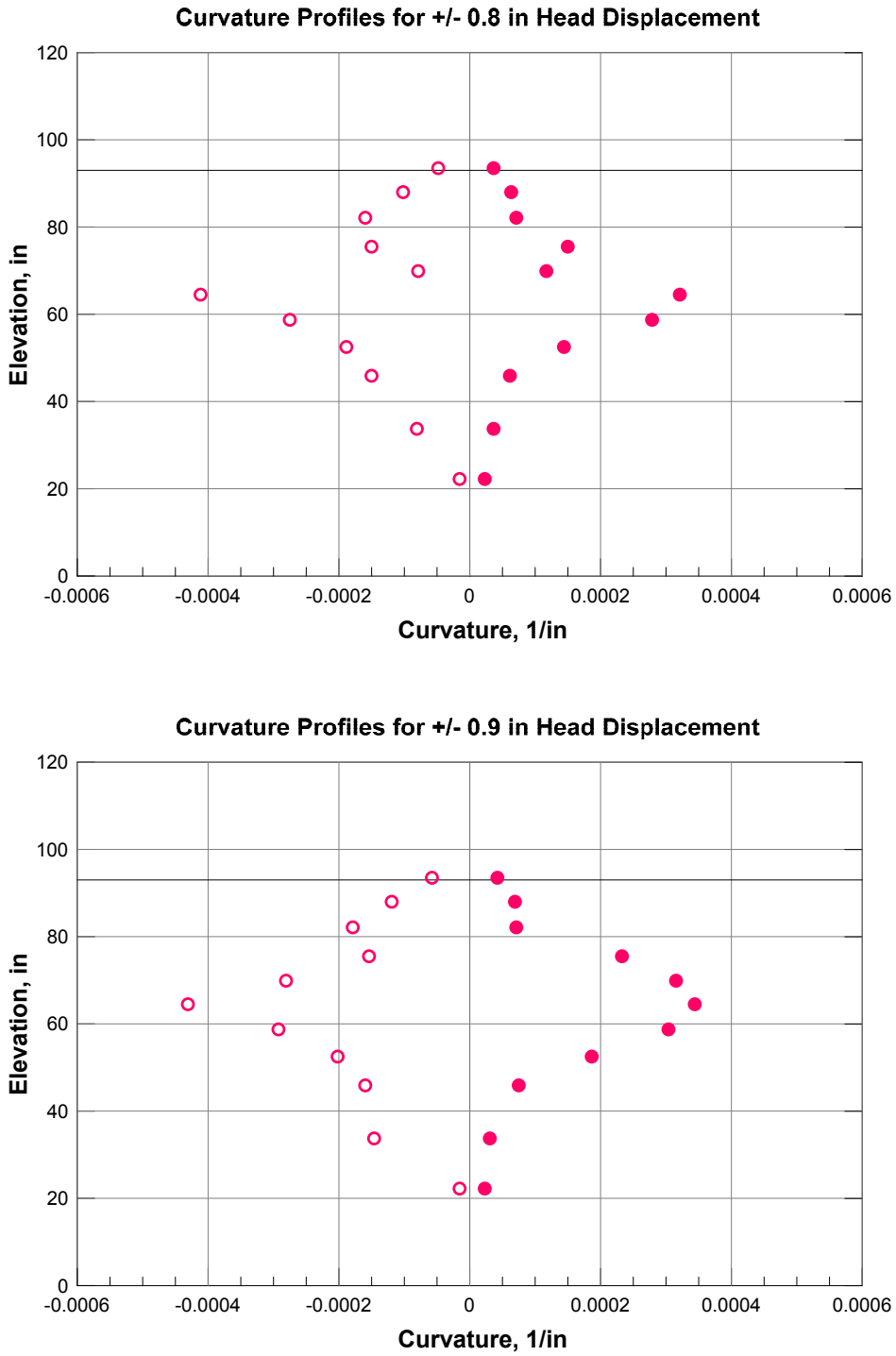

Figure 3.46: Pile *1*: Curvature profiles from 0.2 in to 3.5 in displacement levels. + and - indicate curvature values for positive and negative deflections, respectively.

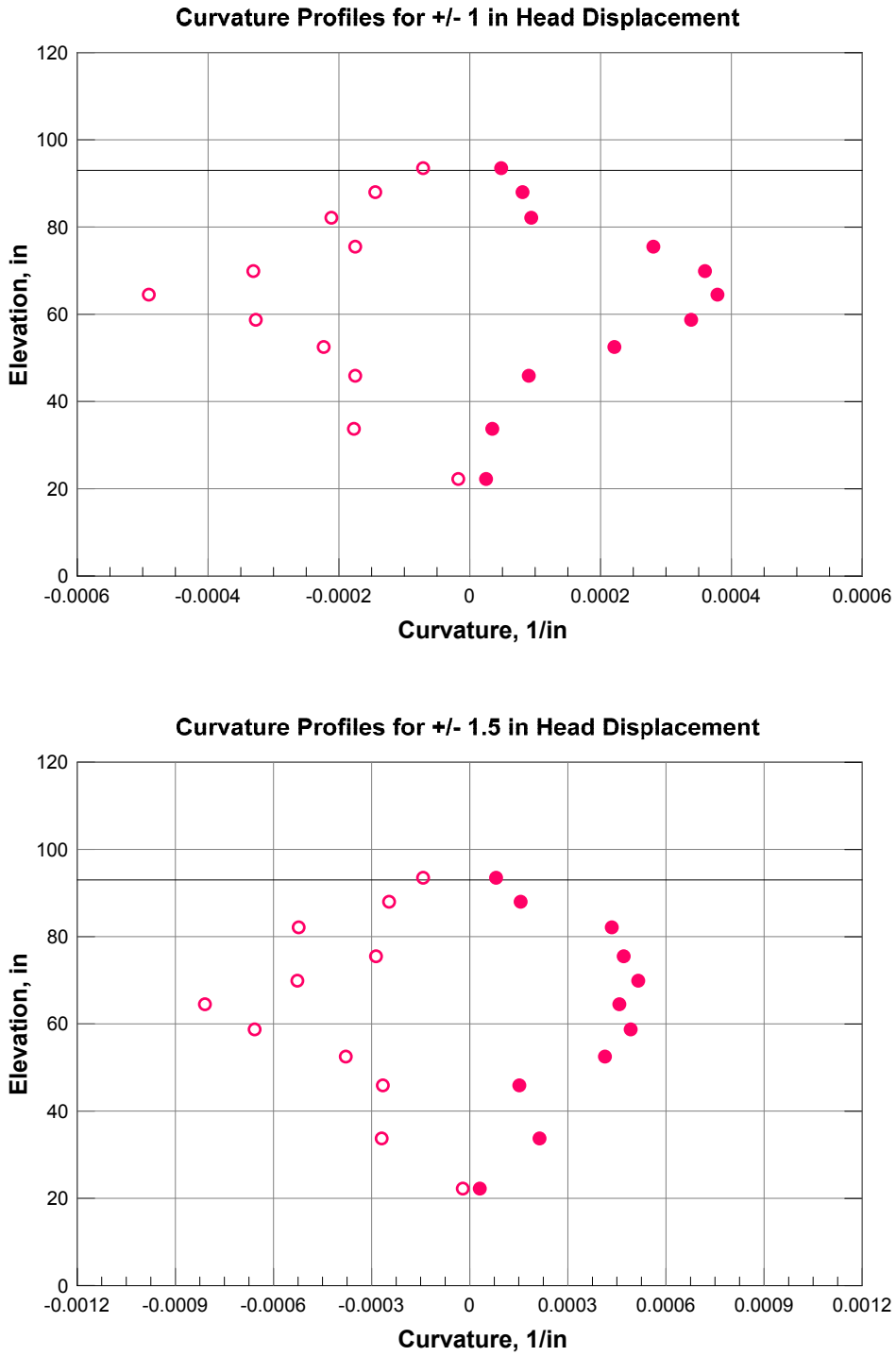

Figure 3.46: Pile *1*: Curvature profiles from 0.2 in to 3.5 in displacement levels. + and - indicate curvature values for positive and negative deflections, respectively (cont.).

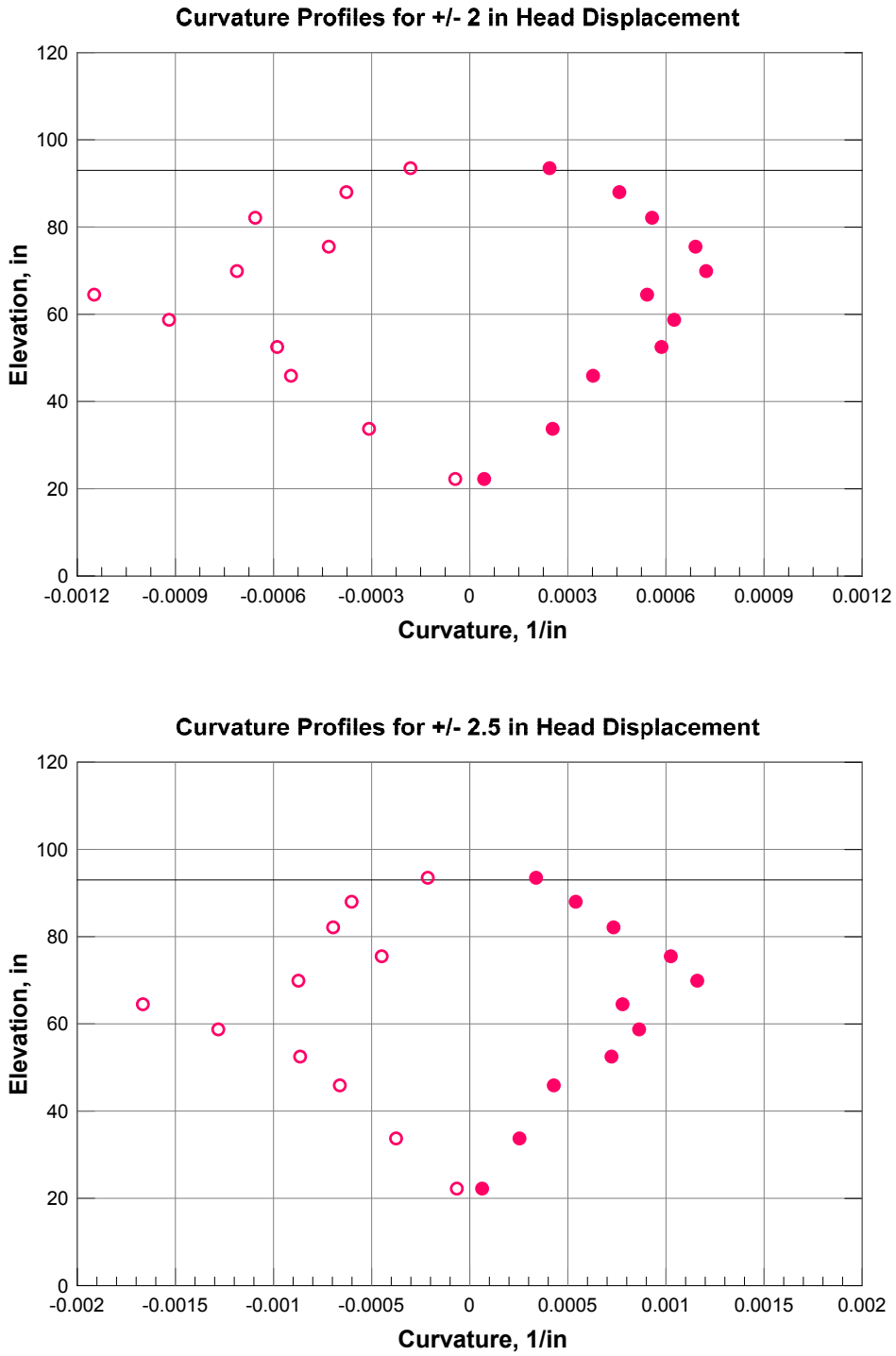

Figure 3.46: Pile *1*: Curvature profiles from 0.2 in to 3.5 in displacement levels. + and - indicate curvature values for positive and negative deflections, respectively.

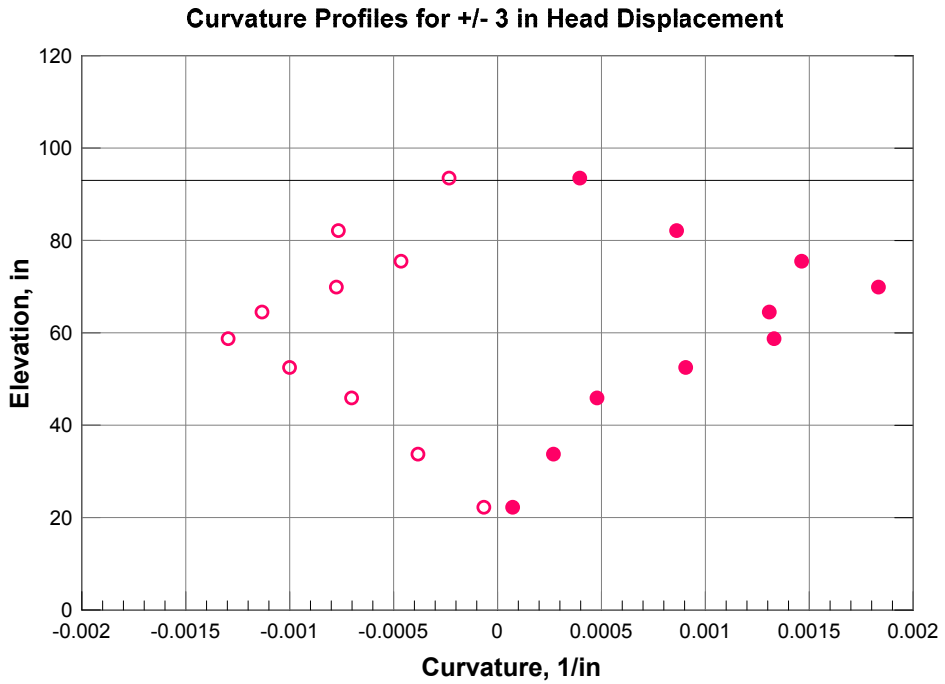

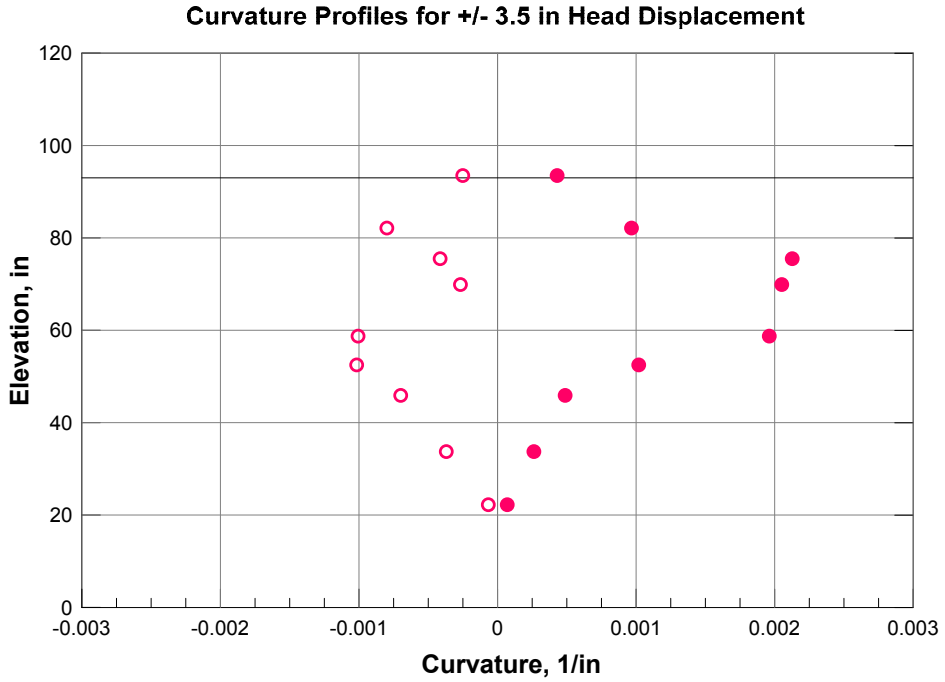

Figure 3.46: Pile *1*: Curvature profiles from 0.2 in to 3.5 in displacement levels. + and - indicate curvature values for positive and negative deflections, respectively (cont.).

Experimental Moment - Curvature Relationship

The bending moments are directly related to the curvatures. In the early stage of a test, when a pile still behaves linearly and elastically, the flexural stiffness (EI) is easy to compute, and the moment distribution is readily achieved by multiplying the curvature distribution by the scale factor EI. However, when strains rise above the threshold of concrete cracking, EI is no longer constant because of tensile concrete cracking and nonlinearity between stresses and strains, causing the variation of the section inertia I and of the elastic modulus E. To overcome the problem of EI variation, a computer program was used to compute the bending moments of a section where the history of both the curvatures and axial forces is known Response2000 [10].

The experimental moment-curvature relationship derived from test data, as well as predicted relationships, are shown in Fig. 3.47. Values of concrete compressive strength and rebar yield were used as presented in Table 3.5. Details of the analytical relationship are included in Fig. 3.48.

Experimental moment-curvature relationships were produced by correlating known moments at the ground surface with curvature measurements derived from strain gauges at approximately same location. The analytical model well capture the stiffness of the experimental data, as shown in Fig. 3.47.

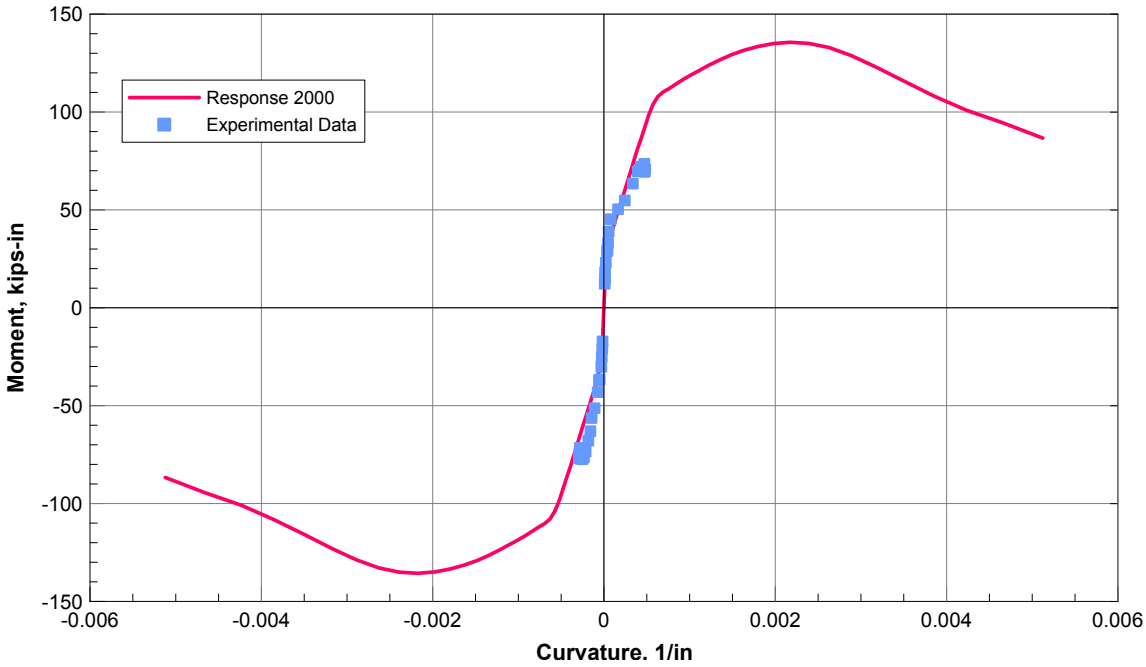

Figure 3.47: Experimental and predicted moment- curvature relationships for Pile 1.

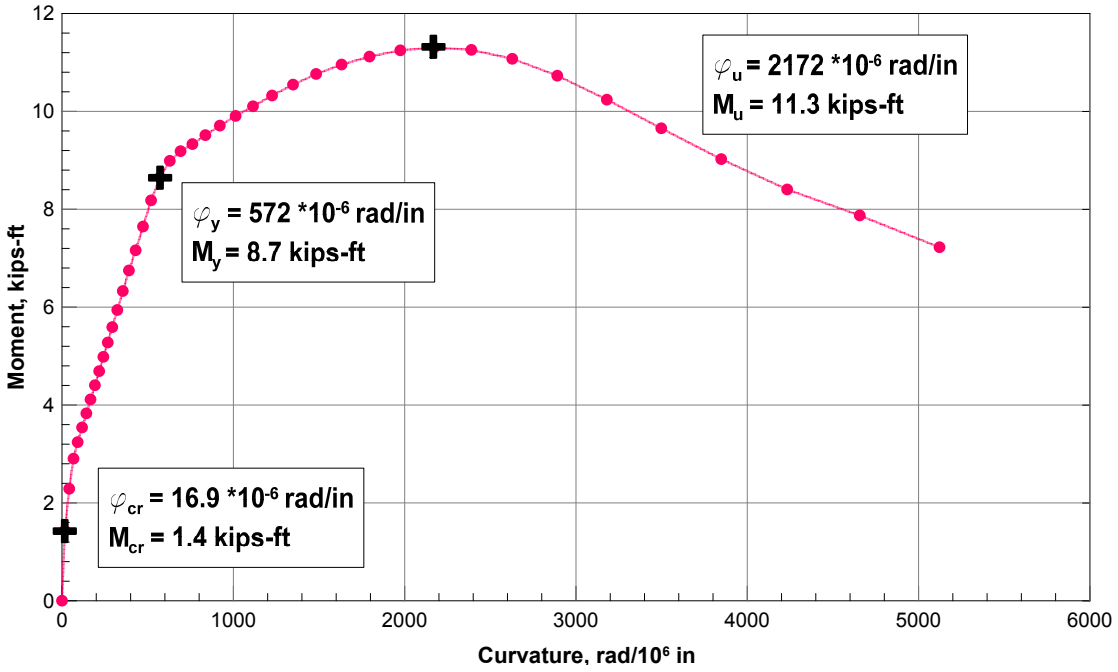

Figure 3.48: Analytical moment- curvature relationship from Response 2000 for the 8 in polymer concrete pile.

3.4.2 8 in Regular Concrete with Geotextile Reinforcement

The test was performed on August, 18th 2017. Selected photographs of the specimen during and after the test are shown in Figs. 3.49 and 3.50.

Once extracted from the sand, Specimen 2 did not present any horizontal or vertical significant crack. The only major crack developed at 73 in of elevation (2.5 pile diameters below the surface) and brought the pile to failure.

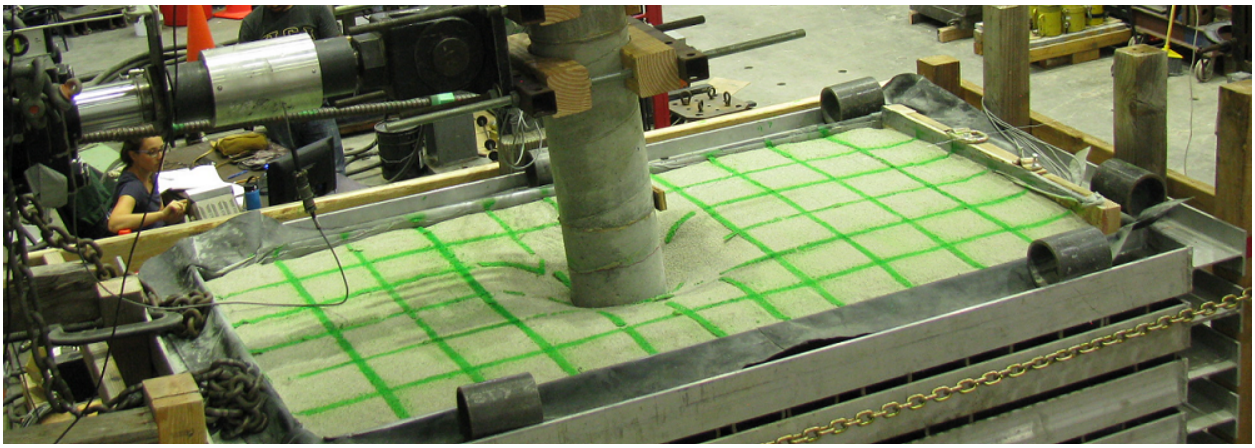

Figure 3.49: Pile 2: Maximum pile head deflection and soil surface' s movements.

Figure 3.50: Pile 2: Cracked pile.

Load vs Deflection

A testing protocol similar to the one developed for Pile 1 was followed to enable general comparisons in force and displacement. The measured cyclic response of the pile is shown

in Fig. 3.51, and backbone load vs. deflection curves are shown in Fig. 3.52. The backbone curve was created using peak values for each cycle in push (positive) and pull (negative) direction. The maximum load observed in the push loading direction was 1.8 kips at 2.0 in of displacement, whereas the maximum load observed in the pull direction was 1.0 kips at 1.5 in of displacement. The yield force in push direction was 0.5 kips at a horizontal displacement of 0.6 in. In the pull direction the yield force measured 0.7 at a displacement of 1.4 in. The maximum displacement of Pile 2 was 2.5 in in both directions.

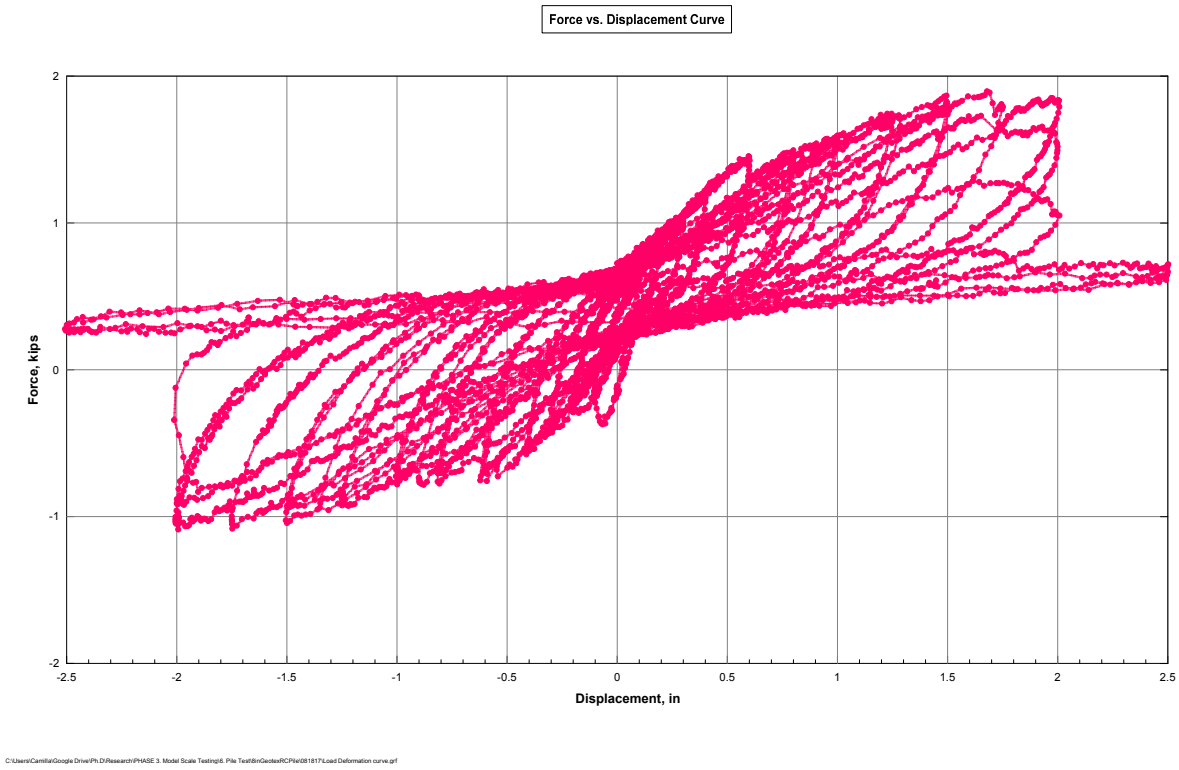

Figure 3.51: Pile 2: Cyclic response of the pile to the 2.5 in displacement level.

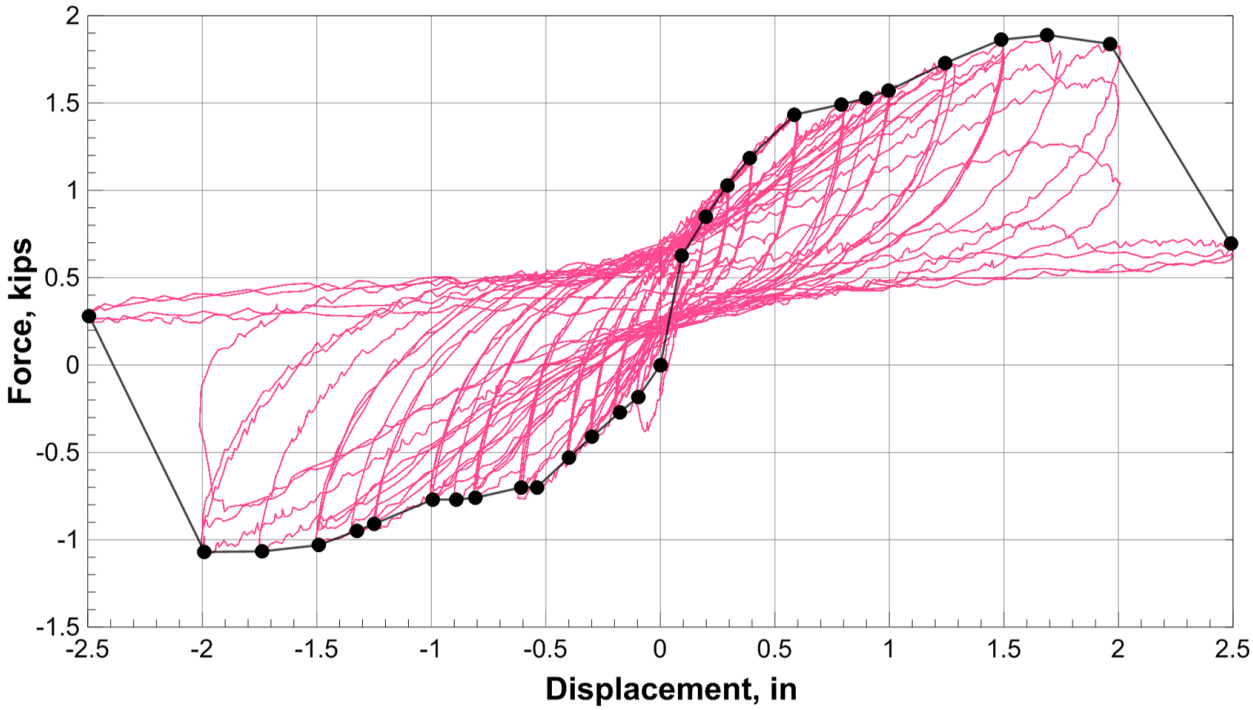

Figure 3.52: Pile 2: Backbone curve.

Representative Sensor Response Histories

The following paragraphs show the output of the strain gauges, string pots, and soil pressure sensors as a function of time. Once the sensors begin to fail and give unrealistic results, the readings are discarded from that point on for future analyses.

Strain Gauges Figs. 3.53 and 3.54 show response histories of 18 strain gauges affixed along the longitudinal geogrid located opposite to each other on the pile cross section (Fig. 3.24). For a displacement of $+/-1.5$ in, the strain gauges recorded approximately a maximum tensile value of 0.014 in the pull direction and 0.009 in the push direction at a depth of 20.5 in in both directions.

The strain gauges recorded approximately a maximum tensile strain of 0.04, corresponding to a -1.75 in displacement, at an elevation of 35.75 3/4 in (2−7). The maximum compressive

strain was found to be approximately 0.02, and it was found at an elevation of 48.75 in for a -2.5 in deflection $(1-6)$

It can be noted that after $+/-$ 1.25 in, the sensors begin to give unrealistic results and progressively fail. Once the gauge begins to fail, the readings are discarded from that point on for future analyses. Strain gauge 2.8 (Fig. 3.54) was damaged and did not provide meaningful readings, hence, its response is represented by the zero value.

String Pots Five string pots and one LVDT were attached to two sides of the laminar soil box (see Fig. 3.16) to monitor its movements during the test. Two string pots were attached to the pile top. Fig. 3.55 shows the time histories of the string pots used in this test and the pile top displacement history as reference.

In order to prevent the laminar soil box to move like during the previous test, a stronger bracing system was put in place with the use of dywidags and chains that braced the box to the strong wall. The string pots did not register significant movement, with a maximum displacement of 0.019 in at the top West Side $(SP-4)$ in the push direction, and 0.02 in at the same location in the pull direction.

The string pot on the pile cap ($SP7$) well matches the movements of the actuator, represented by the bottom graph in Fig. 3.55, which represents the time history of the LVDT located on the actuator.

Soil Pressure Sensors Fig. 3.45 shows the output of the soil pressure sensors as a function of time. The units of measurement were pound per square inch (psi). The maximum pressure value registered was approximately 2 psi at depth of 21 in below the soil surface.

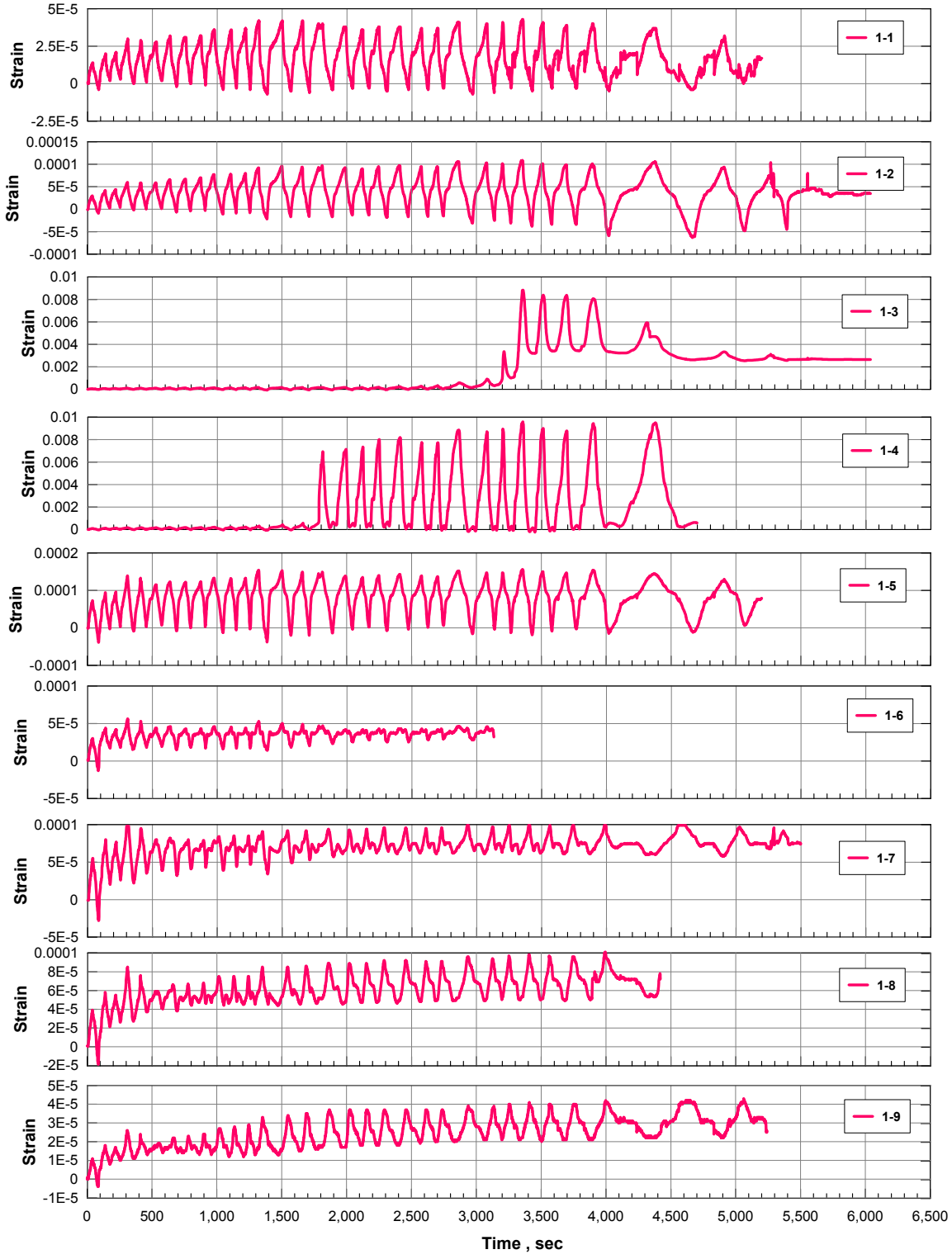

Figure 3.53: Pile 2: Strain gauges histories on longitudinal side 1 (East side) for different pile elevations.

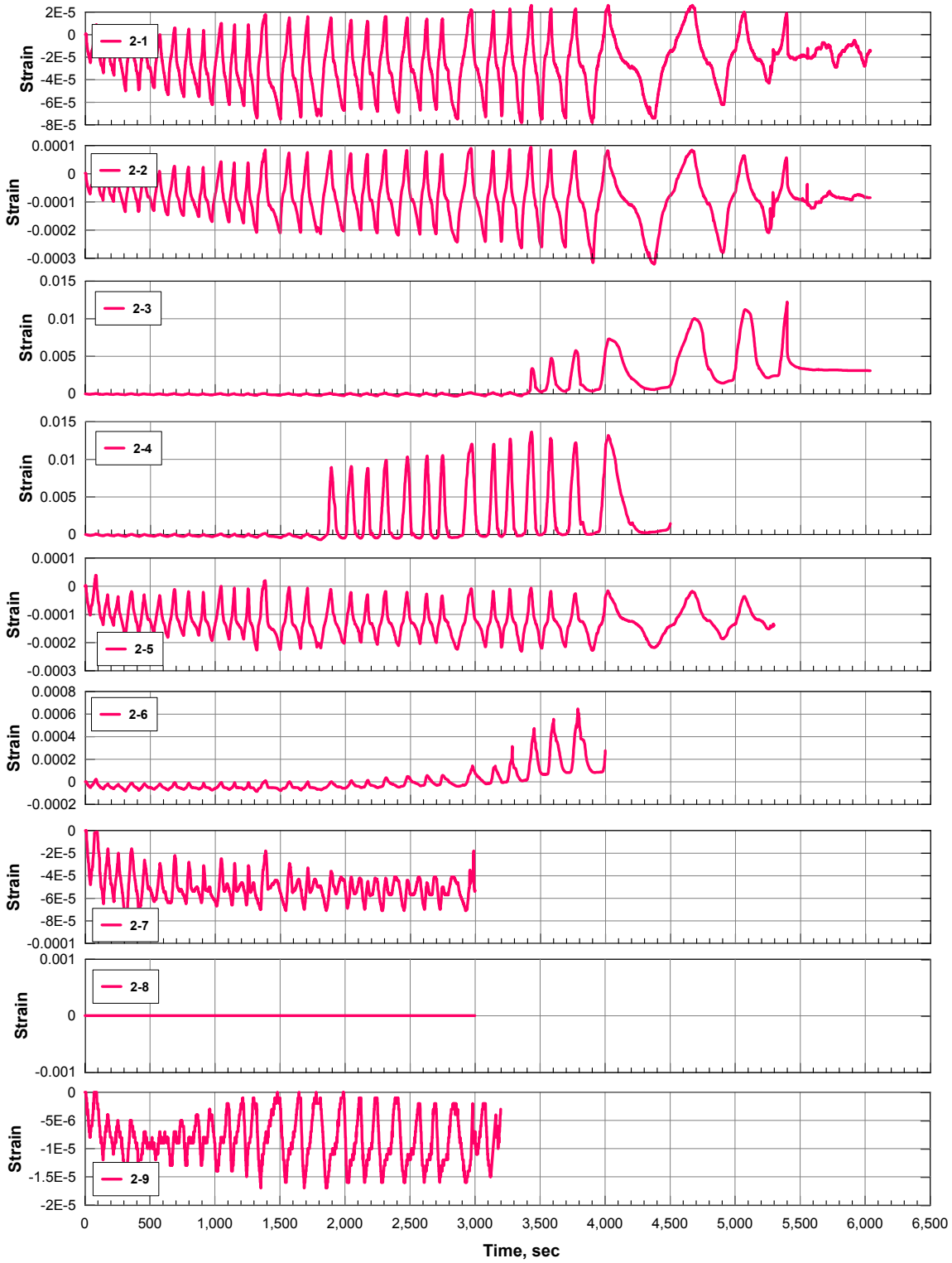

Figure 3.54: Pile 2: Strain gauges histories on longitudinal side 2 (West side) for different pile elevations.

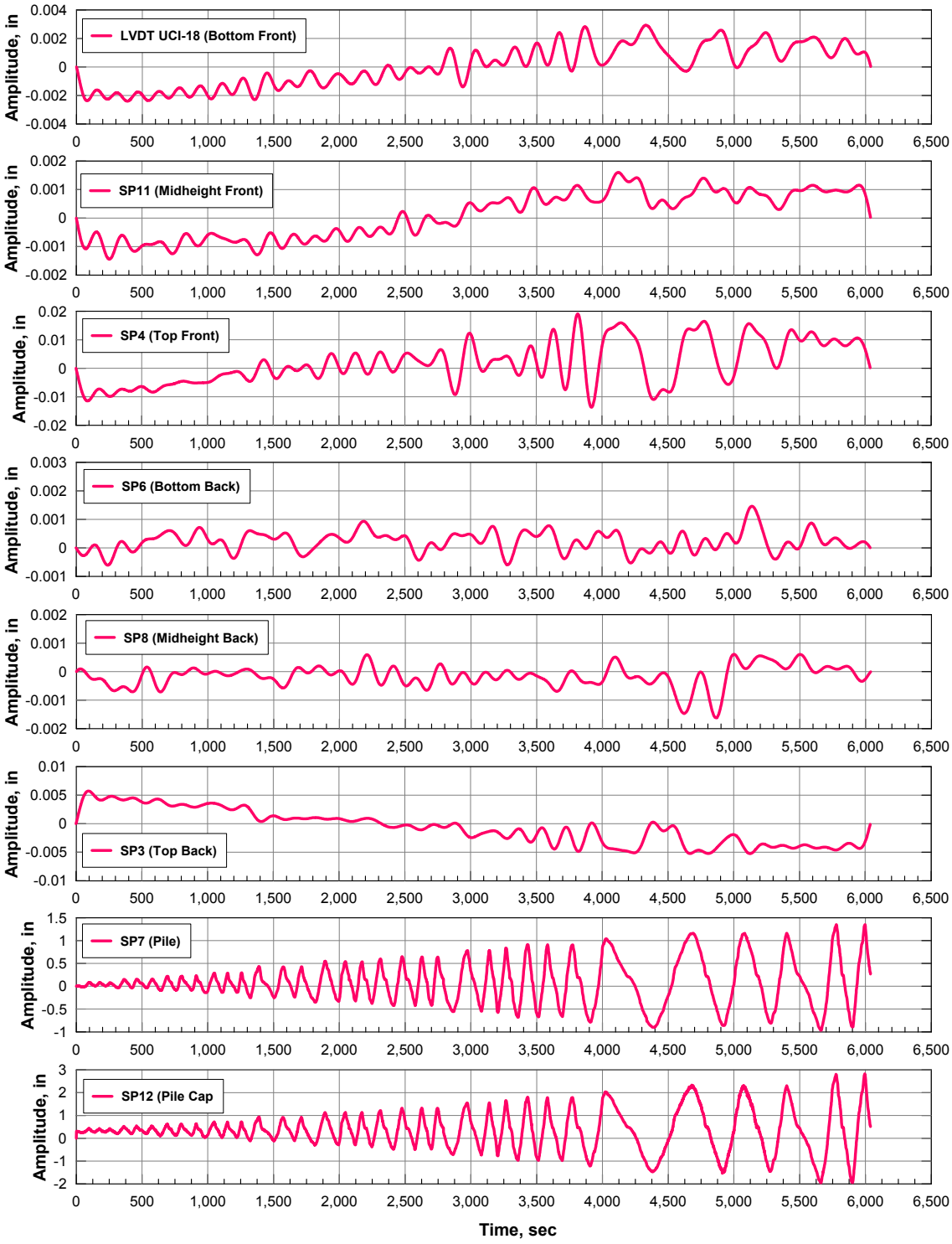

Figure 3.55: Pile 2: String pots time histories.

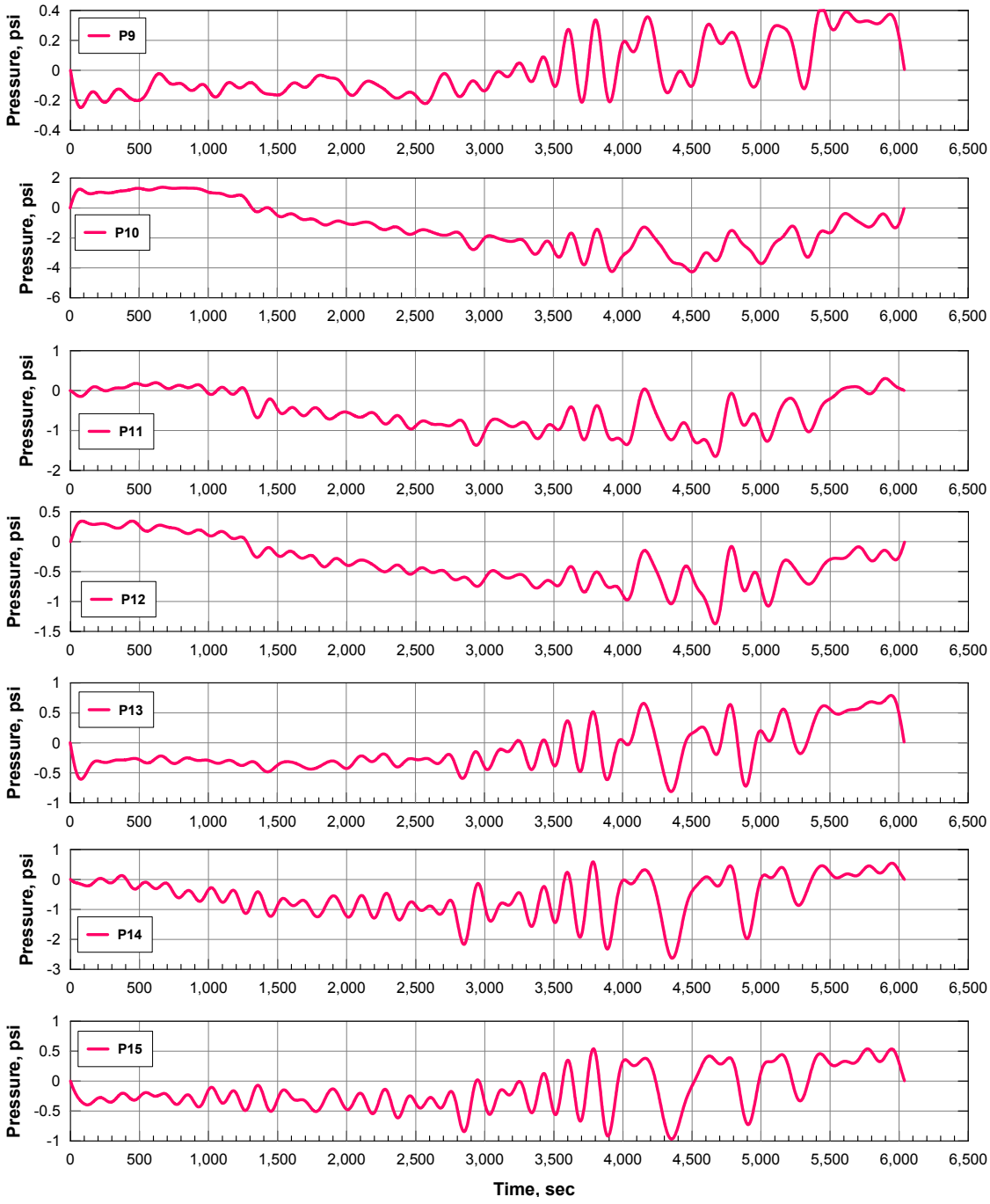

Figure 3.56: Pile 2: Soil pressure sensors' histories.

Curvature Profile

Curvature values with respect to the pile elevation are shown in Fig. 3.57. Curvature profiles for the model piles are calculated from Eq. 3.10. Sensor depths and head displacements are noted on the plots. The largest curvature values were recorded within the yielding region (plastic hinge region) that formed at approximately 20 in (2.5 pile diameters) below ground surface.

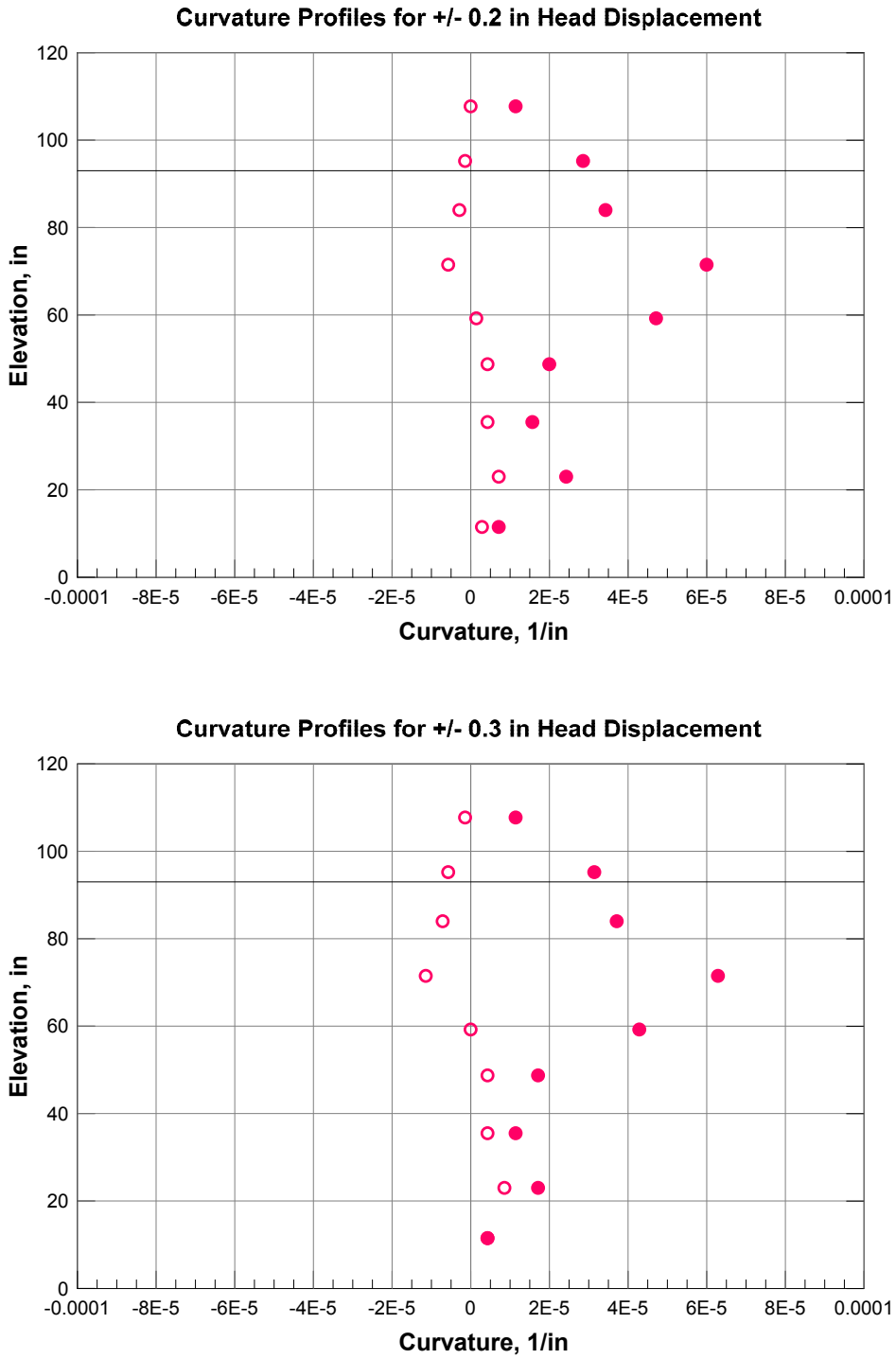

Figure 3.57: Pile *2*: Curvature profiles from 0.2 in to 2 in displacement levels. + and - indicate curvature values for positive and negative deflections, respectively.

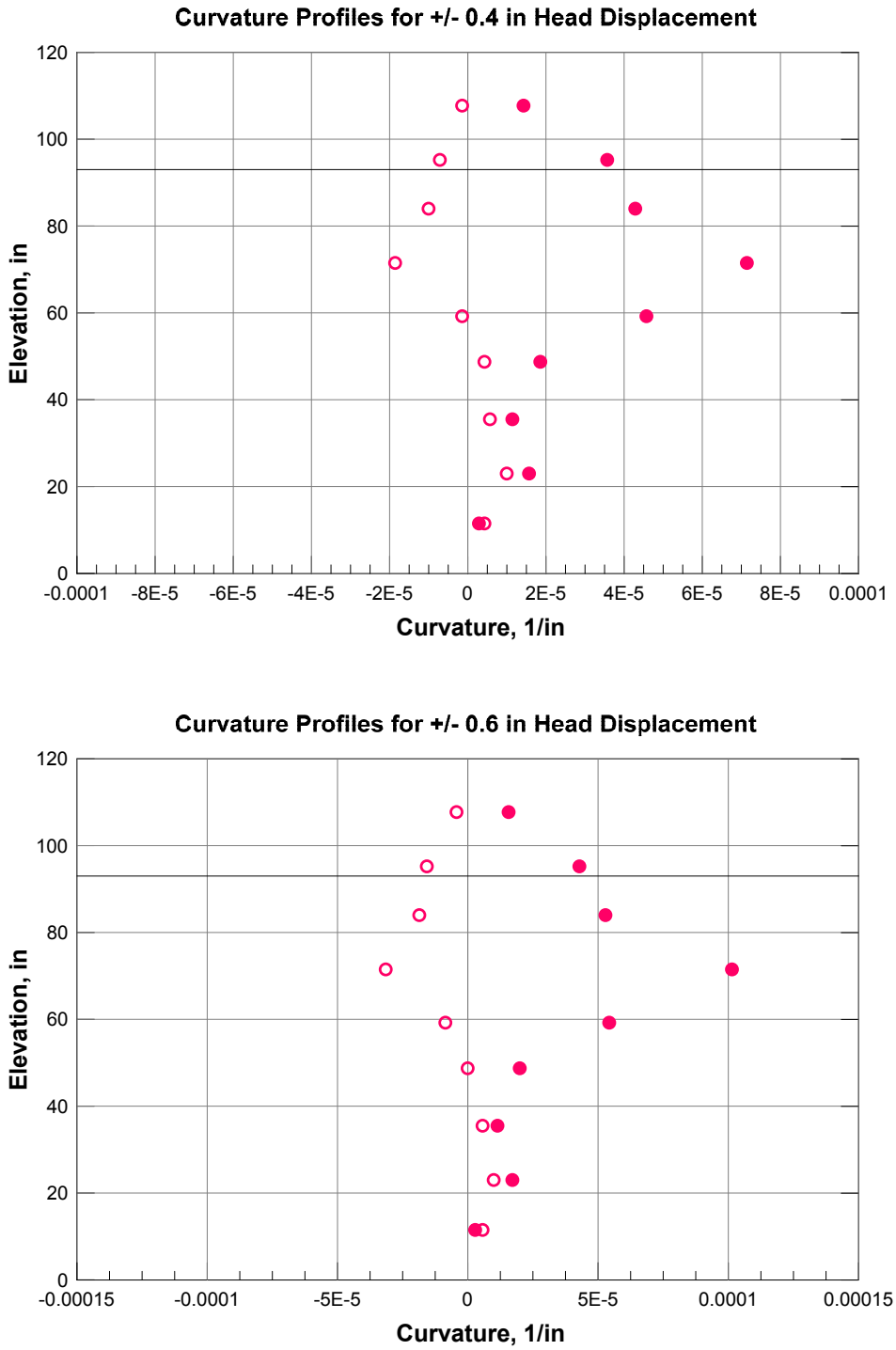

Figure 3.57: Pile *2*: Curvature profiles from 0.2 in to 2 in displacement levels. + and - indicate curvature values for positive and negative deflections, respectively (cont.).

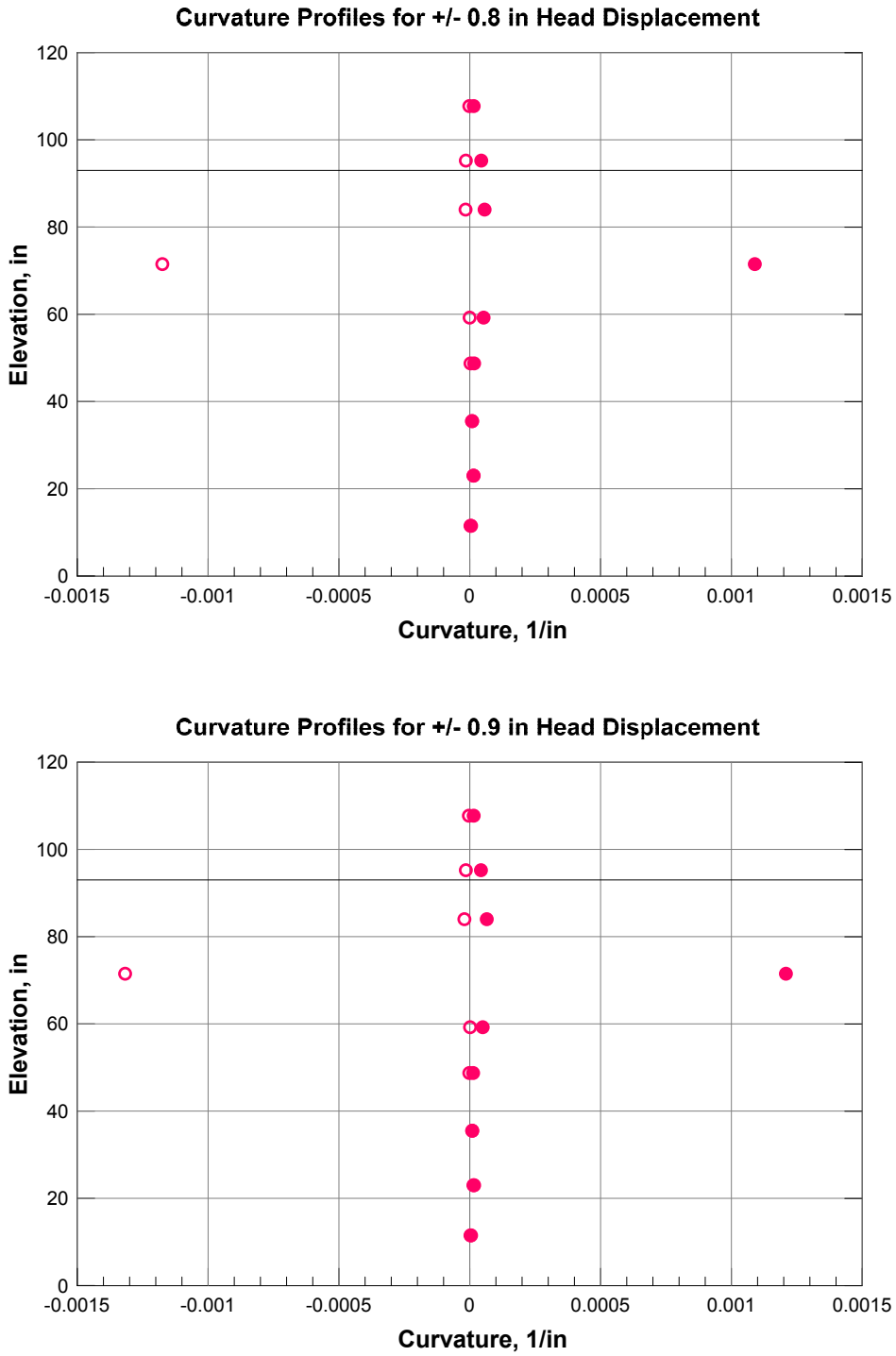

Figure 3.57: Pile *2*: Curvature profiles from 0.2 in to 2 in displacement levels. + and - indicate curvature values for positive and negative deflections, respectively (cont.).

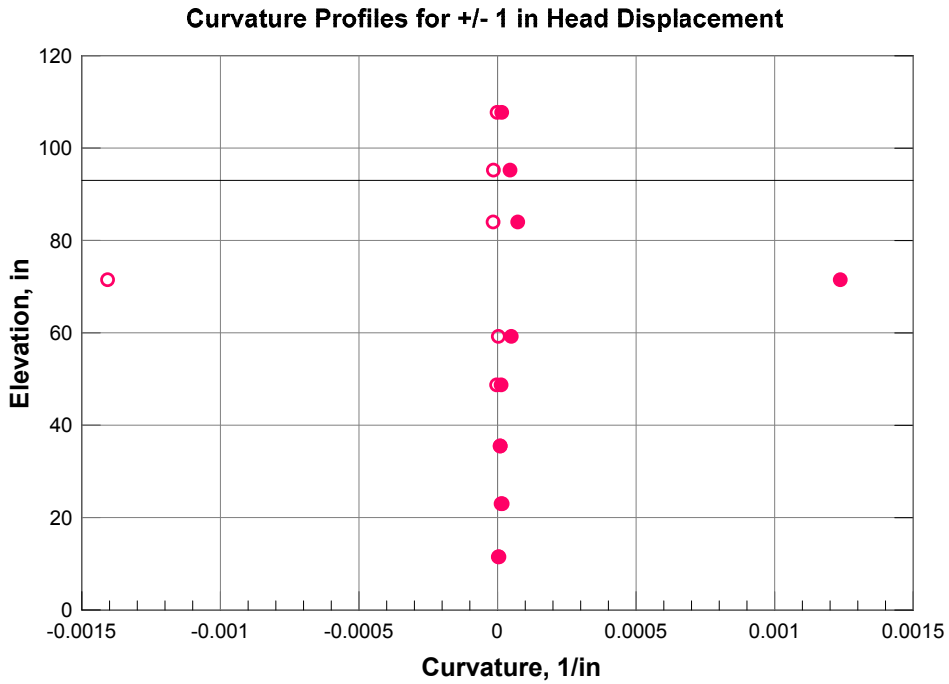

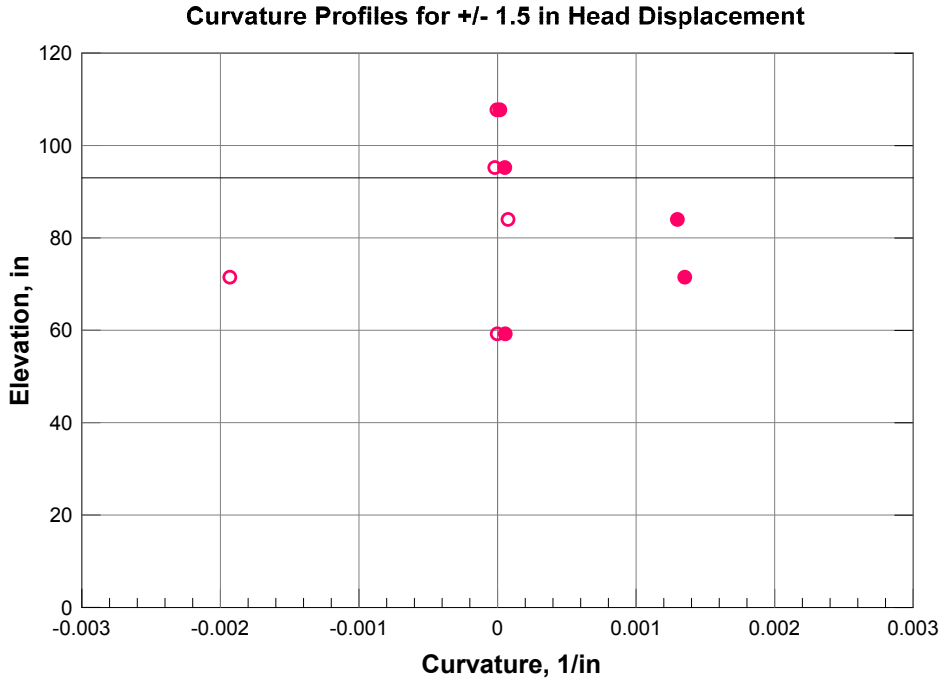

Figure 3.57: Pile *2*: Curvature profiles from 0.2 in to 2 in displacement levels. + and - indicate curvature values for positive and negative deflections, respectively (cont.).

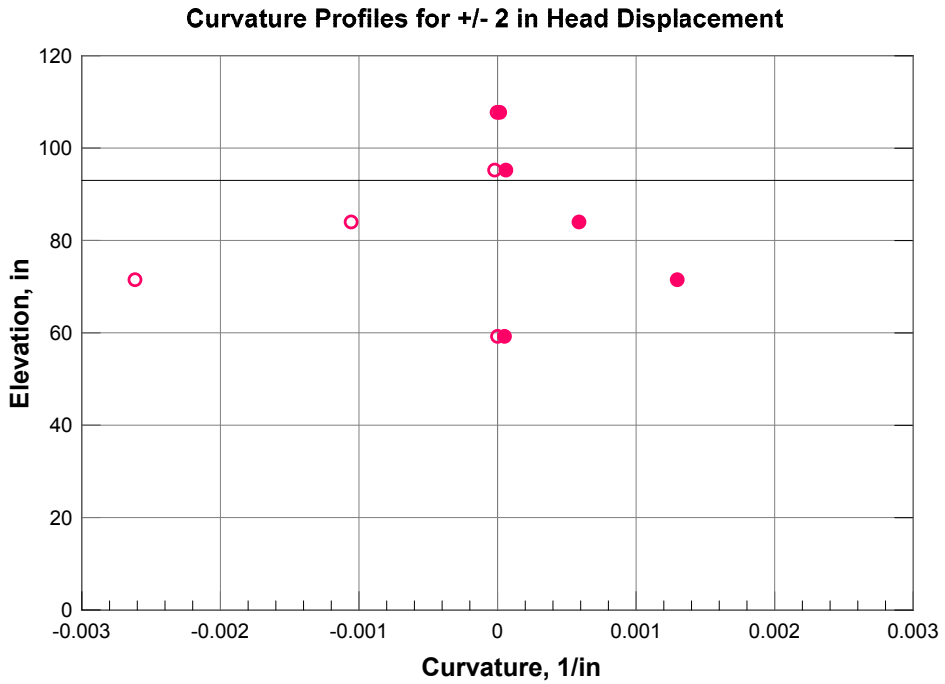

Figure 3.57: Pile *2*: Curvature profiles from 0.2 in to 2 in displacement levels. + and - indicate curvature values for positive and negative deflections, respectively (cont.).

Experimental Moment - Curvature Relationship

The experimental moment-curvature relationship derived from test data, and the analytical relationships, are shown in Fig. 3.58.

The predicted relationship (Fig. 3.59) was produced with the same procedure and software package used for the 8 in polymer concrete with steel reinforcement. Since Response 2000 does not give the possibility to input types of reinforcement that are different from the traditional steel rebars and ties, the polymeric geogrid was represented by a minimum amount of longitudinal and transversal steel. This was the same amount used in the analysis and construction of the first pile. Refer to Table 3.5 for the reinforcement details.

The experimental data show a pile response that is stiffer and higher capacity than that of

the analytical models for the considered location.

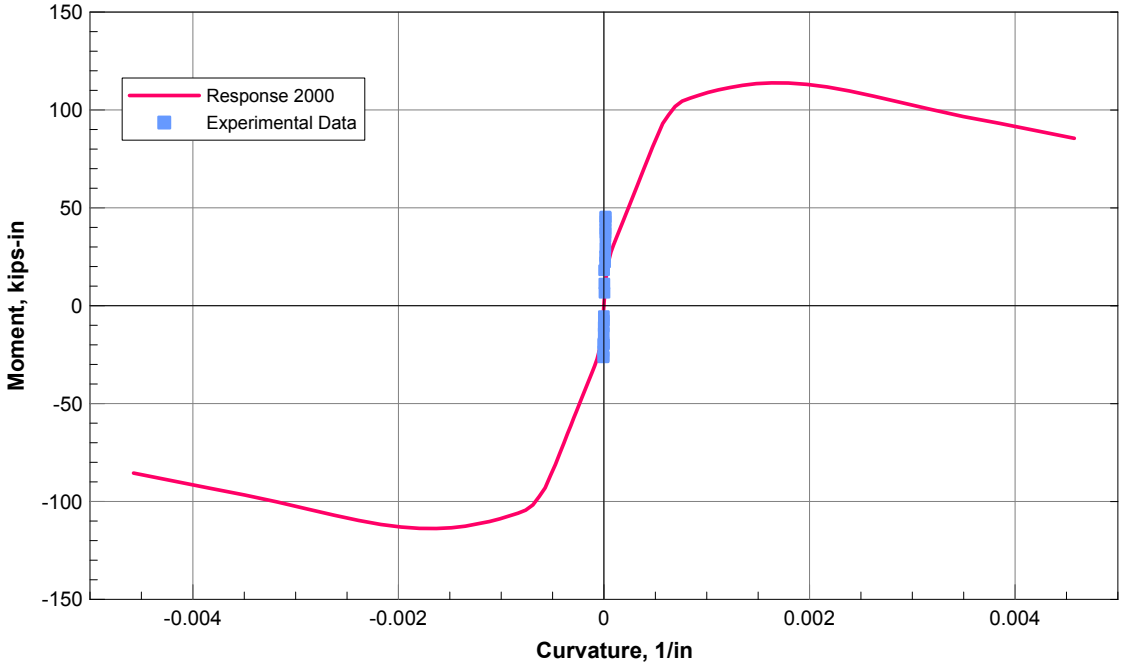

Figure 3.58: Experimental and predicted moment- curvature relationships for Pile 2.

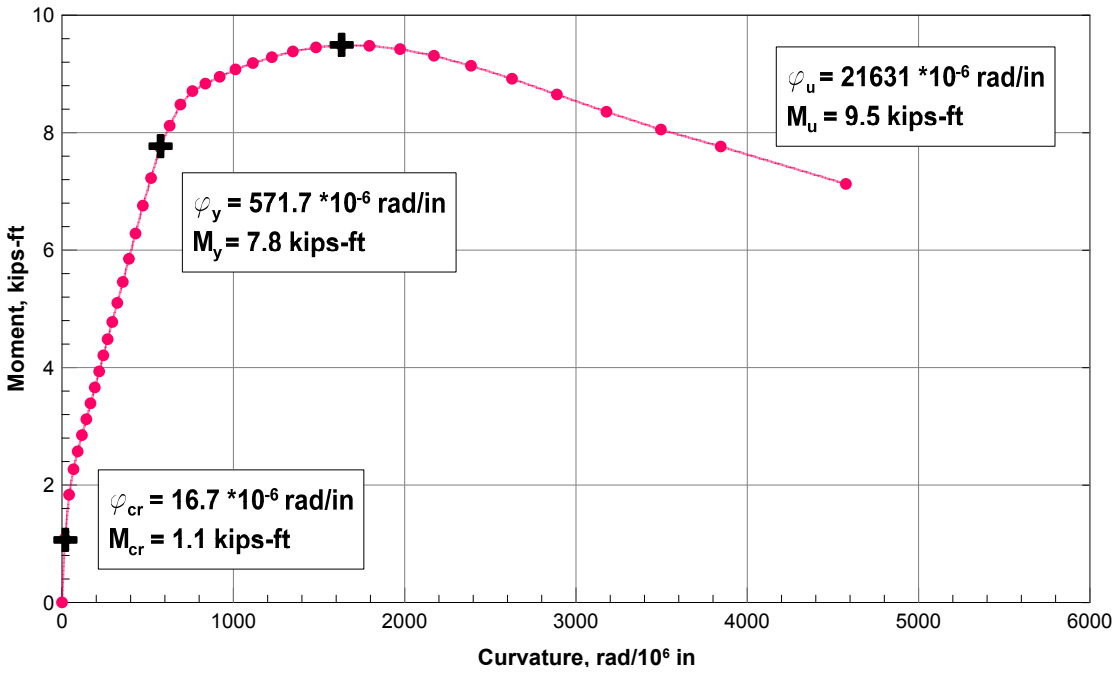

Figure 3.59: Analytical moment- curvature relationship from Response 2000 for the 8 in regular concrete pile.

3.4.3 8 in Polymer Concrete with Geotextile Reinforcement

Construction of the specimen was done on September, 6th 2017. The test was performed on October 13th, 2017. Selected photographs of the specimen during and after the test are shown in Figs. 3.60 and 3.61.

Specimen 3 failed because a plastic hinge that developed at 62 in of elevation (3.5 pile diameters below the soil surface). No other major cracks were detected.

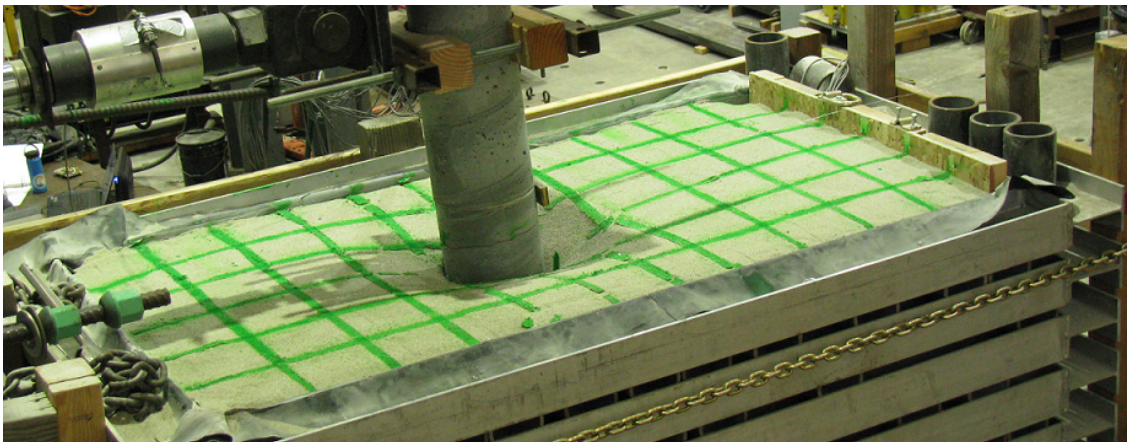

Figure 3.60: Pile 3: Maximum pile head deflection and soil surface.

Load vs Deflection

A testing protocol similar to the ones developed for the previous tests was followed to enable general comparisons in force and displacement. The measured cyclic response of the pile is shown in Fig. 3.62, and backbone load vs. deflection curves are shown in Fig. 3.63. The backbone curve was created using peak values for each cycle in push (positive) and pull (negative) direction. The maximum load observed in the push loading direction was 1.0 kips at 1.25 in of displacement, whereas the maximum load observed in the pull direction was 0.7 kips at 0.8 in of displacement. The yield force in push direction was 1.1 kips at a horizontal displacement of 1.5 in. In the pull direction the yield force measured 0.7 at a displacement

Figure 3.61: Pile 3: Cracked pile.

of 0.75 in. The maximum displacement of Pile 3 was 1.74 in in the push direction and 1.76 in in the pull direction.

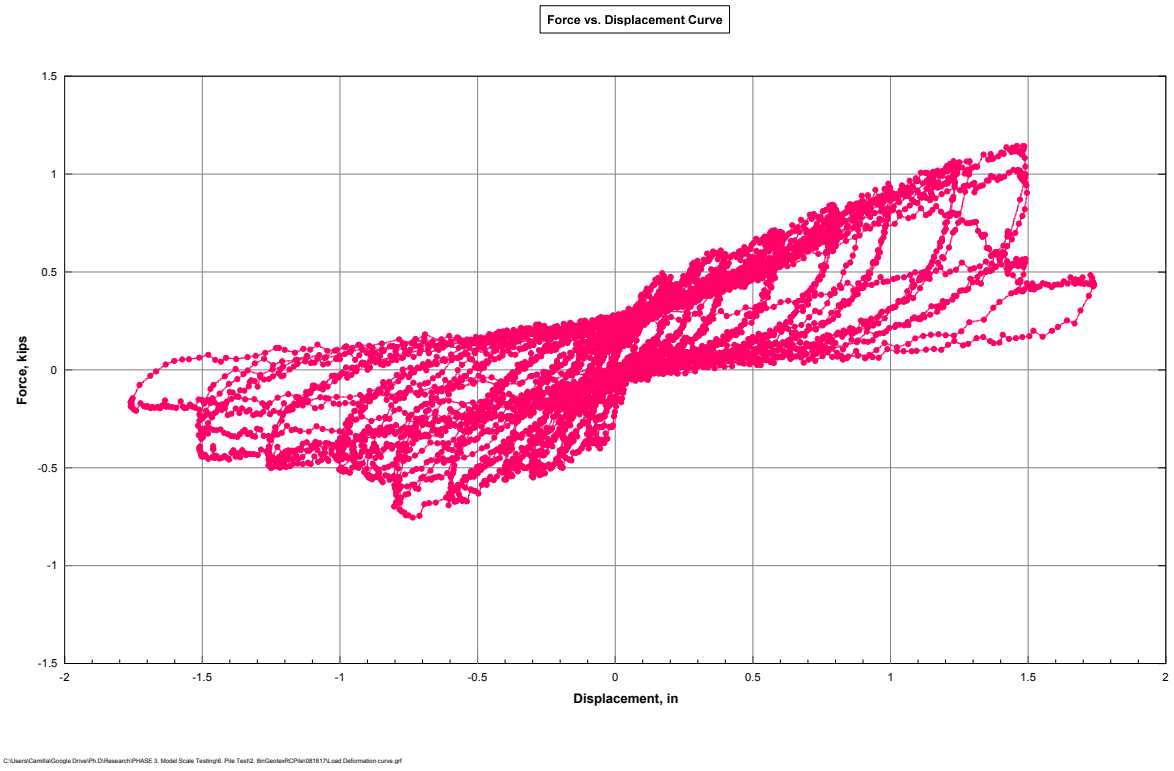

Figure 3.62: Pile 3: Cyclic response of the pile to the 7 in displacement level.

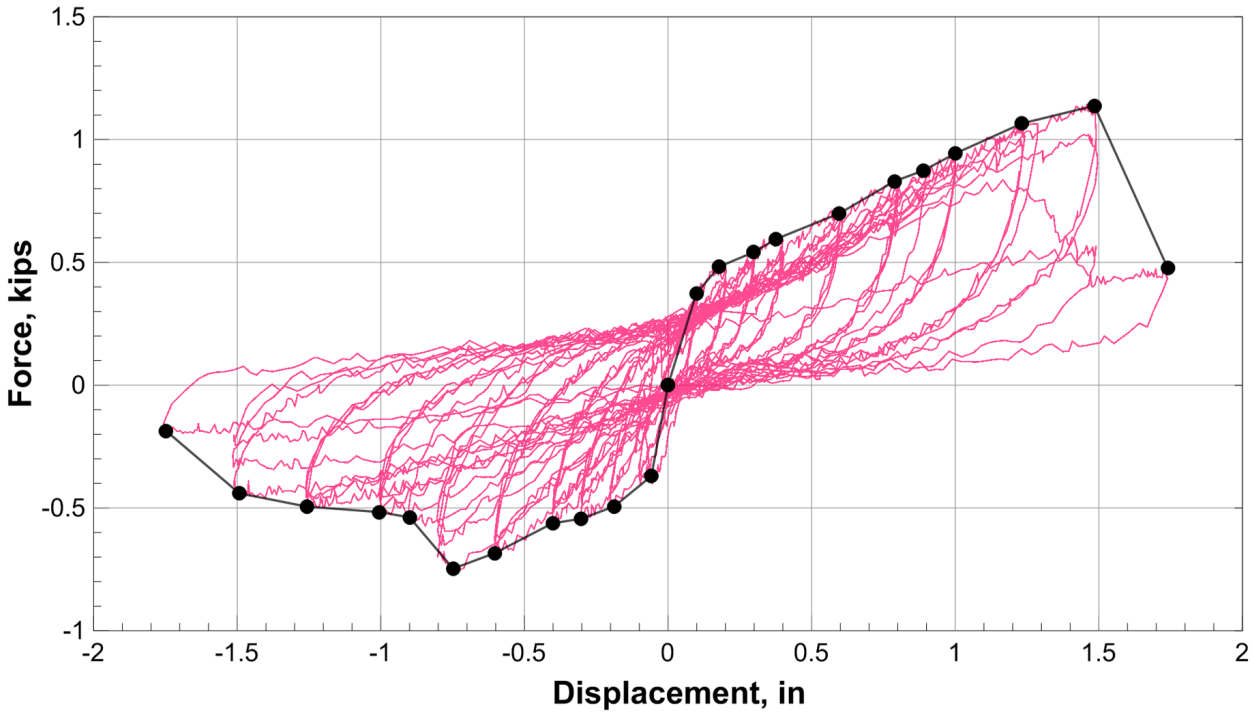

Figure 3.63: Pile 3:Backbone curve.

Representative Sensor Response Histories

The following paragraphs show the output of the strain gauges, string pots, and soil pressure sensors as a function of time. Once the sensors begin to fail and give unrealistic results, the readings are discarded from that point on for future analyses.

Strain Gauges Figs. 3.64 and 3.65 show response histories of 10 strain gauges affixed along the longitudinal grids located opposite to each other on the pile cross section (Fig. 3.25).

The strain gauges recorded approximately a maximum tensile strain of 0.019, corresponding to a +1.2 in displacement, at an elevation of 49.5 in $(1-7)$. The maximum compressive strain was found to be approximately 0.022, and it was found at an elevation of 49 in for a +1.5 in deflection $(2-7)$

String Pots Five string pots and one LVDT were attached to two sides of the laminar soil box (see Fig. 3.16) to monitor its movements during the test. Two string pots were attached to the pile top. Fig. 3.66 shows the time histories of the string pots used in this test and the pile top displacement history as reference. The string pots did not register significant movement, with a maximum displacement of 0.005 in both in the push and pull direction. The maximum displacement was recored at the bottom of the box from $SP-6$ string pot (East side), and $UCI-18$ LVDT (West Side).

The same bracing used in Test 2 was used. For this reason, not significant movements of the laminar soil box were registered.

The string pot on the pile cap ($SP7$) well matches the movements of the actuator, represented by the bottom graph in Fig. 3.66, which represents the time history of the LVDT located

on the actuator.

Soil Pressure Sensors Fig. 3.67 shows the output of the soil pressure sensors as a function of time. The units of measurement were pound per square inch (psi). The maximum pressure value registered was approximately 4 psi at depth of 21 in below the soil surface.

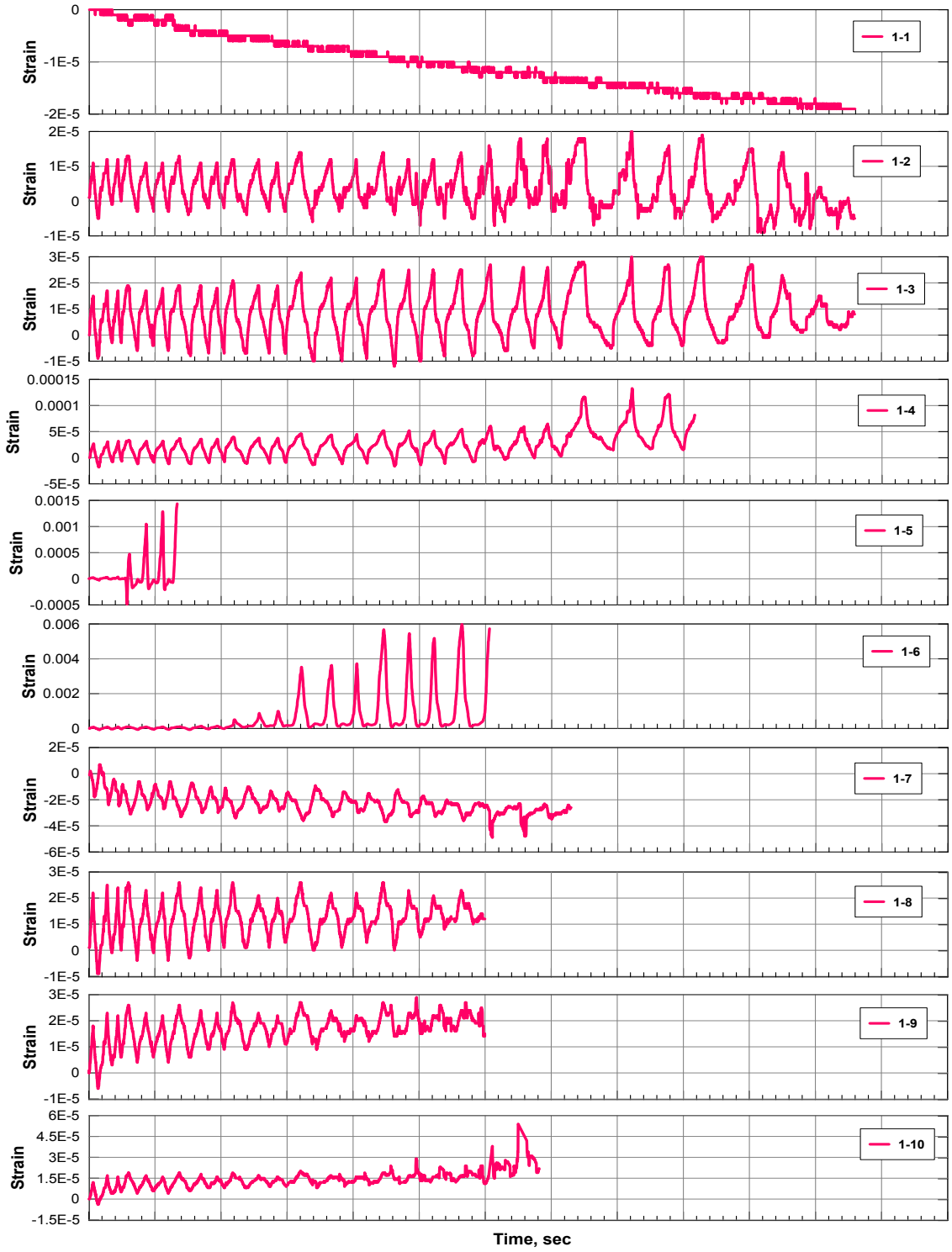

Figure 3.64: Pile 3: Strain gauges histories on longitudinal side 1 (pull side) for different pile elevations.

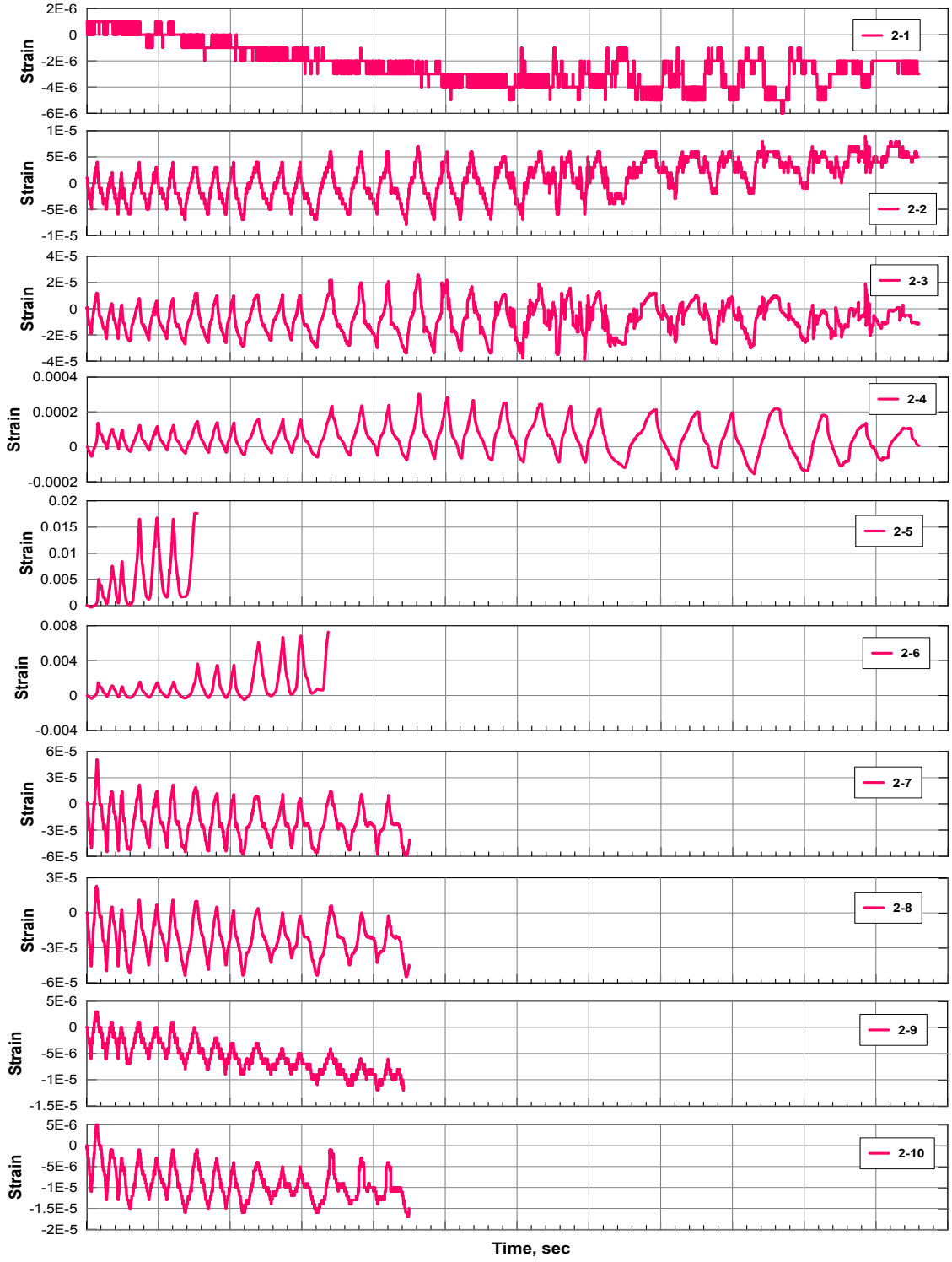

Figure 3.65: Pile 3: Strain gauges histories on longitudinal side 2 (push side) for different pile elevations.

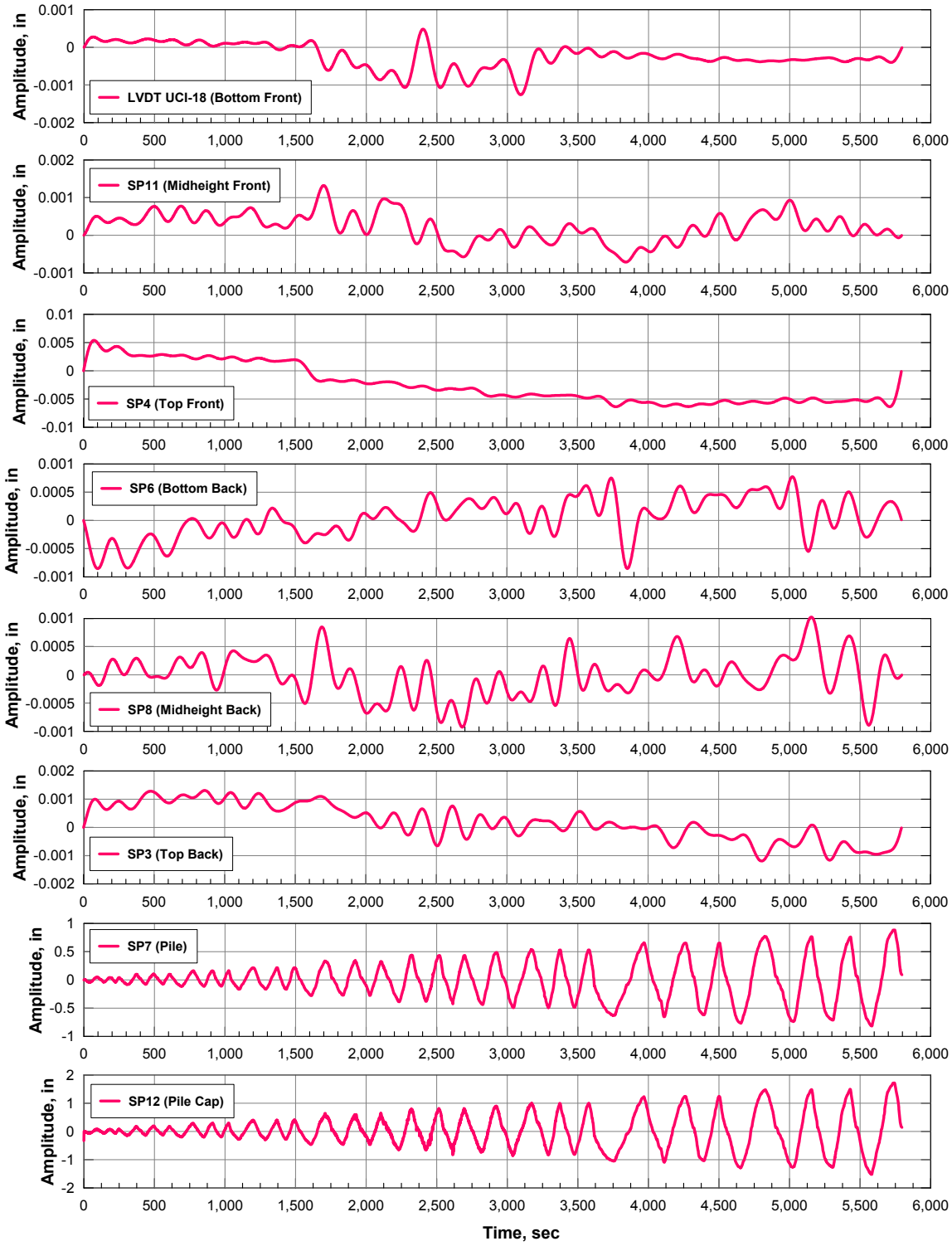

Figure 3.66: Pile 3: String pots histories.

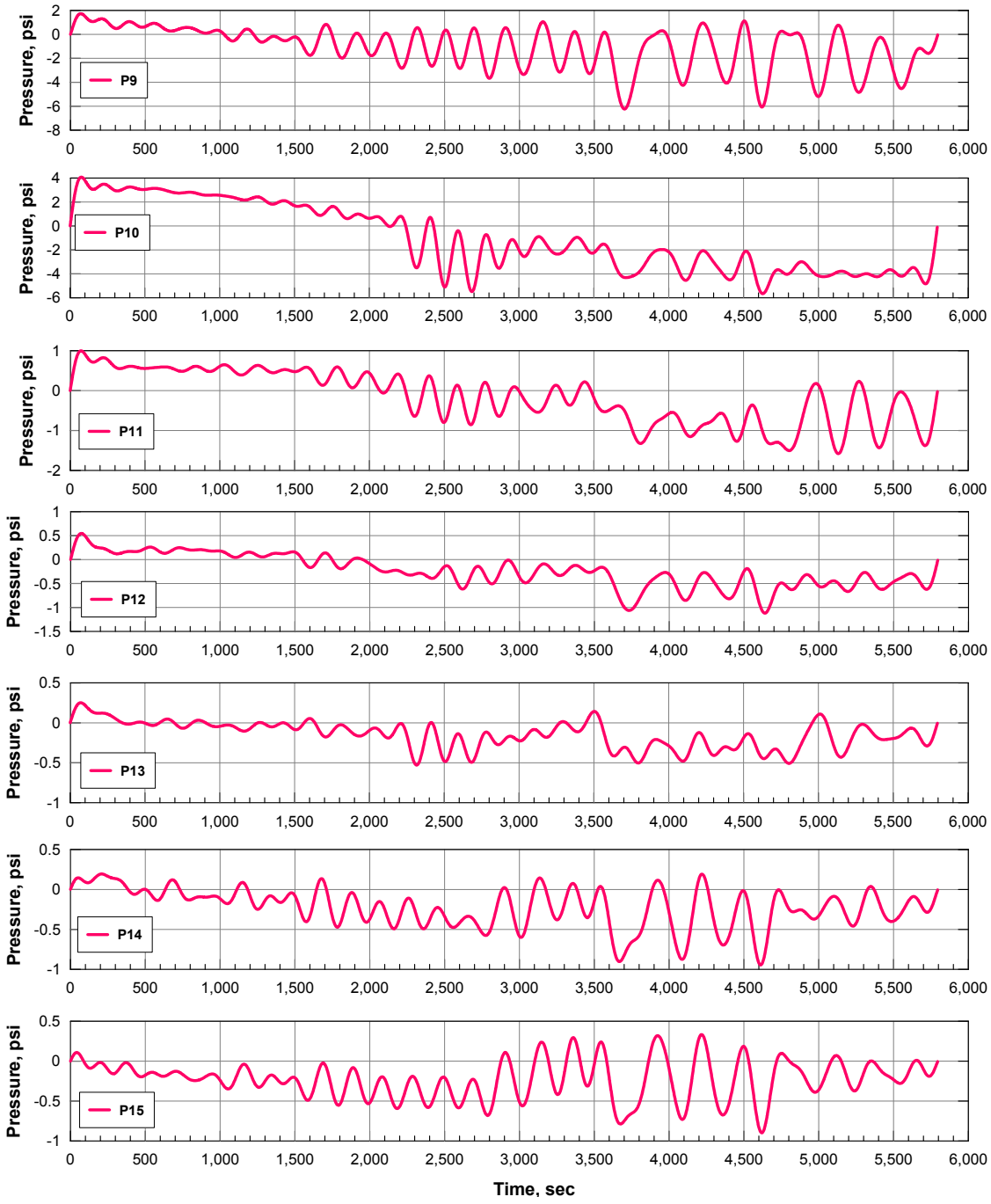

Figure 3.67: Pile 3: Soil pressure sensors' histories.

Curvature Profile

Curvature values with respect to the pile elevation are shown in Fig. 3.68. Curvature profiles for the model piles are calculated from Eq. 3.10. Sensor depths and head displacements are noted on the plots. The largest curvature values were recorded within the yielding region (plastic hinge region) that formed at approximately 30 in (3.5 pile diameters) below ground surface.

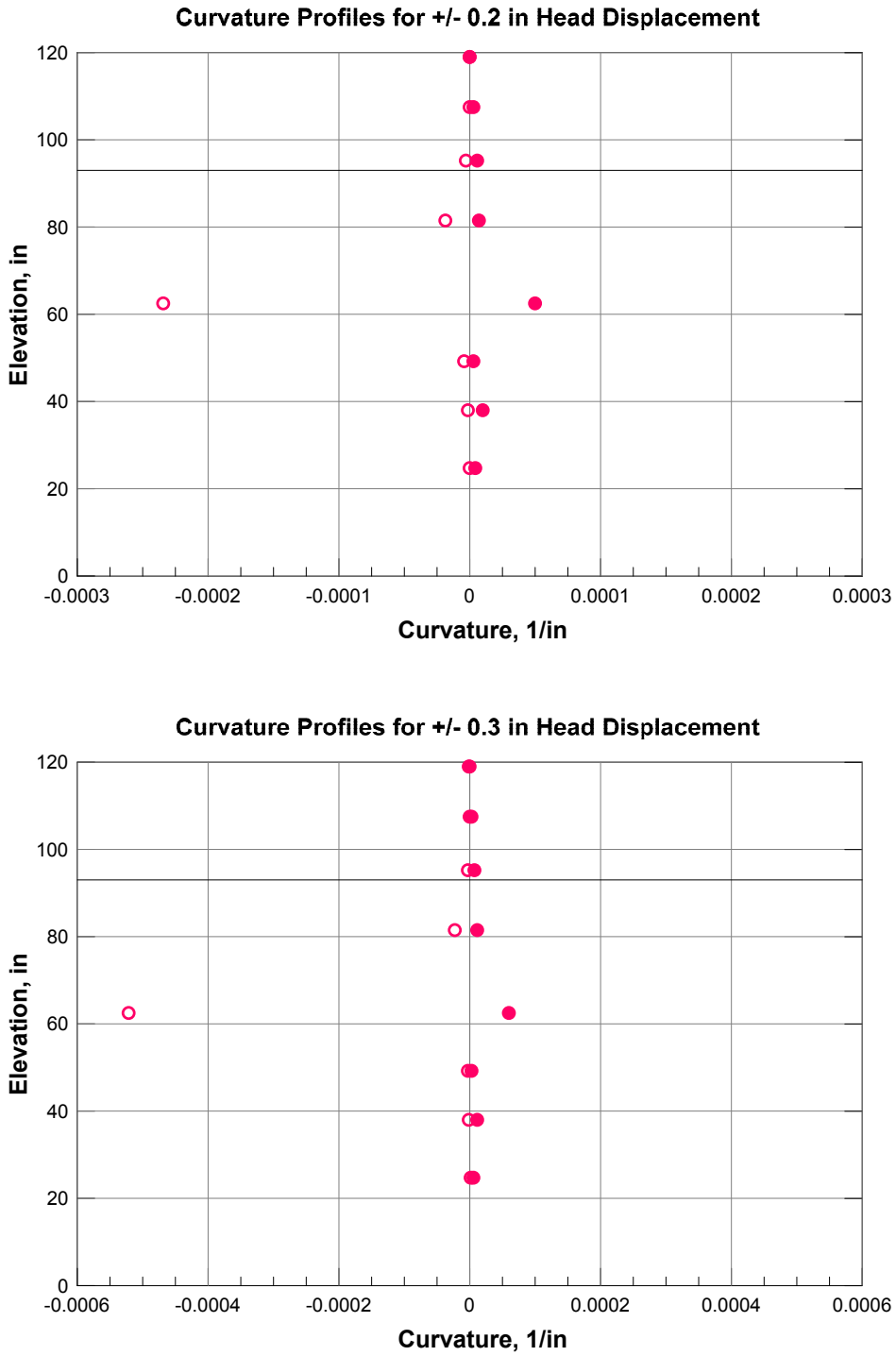

Figure 3.68: Pile *3*: Curvature profiles from 0.2 in to 0.9 in displacement levels. + and - indicate curvature values for positive and negative deflections, respectively.

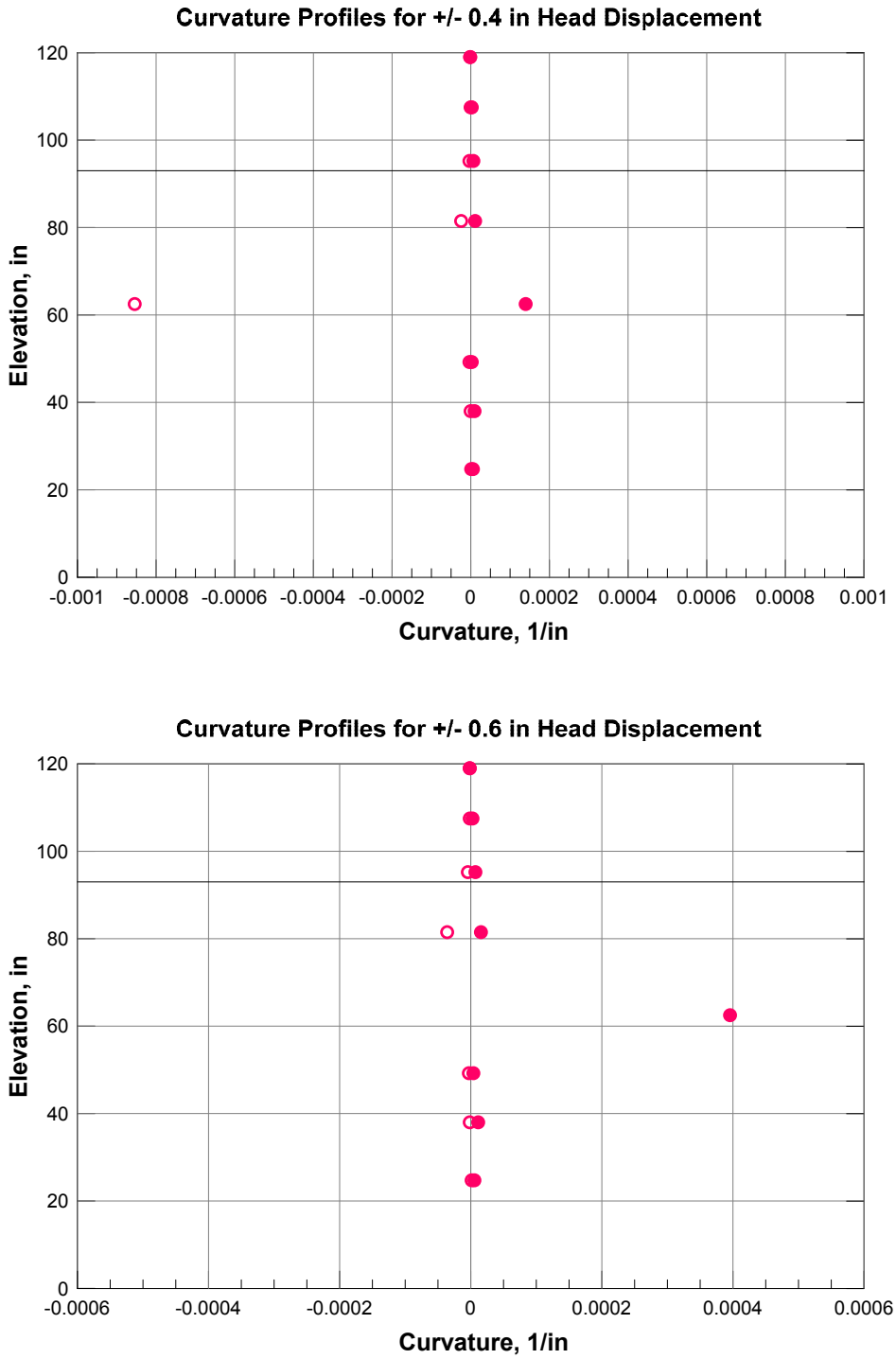

Figure 3.68: Pile *3*: Curvature profiles from 0.2 in to 0.9 in displacement levels. + and - indicate curvature values for positive and negative deflections, respectively (cont.).

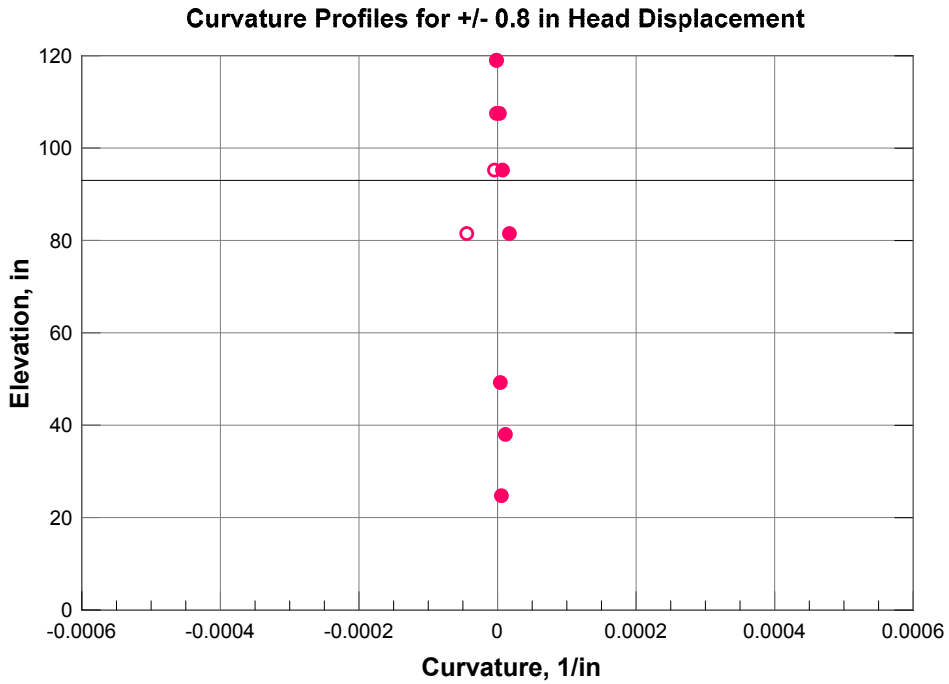

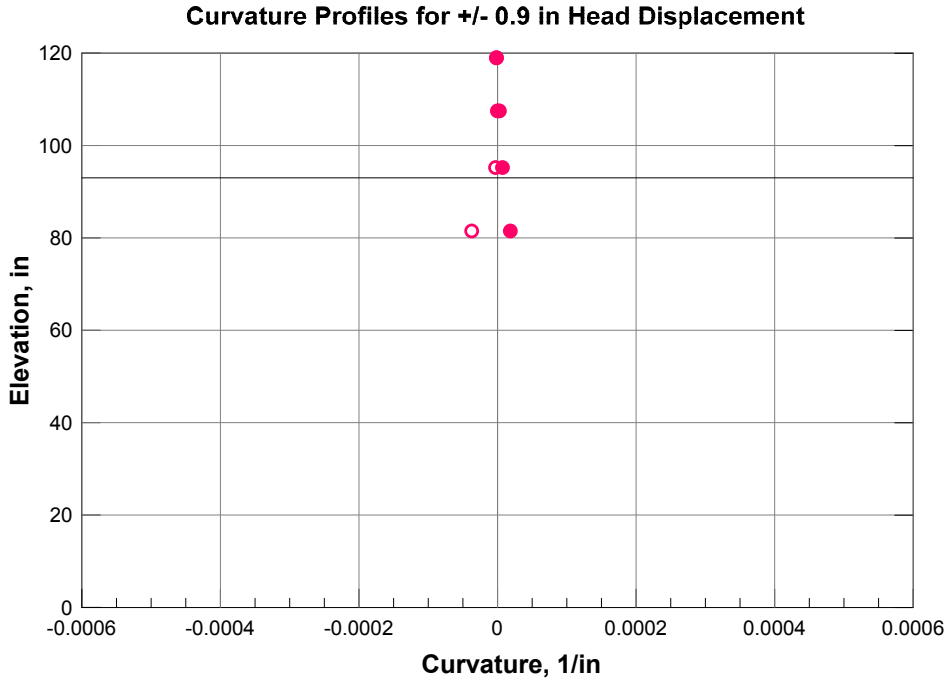

Figure 3.68: Pile *3*: Curvature profiles from 0.2 in to 0.9 in displacement levels. + and - indicate curvature values for positive and negative deflections, respectively (cont.).

Experimental Moment - Curvature Relationship

The experimental moment-curvature relationship derived from test data and predicted relationships, are shown in Fig. 3.69.

The analytical moment-curvature relationship was obtained from Response 2000. Geometric and mechanical properties used were the same implemented for the 8 in polymer concrete pile with steel reinforcement due to the lack of reinforcement choice provided by the software (Fig. 3.48). Nonetheless, the predicted curve well capture the initial stiffness of the experimental data

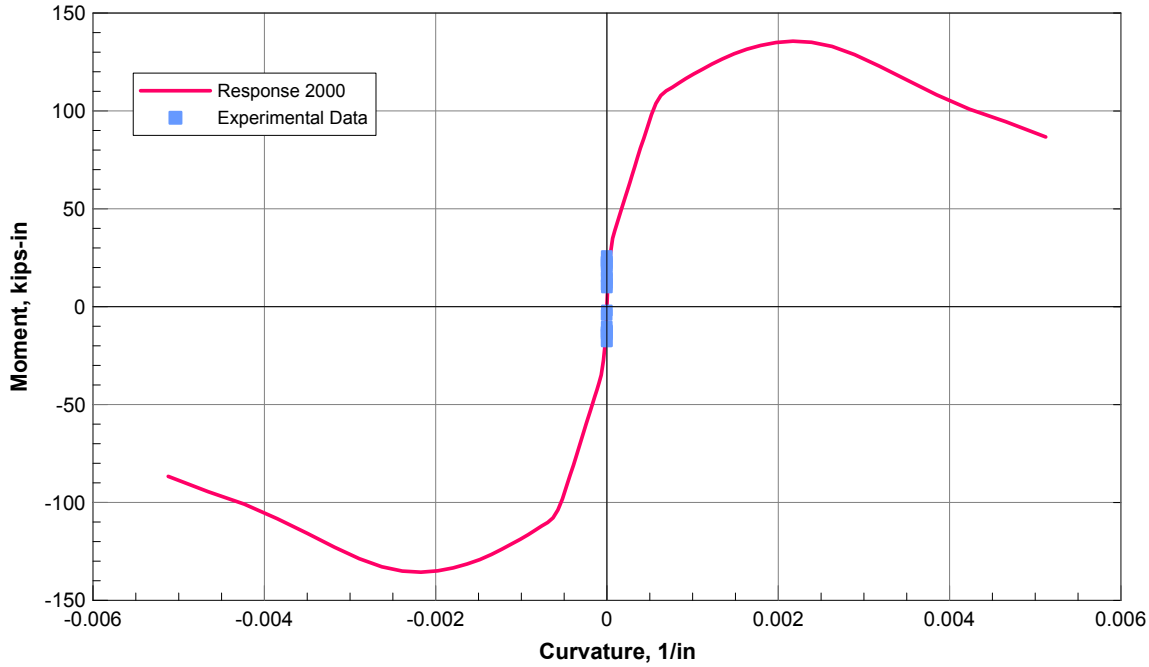

Figure 3.69: Experimental and predicted moment- curvature relationships for Pile 3.

3.4.4 10 in Polymer Concrete with Steel Reinforcement

Construction of the specimen was done on June, 9th 2017. The test was performed on November, 21th 2017. Selected photographs of the specimen during and after the test are shown in Figs. 3.70 and 3.71.

Large horizontal and vertical cracks formed around the pile at different elevations. The most significant cracks developed on the east and west sides (bending direction) of the pile, but they propagated also in the shear sides, causing superficial material detachments. The largest crack (average width= 4 in), where the plastic hinge form, was found at approximately 30 in of elevation from the top of the bedrock (approximately 3 pile diameters below the surface). This crack is also deeper in the east side where the steel reinforcement can be seen. Other two major cracks (larger than 1.5 in) were detected at the elevations of 35 in and 24 in from the bedrock top.

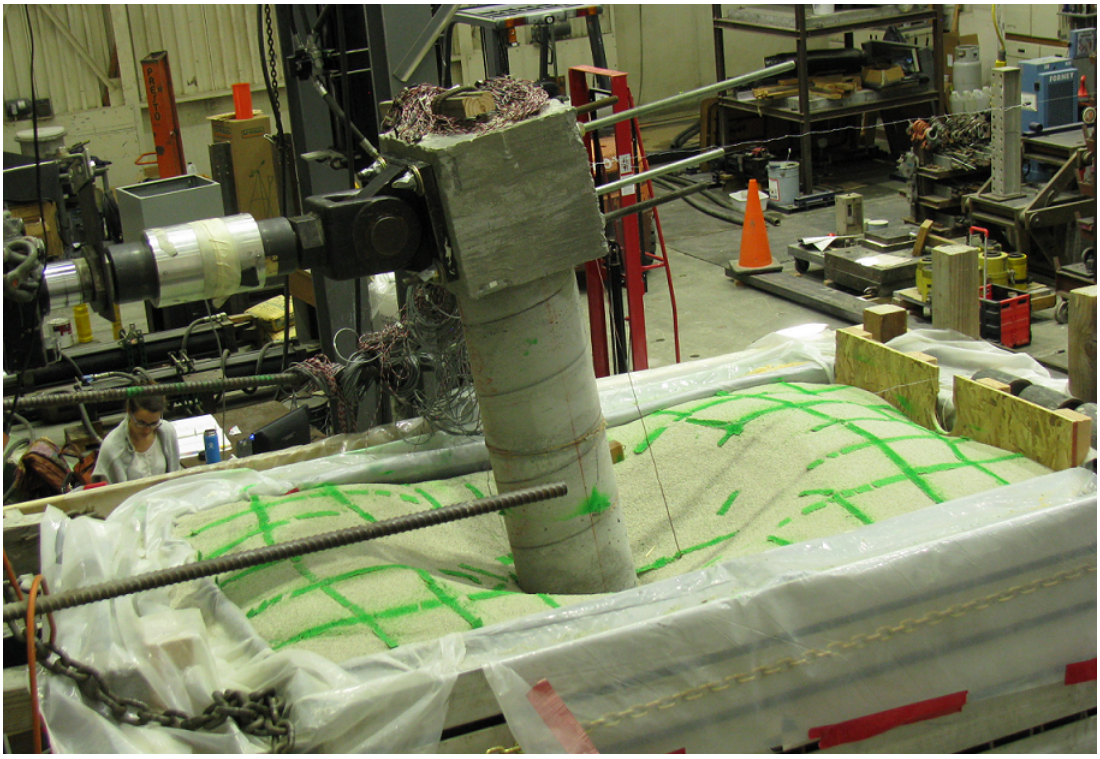

Figure 3.70: Pile 4: Maximum pile head deflection and soil surface.

Load vs Deflection

The measured cyclic response of the pile is shown in Fig. 3.72, and backbone load vs. deflection curves are shown in Fig. 3.73. The backbone curve was created using peak values for each cycle in push (positive) and pull (negative) direction. The maximum load observed

(a) North view.

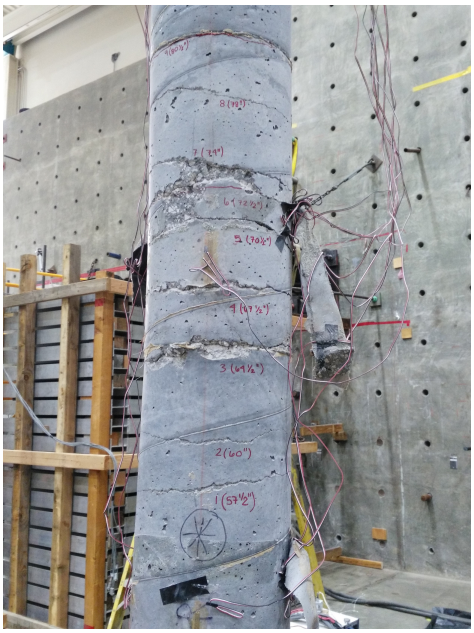

(b) East view.

(c) South view.

(d) West view.

Figure 3.71: Pile 4: Cracks.

in the push loading direction was 4.2 kips at 3.0 in of displacement, whereas the maximum load observed in the pull direction was 4.9 kips at 7.5 in of displacement. The yield force

in push direction was 1.1 kips at a horizontal displacement of 0.1 in. In the pull direction the yield force measured 0.8 kips at a displacement of 0.1 in. The maximum displacement of Pile 4 was 7.5 in both directions.

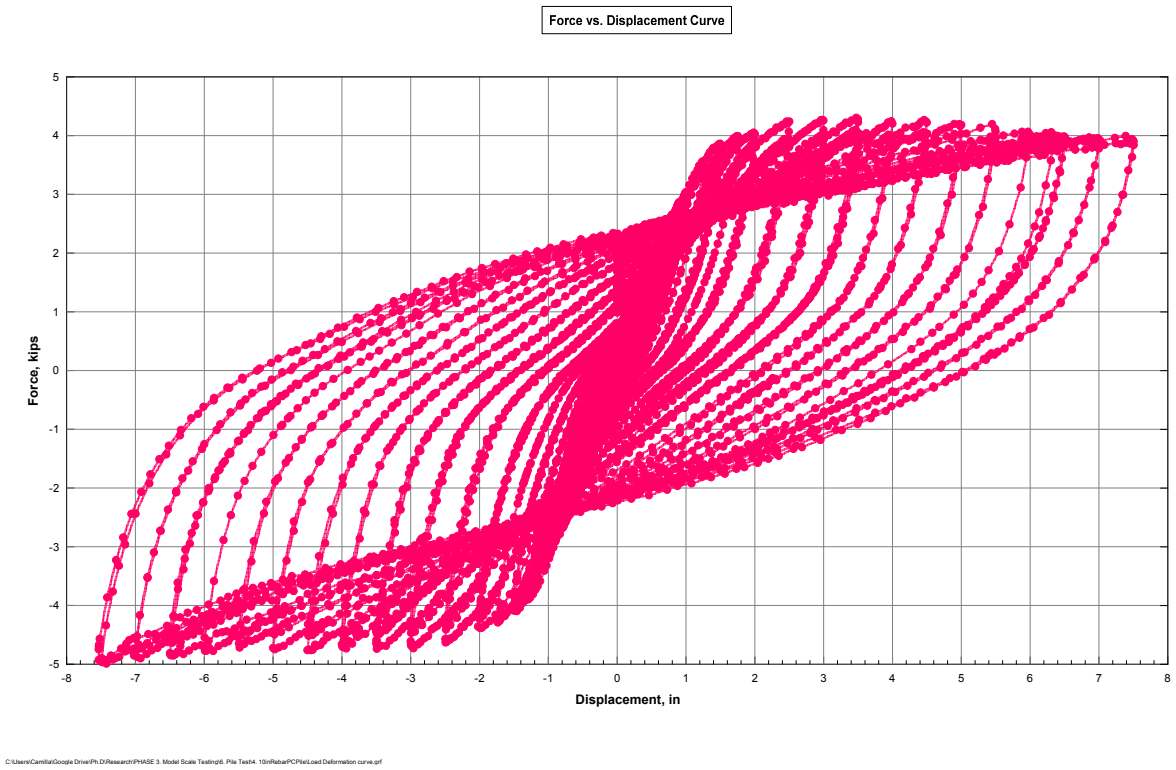

Figure 3.72: Pile 4: Cyclic response of the pile to the 7 in displacement level.

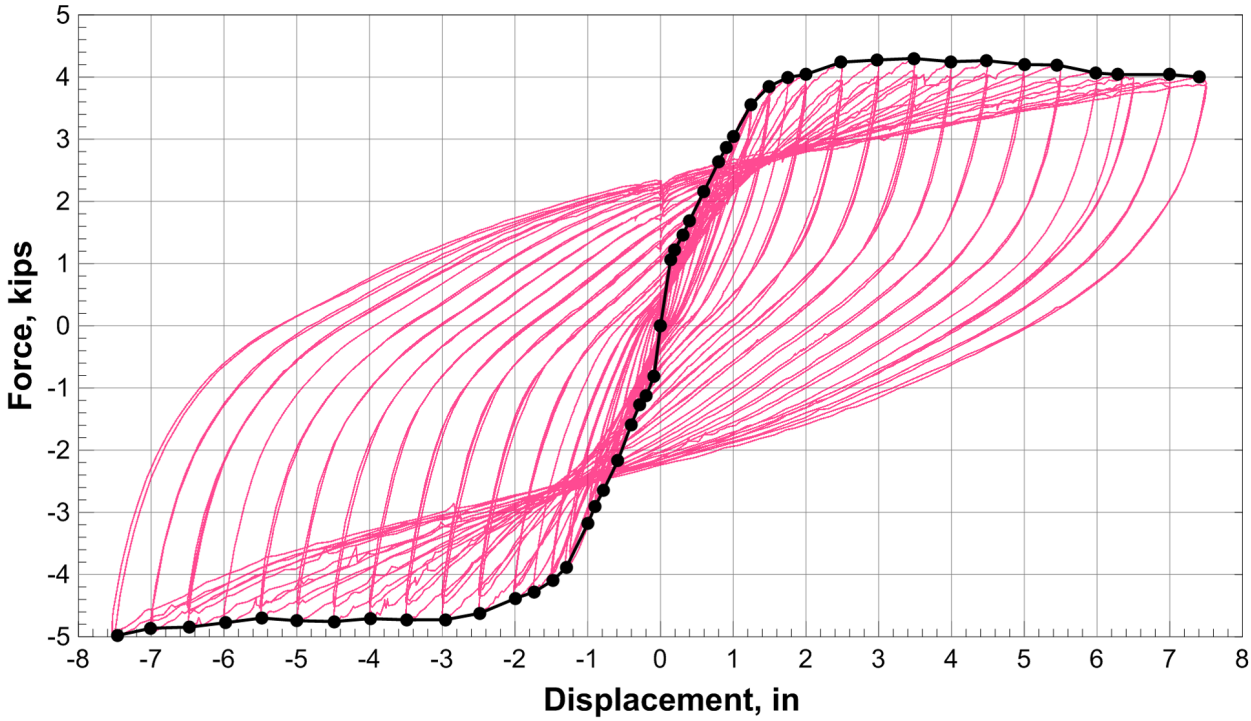

Figure 3.73: Pile 4: Backbone curve.

Representative Sensor Response Histories

The following paragraphs show the output of the strain gauges, string pots, and soil pressure sensors as a function of time. Once the sensors begin to fail and give unrealistic results, the readings are discarded from that point on for future analyses.

Strain Gauges Figs. 3.74 and 3.75 show response histories of 11 strain gauges affixed along the longitudinal rebars located opposite to each other on the pile cross section (Fig. 3.22).

The higher strains obtained from the gauges located on the longitudinal rebars were found in the vicinity of the bedrock. The strain gauges recorded approximately a maximum tensile strain of 0.014, corresponding to a +5.5 in displacement, at an elevation of 44.5 in ($R2-9$). The maximum compressive strain was found to be approximately 0.02, and it was found at an elevation of 32 in for a +5.5 in deflection ($R2-10$).

Tetrahedron 26 tetrahedra were installed inside the pile, for a total of 156 strain gauges (Fig. 3.27). Fig. 3.76 shows the response history of six strain gauges installed in the tetrahedron labeled as *T2* and located at the elevation of 88 3/4 in.

The strain gauges recorded approximately a maximum tensile strain of 0.023, corresponding to a -1.5 in displacement, at an elevation of 25 in from the bedrock. The maximum compressive strain was found to be approximately 0.04, and it was found at an elevation from the bedrock of 6 1/2 in for a $+5.5$ in deflection.

External Strain Gauges Four strain gauges were installed on the pile outside surface. In particular, one longitudinal strain gauge was installed in the pile East side (bending direction), while the remaining three gauges were attached on the pile shear direction (South side), in a rectangular rosette configuration. More details about the external strain gauges' arrangements are included in Fig. 3.27.

Fig. 3.77 shows the response histories of the four external strain gauges.

On the shear side, strain gauges recorded approximately a maximum tensile strain of 0.0005, corresponding to a $+1.75$ in pile head displacement and to the elevation of 46 in from the pile tip. The maximum compressive strain was found to be approximately 0.00015 for a $+2.5$ in deflection.

String Pots Five string pots and one LVDT were attached to two sides of the laminar soil box (see Fig. 3.16) to monitor its movements during the test. Two string pots were attached to the pile top. Fig. 3.78 shows the time histories of the string pots used in this test and the pile top displacement history as reference. The string pots did not register significant movement, with a maximum displacement of 0.003 in at the top West Side ($SP-11$) in both push and pull direction.

In order to prevent the laminar soil box to move like during the previous test, a stronger bracing system was put in place with the use of dywidags and chains that braced the box to the strong wall. The string pots did not register significant movement, with a maximum displacement of 0.018 in at the top front, and 0.005 in at the top back.

The string pot on the pile cap ($SP7$) well matches the movements of the actuator, represented by the bottom graph in Fig. 3.78, which represents the time history of the LVDT located on the actuator.

Soil Pressure Sensors Fig. 3.79 show the output of the soil pressure sensors as a function of time. The units of measurement were pound per square inch (psi). The maximum pressure value registered was approximately 30 psi at depth of 41 in below the soil surface.

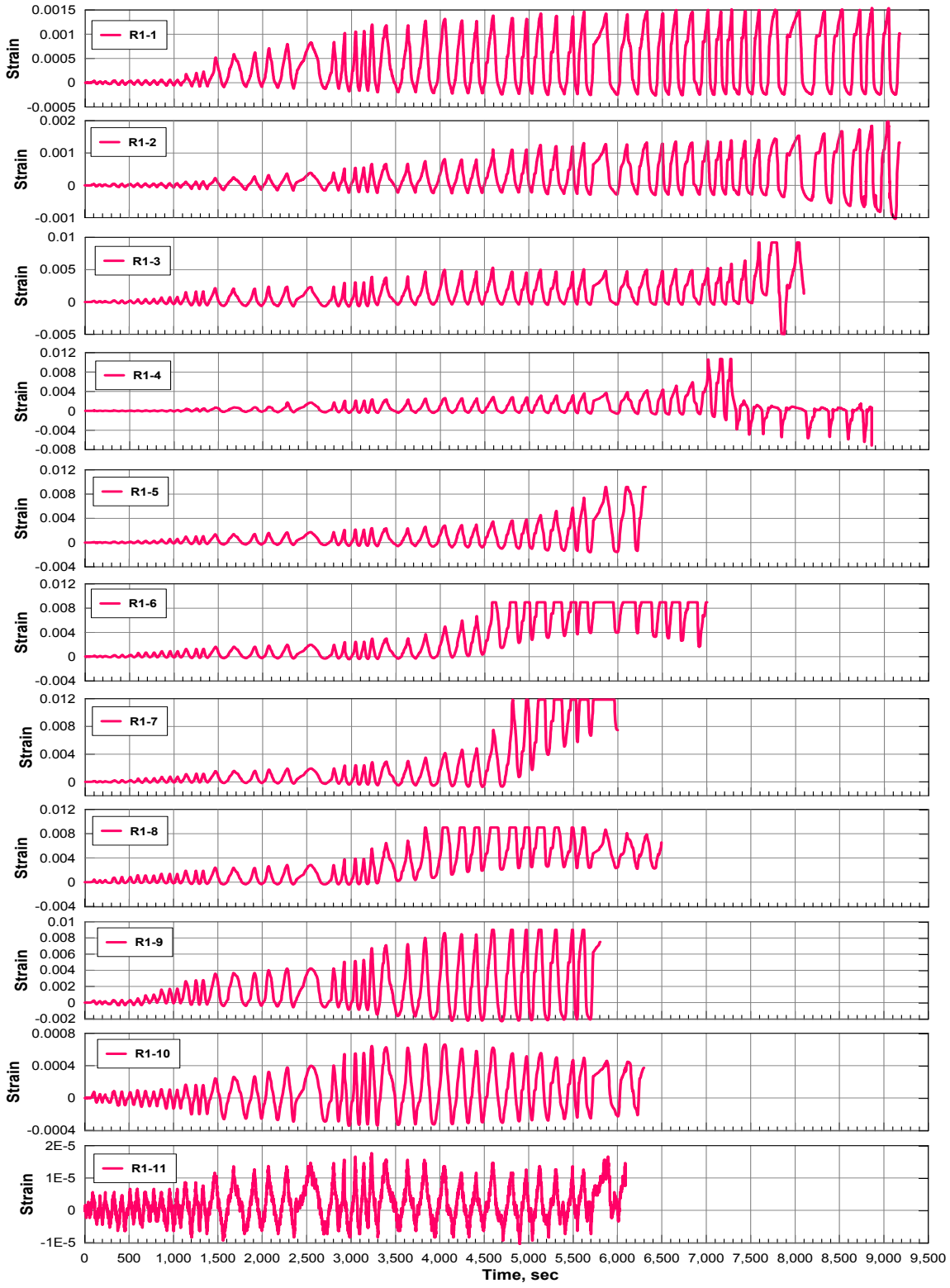

Figure 3.74: Pile 4: Strain gauges histories on longitudinal rebar *R1* (pull side) for different pile elevations.

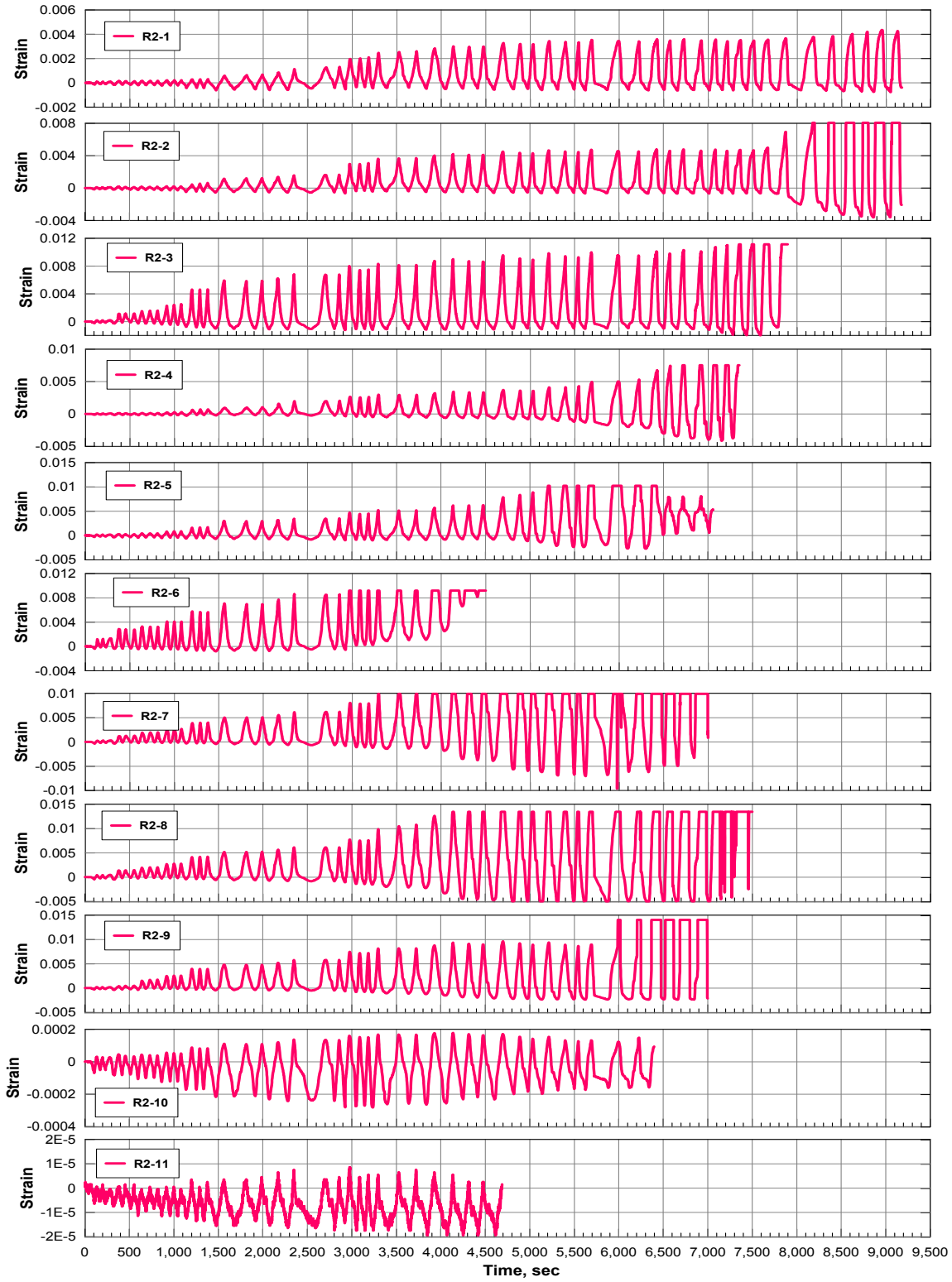

Figure 3.75: Pile 4: Strain gauges histories on longitudinal rebar *R2* (push side) for different pile elevations.

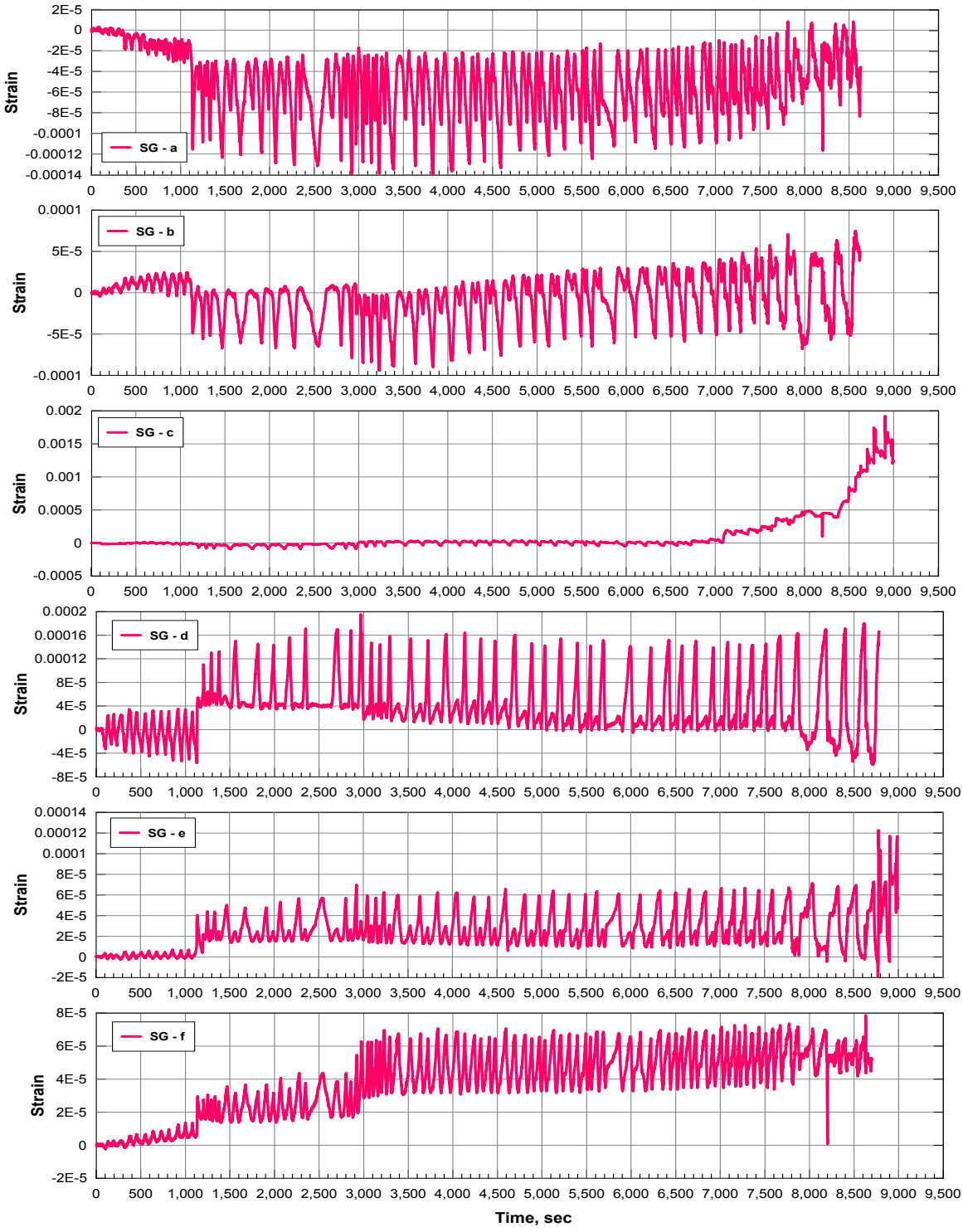

Figure 3.76: Pile 4: Strain gauges histories on *T2* tetrahedron located on the North side of the pile at an elevation of 88 3/4 in.

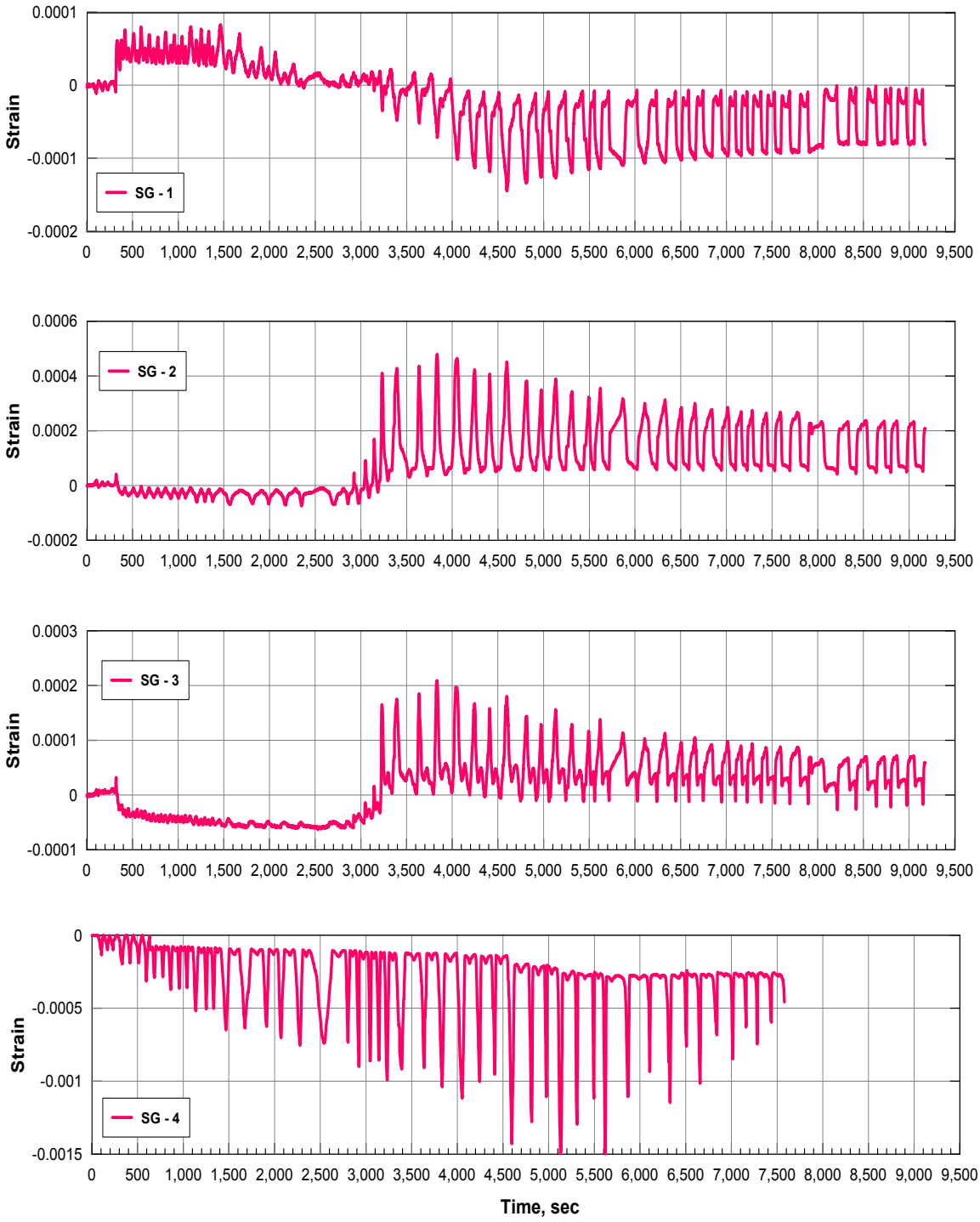

Figure 3.77: Pile 4: External strain gauges histories.

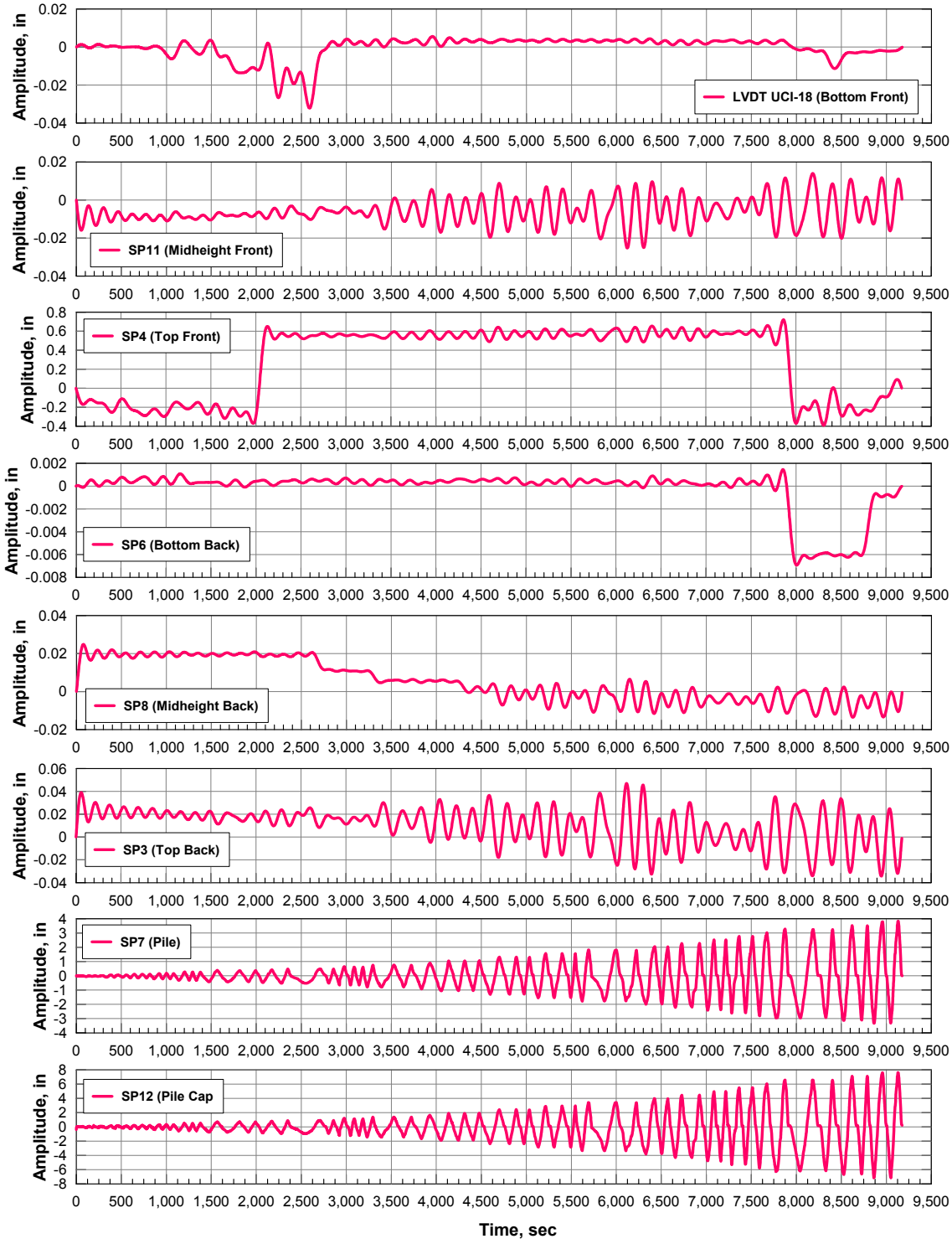

Figure 3.78: Pile 4: String pots histories.

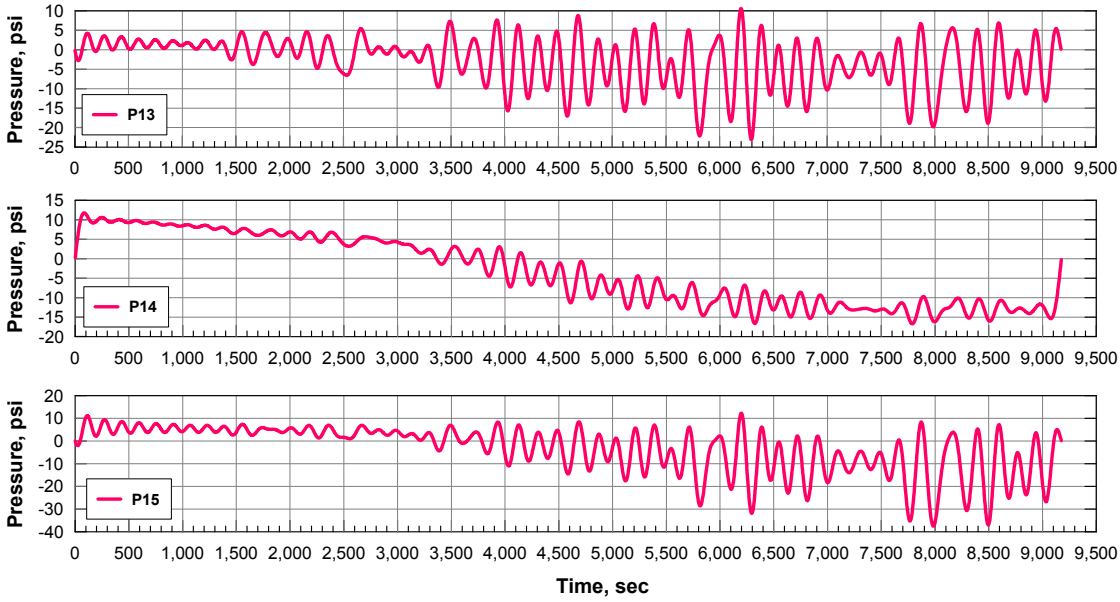

Figure 3.79: Pile 4: Soil pressure sensors' histories.

Curvature Profile

Curvature values with respect to the pile elevation are shown in Fig. 3.80. Curvature profiles for the model piles are calculated from Eq. 3.10. Sensor depths and head displacements are noted on the plots. The largest curvature values were recorded within the yielding region (plastic hinge region) that formed at approximately 23 in (3 pile diameters) below ground surface.

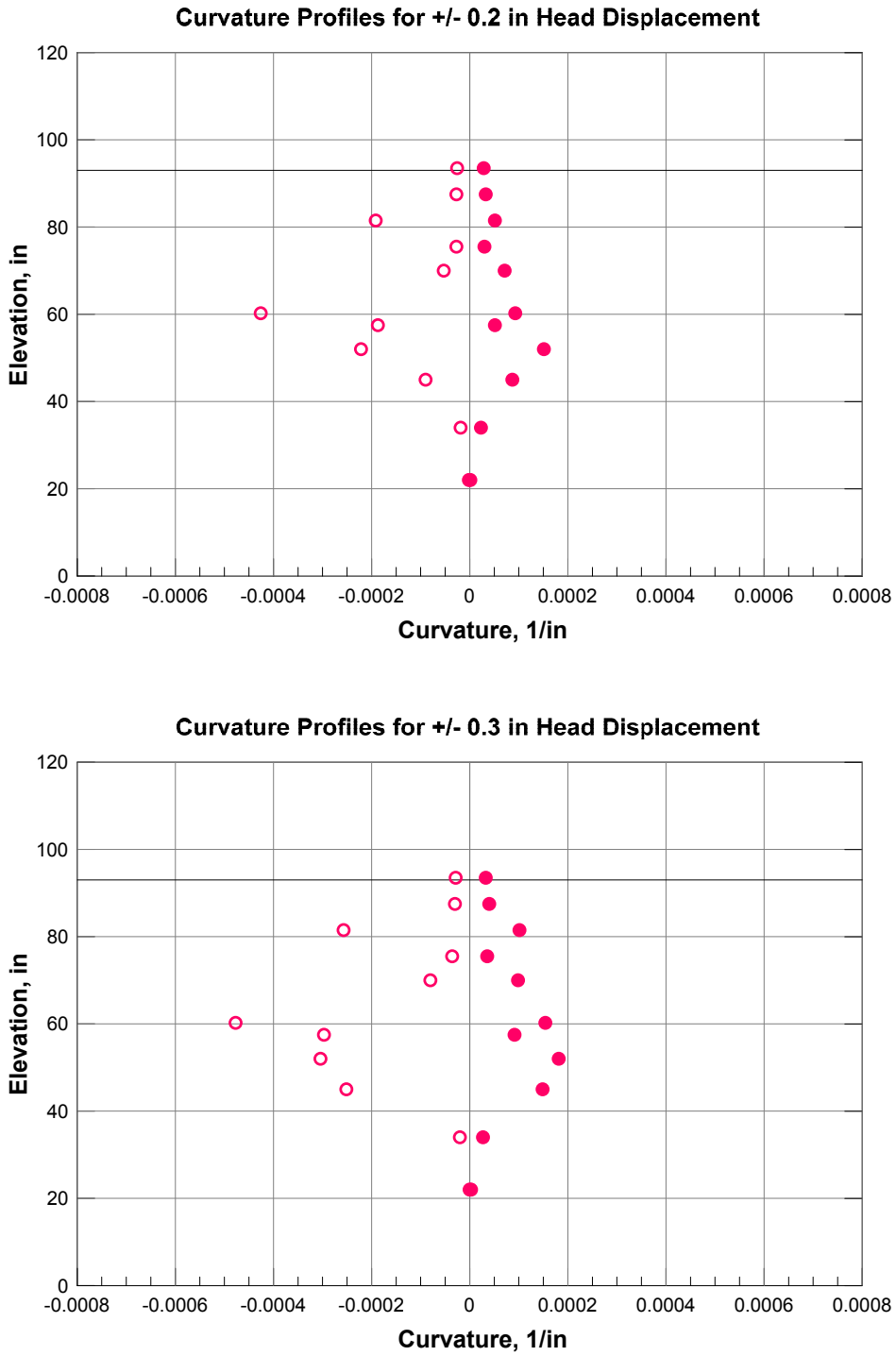

Figure 3.80: Pile *4*: Curvature profiles from 0.2 in to 3.5 in displacement levels. + and - indicate curvature values for positive and negative deflections, respectively.

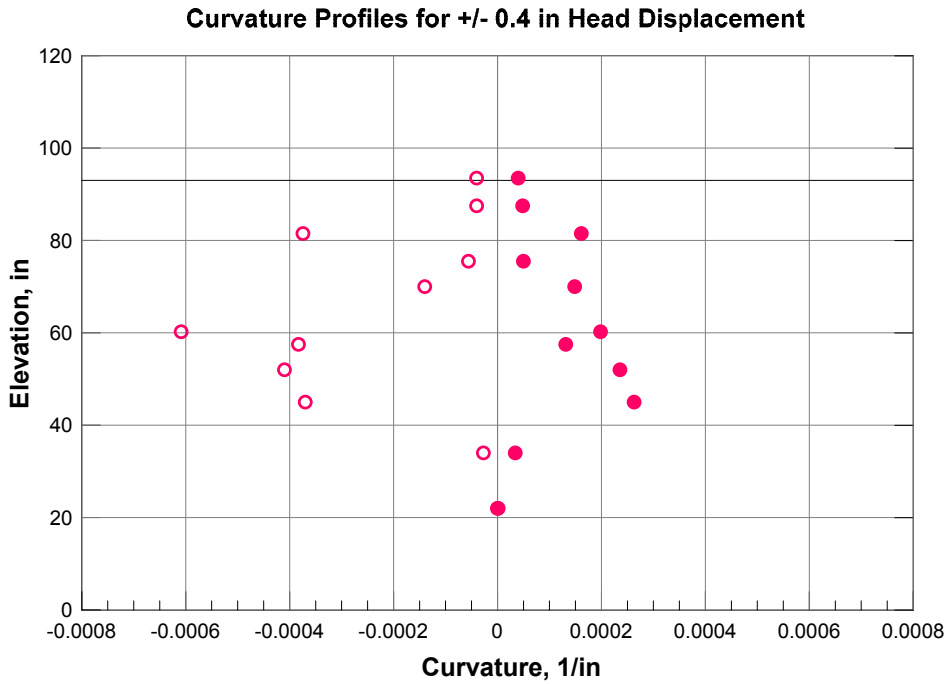

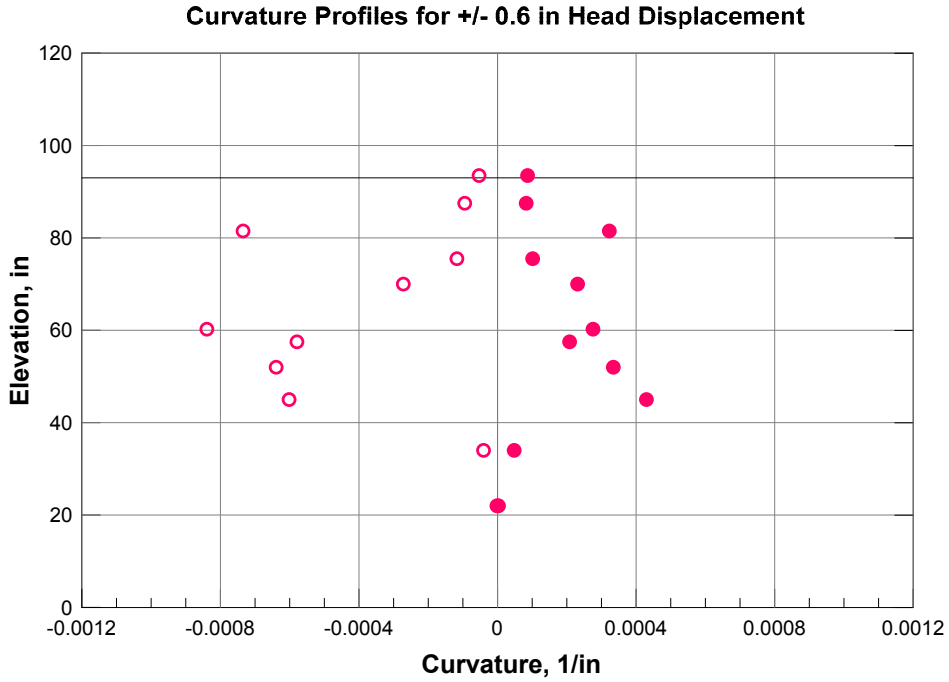

Figure 3.80: Pile *4*: Curvature profiles from 0.2 in to 3.5 in displacement levels. + and - indicate curvature values for positive and negative deflections, respectively (cont.).

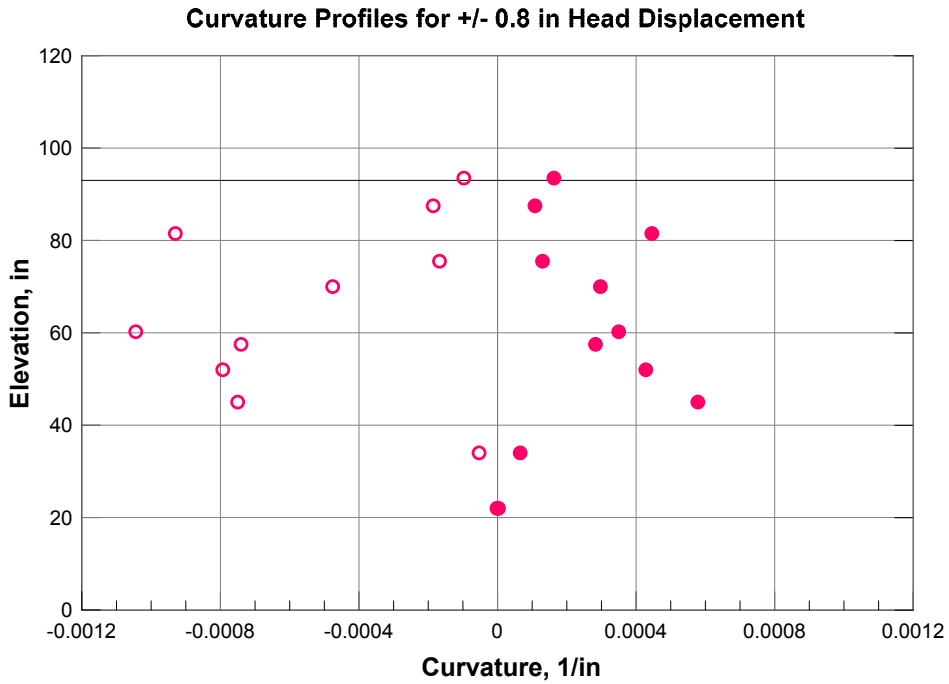

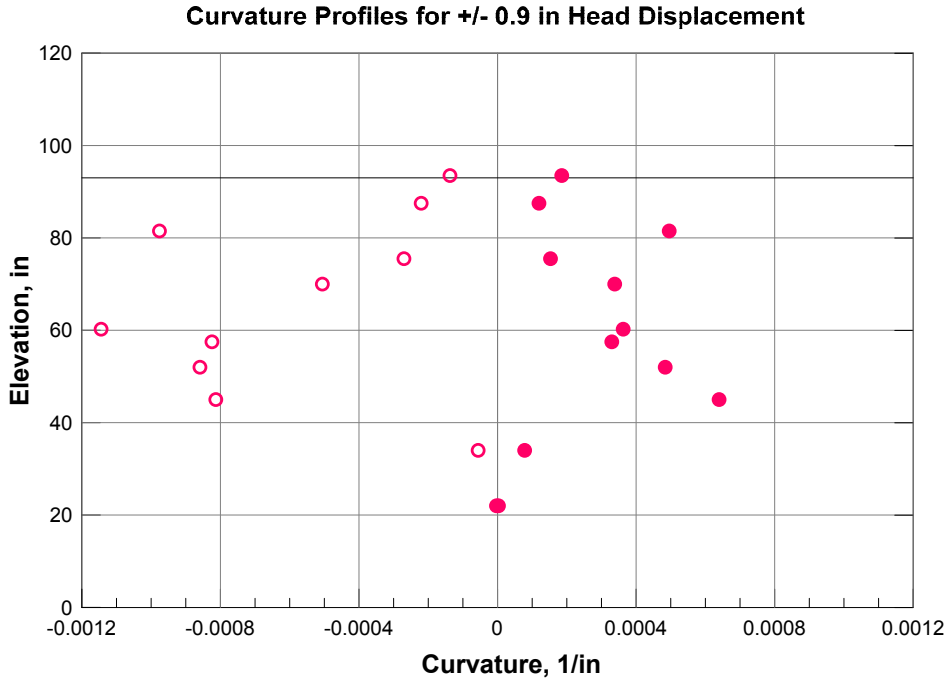

Figure 3.80: Pile *4*: Curvature profiles from 0.2 in to 3.5 in displacement levels. + and - indicate curvature values for positive and negative deflections, respectively (cont.).

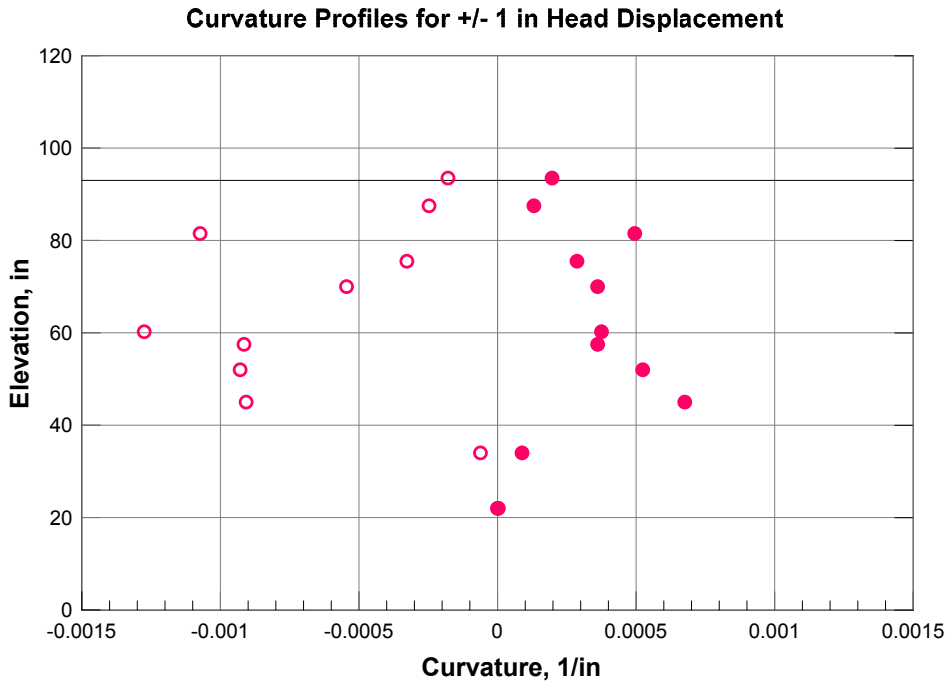

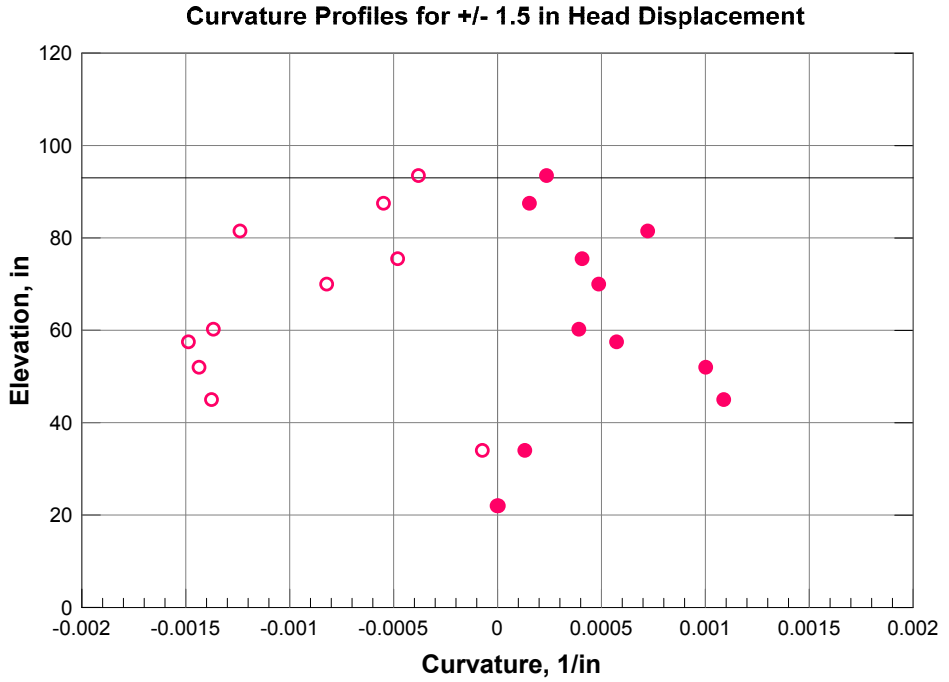

Figure 3.80: Pile *4*: Curvature profiles from 0.2 in to 3.5 in displacement levels. + and - indicate curvature values for positive and negative deflections, respectively (cont.).

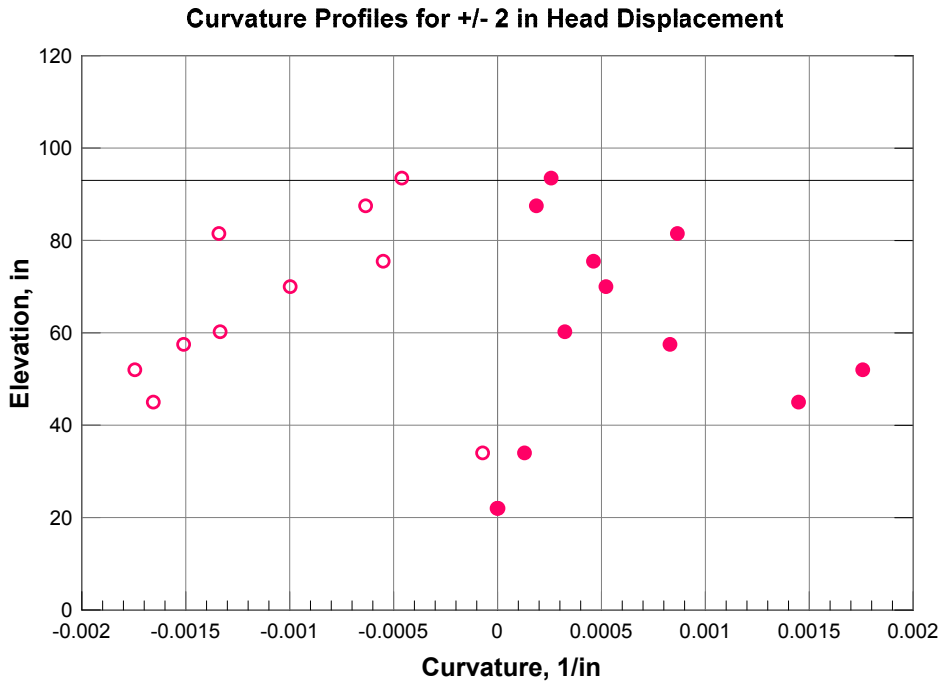

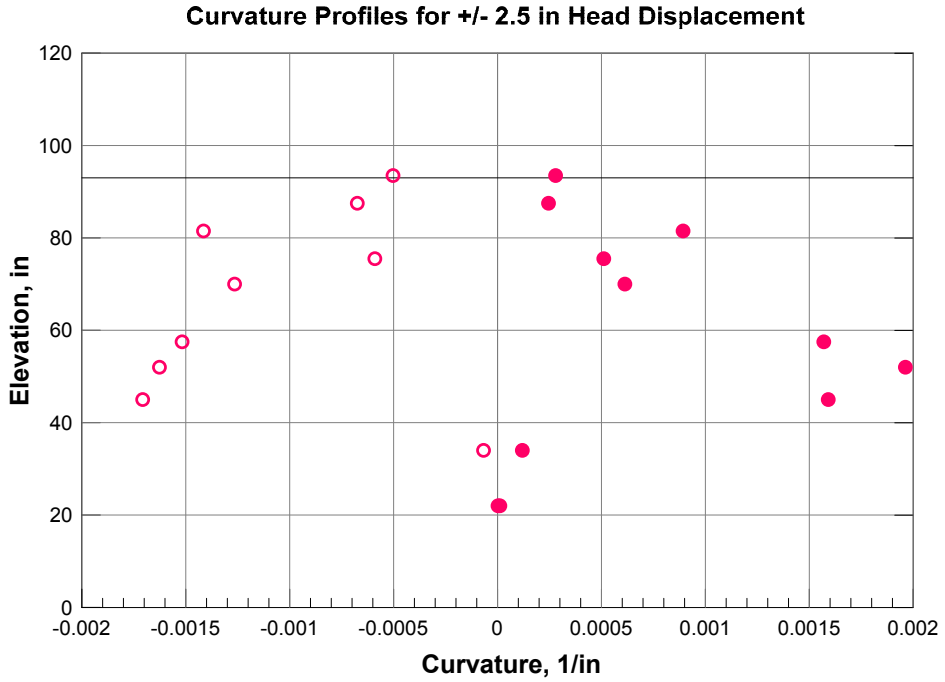

Figure 3.80: Pile *4*: Curvature profiles from 0.2 in to 3.5 in displacement levels. + and - indicate curvature values for positive and negative deflections, respectively (cont.).

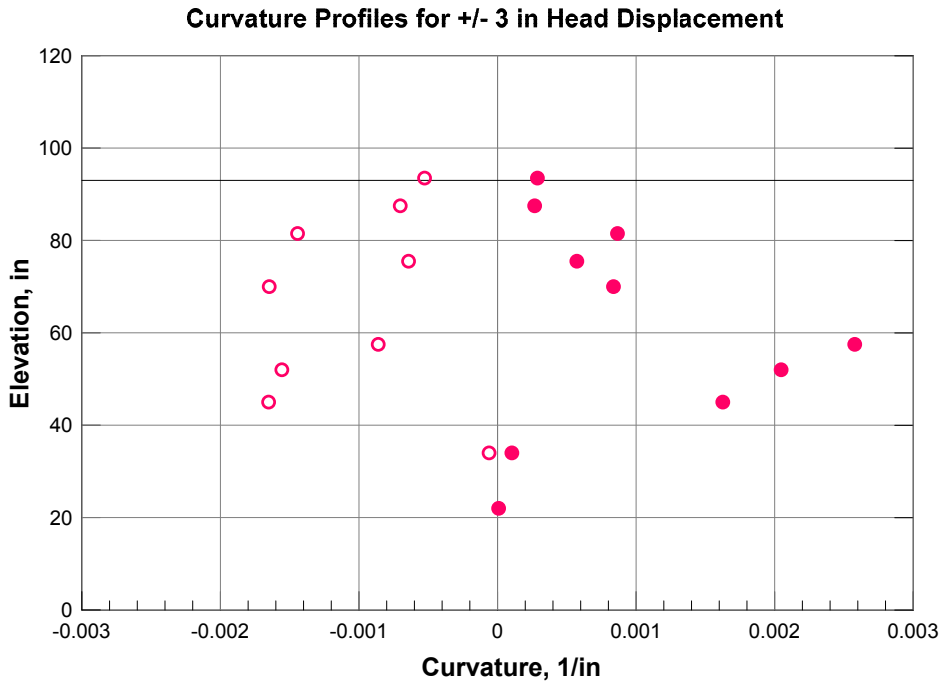

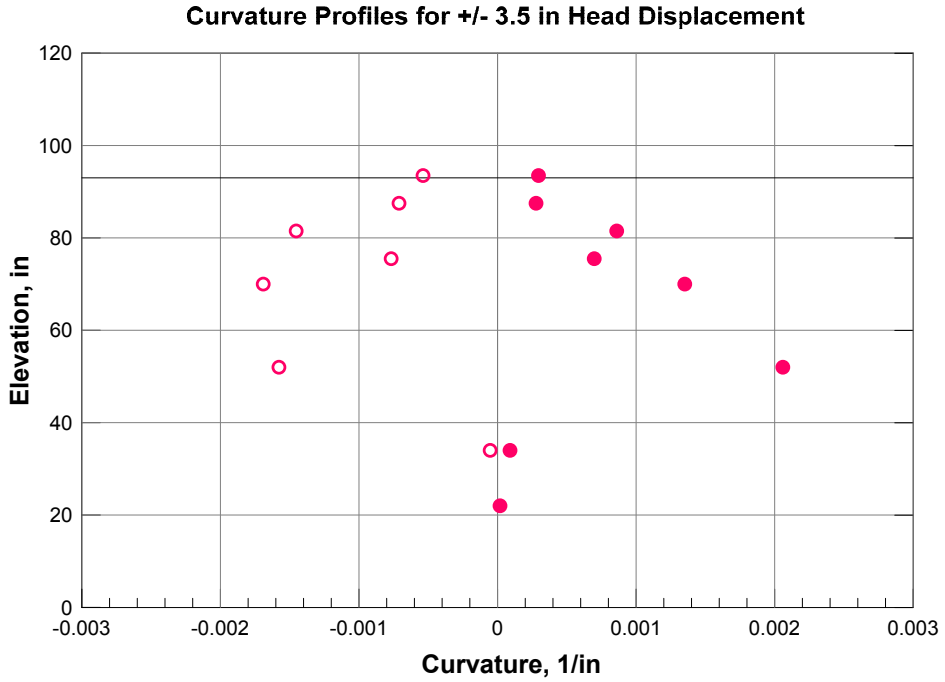

Figure 3.80: Pile *4*: Curvature profiles from 0.2 in to 3.5 in displacement levels. + and - indicate curvature values for positive and negative deflections, respectively (cont.).

Experimental Moment - Curvature Relationship

Experimental and analytical moment-curvature relationships were derived with the same procedures explained for the previous specimens and are presented in Fig. 3.81.

Figure 3.82 shows the details of the sectional analysis done with Response 2000. The predicted results well captured the stiffness and capacity of the experimental data in the positive (push) direction, but it tends to be stiffer in the negative (pull) direction.

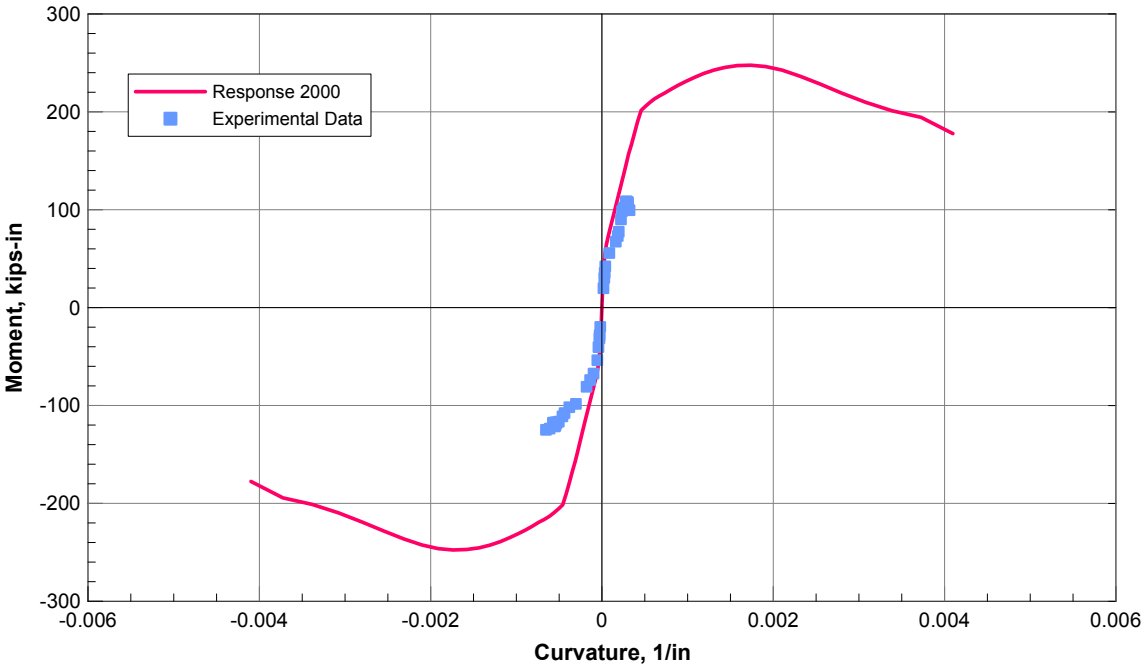

Figure 3.81: Experimental and predicted moment- curvature relationships for Pile 4.

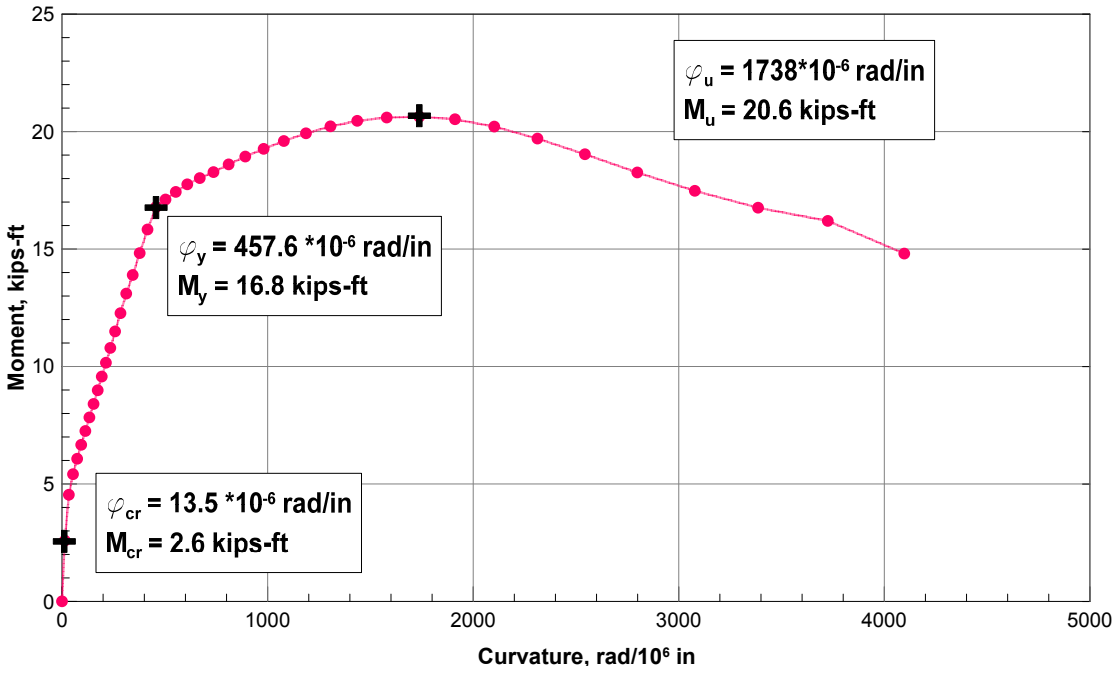

Figure 3.82: Analytical moment- curvature relationship from Response 2000 for the 10 in polymer concrete pile.

Chapter 4

Data Analysis and Discussion

This chapter describes the results of lateral load tests performed on the four piles previously presented in Chapter 3. Fig. 4.1 gives an overview on the lateral response of the four piles in analysis. The load versus deflection curves shown herein are based on pile deflections at the pile cap, which reflect the actuator' s lateral movements.

Comparisons between the four piles are made in order to evaluate the effects of the following factors on the pile lateral resistance:

- Internal reinforcement type;
- Mechanical properties of the concrete; and
- Fixity at the pile tip.

The final part of the chapter focuses on th 3D strains and stresses obtained from the strain gauges attached to the internal tetrahedra and to the external pile surface in Pile *1* and Pile *4*. Particular emphasis is given to the internal shear stress and the external shear friction, which represent key measurements to assess the validity of the proposed instrumentation.

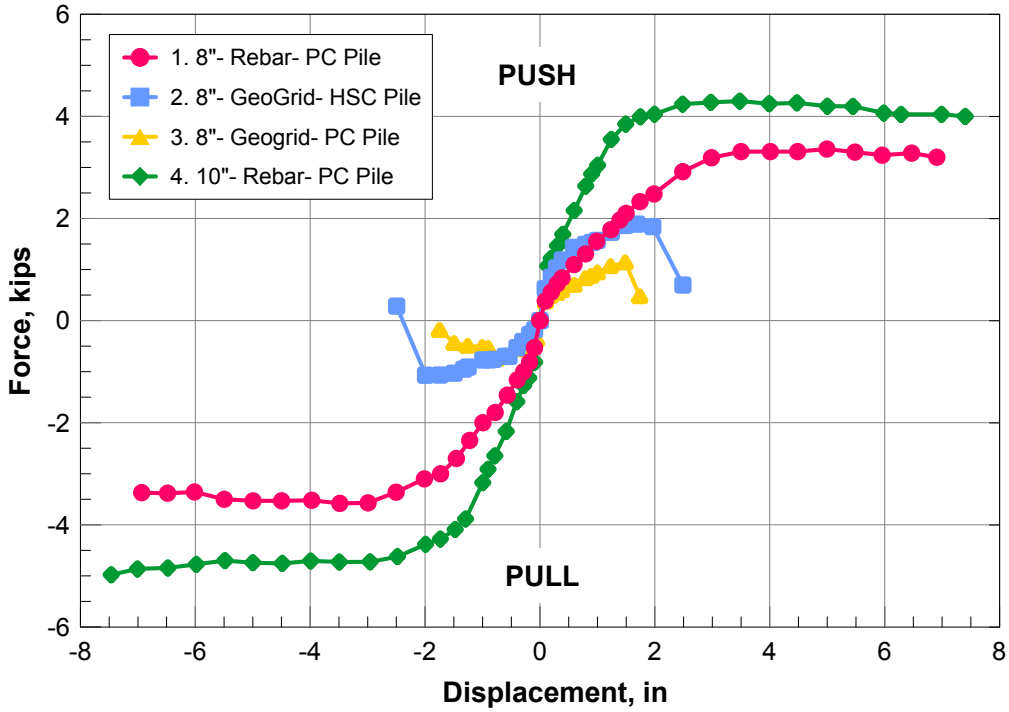

Figure 4.1: Backbone curves of Pile *1*, Pile *2*, Pile *3*, and Pile *4*.

4.1 Comparison with Analytical Methods

As previously said in Chapter 1.2, there are different pile design methodologies, which range from simple analytical models to rigorous three-dimensional numerical solutions.

A common approach among the analytical methods is the **Broms** ([18], [19])' hand calculation method that allows the determination of lateral loads and pile deflections at the ground surface. This method can be used for long and short piles in cohesive and cohesionless soil. The main assumption for short piles is that the ultimate lateral resistance is governed by the passive earth pressure of the surrounding soil. The ultimate lateral resistance for long piles is governed by the ultimate or yield resistance of the pile. To find the ultimate lateral load, Broms used a series of graphs given pile geometry and soil properties as input values. If the pile length is classified as "intermediate", the pile needs to be checked on failure as being a

short pile and as long pile. The smaller value from the two procedures is the pile ultimate lateral load.

Table 4.1 presents the comparison between experimental and analytical data. The soil and pile properties can be found in Tables 3.5 and 3.2, respectively. It can be seen that the Broms' method tends to significantly overestimate the ultimate capacity of Pile *1* and Pile *4*.

Table 4.1: Analytical and experimental ultimate load of Pile *1* and Pile *4*.

Pile Specimens	**1**		**4**	
Load Direction	Push	Pull	Push	Pull
Actuator Peak Reaction Force [kips]	3.4	3.6	4.2	4.9
Broms' Ultimate Load [kips]	9	-9	14.5	-14.5

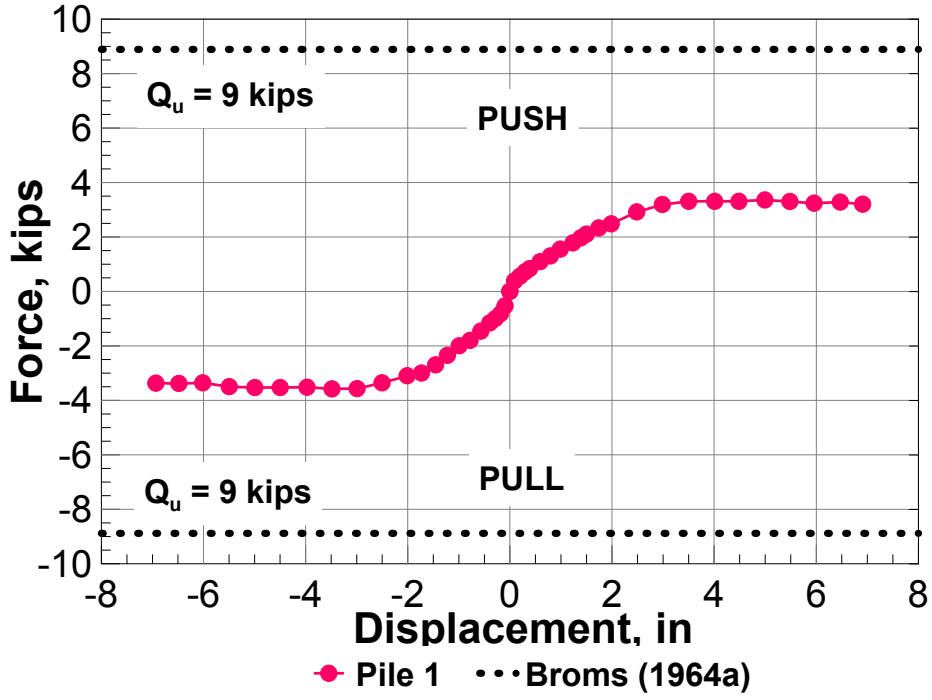

Figure 4.2: Backbone curve of Pile *1* and pile ultimate capacity from Broms' method.

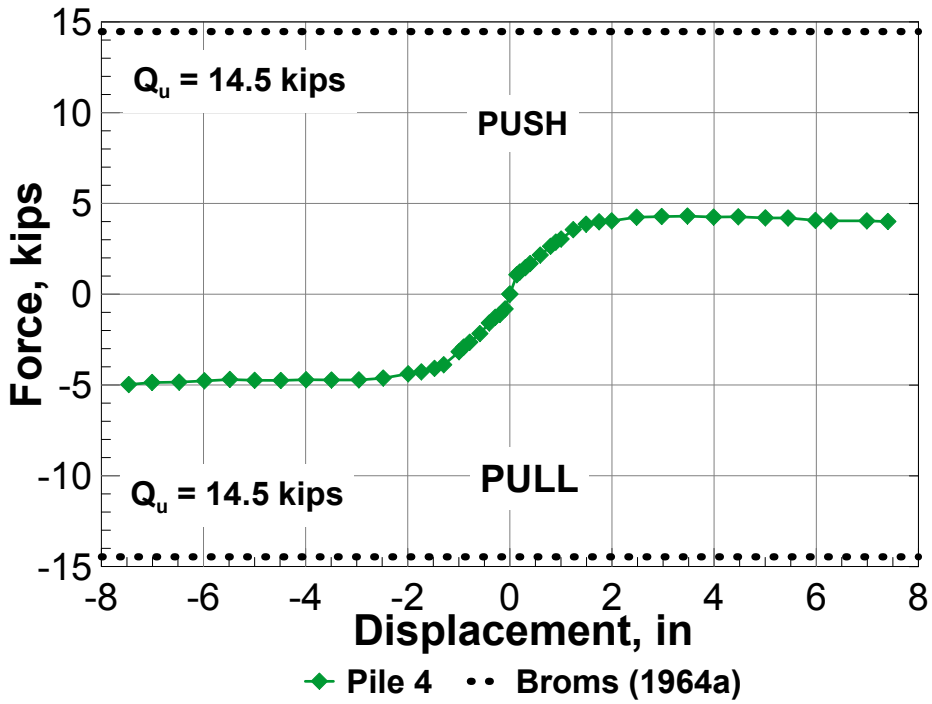

Figure 4.3: Backbone curve of Pile *4* and pile ultimate capacity from Broms' method.

4.2 Discussion on Type of Reinforcement

In this section, the results from Pile *1* (8 in polymer concrete pile with steel reinforcement) and Pile *3* (8 in polymer concrete pile with geotextile reinforcement) are compared in order to evaluate the effect that the choice of internal reinforcement had on the load- deflection behavior of the piles in sand.

The type of concrete, pile diameter, pile length, and surrounding sand were constant in both tests. The two tests only differed on the choice of reinforcement. Traditional steel reinforcement was used in Pile *1*, while Pile *3* was reinforced with stiff polymer grids. This new product have been already installed in ground supported concrete slabs with successful results. However, this was the first time that it was used in a laterally loaded pile.

Table 4.2 summarizes the test results for the two specimens in analysis indicating measured loads at significant displacements. Fig. 4.4 shows the two deflection response curves and

their initial stiffness, *k*. Pile *1*' s response is similar in the two horizontal directions, while Pile *3* has a lateral capacity in the push direction that is 42% larger than the one in the pull direction. As for the maximum displacements, both piles reached similar values in both directions.

In regard to the initial stiffness, both piles are stiffer in the pull direction. If compared with each other, Pile *1* resulted 7% and 67% soften than Pile *3* in pull direction.

Pile *1* has a lateral capacity that is approximately 70% larger than Pile *3*. Moreover, the maximum displacement reached by Pile *1* is 75% larger than Pile *3* in both horizontal directions.

Another observation regards the piles' failure mode. After a lateral deflection of $+/-3$ in, Pile *1*'s capacity reached a plateau without showing a significant decrease with the increase of deflection. This can be explained by the fact the pile wasn't restrained at the tip, and, given its geometry and mechanical properties, it behaved as a short rigid pile. The largest horizontal cracks were found at the depth of 2-3 pile diameter below the soil surface. On the contrary, Pile *3* showed a clear plastic hinge at the depth of 3.5 pile diameter below the soil surface, where the pile broke into two pieces at the deflection level of +1.75 in.

Based on these preliminary results, it seems that the ConForce Grid TE-SCR100 is not ready to substitute a traditional steel reinforcement and it might not be suitable for deep foundations' applications. However, it can be used for confinement purposes or for sign and traffic piles that don't experience high lateral loads. Further pile tests could better determine the pile - geogrid flexural capacity, and make a better assessment of the reinforcement usability.

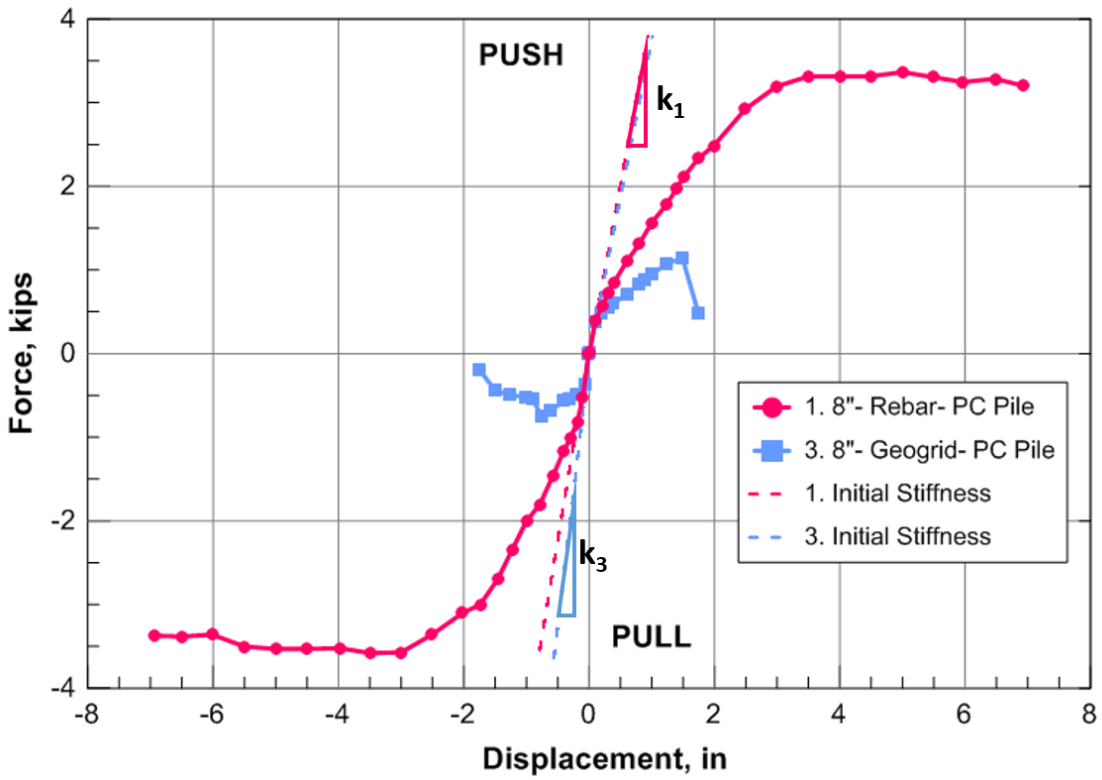

Figure 4.4: Comparison between Pile *1* and Pile *3*: backbone curves.

Table 4.2: Comparison between Pile *1* and Pile *3*: load - deformations properties.

Pile Specimens	**1**		**3**	
Load Direction	Push	Pull	Push	Pull
Actuator Peak Reaction Force [kips]	3.4	3.6	1.2	0.7
Displacement at peak force [in]	5	3.5	1.5	0.8
Max Displacement [in]	6.9	7	1.76	1.74
Actuator Reaction Force at max displacement [kips]	3.2	3.3	0.4	0.2
Yield Load [kips]	0.4	0.8	0.4	0.4
Yield Displacement [in]	0.1	0.2	0.1	0.06
Initial Stiffness [kips/in]	4	4	4	6.7
Observed Damages	Short Rigid Pile		Plastic Hinge	

4.3 Discussion on Type of Concrete

In this section, the results from Pile *2* (8 in regular concrete pile with geotextile reinforcement) and Pile *3* (8 in polymer concrete pile with geotextile reinforcement) are compared in order to evaluate how the concrete mechanical properties affected the pile lateral response. The pile diameter, pile length, internal reinforcement and surrounding sand were kept constant in both tests. However, in Pile *2* a regular concrete was used ($f'_c = 5$ ksi, $E = 3258$ ksi, and $f'_{sp} = 413$ psi), while Pile *3* was made of a polymer concrete with enhanced mechanical properties. In particular this polymer concrete had 37% more compressive strength, 31% more tensile strength, and an elastic modulus that was 25% larger than the regular concrete. More information about the mechanical properties of the concrete used in both specimens can be found in Table 3.5.

Table 4.3 summarizes the test results for the two specimens in analysis indicating measured loads at significant displacements. Fig. 4.5 shows the deflection response curves of the two specimens in analysis and respective initial stiffnesses, *k*.

Both piles have a larger horizontal capacity in the push direction. In particular, Pile *2* and *3* reached respectively 39% and 42% more capacity in the push direction. As for the maximum displacements, not significant differences between push and pull direction were recorded.

In regard to the initial stiffness, Pile *2* and *3* behaved differently in the two loading directions. While Pile *2*' s initial stiffness in the pull direction decreased by 74% with respect to the one in the push direction, Pile *3* was 68% more stiffer in the pull direction than in the push one. If compared with each other, Pile *2* resulted 43% stiffer than Pile *3* in the push direction, while Pile *3* resulted 200% stiffer in the pull direction.

Pile *2* has a lateral capacity that is approximately 33% larger than Pile *3*. The maximum displacement reached by Pile *2* is 30% larger than Pile *3* in both horizontal directions.

In regard to the failure modality, both piles formed a plastic hinge at approximately 3 pile diameter below the soil surface, in correspondence of which the pile broke into two pieces.

Based on this preliminary results, it seems that increasing the mechanical properties of the concrete by approximately 30% did not have any effect in the increase of pile lateral capacity. On the contrary, it caused a decrease of capacity of 30%. However, another factor needs to be taken into account. The type of reinforcement used had the same mechanical properties in both cases since the composition of the geogrid did not change. What did change was the aperture size. In order to facilitate the concrete pouring process, the aperture size was increased by 37.5% in Pile *3*, and this brought a decrease of internal confinement and reinforcement if compared with the other pile.

Based on these results, we cannot asses the influence of the concrete' s mechanical properties in the lateral response of the pile. Further testings are required, as well as more studies on the geogrid' s aperture size and its influence on the pile capacity.

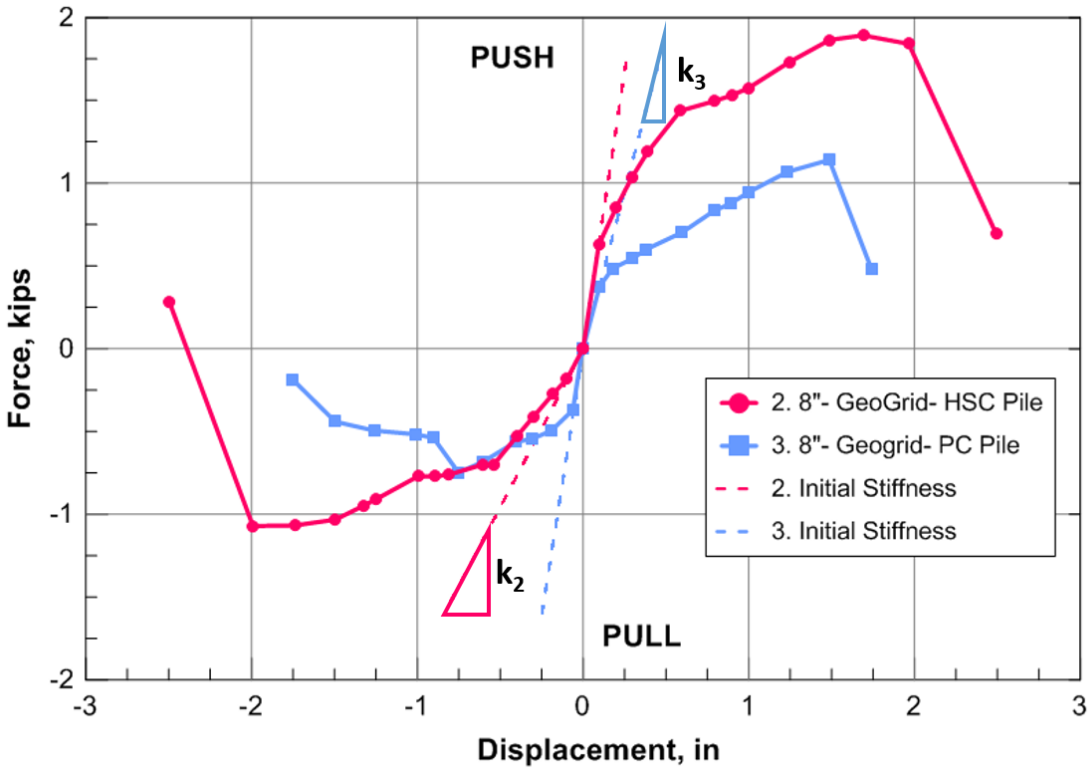

Figure 4.5: Comparison between Pile *2* and Pile *3*: backbone curves.

Table 4.3: Comparison between Pile *2* and Pile *3*: load - deformations properties.

Pile Specimens	**2**		**3**	
Load Direction	Push	Pull	Push	Pull
Actuator Peak Reaction Force [kips]	1.8	1.1	1.2	0.7
Displacement at peak force [in]	2	2	1.5	0.8
Max Displacement [in]	2.5	2.5	1.76	1.74
Actuator Reaction Force at max displacement [kips]	0.7	0.2	0.4	0.2
Yield Load [kips]	0.63	0.18	0.4	0.4
Yield Displacement [in]	0.09	0.1	0.1	0.06
Initial Stiffness [kips/in]	7	1.8	4	6.7
Observed Damages	Plastic Hinge		Plastic Hinge	

4.4 Discussion on Boundary Conditions

In this section, the results from Pile *1* (8 in polymer concrete pile with steel reinforcement) and Pile *4* (10 in polymer concrete pile with with steel reinforcement) are compared in order to evaluate the effect that the tip restraint had on the pile lateral response.

Originally, this two pile tests were thought with the idea to discuss the pile diameter effect on laterally loaded piles. In fact, Pile *4* is 20% larger and 5 in longer than Pile *1*. This was the maximum diameter that could have been chosen given the laminar soil box' s dimension, and considering that a length of at least three pile diameter needed to be left in front and back of the pile in the loading direction. All the other test characteristics (e.g. type of concrete, longitudinal and transversal reinforcement ratio, and sand) were kept constant. However, since Pile *1* behaved like a short rigid pile and experienced rotation, the objective of Pile *4*' s test was changed. Pile *4* was then embedded in a 40 in concrete slab with the dual purpose of restraining the pile tip and to simulate a rock-socket pile.

Table 4.4 summarizes the test results for the two specimens in analysis indicating measured loads at significant displacements. Fig. 4.6 presents the two deflection response curves. The respective initial stiffness, k, is also annotated

Pile *1*' s response is similar in the two horizontal directions, while Pile *4* has a lateral capacity in the pull direction that is 17% larger than the one in the opposite direction.

In regard to the initial stiffness, Pile *1* has an initial stiffness of approximately 4 kips/in in both directions; Pile *4* is slightly stiffer in the push direction. If compared with each other, Pile *4* resulted 64% and 50% stiffer than Pile *1* in the push and pull direction, respectively.

Pile *4* has a lateral capacity that is approximately 23% larger than Pile *1* for similar deflection levels.

Another observation regards the piles' failure mode. After a lateral deflection of +/−3 in, both piles' capacity reached a plateau without showing a significant decrease with the increase of deflection. The largest horizontal cracks were found at the depth of 2-3 pile diameter below the soil surface in the case of Pile *1*. Pile *4* developed a plastic hinge at approximately 30 in of elevation from the top of the bedrock (approximately 3 pile diameters below the surface).

In conclusion, considering negligible the difference in size among the two piles, the tip restrain in Pile *4* brought an improvement of 20% in the specimen lateral capacity.

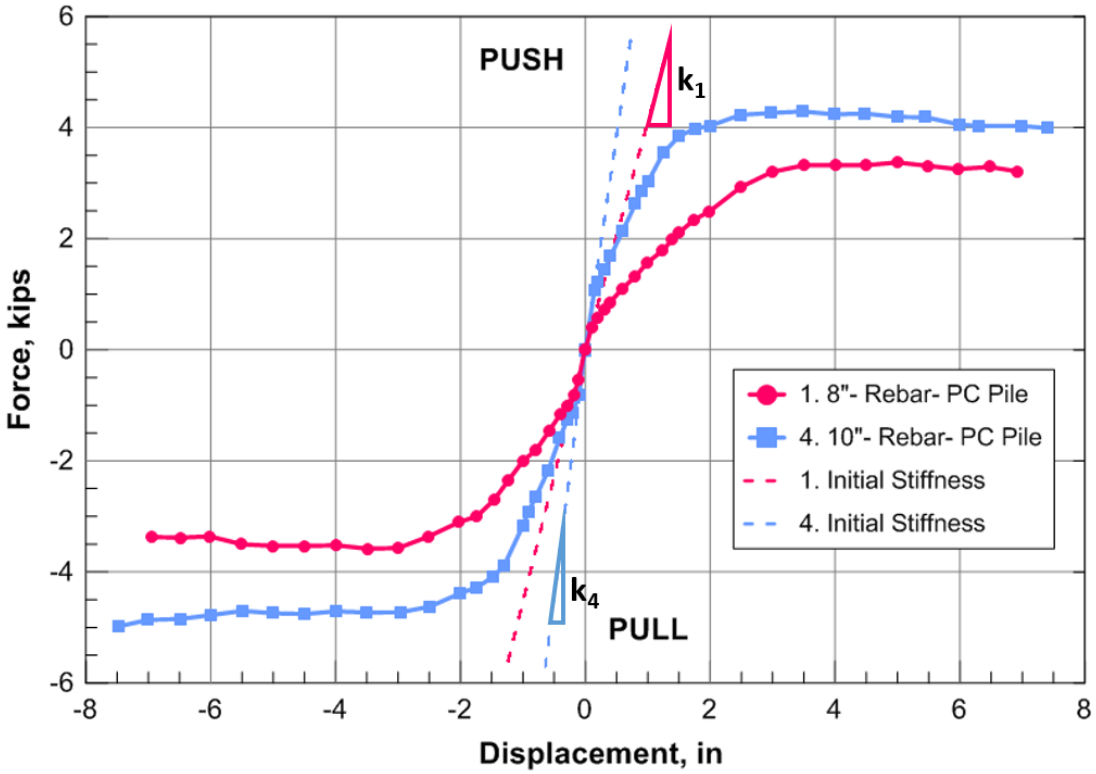

Figure 4.6: Comparison between Pile *1* and Pile *4*: backbone curves.

Table 4.4: Comparison between Pile *1* and Pile *4*: load - deformations properties.

Pile Specimens	**1**		**4**	
Load Direction	Push	Pull	Push	Pull
Actuator Peak Reaction Force [kips]	3.4	3.6	4.2	4.9
Displacement at peak force [in]	5	3.5	3	7.5
Max Displacement [in]	6.9	7	7.5	7.5
Actuator Reaction Force at max displacement [kips]	3.2	3.3	3.9	4.9
Yield Load [kips]	0.4	0.8	1.1	0.8
Yield Displacement [in]	0.1	0.2	0.1	0.1
Initial Stiffness [kips/in]	4	4	11	8
Observed Damages	Short Rigid Pile		Plastic Hinge	

4.5 Discussion on Shear Data

The total soil resistance (p) to the lateral movement of the pile element (y) is the composed by friction resistance and front resistance. However, the analysis of the side friction contribution has been traditionally been neglected since the determination of the shear is difficult and there are not experimental data regarding the shear in the literature. For this reason, an accurate separation between side friction and direct pressure has not been made yet.

The ability to characterize the maximum shear developed on the sides of the pile through the proposed instrumentation is examined in this section, by presenting the results obtained from the tetrahedra and the external strain gauges mounted in *Pile 1* and *Pile 4*.

4.5.1 Tetrahedron

As presented in Chapter 3.2.4, from each tetrahedron, six strain readings are obtained, which can be transformed in six strain components (Eq. 3.3), and then in six stress components (Eq. 3.5). However, these equations allow the derivation of the 3D state of strain and stress based on a local coordinate system (x', y', z') that is common to all the tetrahedra, but that may differ from the global coordinate system (x, y, z). Therefore, further passages are required in order to have all the measurements in the same global coordinate system, and allow comparisons.

The local coordinate system is represented in detailed in Fig. 3.20b, where the $a-$ gauge is parallel to the y direction. Fig. 4.7 contextualize the tetrahedra location within the pile cross section and the laminar soil box. The tetrahedra are divided in North and South sets, according to their position in the pile. It can be noted that the local coordinate system of the South tetrahedra corresponds to the global system. The positive direction of the x' axis is from south to north, the positive direction of the y' axis is from east to west (push direction of the actuator), and the z' axis is positive when upward. For the North tetrahedra, the x' and y' axes' positive directions are opposite to the global x and y axes, while the z' axis has the same positive direction of the global z axis.

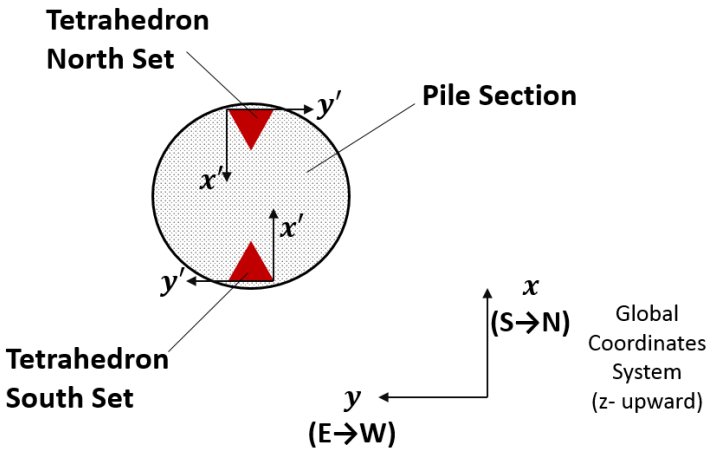

Figure 4.7: Pile global coordinate system and tetrahedron local coordinate system.

In order to enable comparisons among the two sets of tetrahedra, the 3D strains and stresses from the North set need to be transformed from the x'- y'- z' coordinates into the global coordinate system (x, y, z). To do that, the local coordinate system is rotated by an angle $\theta = 180°$ around the z axis to create the global one.

The 3D stress transformation equation is as follows:

$$[\sigma] = [T]\,[\sigma']\,[T]^T \tag{4.1}$$

with the transformation matrix [T] expressed as:

$$[T] = \begin{bmatrix} \cos(x, x') & \cos(x, y') & \cos(x, z') \\ \cos(y, x') & \cos(y, y') & \cos(y, z') \\ \cos(z, x') & \cos(z, y') & \cos(z, z') \end{bmatrix} \tag{4.2}$$

The same procedure can be applied to the 3D strains. Based on Fig. 4.8, it can be seen that:

(x, x') $= \theta$	(x, y') $= 90° - \theta$	(x, z') $= 90°$
(y, x') $= 90° + \theta$	(y, y') $= \theta$	(y, z') $= 90°$
(z, x') $= 90°$	(z, y') $= 90°$	(z, z') $= 90°$

Eq. 4.2 gives the following transformation matrix:

$$[T] = \begin{bmatrix} -1 & 0 & 0 \\ 0 & -1 & 0 \\ 0 & 0 & 1 \end{bmatrix} \tag{4.3}$$

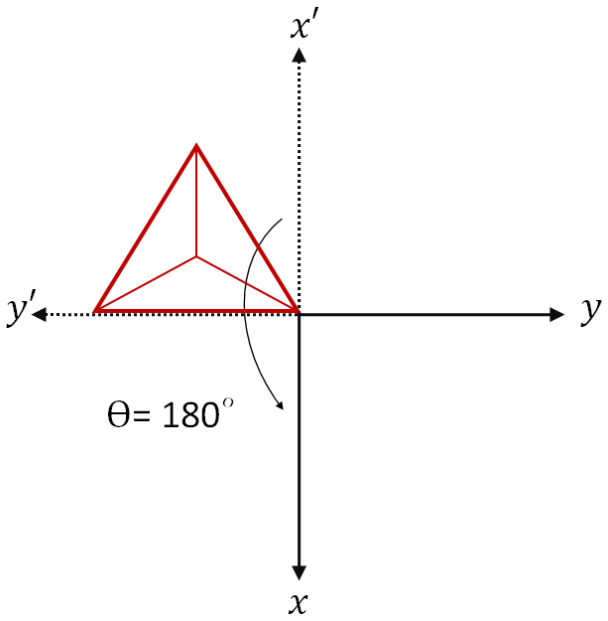

Figure 4.8: Transformation of coordinates about the z axis for the North set of tetrahedra.

The transformed strains can be determined by means of:

$$[\sigma] = \begin{bmatrix} -1 & 0 & 0 \\ 0 & -1 & 0 \\ 0 & 0 & 1 \end{bmatrix} \begin{bmatrix} \sigma_{x'} & \tau_{x'y'} & \tau_{x'z'} \\ \tau_{x'y'} & \sigma_{y'} & \tau_{y'z'} \\ \tau_{x'z'} & \tau_{y'z'} & \sigma_{z'} \end{bmatrix} \begin{bmatrix} -1 & 0 & 0 \\ 0 & -1 & 0 \\ 0 & 0 & 1 \end{bmatrix}^T \tag{4.4}$$

where the transformed stress components $[\sigma]$ will become:

$$\sigma_x = \sigma_{x'} \cos^2\theta + \sigma_{y'} \sin^2\theta + \gamma_{x'y'} \sin 2\theta \tag{4.5a}$$

$$\sigma_y = \sigma_{x'} \sin^2\theta + \sigma_{y'} \cos^2\theta - \gamma_{x'y'} \sin 2\theta \tag{4.5b}$$

$$\sigma_{yz} = \sigma_{z'} \tag{4.5c}$$

$$\tau_{xy} = -\frac{1}{2}\sigma_{x'} \sin 2\theta + \frac{1}{2}\sigma_{y'} \sin 2\theta + \gamma_{x'y'} \cos 2\theta \tag{4.5d}$$

$$\tau_{yz} = \tau_{y'z'} \cos\theta - \tau_{z'x'} \sin\theta \tag{4.5e}$$

$$\tau_{zx} = \tau_{y'z'} \sin\theta + \tau_{z'x'} \cos\theta \tag{4.5f}$$

The 3D strains and stresses of Pile *1* and *4*, obtained through the previously explained

procedure, are presented in the following sections.

8 in Polymer Concrete Pile with Steel Reinforcement

This section discusses the 3D state of strain and stress, calculated from the tetrahedra of Pile *1*, based on the calculations provided in Chapter 3.2.4.

Figures 4.10 and 4.11 show the 3D strains and stresses obtained from the *T2* tetrahedra embedded in Pile *1* as function of pile deflection. Since strains and stresses were directly derived from the strain gauges readings, once the sensors began to give unrealistic results, the readings were discarded. Also, if a sensor among the six composing a tetrahedron fails, the 3D state of strain and stress for that tetrahedron cannot be calculated. For these reasons, stresses and strains are not always available for all deflection levels and for all the tetrahedra.

The shear component τ_{xy} obtained from the tetrahedra is representative of the shear stress developed in the pile cross section in the direction of the loading. This value will be compared with the shear stress generated as output from LPILE [91].

The pile was modeled in LPILE by inputting basic dimensions and properties. The pile length from the load point to the toe was 125 in, divided in 100 increments at 1.2 in each. The pile top was placed at 33 in above the ground surface. The pile cross section was circular with diameter of 8 in and cross sectional area of 50.3 in^2. The compressive strength used for the polymer concrete was 10 ksi, and the yield stress of the 6-#3 longitudinal rebars was 60 ksi. The soil layer and properties were input based on the results of the geotechnical investigations discussed in Chapter 3.1.2. One uniform 93 in sand layer was modeled in LPILE. The selected *p-y* curve model was the one from Reese et al. [86]. The sand had a unit weight of 105 lb/ft^3, a friction angle of 30°. The default value of the coefficient of subgrade reaction was chosen.

The internal force obtained by LPILE needs to be converted into a shear stress in order to be compared with the tetrahedra τ_{xy}. For a beam with a circular cross section, the maximum shear stress, τ, occurs on the neutral axis, as shown in Fig. 4.9 and it is expressed by the following equation:

$$\tau = \frac{Q * V}{I * D} \tag{4.6}$$

where Q is the first moment of inertia (Eq. 4.7), V is the internal shear force obtained from LPILE, I is the second moment of inertia I (Eq. 4.8), and D is the pile diameter. Eqs. 4.7 and 4.8 are specific for a circular beam.

$$Q = A\bar{y} = \frac{\pi(D/2)^2}{2} * \frac{4(D/2)}{3\pi} \tag{4.7}$$

$$I = \frac{\pi D^4}{64} \tag{4.8}$$

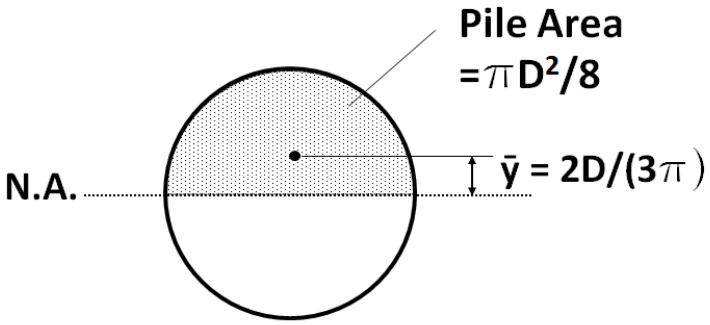

Figure 4.9: Shear stress in a circular beam.

Figure 4.14 shows the comparison between experimental values of the shear component τ_{xy} and the calculated values from LPILE. This discussion takes into consideration shear stress values for eight deflection levels, ranging from $+/-0.4$ in to $+/-3.0$ in. After $+/-3.0$ in, the strain readings started to give unrealistic values, and therefore they were discharged.

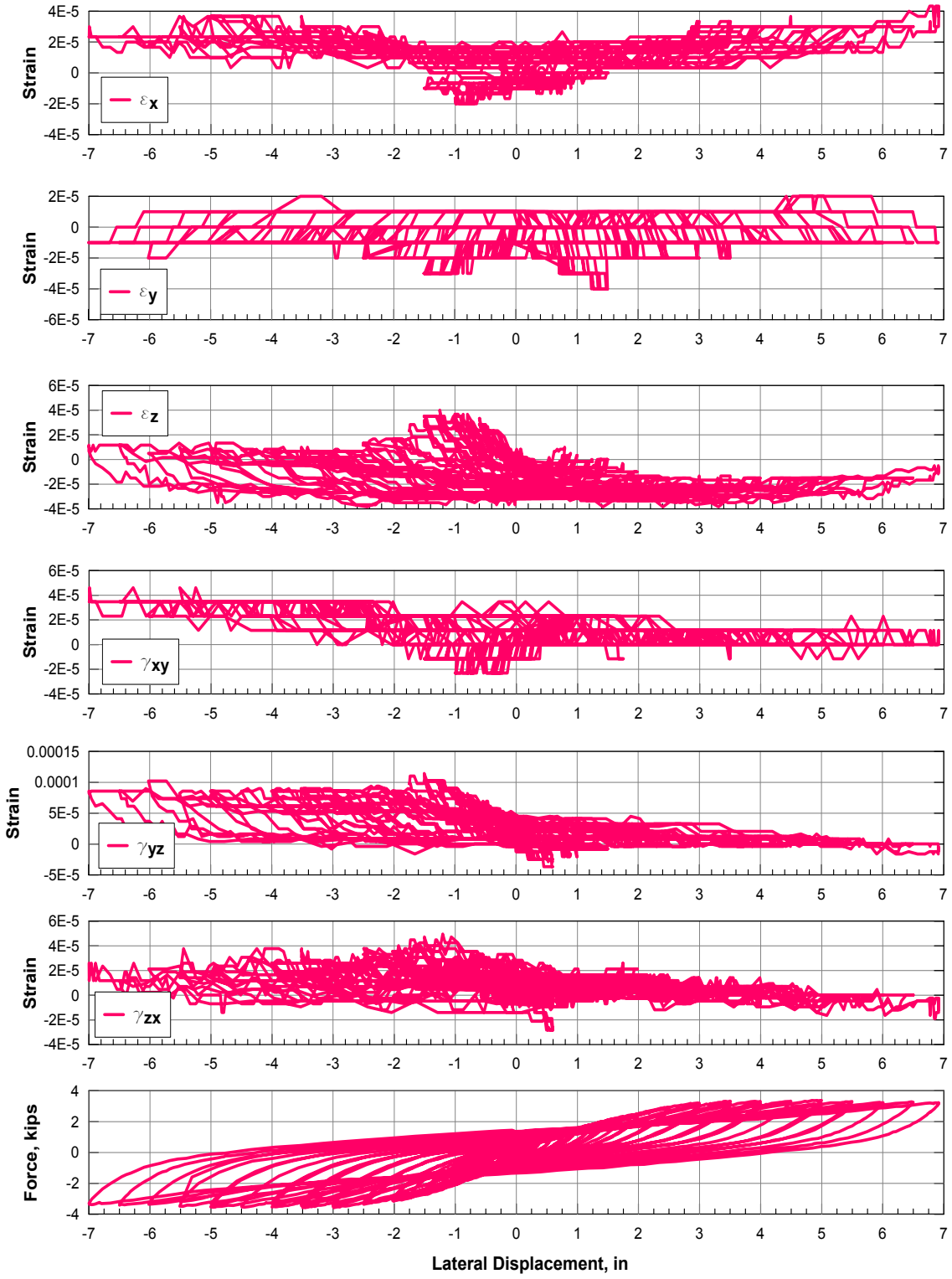

Figure 4.10: Pile 1: 3D strains vs. pile head displacements of *T2* tetrahedron located on the pile North side.

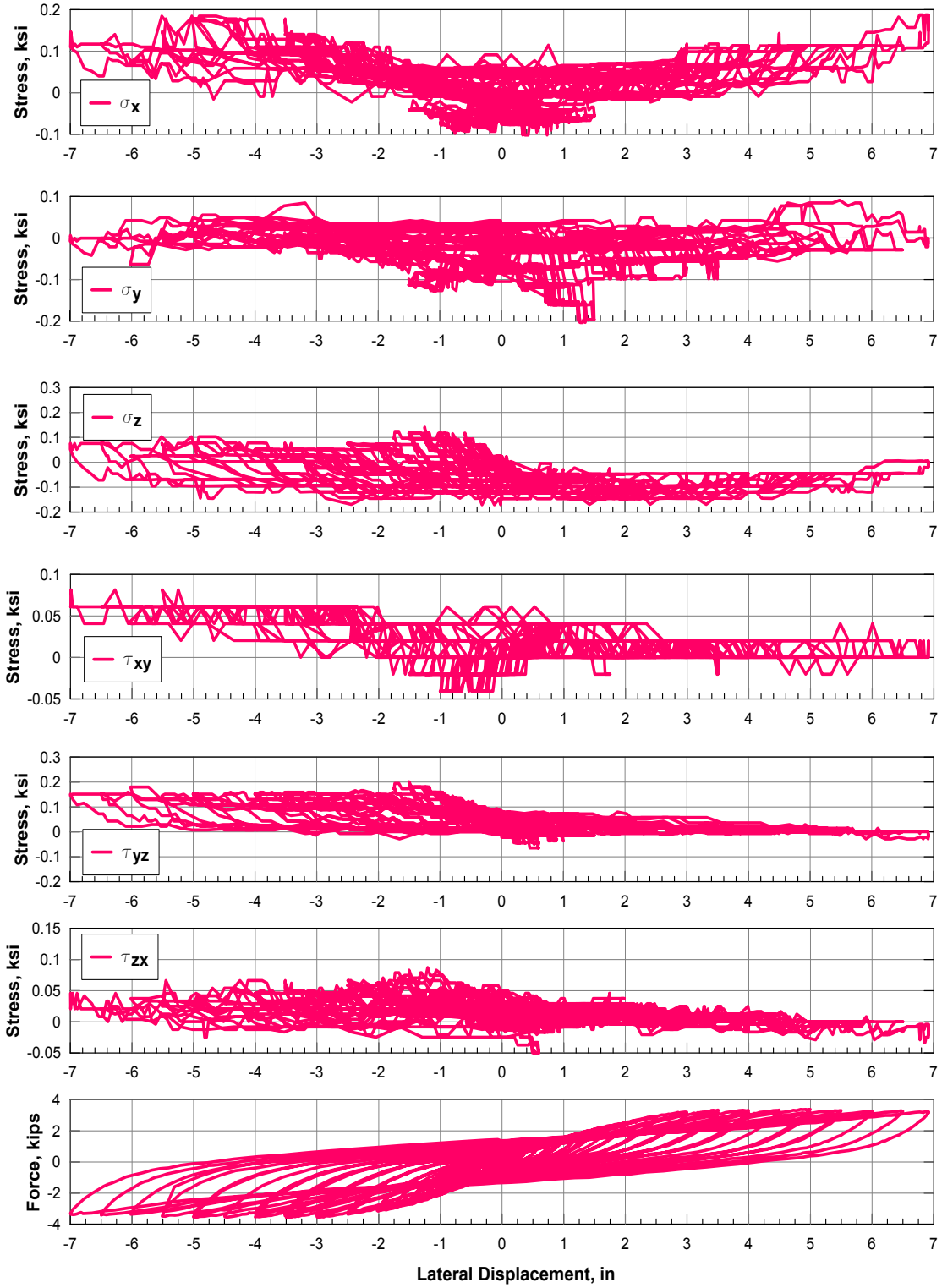

Figure 4.11: Pile 1: 3D stresses vs. pile head displacements of *T2* tetrahedron located on the pile North side.

10 in Polymer Concrete Pile with Steel Reinforcement

This section discusses the 3D state of strain and stress, calculated from the tetrahedra installed in Pile *4*, based on the calculations provided in Chapter 3.2.4.

Figures 4.12 and 4.13 show the 3D strains and stresses obtained from the *T2* tetrahedra embedded in Pile *4* as function of pile deflection. The considerations about the quality of the strain readings done in Chapter 4.5.1 apply here as well.

The shear stress component τ_{xy} was calculated from the tetrahedra embedded in Pile *4* and compared with results generated by LPILE [91].

In LPILE the pile length from the load point to the toe was 120 in, divided in 100 increments at 1.2 in each. The pile top was placed at 27 in above the ground surface. The pile cross section was circular with diameter of 10 in and cross sectional area of 78.5 in^2. The compressive strength used for the polymer concrete was 9 ksi, and the yield stress of the 5-#4 longitudinal rebars was 60 ksi. Two soil strata were modeled: the top one was 47 in thick and was composed by API sand [78]; the bottom one was 40 in bedrock, modeled as weak rock [85]. The sand layer and its properties were input based on the results of the geotechnical investigations discussed in Chapter 3.1.2.The sand had a unit weight of 104 lb/ft^3, and a friction angle of 43°. The default value of the coefficient of subgrade reaction was chosen. The weak rock had the properties of the concrete constituting the bedrock: a unit weight of 145 lb/ft^3, an uniaxial compressive strength of 4063 lb/in^2, an initial modulus of rock mass of 3200 $kips/in^2$, a RQD of 100%, and a strain factor of 0.0015.

Fig. 4.15 shows the comparison between experimental values of the shear component τ_{xy} and the calculated values from LPILE. This discussion takes into consideration shear stress values for eight deflection levels, ranging from $+/-0.4$ in to $+/-3.0$ in. After $+/-3.0$ in, the strain readings started to give unrealistic values, and therefore they were discharged.

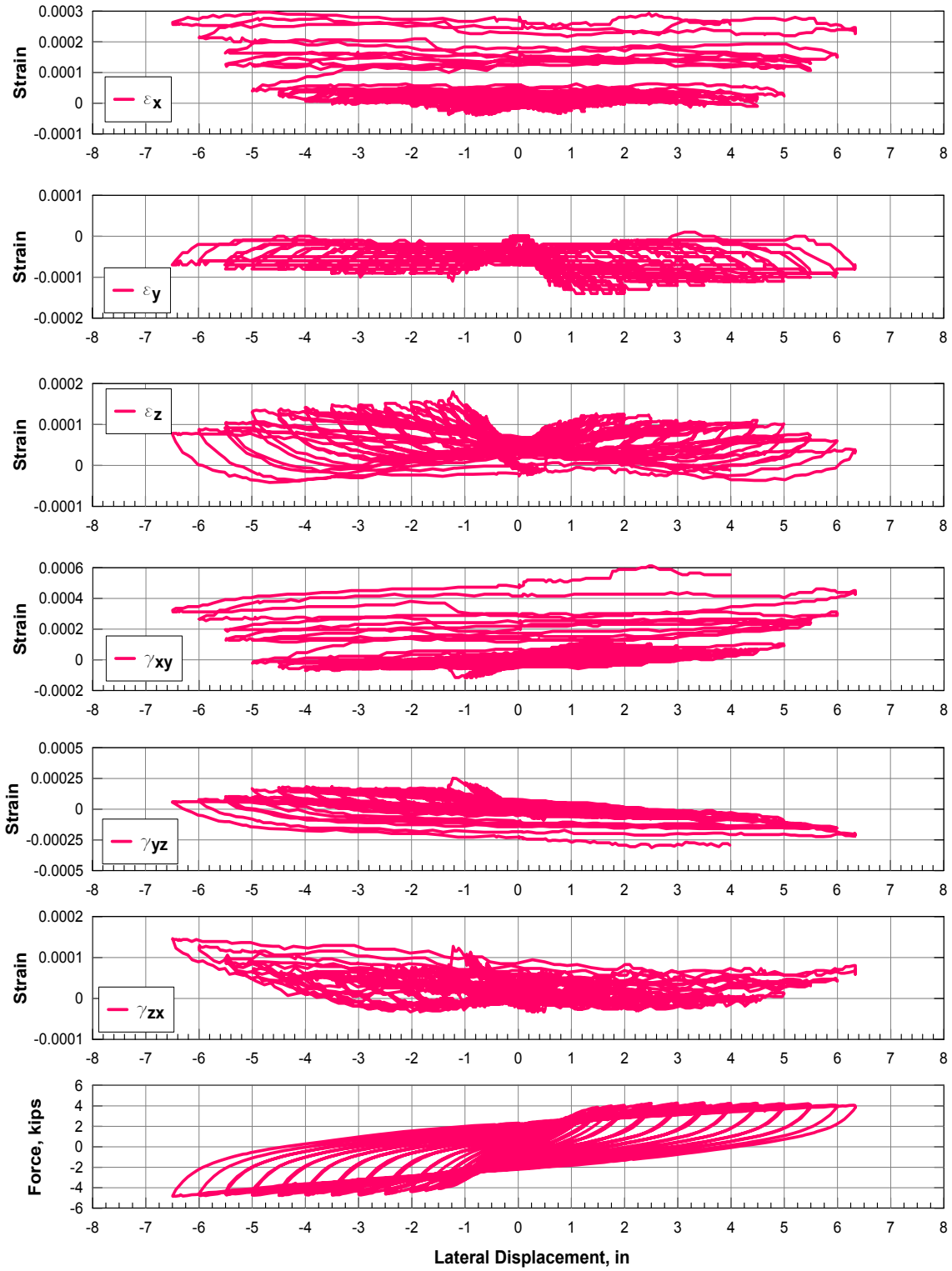

Figure 4.12: Pile 4: 3D strains vs. pile head displacements of *T2* tetrahedron located on the pile North side.

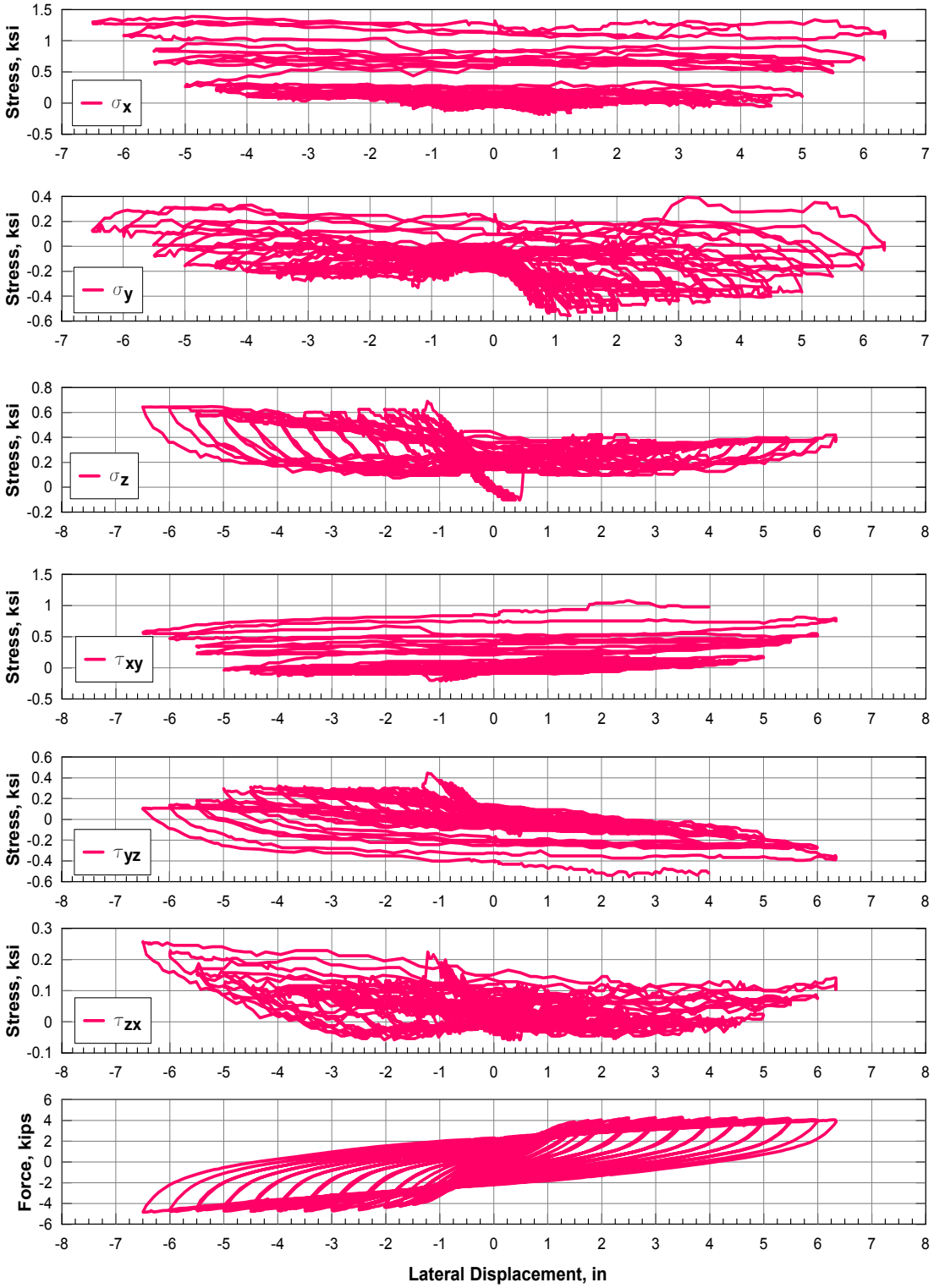

Figure 4.13: Pile 4: 3D stresses vs. pile head displacements of *T2* tetrahedron located on the pile North side.

Discussion of Shear Stress Component τ_{xy}

It can be seen that the tetrahedra embedded in Piles *1* and *4* were not able to properly capture the internal shear stress. First, the tetrahedra τ_{xy} seems not be sensitive to the direction of lateral loading. However, this can be explained with the fact that most of strain gauges readings were characterized by a initial drift that on one side did not affect their ability to follow the loading cycles, but on the other did not allow them to change sign (e.g. go from positive to negative and vice versa, like the push and pull cycles). Secondly, even if the tetrahedra τ_{xy} values are generally within the range of the ones obtained from LPILE, it can be said that the tetrahedron method did not capture well the shear stress profile along the pile length. The main reason for this low performance could be that the pile-tetrahedron system did not move as a rigid unit, and therefore the stresses generated from the tetrahedron were not representative of the pile stresses. Further tests are suggested in order to evaluate the performance of tetrahedra built with different material and technique. The possibility of 3D printed tetrahedra should be explored in order to avoid the tetrahedron to break and to allow a more precise construction.

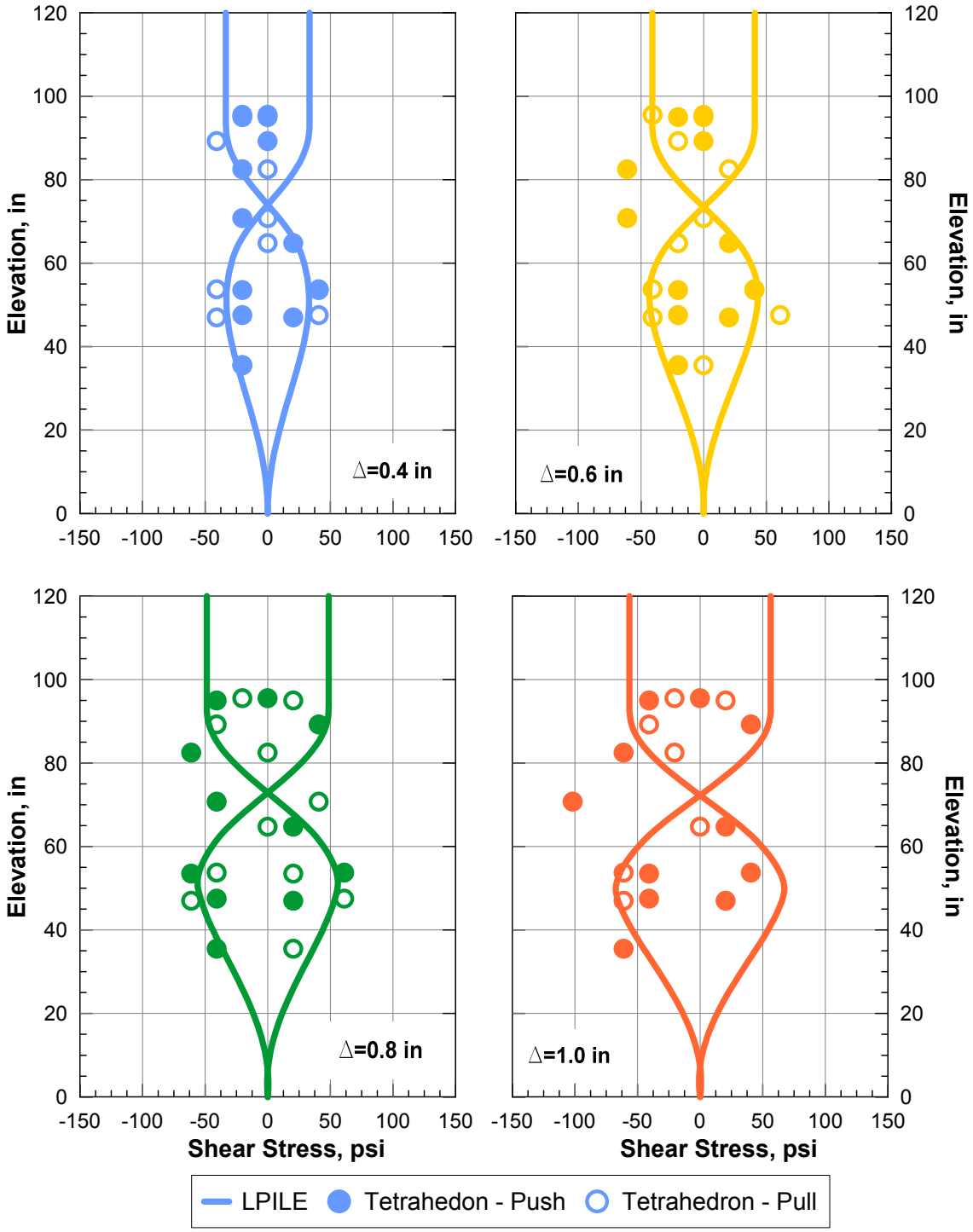

Figure 4.14: Pile *1*: Comparison between shear stress calculated from LPILE and the τ_{xy} shear component derived from selected tetrahedra.

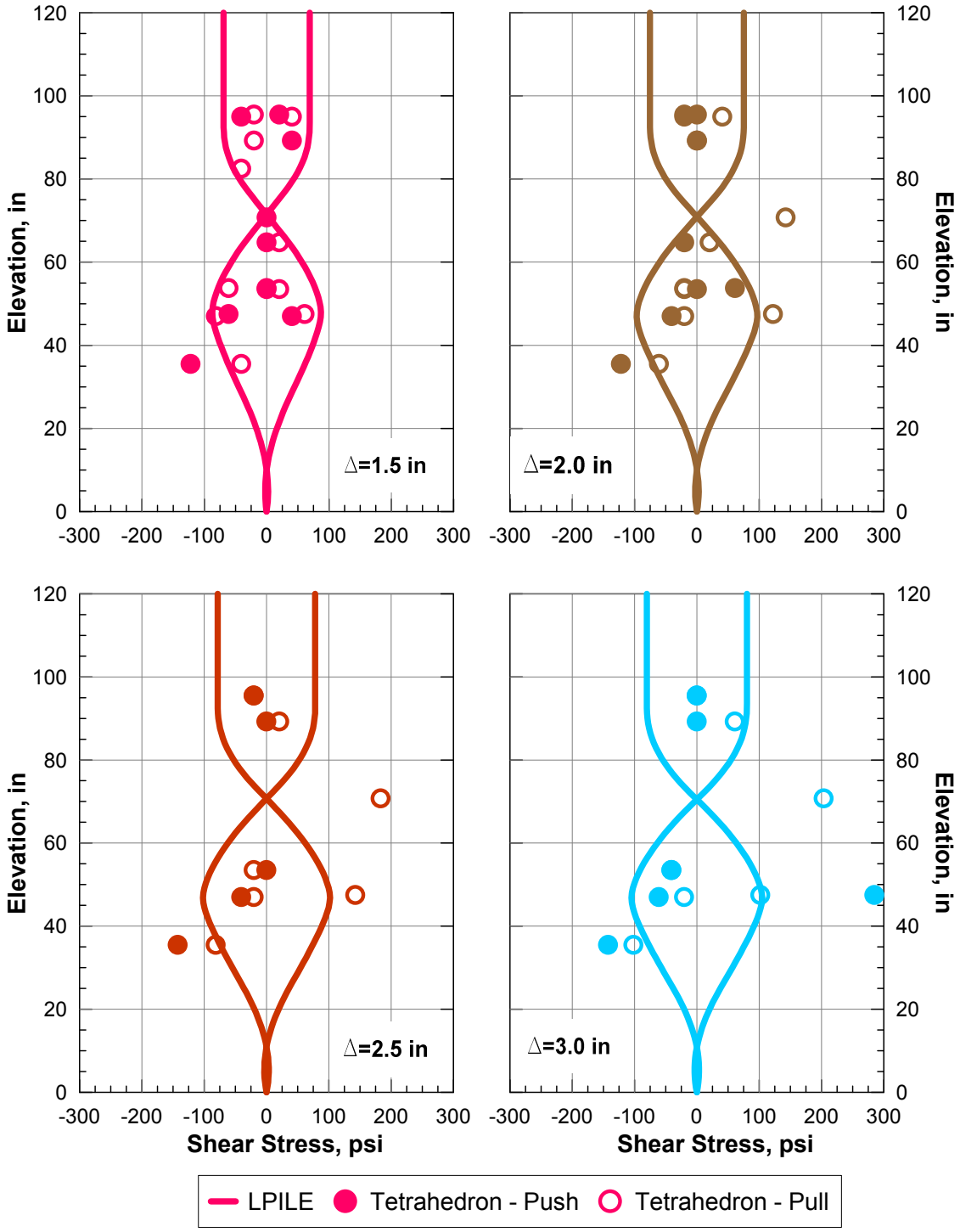

Figure 4.14: Pile *1*: Comparison between shear stress calculated from LPILE and the τ_{xy} shear component derived from selected tetrahedra (cont.).

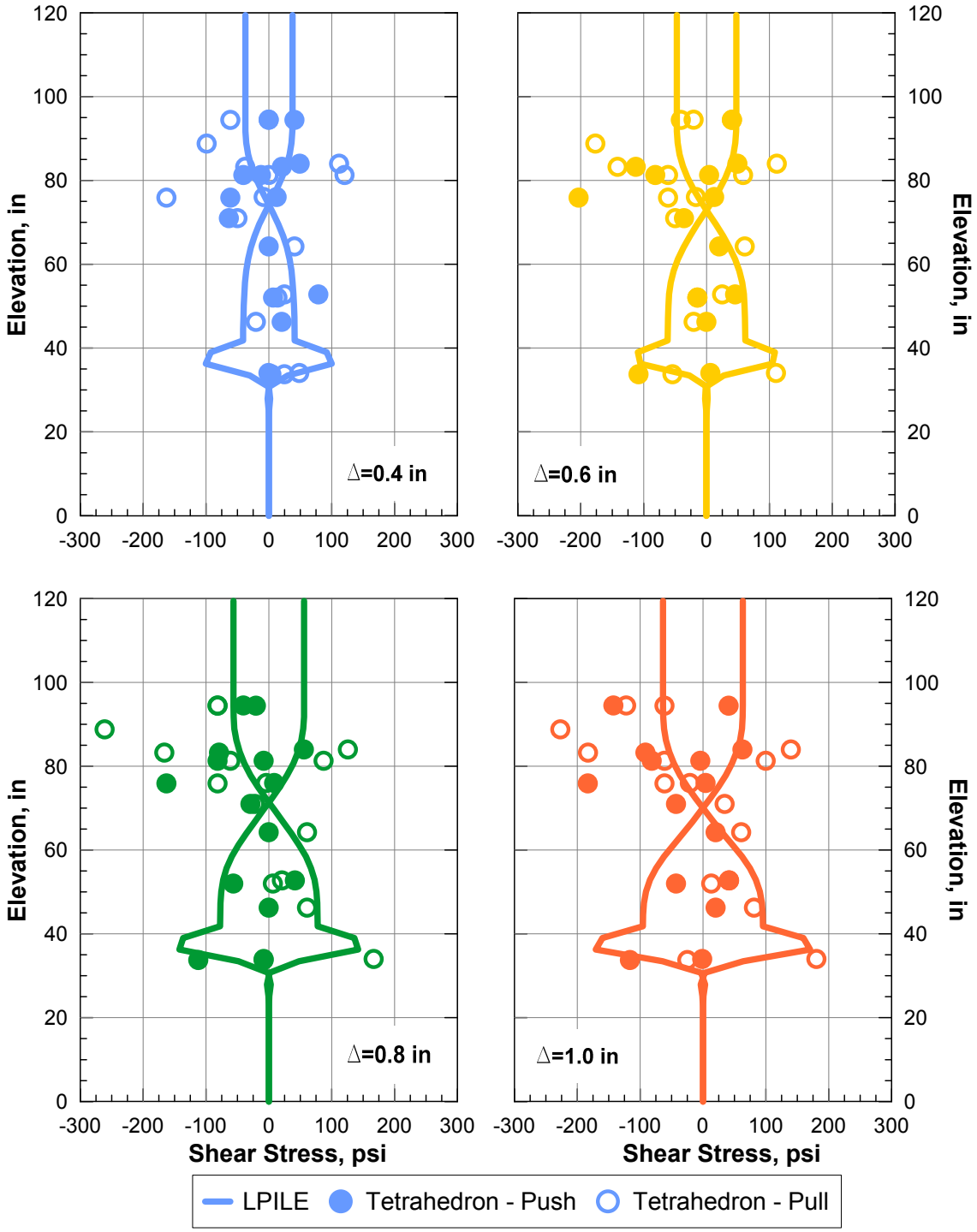

Figure 4.15: Pile *4*: Comparison between shear stress calculated from LPILE and the τ_{xy} shear component derived from selected tetrahedra.

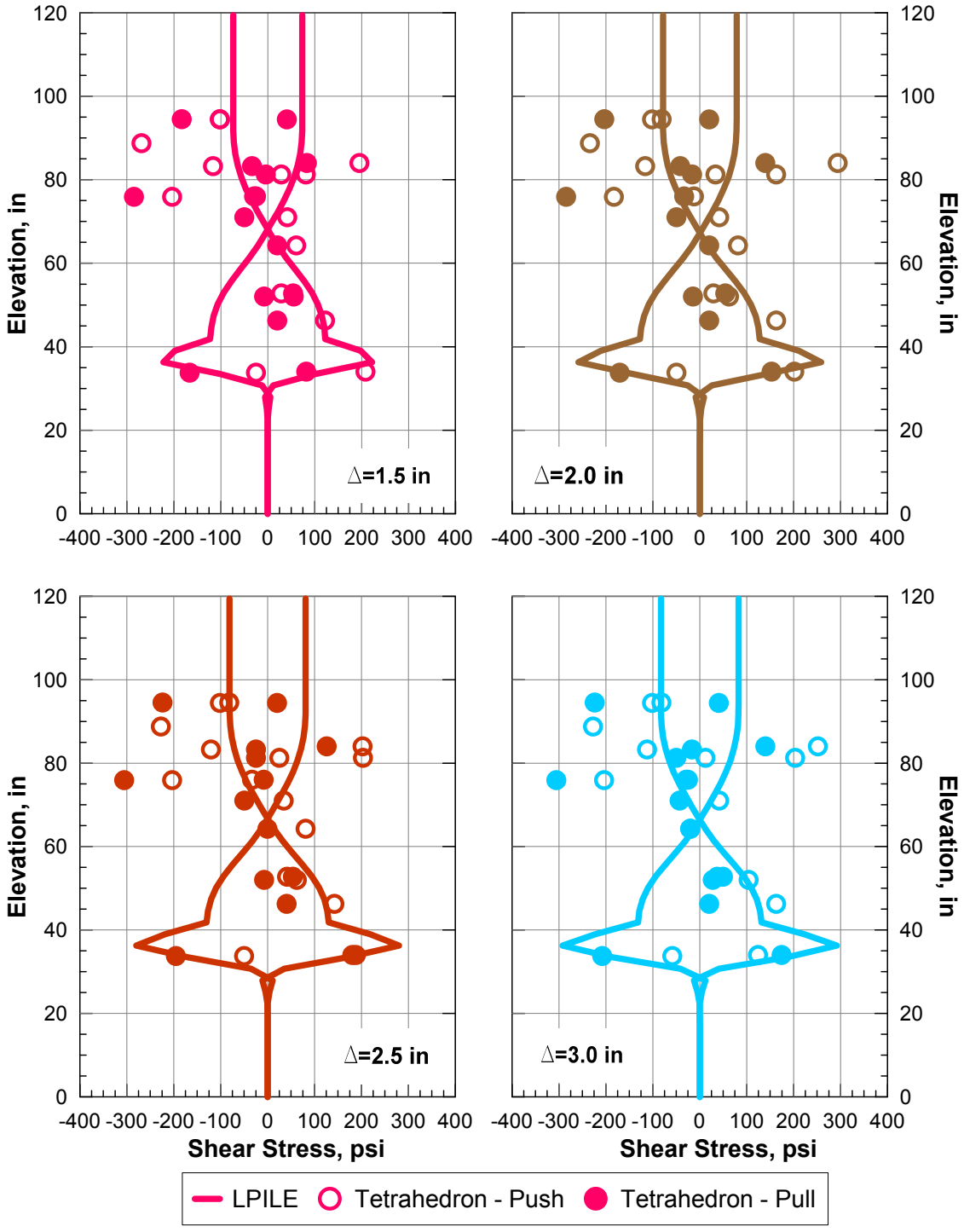

Figure 4.15: Pile *4*: Comparison between shear stress calculated from LPILE and the τ_{xy} shear component derived from selected tetrahedra (cont.).

4.5.2 External Stran Gauges

Rectangular rosettes were attached on the shear sides (North and South) of Pile *1* and *4*. It is possible to determine 2D strains from three strain readings as follows:

$$\varepsilon_a = \varepsilon_x \cos^2\theta_a + \varepsilon_y \sin^2\theta_a + \gamma_{xy} \sin\theta_a \cos\theta_a \tag{4.9a}$$

$$\varepsilon_b = \varepsilon_x \cos^2\theta_b + \varepsilon_y \sin^2\theta_b + \gamma_{xy} \sin\theta_b \cos\theta_b \tag{4.9b}$$

$$\varepsilon_c = \varepsilon_x \cos^2\theta_c + \varepsilon_y \sin^2\theta_c + \gamma_{xy} \sin\theta_c \cos\theta_c \tag{4.9c}$$

Each of the three strain component can be expressed as a linear function of the three stress components using Hooke' s law as follows:

$$\begin{bmatrix} \sigma_x \\ \sigma_y \\ \tau_{xy} \end{bmatrix} = \frac{E}{(1-\upsilon^2)} \begin{bmatrix} 1 & \nu & 0 \\ \nu & 1 & 0 \\ 0 & 0 & \frac{(1-\nu)}{2} \end{bmatrix} \begin{bmatrix} \varepsilon_x \\ \varepsilon_y \\ \gamma_{xy} \end{bmatrix} \tag{4.10}$$

Considerations about the coordinate system need to be done also in the case of the rectangular rosette, in order to have all the measurements in the same global coordinate system, and allow comparisons. The disposition of the south and north rectangular rosettes is represented in Fig. 4.16 with respect to the global coordinate system (x, y, z). Strain gauges a and c lie on the y and z axis, respectively. The x axis is perpendicular to the the plane yz.

In the south set of rectangular rosettes, the gauges, labeled as a, b, and c, are 45° degree apart and their orientations is given as follows: Therefore Eq. 4.9 becomes, with respect to

$$\theta_a = \text{- } 180° \qquad \theta_b = \theta_a \text{ - } 45° \qquad \theta_c = \theta_a \text{ - } 90°$$

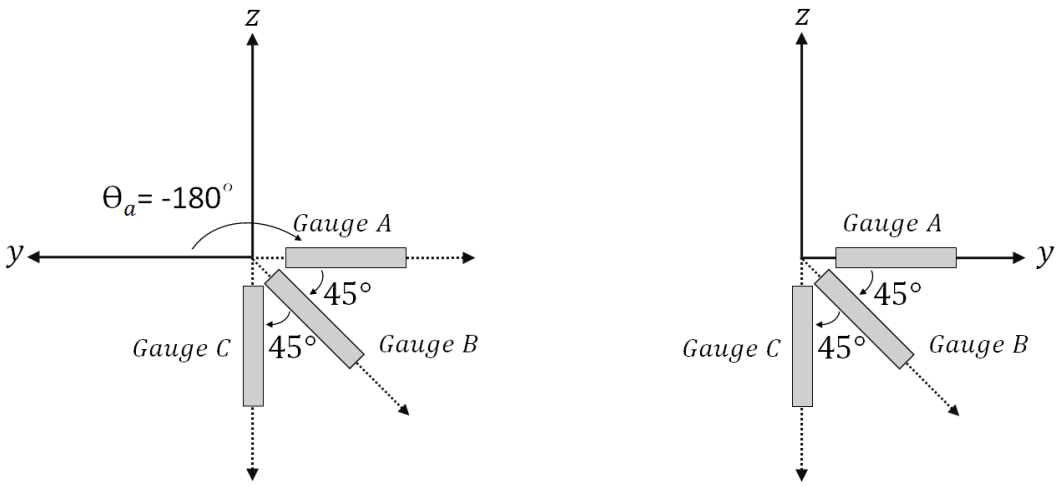

(a) South side (b) North side

Figure 4.16: Rectangular rosette disposition with respect to the global coordinate system (x, y, z).

the global reference system yz:

$$\varepsilon_a = \varepsilon_y \tag{4.11a}$$

$$\varepsilon_b = \frac{1}{2}\varepsilon_y + \frac{1}{2}\varepsilon_z - \frac{1}{2}\gamma_{yz} \tag{4.11b}$$

$$\varepsilon_c = \varepsilon_z \tag{4.11c}$$

In the north set of rectangular rosettes, the orientation of the three gauges is given by: In

$$\theta_a = 0 \qquad \theta_b = \text{- } 45^\circ \qquad \theta_c = \text{- } 90^\circ$$

this case, Eq. 4.9 becomes as Eq. 4.11.

Each of the three strain component can be expressed as a linear function of the three stress components using Hooke' s law as follows:

$$\begin{bmatrix} \sigma_y \\ \sigma_z \\ \tau_{yz} \end{bmatrix} = \frac{E}{(1-\upsilon^2)} \begin{bmatrix} 1 & \nu & 0 \\ \nu & 1 & 0 \\ 0 & 0 & \frac{(1-\nu)}{2} \end{bmatrix} \begin{bmatrix} \varepsilon_y \\ \varepsilon_z \\ \gamma_{yz} \end{bmatrix} \tag{4.12}$$

In particular, the shear component (τ_{yz}) is representative of the shear friction developed at the two sides of the pile during the test.

8 in Polymer Concrete Pile with Steel Reinforcement

This section discusses the 2D state of strain and stress, calculated from the four rectangular rosettes attached on the outside surface of Pile *1*. The rosettes were installed in the pile shear sides at different elevations, as shown in Fig. 3.23.

Figures 4.17 and 4.18 show the 2D strains and stresses obtained from the North rosettes attached on Pile *1*' s surface as function of pile deflection. Since strains and stresses were directly derived from the strain gauges readings, once the sensors begin to give unrealistic results, the readings were discarded. For this reason, stresses and strains are not always available for all deflection levels.

The shear component τ_{yz} obtained from the external rosette is representative of the friction developed at the sides of the pile when it is laterally loaded. Fig. 4.19 shows the friction values obtained from the external strain gauges (τ_{yz}), and the tetrahedra (t_y) at four different depths on the North and South sides of the pile. The depths annotated in Fig. 4.19 represent the location of the external strain gauges as found in Fig. 3.23; the shear friction of closest tetrahedron was used as a term of comparison. It can be seen how the friction tends to increase with the increase of pile head deflection especially at shallow depths. At bigger depths, the friction seems to be negligible.

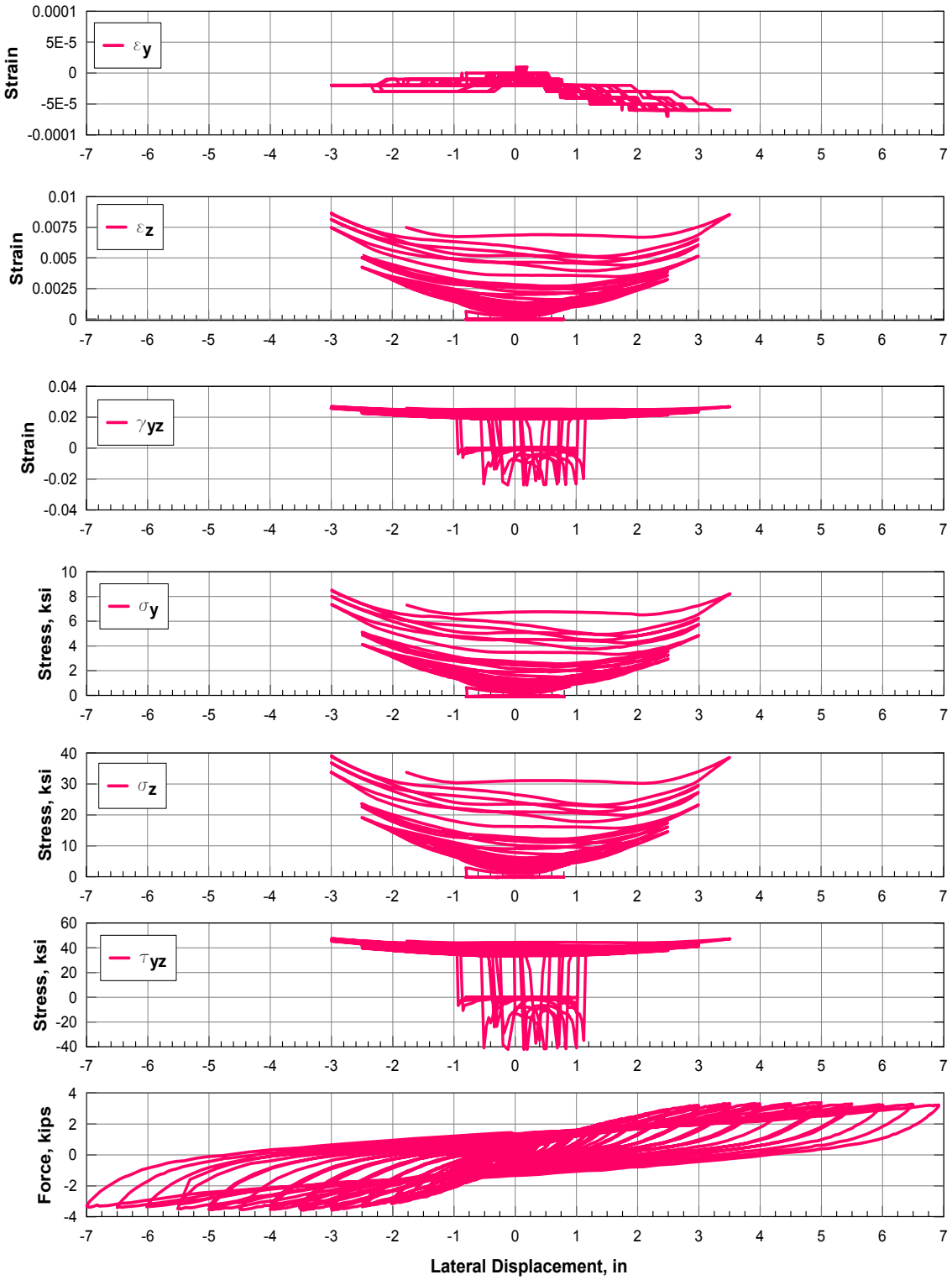

Figure 4.17: Pile 1: Strain and stresses vs. pile head displacements from external gauges located on the North side (shear direction) at the elevation of 70 1/4 in.

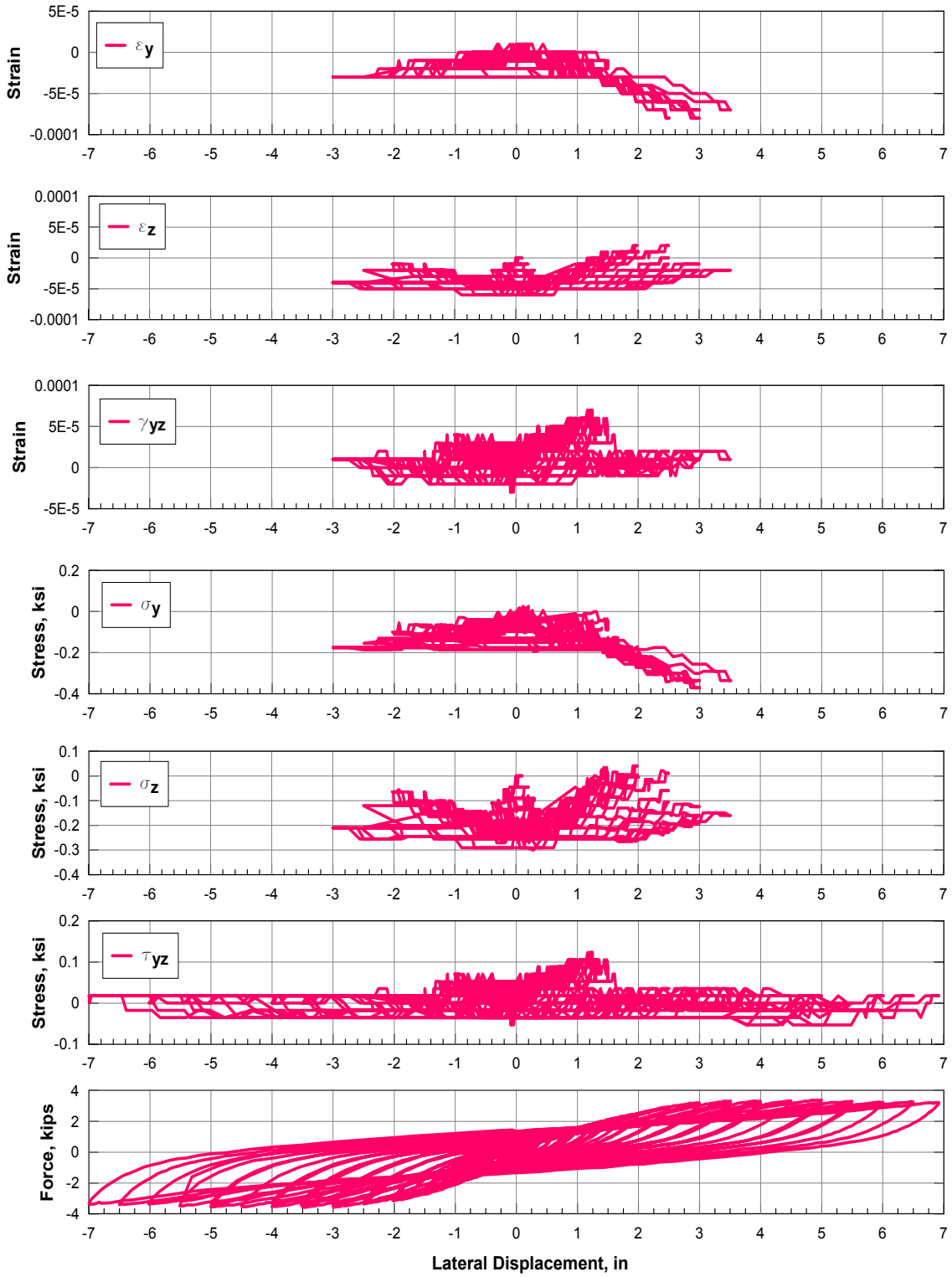

Figure 4.18: Pile 1: Strain and stresses vs. pile head displacements from external gauges located on the North side (shear direction) at the elevation of 52 1/4 in.

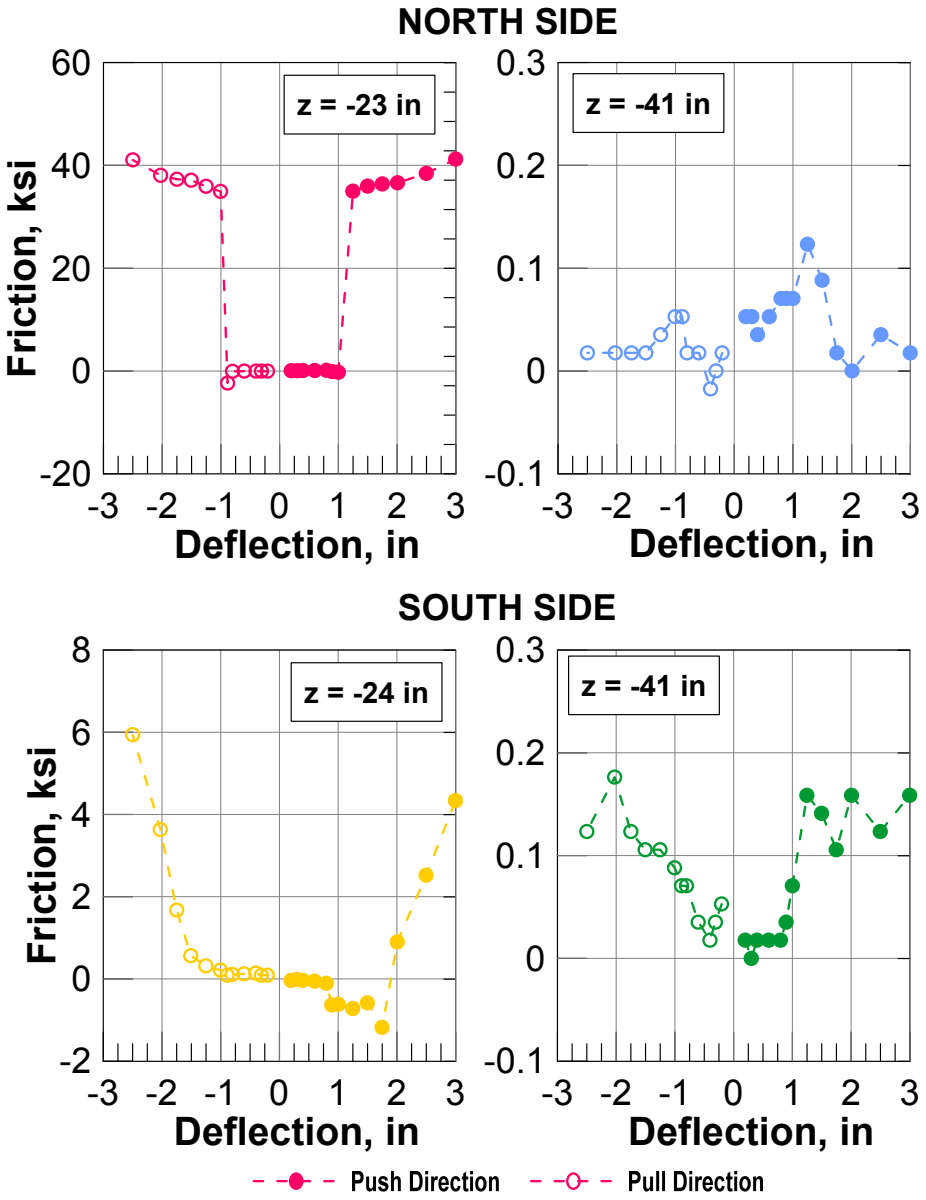

Figure 4.19: Pile 1: Friction values (τ_{yz}) obtained from external strain gauges at different depths.

10 in Polymer Concrete Pile with Steel Reinforcement

This section discusses the 2D state of strain and stress, calculated from the rectangular rosette attached on the outside surface of Pile *1*. The rosettes were installed in the pile

South shear side, as shown in Fig. 3.27.

Figure 4.20 shows the 2D strains and stresses obtained from the South rosette attached on Pile *4*' s surface as function of pile deflection.

The shear component τ_{yz} obtained from the external rosette is representative of the friction developed at the sides of the pile when it is laterally loaded. Fig. 4.21 shows the friction values obtained from the external strain gauges (τ_{yz}), and the tetrahedra (t_y) at the depth of -47 in from the soil surface. The location of the external strain gauge rosette can be reviewed in Fig. 3.27; the shear friction of closest tetrahedron was used as a term of comparison. The friction at the selected depth seems to be negligible.

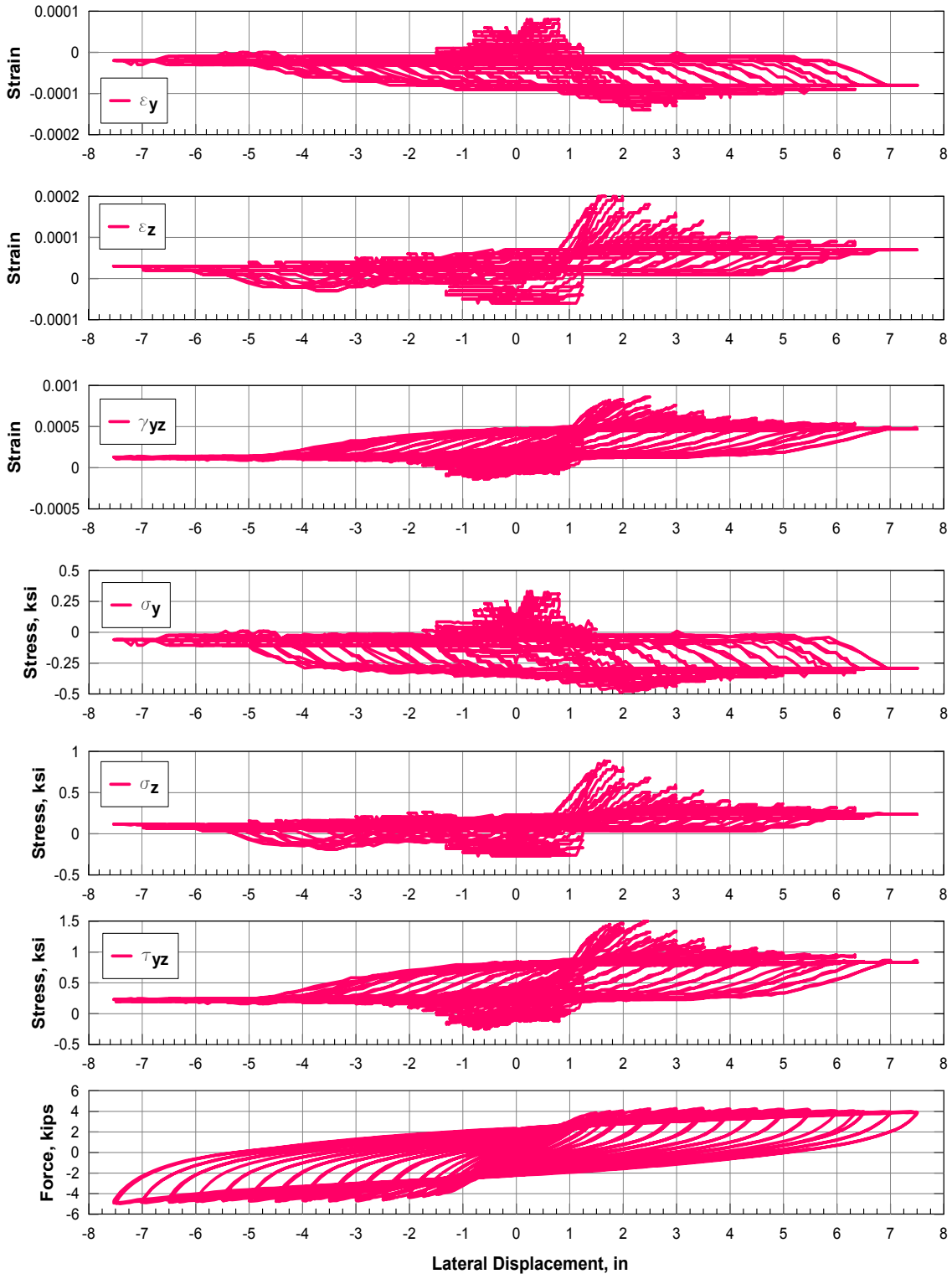

Figure 4.20: Pile 4: 3D strains and stresses vs pile head displacements.

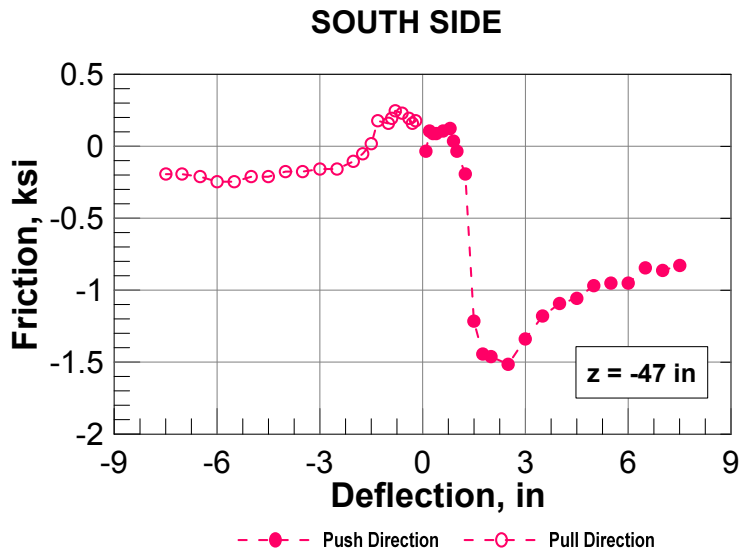

Figure 4.21: Pile 4: Friction values (τ_{yz}) obtained from external strain gauges.

Discussion of of Shear Stress Component τ_{yz}

The τ_{yz} value obtained from the external strain gauges can be compared to the y component of the external traction vector $[t]$, derived from the internal 3D state of stress of the tetrahedron. The procedure to calculate the traction vector is illustrated in Chapter 3.2.4, and in particular by the Eq. 3.7.

The results of this comparisons are presented in Fig. 4.22 and 4.23, for Pile *1* and Pile *4*, respectively.

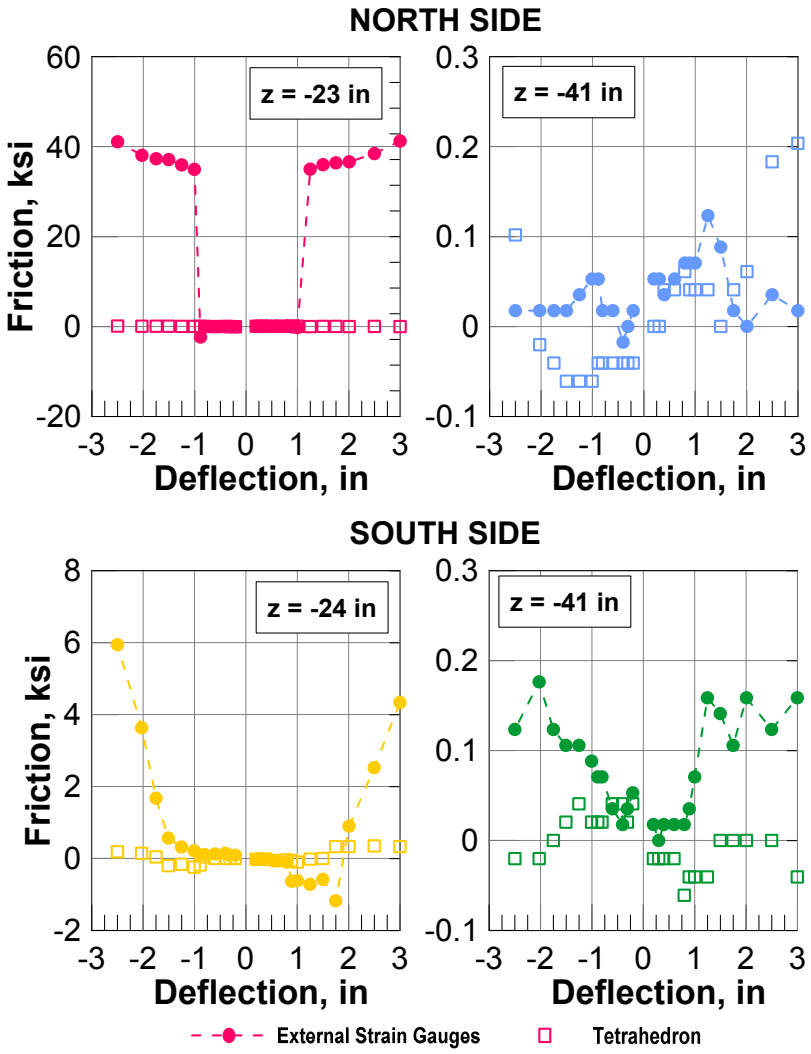

Figure 4.22: Pile *1*: Comparison among the friction values (τ_{yz}) obtained from external strain gauges and tetrahedra.

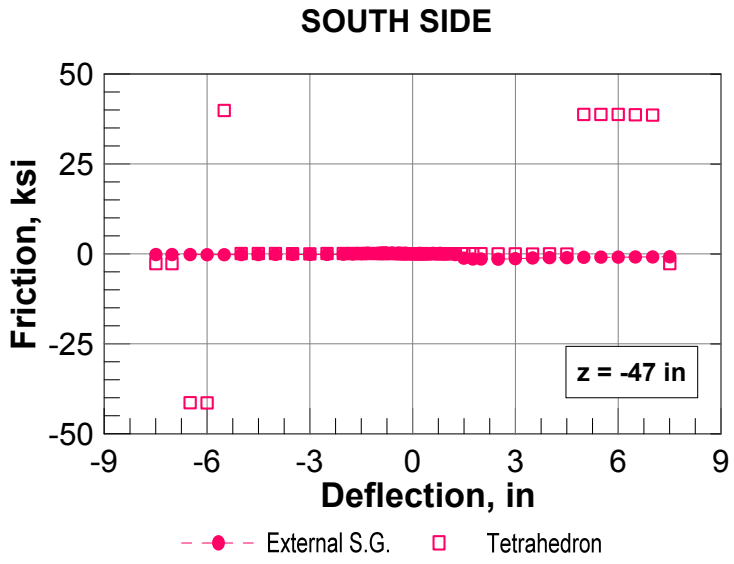

Figure 4.23: Pile *4*: Comparison among the friction values (τ_{yz}) obtained from external strain gauges and tetrahedra.

Chapter 5

Discussion on Soil-Structure Interactions

In Chapter 1 the *p-y* curve method is presented in detail, along with the review of *p-y* relationships that are widely used in the engineering practice. The importance of experimentally deriving *p-y* curves is emphasized, since traditional models may not well capture the unique characteristics of the soil-structure interactions in analysis.

Therefore, the main purpose of this Chapter is to derive realistic *p-y* curves from strain gauge readings installed on the longitudinal reinforcement in Pile *1* and Pile *4*. The data analysis process is presented in detail with challenges and proposed solutions.

5.1 Curvature and Moment Fitting Techniques

Derivations of *p-y* curves using strain gauges readings from laterally loaded pile tests require five steps:

1. Fit of the curvature experimental data obtained through strain gauges;
2. Derivation of the deflection (y) with respect to the pile depth using double integration techniques on curvature fit;
3. Determination of the moment profile along the pile depth from the curvature data by using a reliable moment- curvature relationship;
4. Fit of bending moment data;
5. Derivation of the soil resistance (p) versus the pile length through a process of double differentiation of the moment profile.

Mathematically speaking, double integration of discrete data points with respect to depth would not incur numerical errors and may tend to minimize the measurement errors of strain gauges. On the contrary, double differentiation of discrete data points results in amplification of measurement errors and consequently inaccurate soil reaction [119]. Therefore, several techniques have been proposed to minimize numerical errors due to double differentiation of the moment data, and consequently to derive more reliable p-y curves. The most used methods include:

- *Regression techniques*, such as weighted residuals method (e.g. Wilson [116]; Janoyan et al. [44]; Brandenberg et al. [14]), and smoothed residuals method (Yang et al. [120]);
- *Numerical methods*, such as B-spline functions, high order global polynomial interpolations (e.g. Reese and Welch [90]), piecewise polynomial curve fitting (e.g. Matlock and Ripperger [61]), and cubic spline fitting method (e.g. Dou and Byrne [26]); and
- A combination of the first two methods (e.g. Countinho [108]; Stewart et al. [109]).

Each method has its own advantages and disadvantages, and the choice of the fitting method is highly dependent on the data set in analysis. For example, regression techniques work best with many data points and it is applicable only when the trend of the data set can be capture. In other cases, it can be observed that a reliable fitting function for the data set should be a function fitted in piecewise. An efficient method for representing a piecewise polynomial function is by means of a spline fitting technique (e.g. B-spline). The result is a piecewise polynomial that can be infinitely integrated and differentiated. The major drawback of a spline is that it is prone to high frequency noise upon differentiation, since it fits every point exactly [116]. This was also noted in the studies conducted by Stewart et al. [109] and Lemnitzer et al. [52], where a weighted residuals and B-spline approaches were used for the curvature and moment fitting profiles. The results were found to be unstable because of the extreme sensitivity of the soil reaction profile to the subtle features of the curvature profile and the nonlinear moment-curvature relationship [47]. This instability was reflected by physically unrealistic features, such as decreasing stiffness of the p-y curve with depth [52].

Some studies attempted to evaluate the various methods used for deducing p-y curves from lateral load test data and to recommend the most robust and accurate one (e.g. Scott [103], Wilson [116], Countinho [108], Yang and Liang [119], Brandenberg et al. [14]). For example, Coutinho [108] used different degree polynomials and B-splines to fit curvature experimental values by a weighted least-squares algorithm. It was concluded that B-splines were superior to the polynomial in presence of sudden variation in the strain readings, non homogeneous soil, and nonlinear pile material. In another study, Brandenberg et al. [14] proposed a differentiation technique based on minimizing weighted residuals and compared it with the common differentiation techniques of fitting cubic splines and high-order polynomials to the moment data obtained from a centrifuge test program [15]. The weighted residuals method provided comparable performance with cubic spline fitting and both of these methods yielded better results than polynomial regression for the given moment distributions. It was also

noted that the weighted residuals method slightly outperformed the cubic spline method when differentiating noisy data at small sampling intervals because of the smoothing effect of the weak form of the weighted residuals equation.

There is not a universally applicable method currently available since each study proposed methods that worked best with a specific data set. This is due to the high sensitivity of the interpreted p-y curves to even small errors in strain gauge readings [119].

This research explores different interpolation techniques to apply to the curvature and bending moment data obtained from the lateral load tests on Pile *1* and Pile *4*. An optimization technique on independent fitting parameters was implemented in a genetic algorithm framework with the objective to facilitate data interpretation even in presence of disturbed data readings and pile nonlinearity. Hyper parameter optimization is a machine learning technique for selecting independent model parameters (e.g. knots locations, weights, function degree, and smoothing factor), based on an objective fitness function. This has been traditionally left out to the user. Stewart et al. [109] attempted a one dimensional version of this technique in order to choose the optimum location of the interior knot. The least-squares composite error term was calculated for multiple locations, and the knot was set at the location with the smallest value. The use of a genetic algorithm framework will allow to take into consideration many more variables as well as to reduce initial assumptions regarding the data set in analysis.

5.1.1 Genetic Algorithm

This research presents a generic framework for fitting experimental curvature and moment measurements through minimization of an objective function. The framework uses a genetic programming algorithm (GA), which is evolutionary search, or optimization, method that is based on the principles of genetics and natural selection [35]. GA was first introduced by

Holland [46], and later developed by Goldberg [35]. This stochastic optimization algorithm selects fitter individuals among a population based on the principle of "survival of the fittest." After generations of reproducing and selecting better individuals, the search is guided based on probabilistic rules toward a region of the search space with likely improvement.

A genetic algorithm normally comprises six parts, as shown in Fig. 5.1:

1. *Generation of a random population*: The design variables are coded into random strings.

2. *Evaluation of the fitness of each solution string*: An objective function is used to measure the accuracy of each fitting.

3. *Selection*: In the reproduction process, individuals with higher fitness value have a higher probability of being selected and producing offspring in the next generation. At each iteration, the algorithm evaluates each string by fitting a spline and returning a resulting score from the objective function. The top 10% of parameter strings are selected by score and used to generate the next population of strings.

4. *Crossover*: It is a major genetic operator that produces new designs in the optimization process. Two individual strings chosen from the mating pool are combined to form a new design in the search space.

5. *Mutation*: Each new string in the next population is a random sample of the best scored strings where each position in the string has a given probability of mutation. A mutation is defined as a random change in an input.

6. *Termination*: The search algorithm concludes when the change in the average fitness for the next population falls under a preselected threshold.

The GA' s parameters used in this study are presented in Table 5.1. They include the following: population size, mutation rate, which represents the probability that a random

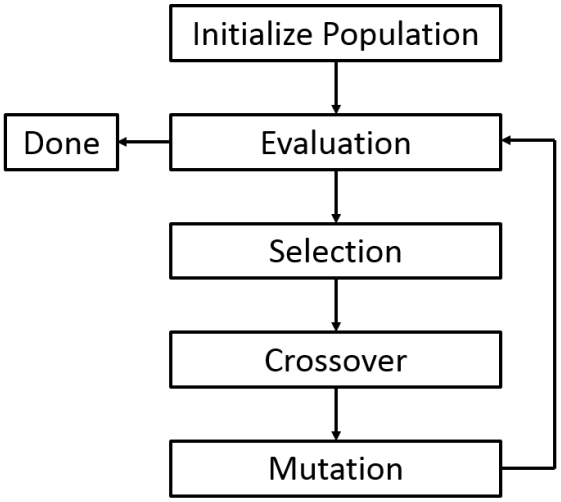

Figure 5.1: Genetic algorithm flow chart.

change occurs at each location, crossover, which is the probability of selecting a random spot in two strings and swapping all data beyond that point between the two strings, and stopping criteria, or tolerance. Mutation rate and crossover are two genetic operators that ensure genetic diversity from one generation of a population to the next one.

Table 5.1: Genetic algorithm's parameters.

Pile Specimens	**1**	**4**
Population Size	200	200
Mutation Rate	0.05	0.05
Crossover	0.7	0.7
Stopping Criteria	0.01	0.01

Geotechnical Applications

Genetic algorithms and, more in general, machine learning (ML) have been applied successfully to many geotechnical engineering problems. Examples of available ML techniques are artificial neural networks (ANNs), genetic programming, evolutionary polynomial regres-

sion, support vector machines, M5 model trees, and k-nearest neighbors [30]. These ML techniques were used to predict and model the behavior of pile foundations, including the ultimate bearing capacity (e.g. Goh [34], Goh et al. [33], Shahin [104]), settlement estimation (e.g. Nawari et al. [73], Nejad et al. [74]), and load-settlement response (e.g. Shahin [105], Ismail and Jeng [42], Alkroosh and Nikraz [6]).

From these studies it can be observed that ML has been used mostly for the prediction of load carrying capacity of vertical piles, while there are very few studies that regard laterally loaded piles. Ahangar-Asr et al. [3] and Das and Basudhar [25] used ANNs to predict lateral load capacity and then compared it to the analytical results from limit state models (e.g. Hansen and Christensen [36], and Broms [18] and [19]). Xue et al. [118] applied a GA to determine p-y curves in sand. However, their approach doesn't follow the traditional double differentiation of the bending moment profile to derive the soil reaction, since their starting point is the assumption that the soil reaction can be fit by a fourth order polynomial equation. The difference between measured and predicted moment was then minimize trough an optimization technique.

While more modern machine learning methods, such as ANNs, were initially used to derive for curvature and moment functions from strain gauge readings, they were disregarded for this application since they cannot be represented as a continuous and infinity differentiable function. Each neural network is stochastically constructed from many linear combinations of inputs with a hyperbolic transfer function. Local behavior of these functions does not consistently follow smooth trajectories and the resulting numerical differentiation amplifies this effect.

Proposed Implementation

Different GA procedures were attempted before finding the one that was able to reach satisfactory results, which meant physically realistic p-y curves. Hereafter, a brief discussion on previously attempted methods will precede the presentation of the proposed implementation, in order to give a better overview of the different challenges affecting the experimental derivation of p-y curves.

In previous analyses, the GA was producing a population of strings, which were random combinations of the input values of the chosen curvature/moment fitting techniques (e.g. B-Spline and the least square error methods). The GA was evaluating the curvature and moment fitted profiles based on a "penalty" function that was penalizing those profiles that did not meet the top boundary conditions, had many local extrema, and a residual higher than the prescribed limit. Lower penalty value meant higher fitness of the fitted profile and more probability of being selected for p-y generation. An example of objective penalty function is expressed as follows:

$$\phi_i = \sum_{j=1}^{m} \phi_{i,j}^{e} + \phi_i^{b} + \phi_i^{s} \tag{5.1}$$

where $\phi_{i,j}^{e}$ is the penalty value assigned to the mean squared error (MSE) between interpolated values and observed measurements along the pile depth; ϕ_i^{b} is the penalty value assigned to the error between the top boundary conditions and the values obtained from the fitting profiles; and ϕ_i^{s} is the smoothing value that penalizes polynomial fitting with many local extrema. These values are measured at the i- deflection and the j-data point. The penalty values for these constraints are defined, respectively, using bilinear functions as:

$$\phi_{i,j}^{e} = \begin{cases} 0, & \text{if } r_{i,j}^{e} \leq 1 \\ k_1 r_{i,j}^{e}, & \text{otherwise} \end{cases} \quad \phi_i^{b} = \begin{cases} 0, & \text{if } r_i^{b} \leq 1 \\ k_2 r_i^{b}, & \text{otherwise} \end{cases} \quad \phi_i^{s} = \begin{cases} 0, & \text{if } r_i^{s} \leq 1 \\ k_3 r_i^{s}, & \text{otherwise} \end{cases} \tag{5.2}$$

where k_1, k_2, and k_3 are the weighting factors that measure the importance of the corresponding type of constraints, while r is normalized error with respect to its corresponding limit:

$$r^e_{i,j} = \frac{MSE_{i,j}}{MSE_{all}} \quad r^b_i = \frac{BCE_i}{BCE_{all}} \quad r^s_i = \frac{NE}{NE_{all}} \tag{5.3}$$

where MSE_{all}, BCE_{all}, and NE_{all} are the maximum allowable errors related to the data fit, boundary conditions, and maximum number of extrema in the polynomial fitting profile, respectively.

Based on the penalty function, the GA was then selecting the best fitting of curvature and moment data. Double integration and double differentiation of the two profiles were resulting in deflection and soil reaction profiles, which were assembled to form p-y curves. These two iterative processes are summarized in Fig. 5.2.

This approach was disregarded in the successive analyses because the p-y curves derived from the GA pile responses were not completely satisfactory. The major shortcomings of this GA approach were:

1. While the p-y initial stiffness was generally increasing with depth, the ultimate soil capacity was not. Moreover, it was decreasing with the increase of pile deflection. This behavior could be only explained with a not appropriate data fitting, since sands tend to reach a maximum value of ultimate capacity and hold on it as the pile deflection increases.

2. The penalty function presented in Eq. 5.1 was not affecting the curvature and moment data fitting in such a way that the GA was always able to narrow down a singular and stable solution (e.g. many local extrema).

3. Finally, the GA was finding the best curvature and moment fitting considering only

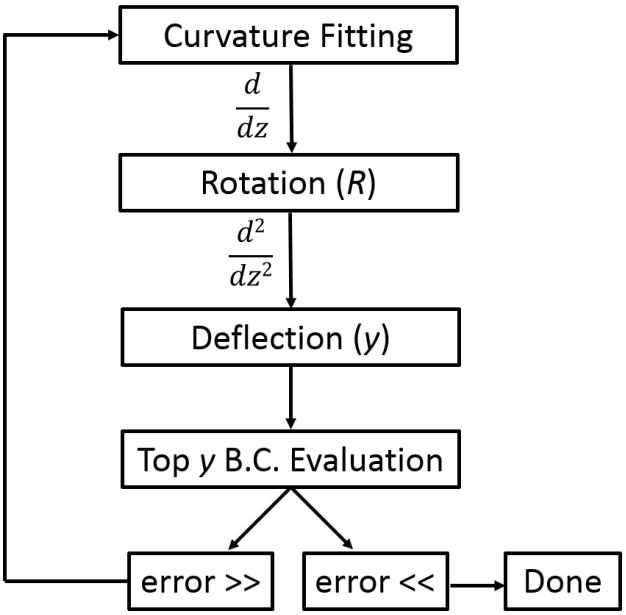

(a) Double integration

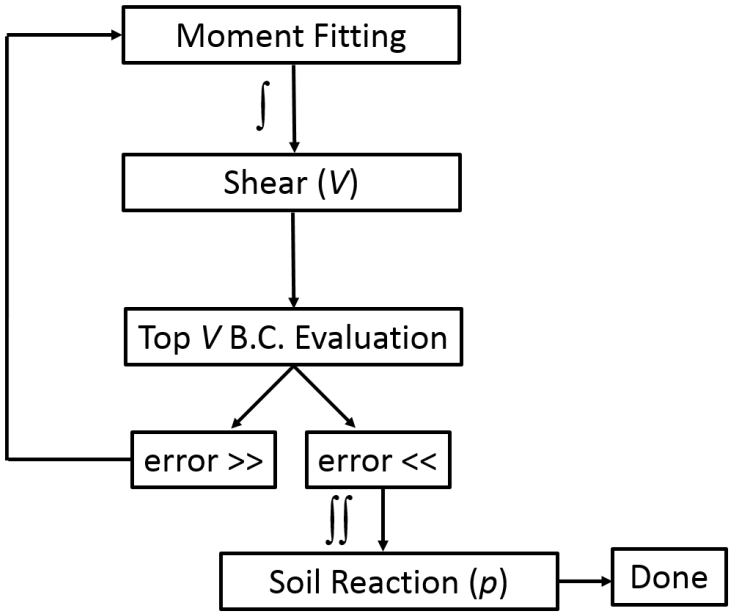

(b) Double differentiation

Figure 5.2: Iterative fitting process of curvature and moment data in GA previous versions.

experimental data and top boundary conditions relative to the pile deflection and shear. The GA did not include in the evaluation of strings' fitness the accuracy of physically realistic *p-y* curves, ultimate goal of the analysis.

Based on the aforementioned lessons, it was evident that the new GA needed to target directly the *p-y* curves with a fitness function able to evaluate their accuracy. Another change that was introduced in the new GA was the choice of the fitting technique as a variable in the population string and not anymore as an *a priori* decision. This new approach will allow to generate *p-y* curves from an *ensemble* of different statistical methods. In this way, the GA ensures the best solution across many variables and methods, and it can be extended to any data set since it is not dependent on the choice of fitting technique.

The new GA process to select the best suite of *p-y* curves is shown in Fig. 5.3 and it is described hereafter. The GA starting point is the generation of 200 strings (chosen population size); each of them represents as many random combinations of input parameters for the curvature and moment fitting as the number of deflections. For both Piles *1* and *4*, the total deflections taken into considerations were 26 (13 positive and 13 negative deflections), ranging from +/- 0.2 in to +/- 2.0 in. Note that the analyses of positive and negative deflections were done separately, since the pile behavior in the two directions was slightly different. Eq. 5.4 represents a typical string, which includes the GA input parameters as follows:

$$\text{GA}= [w_{c1}\ t_{c1}\ k_{c1}\ s_{c1}\ F_{c1}\ w_{m1}\ t_{m1}\ k_{m1}\ s_{m1}\ F_{m1},\ldots,\ w_{ci}\ t_{ci}\ k_{ci}\ s_{ci}\ F_{ci}\ w_{mi}\ t_{mi}\ k_{mi}\ s_{mi}\ F_{mi}] \tag{5.4}$$

where c and m stand for curvature and moment at the $-i^{th}$ deflection, which ranges from 1 to 13; w is data point weight vector; $t = [N_1, N_2, N_3]$ is a three interior knots vector; k is the

degree vector, whose values can be picked among the [2, 3, 4, 5] interval; s is the smoothing factor whose value can range from 0 to 1; and F is the fitting function on the curvature and moment data, which includes the univariate, least square, and B-Spline methods. This methods are presented in Chapters 5.1.2 and 5.1.3.

The first generation of strings is then double integrated and differentiated to obtain a series of p-y curves at various pile depths. The p-y points for a given input string need to be monotonic increasing. This means that an increase of soil reaction corresponds an increase of deflection. If this condition is not met, the string is penalized in such a way that won't be considered any further.

After p-y curves' assemble, the data points need to be fitted. The chosen fitted function was a sigmoid, which is a bounded, differentiable, and real. More details about the fitting of the p-y curves are presented in Chapter 5.5.1.

A condition of depth dependency among curves at different pile depths was taken into consideration. However, it was not eventually implemented in the GA since it was a condition impossible to achieve along the entire length of the pile, given the typical oscillatory behavior of the soil reaction profile. At every inflection point of the p function, the soil reaction relationship with depth is reversed from the previous one.

The fitness function evaluates explained variance between the raw and fitted p-y curves values and it is represented by the minimization of the following score function:

$$Score = \sum_{z=1}^{m} EV_z \tag{5.5}$$

where EV_z is the explained variance, and z is the number of depths considered in the analysis.

The interpolation methods implemented in the optimization are presented in Chapters 5.1.2 and 5.1.3.

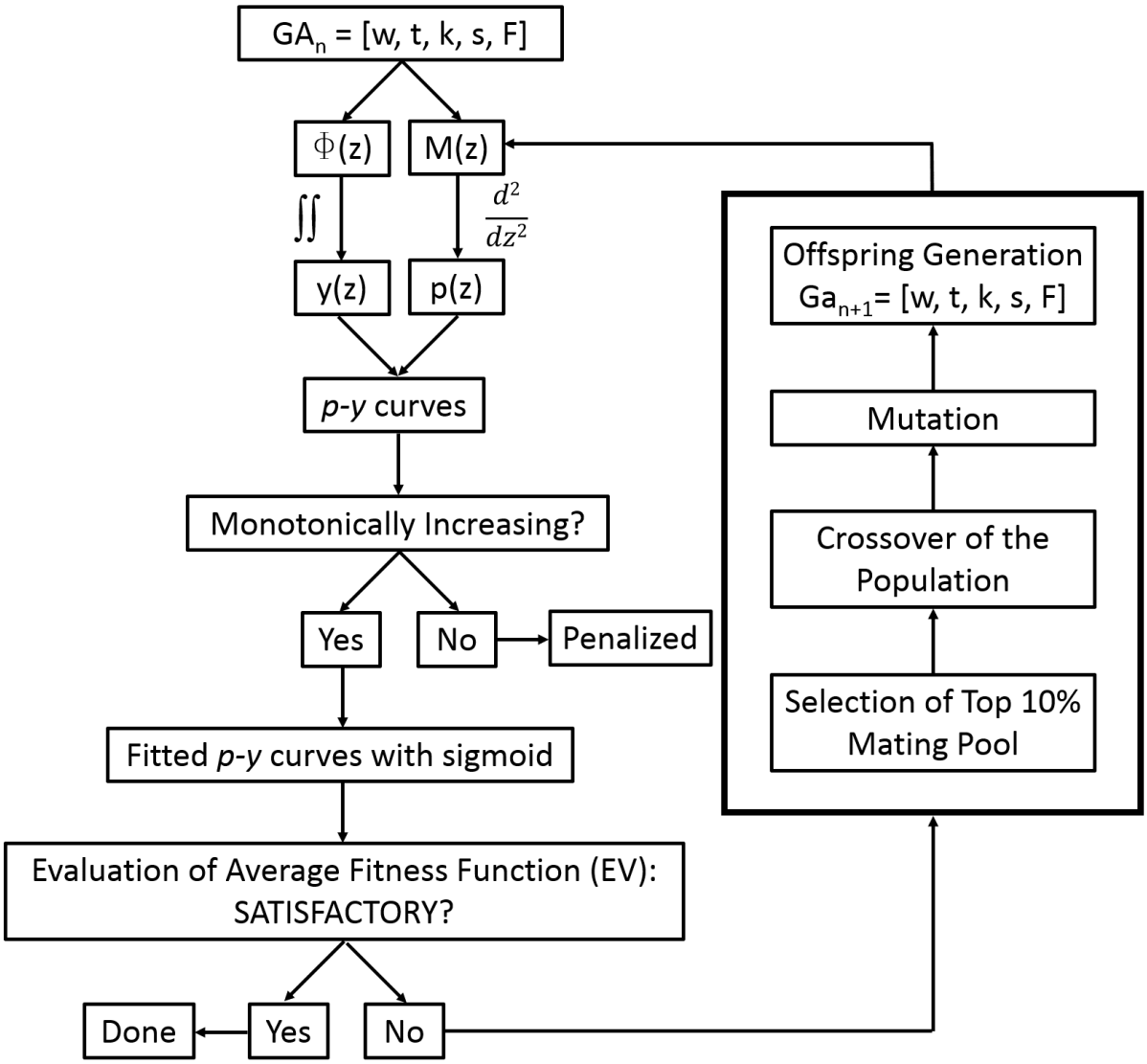

Figure 5.3: Improved GA's process.

5.1.2 Least Squared Error Interpolation Method

Wilson et al. [116] and Brandenberg et al. [14] used a differentiation technique based on minimizing wighted residuals to fit the moment data and to compute the load transfer between pile foundations and liquefied sand. This method was used to fit the experimental curvature and moment data with a piecewise polynomial in the following way.

The method of weighted residuals considers the function $u(x)$, and the approximation function, $a(x)$, over the interval $x \in (0, L)$, with L as the pile length. Since $u(x) \neq a(x)$, the difference $a(x) - u(x) = R(x)$ is the residual. The approximation function a(x) can be chosen such that $R(x)$ is zero in an average sense by requiring that $\int_0^L R(x) \cdot \Psi(x) dx = 0$, where $\Psi(x)$ is selected from a set of weighting functions. This is commonly referred to as saying $a(x) = u(x)$ "weakly" [11].

The pile can be discretized into finite elements with nodes at each gauge location. The function $f(z)$ represents the actual bending moment distribution of the pile as a function of depth z and its value is known at the nodes. Let $g(z) = \dfrac{d}{dz} f(z) = f'(z)$ "weakly", where $g(z)$ represents the first derivative of the bending moment distribution or the shear force distribution as a function of depth. This is written as:

$$\int [g(z) - f'(z)] \cdot \Psi(x) = 0 \tag{5.6}$$

where Ψ(x) is any arbitrary weighting function. Both $f(z)$ and $g(z)$ are written as linear combinations of basis functions of finite element type (e.g. linear "hat" functions shown in Fig. 5.4) and $\Psi(z)$ is taken to be each basis function in turn to generate a system of linear equations for the coefficients of $g(z)$:

$$f(z) = \sum_{i=0}^{n} f_i \Psi_i(z), \quad g(z) = \sum_{i=0}^{n} g_i \Psi_i(z) \tag{5.7}$$

with Ψ_i as the basis function corresponding to node i.

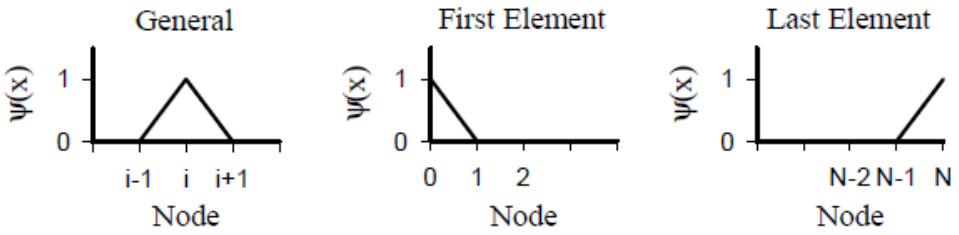

Figure 5.4: The linear basis functions used in the weighted residuals method [116].

The piecewise linear approximation $g(z)$ is then differentiated by repeating the procedure to obtain an approximation of lateral resistance as a function of depth, z. Let $h(z) = g'(z)$ "weakly", and solve for $h(z)$ using the WR derivative as previously described. Finally, since $h(z)$ is piecewise linear, the approximation to the distribution of lateral resistance $p(z)$ is obtained by sampling $h(z)$ at element midpoints.

Note the bending moment distribution $f(z)$ was approximated as piecewise linear using the basis functions $\Psi(z)$. The derivative of a piecewise linear function is discontinuous piecewise constant, and the second derivative consists of Dirac-delta singularities at the nodes and is zero elsewhere. The WR approximation to the derivative of $f(z)$, however, is piecewise linear, and can be applied a second time to obtain a piecewise linear approximation to the second derivative. Thus, this method of differentiation provides a means of obtaining, from discrete data, a derivative that has the same smoothness properties as the original WR interpolation of the data.

Implementation

The LSQ method was implemented by using standard Scipy libraries. To construct a spline composite function using least-squares criteria, the functions *UnivariateSpline* and *LSQUnivariateSpline* were used.

UnivariateSpline is a one-dimensional smoothing spline fit to a given set of data points. The smoothing factor s specifies the number of knots by specifying a smoothing condition. It is expressed in the form of:

$$\text{spline}_{UNI} = \text{UnivariateSpline}(x, y, w, k, s)$$

where x and y are the data points, w is an array of the weights at the data locations, k is the polynomial order, s is the smoothing factor.

LSQUnivariateSpline is a subclass of the previous function in which knots are user-selected instead of being set by smoothing condition. It is expressed in the form of:

$$\text{spline}_{LSQ} = \text{LSQUnivariateSpline}(x, y, t, w, k)$$

where x and y are the data points, t is an array of knots locations, w is an array of the weights at the data locations, k is the polynomial order, s is the smoothing factor. These input values were chosen through the genetic algorithm presented in Chapter 5.1.1.

5.1.3 B-Spline Interpolation Method

Stewart et al. [109] employed polynomial data fitting to formulate a least-squares fit for the curvature and moment profile, as well as known boundary conditions at ground-level and at the tip of the shaft. The piecewise polynomial function was represented by a linear combination of basis or B-splines.

To generate a composite spline from a set of B-splines, a knot sequence [u_0, u_{10},..u_m], in non-decreasing order, and a spline degree, p, must be specified. The B-splines components ($N_{i,p}$)

are generated recursively starting with the i-th degree zero B-spline:

$$N_{i,0}(u) = \begin{cases} 1 & if \quad u \in [u_i, u_{i+1}) \\ 0 & otherwise \end{cases} \tag{5.8}$$

The i-th B-spline of degree p is then:

$$N_{i,p}(u) = \frac{u - u_i}{u_{i+p} - u_i} N_{i,p-1}(u) + \frac{u_{i+p+1} - u}{u_{i+p+1} - u_{i+1}} N_{i,p-1}(u) \tag{5.9}$$

The composite spline is then defined as:

$$C(u) = \sum_{i=0}^{n} N_{i,p}(u) P_i \tag{5.10}$$

where *m+1* is the number of knots, *n=m+p+1*, and P_i are the B-spline coefficients.

The coefficients P_i are determined by solving a system of equations generated from least-square criteria [108]. The system equations are given by:

$$\frac{\partial}{\partial P_i} \sum_{j=1}^{q} [C(u_j) - \phi(u_j)]^2 w(u_j) = 0, \quad for \quad i = 0, .., n \tag{5.11}$$

where q is the number of curvature data points, $\phi(u_j)$ is the curvature data point at depth u_j, and $w(u_j)$ is the weight assigned to the data point at u_j.

Implementation

The B-Spline method was implemented by using standard Scipy libraries. To construct a B-spline composite function using least-squares criteria, the function *splrep* was used in the form of:

$$\text{spline}_B = \text{splrep}(x, y, w, k)$$

where x and y are the data points, w is an array of the weights at the data locations, and k is the polynomial order. These input values were chosen through the genetic algorithm presented in Chapter 5.1.1.

5.2 Curvature Fitting Procedure

The first step in the curvature fitting procedure is to analyze the curvature data along the pile profile for a specific pile head displacement. In Chapter 3.4, the response histories of each sensor were analyzed and it was determined the point at which the given sensor became unreliable due to malfunction or failure. The values after that point were disregarded from the analysis. Moreover, since each curvature value is the difference of two strain gauges readings, if one sensor in the pair fails, the curvature data based on that pair are useless. In both piles, the maximum deflection level considered in the *p-y* curves derivation is +/− 3 in.

Table 5.2 summarizes the top and boundary conditions of the two pile specimens, which helped guiding the curvature and moment data fitting as well as the double integration and double integration process. It can be noted that the boundary conditions are the same at the top, but they differ at the bottom to account for the bedrock's presence in Pile *4*. In Piles *1* and *4*, the top values of curvature, rotation, and deflection are known, since they were directly derived from instrumentation (e.g. strain gauges on longitudinal rebars and string pots attached to the pile). The bottom boundary conditions are different among the two specimens, because of their failure modes. Pile *1* behaved like a rigid pile and experienced tip rotation. No data are available at the pile's tip since no strain gauges were installed below the depth of -70 in. However, while no assumptions can be made on the tip rotation

and tip deflection, it is safe to assume the tip curvature equal to zero, since a rigid pile rotates but does not bend at large depths. Pile *4* bended like a flexible pile with a fixed end: curvature, rotation, and deflection are therefore zero at the pile tip.

The only boundary condition implemented in the curvature fitting process is the bottom curvature value, through the introduction of artificial points. In particular, one artificial point at the depth of -93 in was enough to enforce the zero curvature value in the case of Pile *1*, while two artificial points were used in the fitting of Pile *4*'s curvature, at the depths of -93 in and -88 in. All the other known top values were just used as validation of the results.

The curvature fits from the three techniques presented in Chapters 5.1.2 and 5.1.3 for the -2 in displacement during Pile *1* and Pile *4* tests are shown in Figs. 5.5a and 5.5b, respectively. It can be observed that the three methods yielded similar curvature fitting, and in all the three cases the GA was able to reach a relative smooth profile by neglecting outliers among the data points.

Table 5.2: Top and bottom boundary conditions considered in the curvature and moment fitting of Pile *1* and Pile *4*.

Pile Specimens	**1**		**4**	
Boundary Conditions	**Top**	**Bottom**	**Top**	**Bottom**
Curvature, ϕ	known	0	known	0
Rotation, R	known	$\neq 0$	known	0
Deflection, y	known	$\neq 0$	known	0
Moment, M	known	$\neq 0$	known	0
Shear, V	known	unknown	known	unknown
Soil Reaction, p	0	unknown	0	unknown

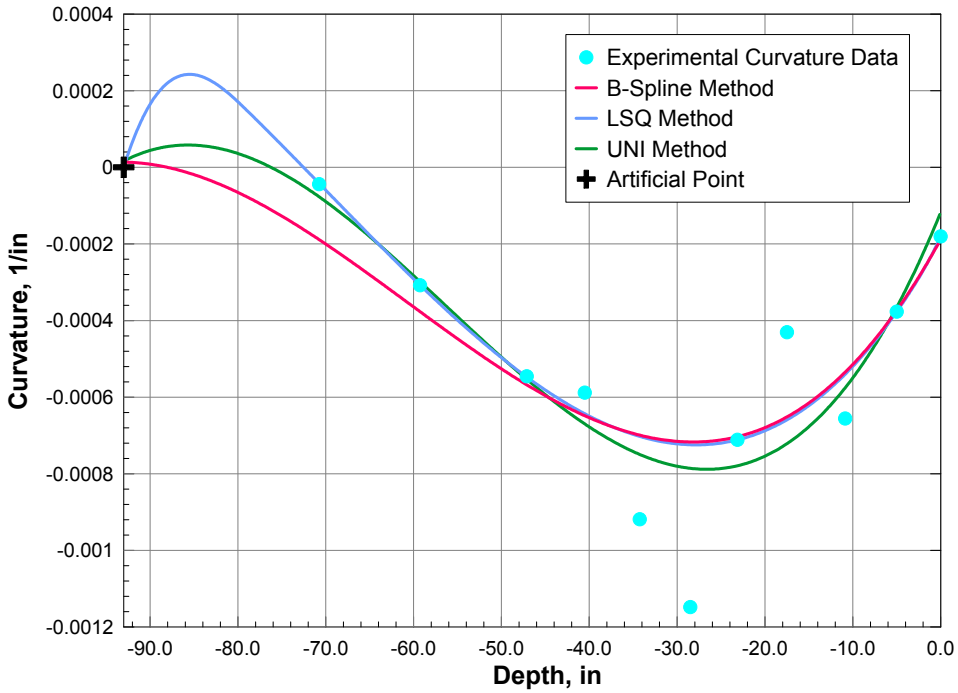

(a) Pile *1*

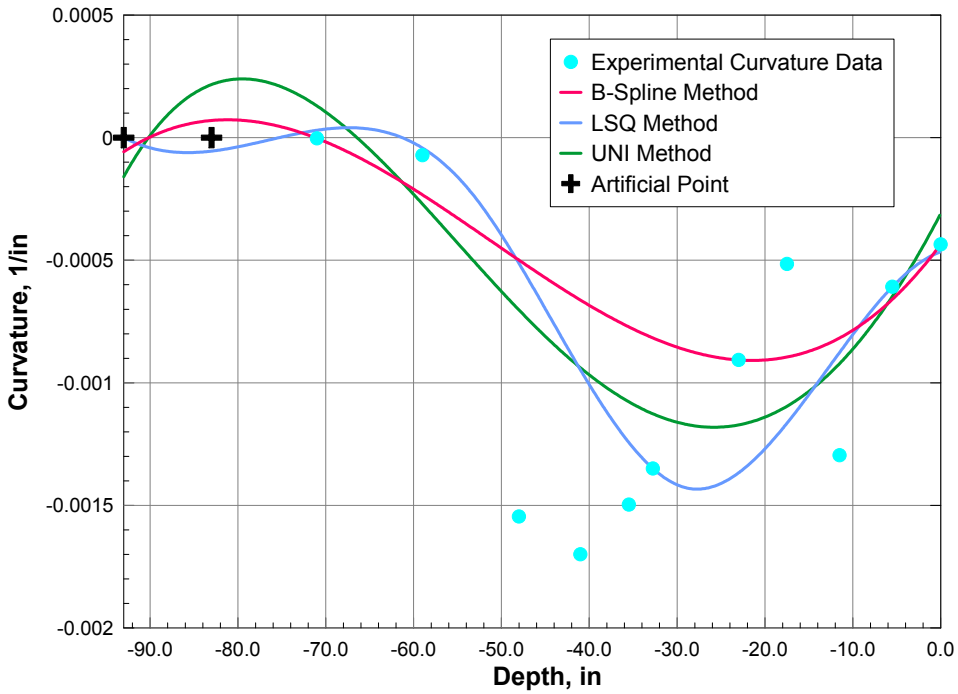

(b) Pile *4*

Figure 5.5: Spline fit of curvature data for -2 in pile head deflection: curvature vs depth.

5.3 Moment Fitting Procedure

Moment profiles must be fitted as well in order to achieve reasonable soil reaction profile from the double differentiation of the moment with respect to depth. As previously said, the differentiation process is very sensitive of any error or oscillation; for this reason a balance between desired smoothing and acceptable differentiation performance must be obtained.

Analytical moment - curvature relationships obtained from Response 2000 were used to convert curvature data into moment data. The said relationships are presented in Chapter 3.4.1 for Pile *1*, and in Chapter 3.4.4 for Pile *4*. Once curvature data are transformed into moment data using the moment-curvature relationship, the moment data are fit using similar procedures to the ones used for the curvature fitting (Chapters 5.1.2 and 5.1.3).

In regard to the boundary conditions that affected the differentiation process, bending moment, and shear have known values at the ground surface (Table 5.2). In particular, top moment and shear can be calculated using the measured forces of the actuator and distance between the load application point and the ground surface, as shown by the pile diagram presented in Fig. 5.6. The soil reaction at the ground surface is supposedly zero since the test was done in sand. However, no assumptions were made in regard to the soil reaction. The bottom boundary conditions are generally unknown for both specimens.

The two top moment boundary condition were implemented in the moment data fitting through the introduction of an artificial point. The top shear value was just used as validation of the results, as well as the top soil reaction value.

The moment fits obtained from the three proposed methods for the -2 inch displacement level during Pile *1* and Pile *4* tests are shown in Figs. 5.7a and 5.7b, respectively.

It can be observed that the moment profiles obtained from the two least square error fitting methods and the B-Spline method are very different. The B-Spline method tends to better

approximate the data points than the two LSQ methods, at the cost of an irregular profile. Vice versa, the fitted profiles obtained through the LSQ methods are generally very smooth since they neglects outliers among the data points. Among the three fitting techniques, the UNI method tends generally to yield a the smoothest profile. This different behavior may have been caused by the way the number and location of the knots were implemented. In the UNI method, the knots are specified by the smoothing conditions and the result was a polynomial function (e.g. zero knots); in the LSQ_{UNI} the knots are user selected, and in the B-Spline the knots are selected with the purpose of finding the best fit to the experimental data. Hence, the obtained profile has many local extrema that will affect negatively the moment double differentiation.

However, this explanation is only partially satisfactory, since it does not explain the fact that this type of behavior didn't seem to affect the curvature fitting. As noticed in Chapter 5.2, the fitted curvature profiles obtained from the two methods favor smoothness over data fit. The reason for this may have a computational nature. The GA tends to favor overall the least complex profile. So in the case of the curvature, the simplest B-Spline profile was reached by neglecting outliers in favor of a smoother profile, while in the case of the moment fitting, this was achieved by having a very good data fit at the cost of a smooth profile. This behavior seems to affect only the B-Spline method. The two LSQ methods seem to have a consistent behavior when fitting the curvature and moment data.

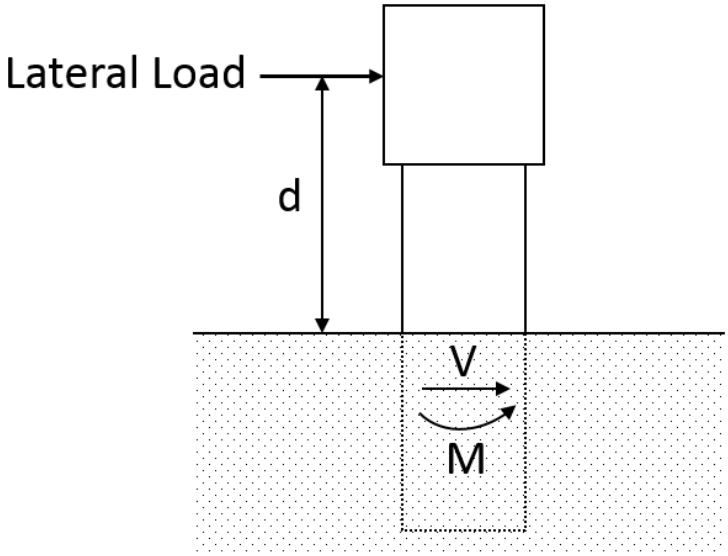

Figure 5.6: Free-body diagram of Pile *1* and *4* above the ground.

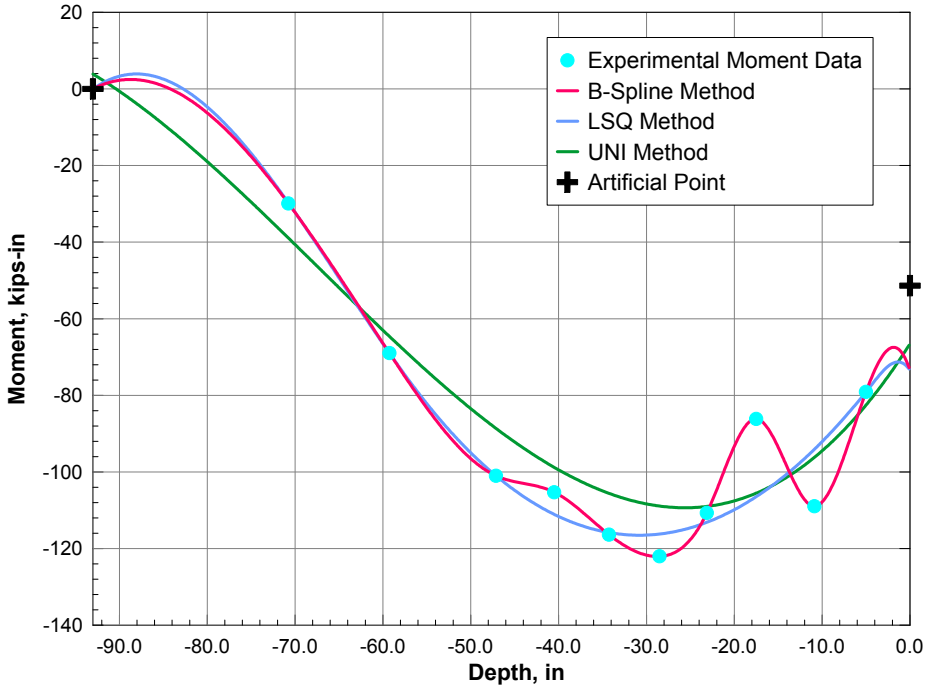

(a) Pile *1*

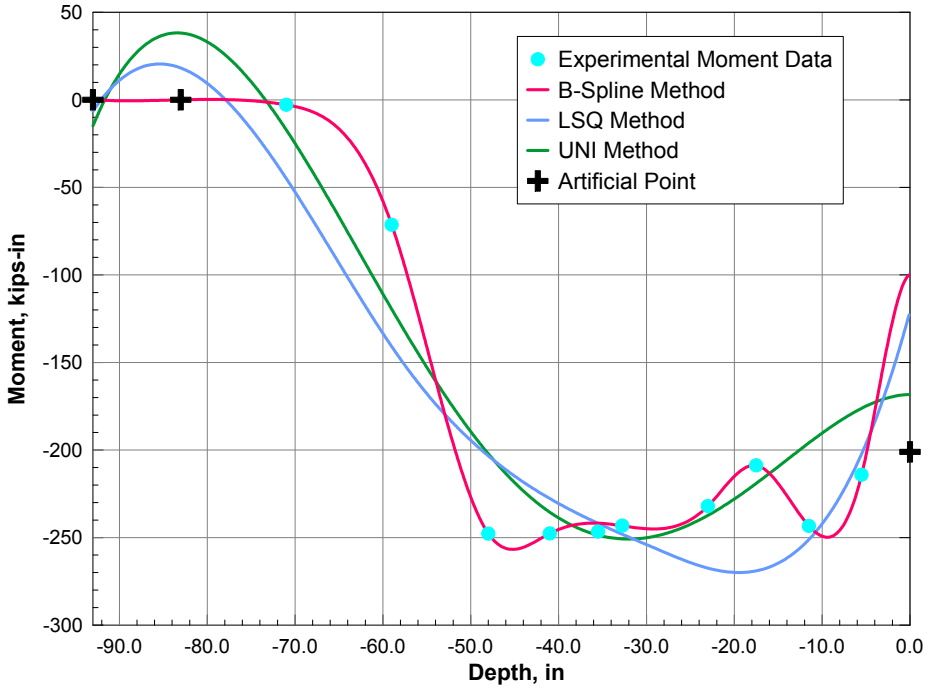

(b) Pile *4*

Figure 5.7: Polynomial fit of moment data for -2 in pile head deflection: moment vs. depth.

5.4 Deflection and Soil Reaction Profiles

The standard approach for obtaining soil reaction (p) and deflection (y) profiles is to doubly differentiate the moment profile and doubly integrate the curvature profile. This process is schematically shown in Fig. 1.8.

Results for the selected displacement level of -2 in, obtained through different fitting techniques, are shown in Figs. 5.8 and 5.9 for Pile *1* and Pile *4*, respectively.

The deflection profiles generated for the Piles *1* and *4* seems to match the string pots displacement well most of the time. Also, no significant differences were noticed among the different fitting techniques.

Shear and soil reaction profiles obtained from the three methods differ in shape and magnitude. The B-Spline values are significant bigger than the LSQ values, since they result from the double differentiation of a overfit moment profile. Therefore, the values obtained from the LSQ methods are considered more reliable and subjected to a smaller numerical error. It is worth noting that even if the LSQ profiles are generally more reliable, the results of their double differentiation can significantly vary with the polynomial degree chosen for the moment fitting. Figure 5.10 presents three soil reaction profiles vs. pile depth obtained from positive deflections of Pile *1*. The soil profiles were derived from the double differentiation of different polynomial fittings obtained through the UNI method. It can be seen how the soil reaction changes profiles from linear ($k_m = 3$) to parabolic ($k_m = 4$), and cubical shape ($k_m = 5$), with k_m as the order of the moment polynomial fitting. Figure 5.10 emphasizes the importance of the moment fitting that not only is well representative of the moment data, but also is able to yield a realistic soil reaction profile to use in the construction of p-y curves.

In terms of boundary conditions, fairly good matches were obtained between top measured

shear and predicted shear values, independently from the specimen and fitting technique for deflections smaller than 1.5 in. After that deflection, the predicted shear profiles tend to overestimate the ground surface shear, without capturing well the correct force direction (e.g. positive or negative). This is due to the differentiation process that is sensitive to any little change of the fitted moment profile.

Figures 5.11 and 5.12 show the six pile profiles for Piles *1* and *4*, respectively, at top head deflections ranging from +/- 0.2 in to +/- 2.0 in.

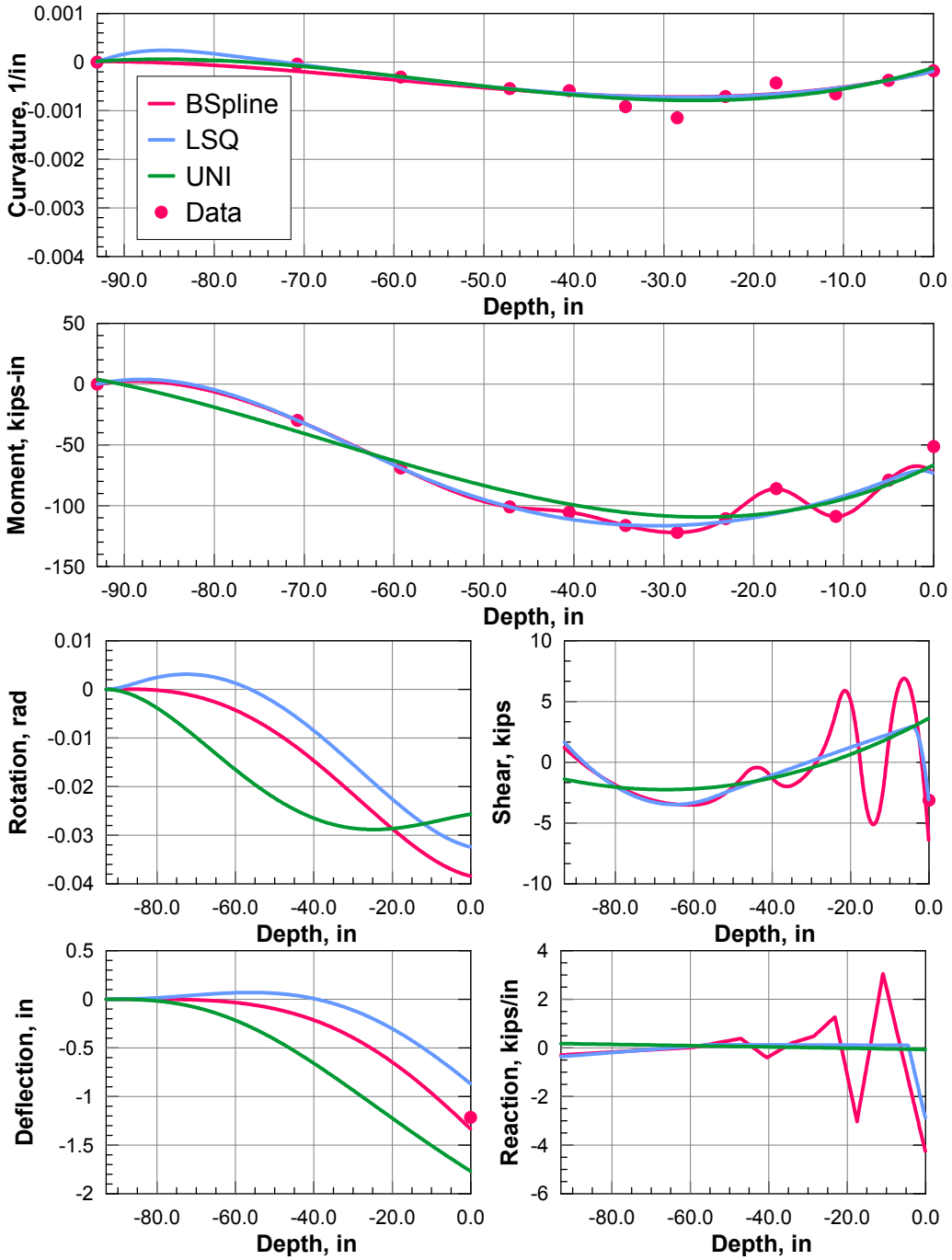

Figure 5.8: Pile *1*: curvature and moment fits; differentiation and integration of fits to soil reaction (p) and shaft deflection (y) at the pile head deflection of $-$ 2 in.

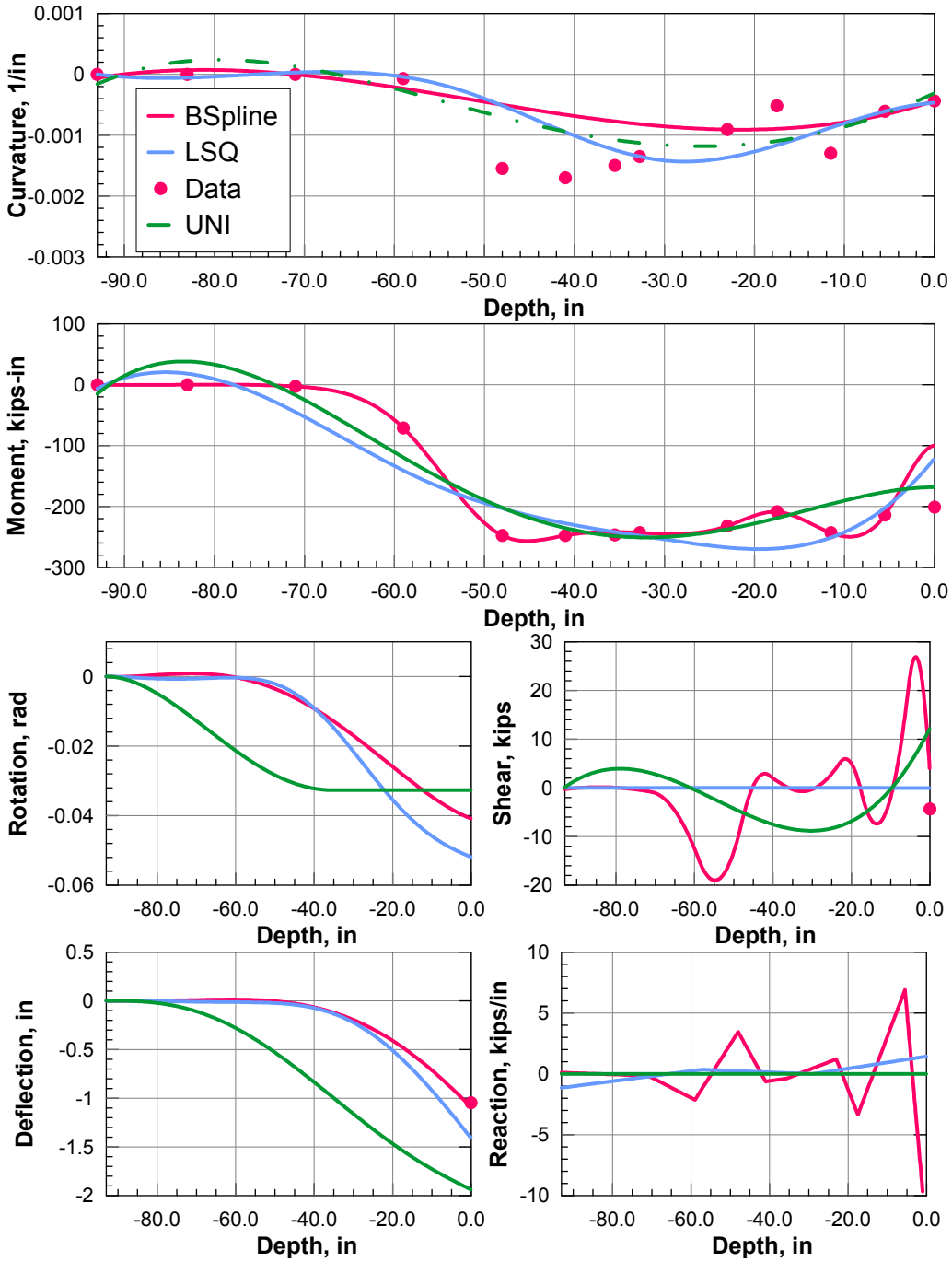

Figure 5.9: Pile *4*: curvature and moment fits; differentiation and integration of fits to soil reaction (p) and shaft deflection (y) at the pile head deflection of $-$ 2 in.

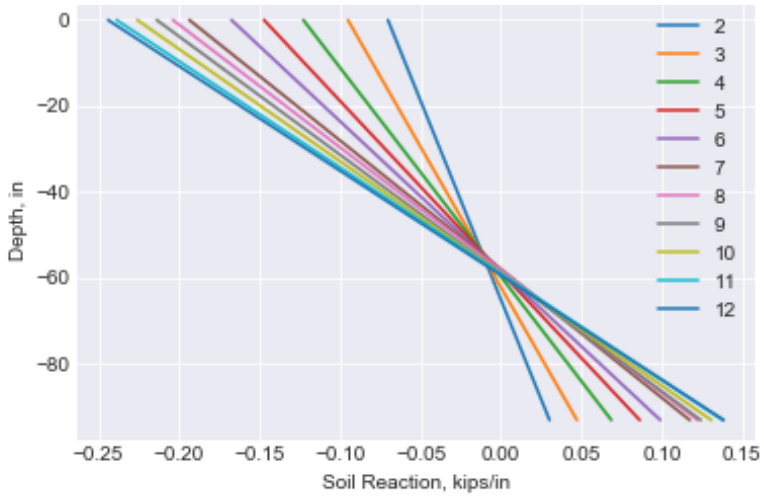

(a) k_m=3

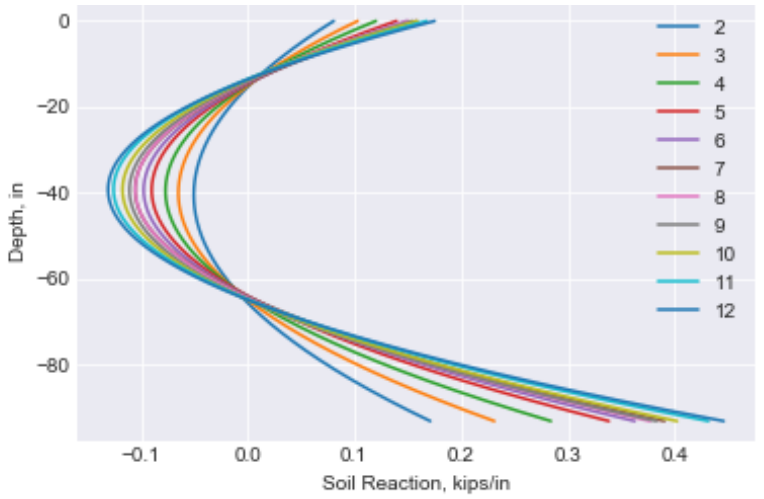

(b) k_m=4

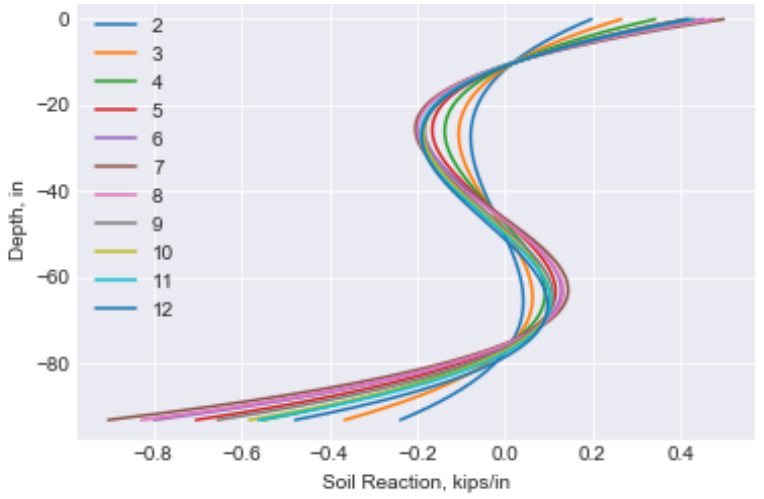

(c) k_m=5

Figure 5.10: Second derivative of the k_m^{th} polynomial fit of the moment data at various pile head deflections: soil reaction vs. depth.

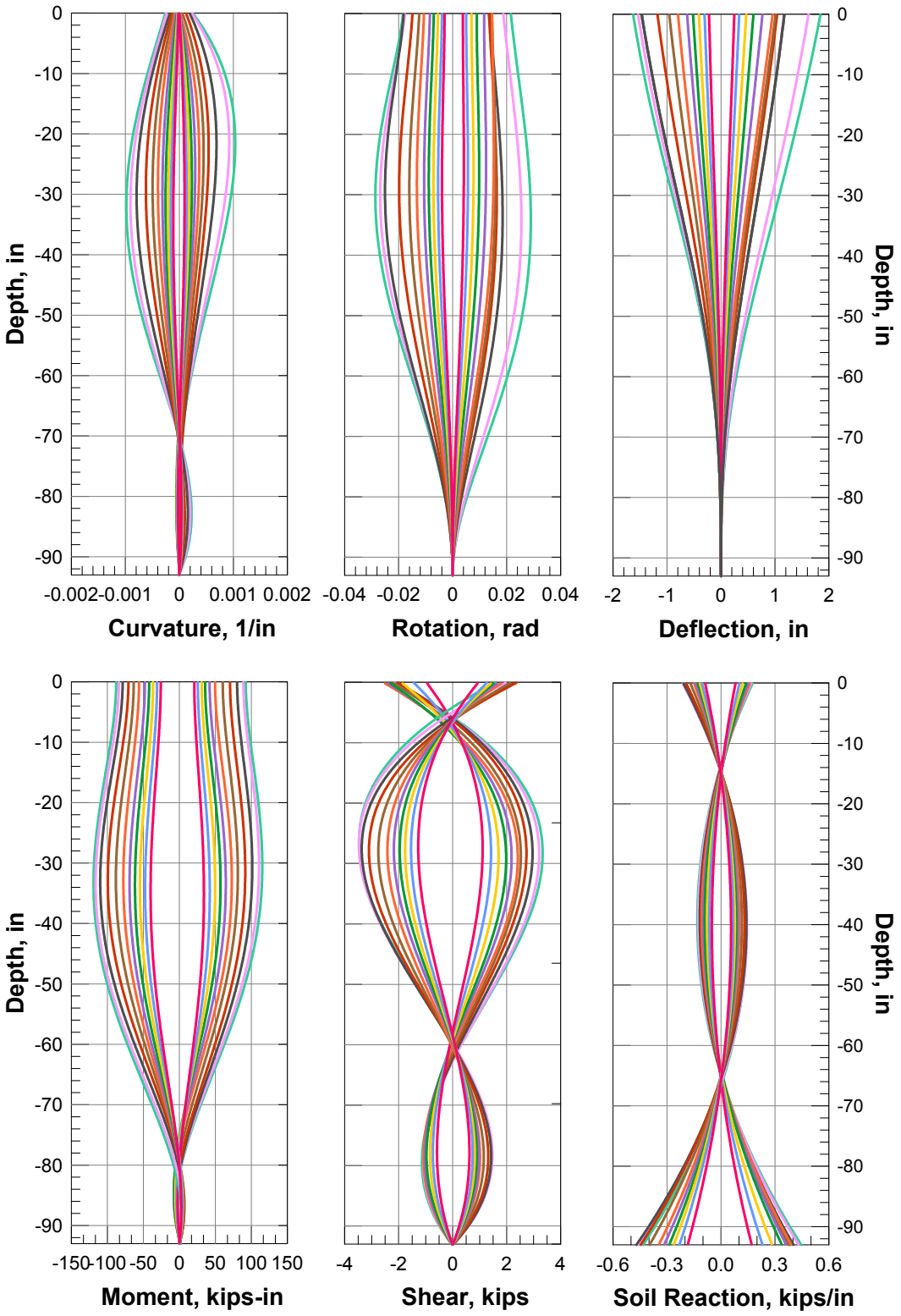

Figure 5.11: Response profiles of Pile *1* obtained through double integration and differentiation process for pile head deflections ranging from +/- 0.2 in to +/-2 in.

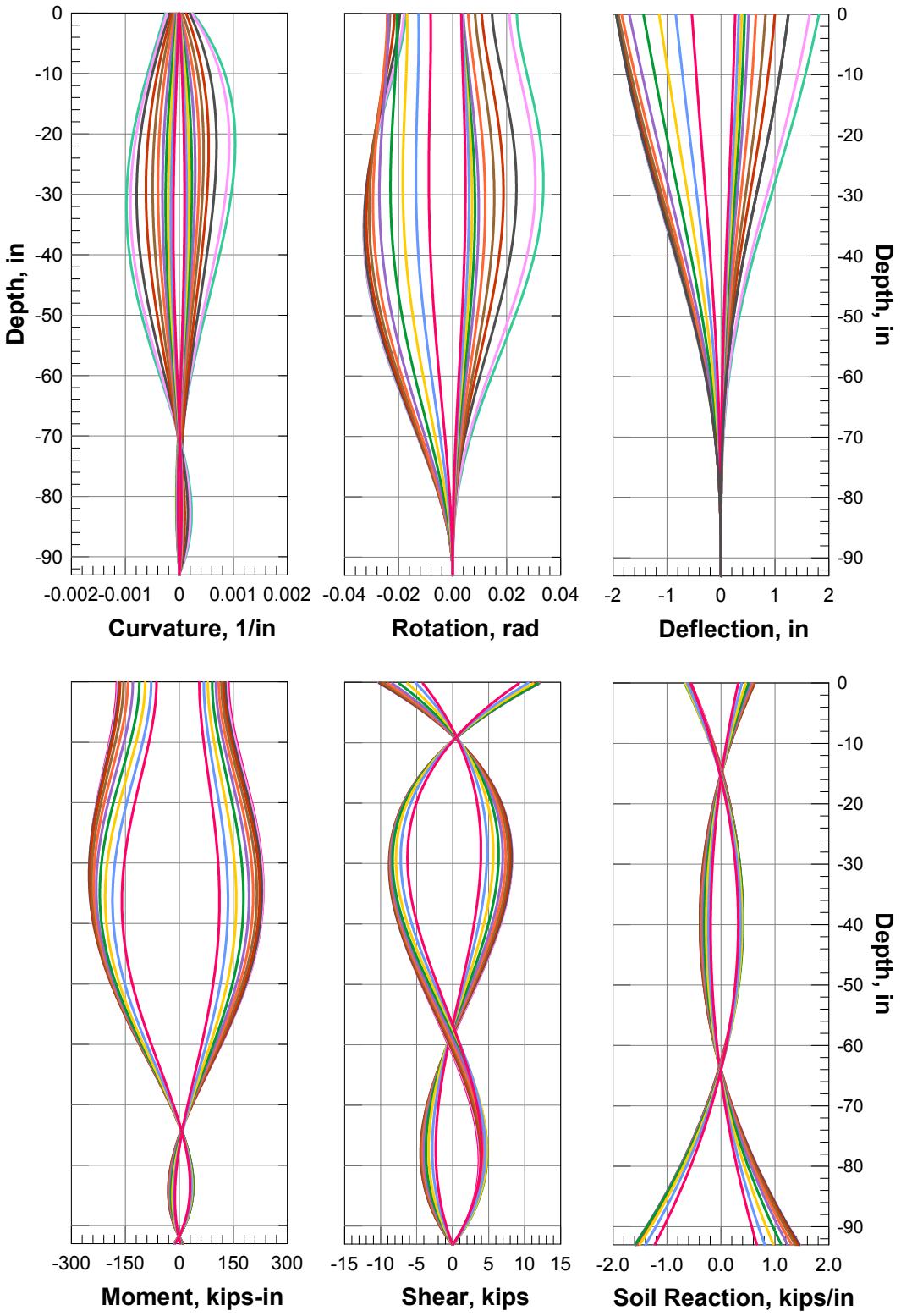

Figure 5.12: Response profiles of Pile *4* obtained through double integration and differentiation process for pile head deflections ranging from +/- 0.2 in to +/-2 in.

5.5 *p-y* Curves

A *p-y* curve for a given soil depth is assembled by evaluating the deflection and soil reaction at a particular depth for various head displacement levels. Each deflection and soil reaction at the given depth forms a point on the *p-y* curve. When repeated over a range of depths, this process gives a suite of *p-y* curves for the specific soil and pile conditions [109].

A condition imposed to the GA process was that *p-y* curves were increasingly monotonic. This means that, within the same depth, an increase of soil reaction implies an increase of pile deflection.

No conditions on curves' depth dependency was implemented in the GA, since the oscillatory behavior of the soil reaction profile changes depth relationship at every inflection point. This variable depth dependency along the pile length for experimentally derived curves is a concept that is generally disregarded in the literature. The majority of *p-y* curves are derived for long piles, which don't develop enough deflection to form *p-y* curves at deep soil layers. In these cases, the *p-y* derivation is done in those top layers where the depth dependency among curves is clear. These *p-y* relationships are then extended to all the depths, based on the theory that the modulus of subgrade reaction increases linearly with depth and the ultimate soil resistance is function of the overburden pressure (Reese et al. [86]).

In the case of a short piles, such as Piles *1* and *4*, the derivation of *p-y* curves is more challenging, since they present significant deflections all along the pile length. Therefore, a careful evaluation of the depth dependency needs to be done in order to pick a range of depths from where realistic *p-y* curves can be derived.

As it can be seen in Figs. 5.11 and 5.12, the soil reaction profiles of both piles have a parabolic shape and they can be divided in three parts that are approximately in both piles: top one from 0 to -15 in, a central one from -15 in to -65 in, and a bottom one that goes until

the pile tip at -93 in. Even if the two profiles might slightly differ in the locations of the inversion points, the following evaluations can be applied to both tests results. The bottom part of the soil reaction profile (below -65in) can be safely excluded from the p-y derivation for the unrealistic p values developed at the pile tip. The soil reaction at the pile tip is higher than at shallower depths where the pile experiences more moment and deflection, and this can be considered as a consequence of the double differentiation process. The very top part in both piles is characterized by a reversed depth dependency: the top curves are stiffer and stronger than the ones located at lower depths. However, this portion of the soil reaction cannot be considered extremely reliable given the fact that during the tests, the piles lateral movements moved the surrounding soil creating a hole of 10 in all around the pile. Therefore, the depths of interest in the p-y analysis are included approximately between -20 in and -70 in.

The experimental curves were generated using data from the peak of the first-cycle at the corresponding displacement level (using only data for head displacement levels ≤ 3 in) and in the depth interval from -20 in to -70 in.

The assembled p-y relationships at various depths along the pile are presented in Figs. 5.13 and 5.14 for Pile 1 and 4, respectively. Note that the data referring to positive and negative deflections were analyzed separately.

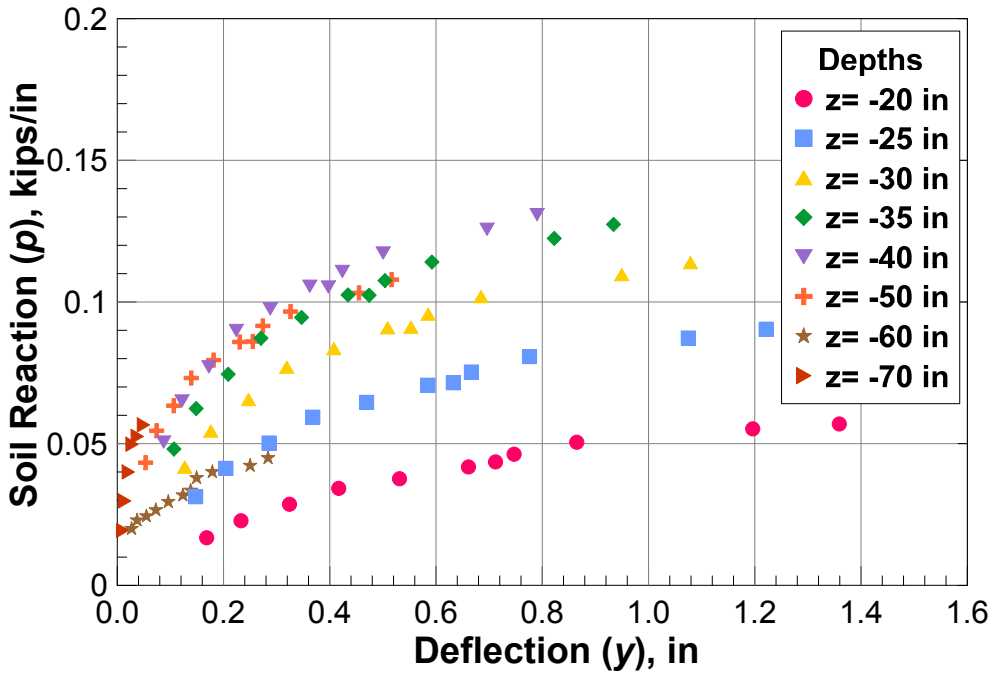

(a) Pile *1*: positive deflections

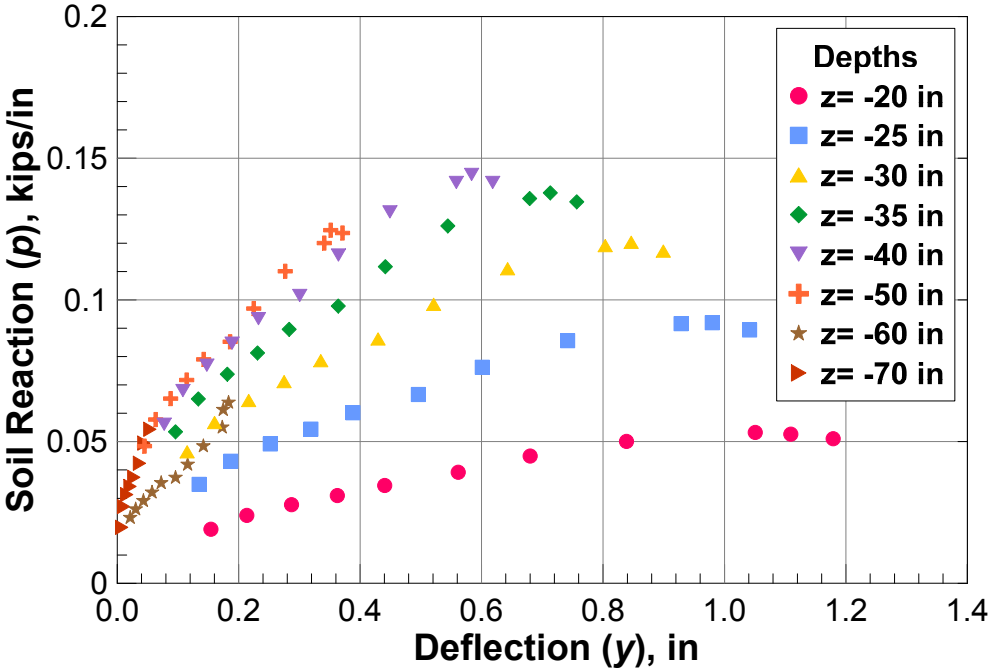

(b) Pile *1*: negative deflections

Figure 5.13: Pile *1*' s experimental *p*-*y* curves obtained from the GA at various depths.

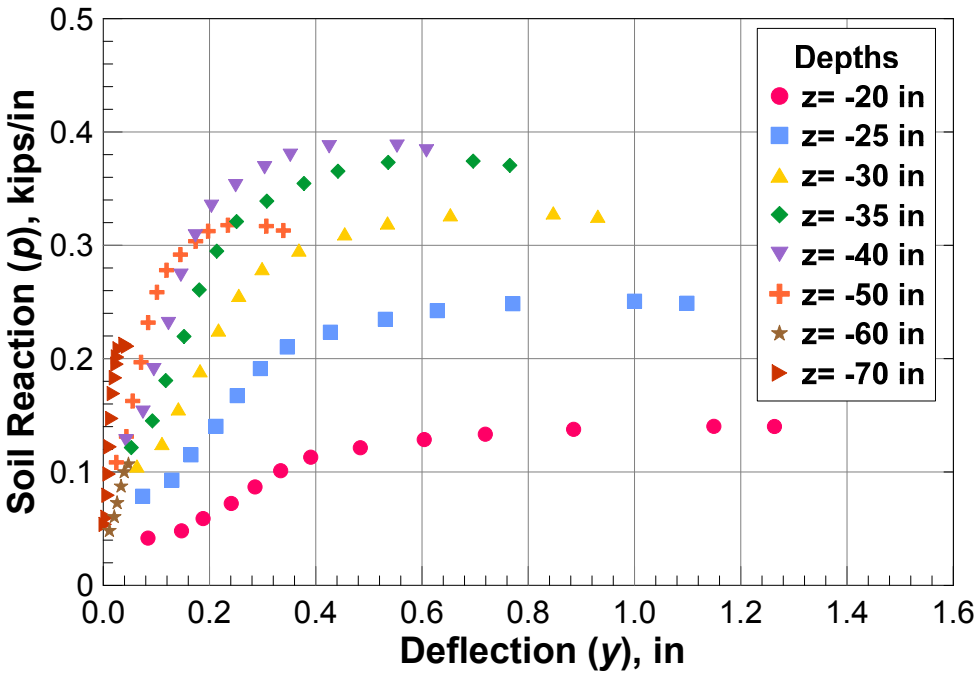

(a) Pile *4*: positive deflections

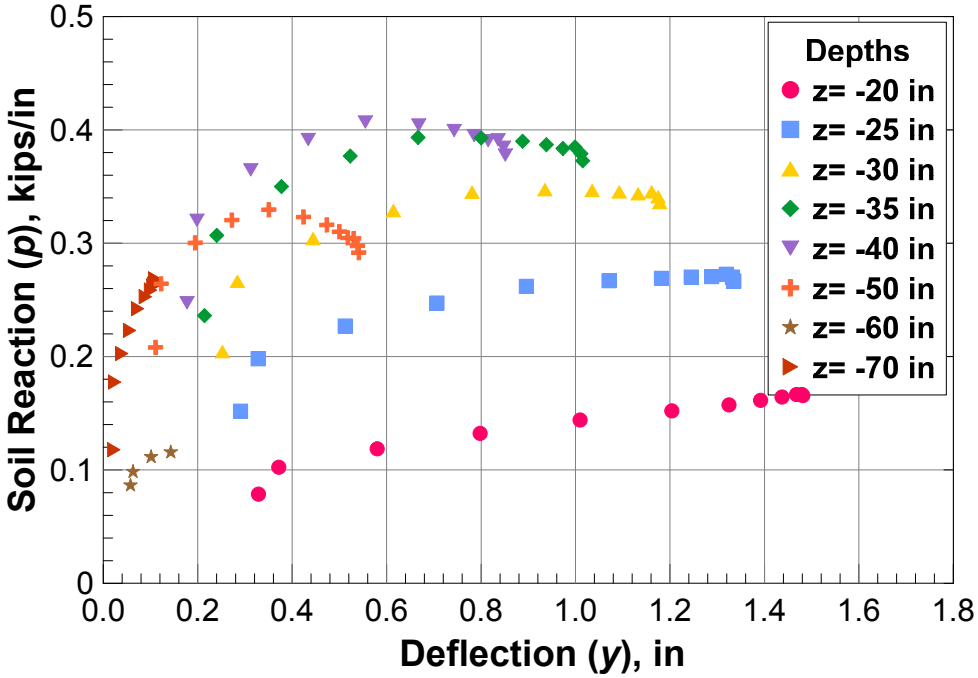

(b) Pile *4*: negative deflections

Figure 5.14: Pile *4*' s experimental *p*-*y* curves obtained from the GA at various depths.

5.5.1 *p-y* Curves Fitting

After the assemble of *p-y* curves, the data points need to be fitted. The chosen fitted function was a sigmoid, which is a bounded, differentiable, and real. More details about the fitting of the *p-y* curves are presented in Chapter 5.5.1. In general, a sigmoid function is monotonic and constrained by a pair of horizontal asymptotes as $x \to \pm\infty$. The sigmoid function, shown in Fig. 5.15, can be expressed as:

$$f(x) = \frac{max_{value}}{1 + e^{-x}} \tag{5.12}$$

where max_{value} represents the top bound of the sigmoid.

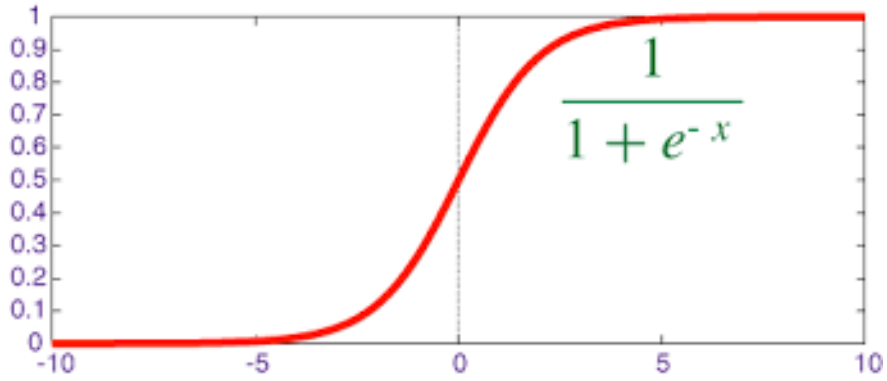

Figure 5.15: General sigmoid function.

In order to have the sigmoid' s midpoint at the intersection of x and y axes, and therefore ensuring the p-y curves' starting point at zero, Eq. 5.12 needs to be modified as follows:

$$f(x) = \frac{2max_{value}}{1 + e^{-x}} - \frac{2max_{value}}{2} \tag{5.13}$$

The fitted *p-y* relationships at various depths along the pile are presented in Figs. 5.16 and 5.17 for Pile 1 and 4, respectively.

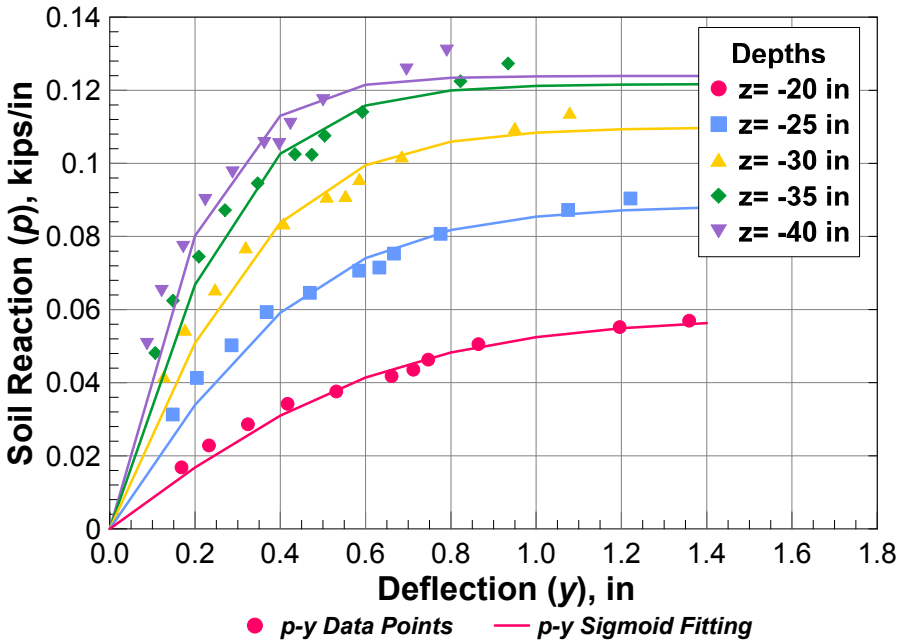

(a) Pile *1*: positive deflections

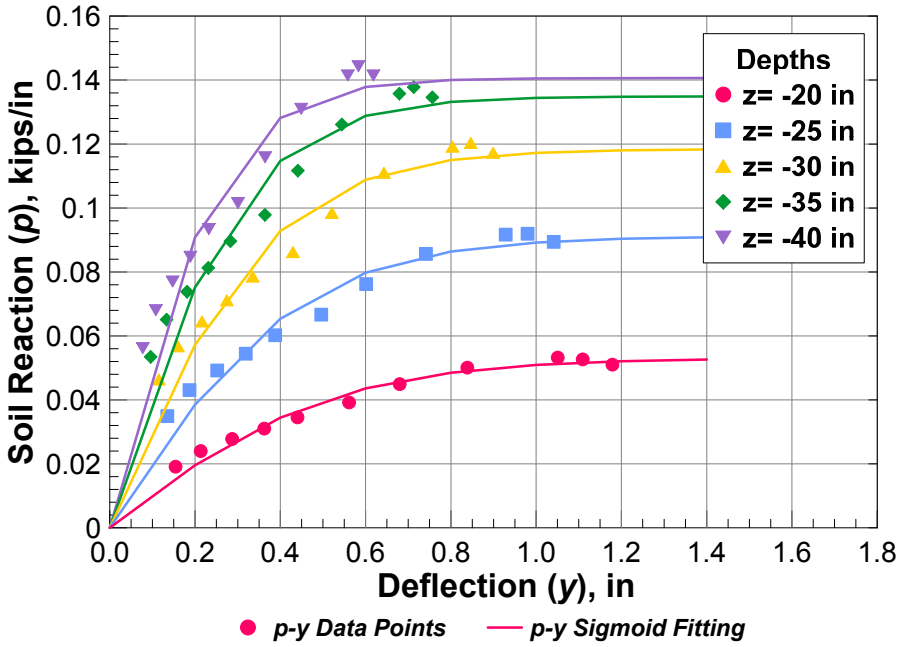

(b) Pile *1*: negative deflections

Figure 5.16: Pile *1*' s experimental and fitted *p-y* curves obtained for various depths.

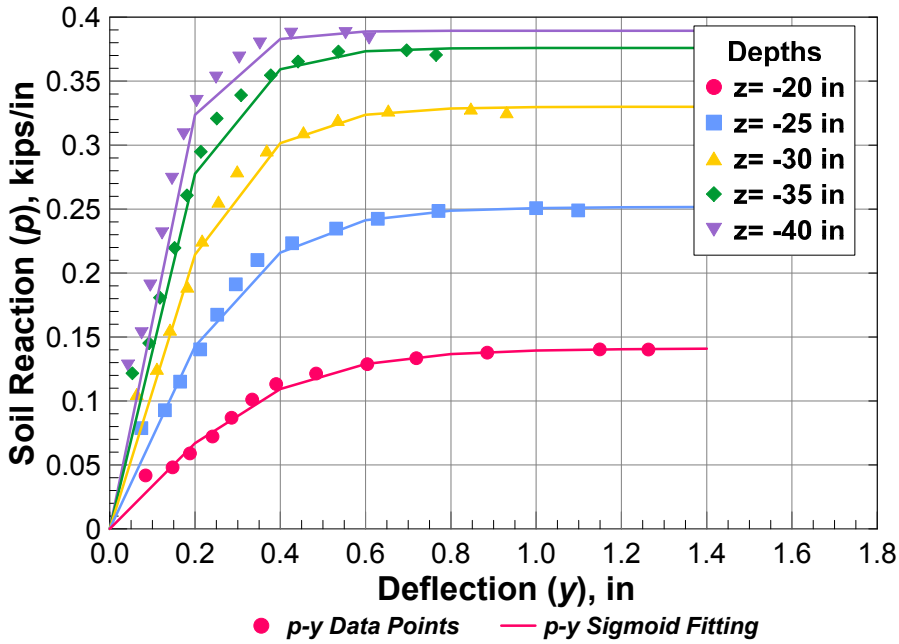

(a) Pile *4*: positive deflections

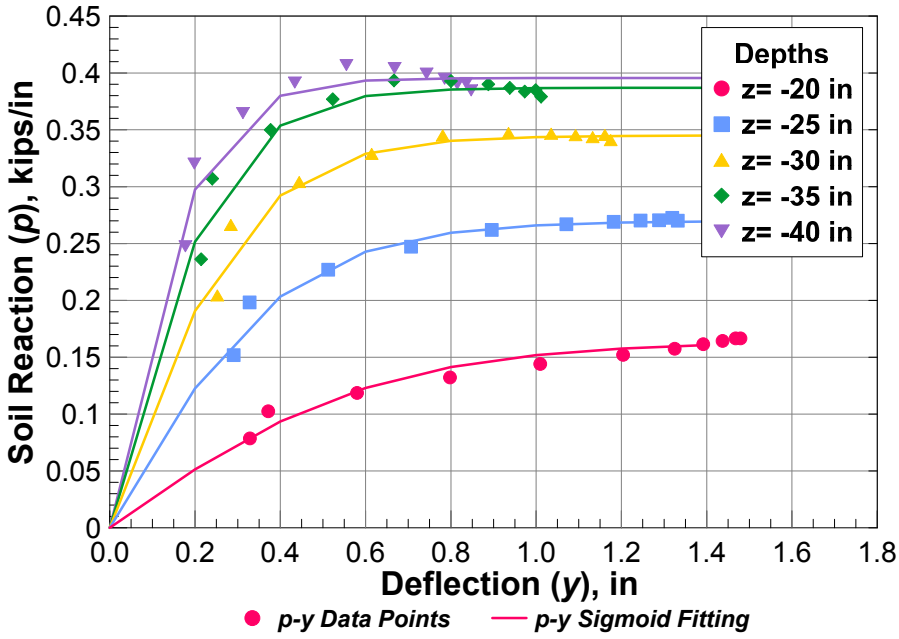

(b) Pile *4*: negative deflections

Figure 5.17: Pile *4*' s experimental and fitted *p-y* curves obtained for various depths.

5.6 Comparison of Experimentally Derived *p-y* Curves

A comparison of the *p-y* curves generated from Pile *1* and Pile *4* reveals that the soil capacity obtained from Pile *4* is significant higher than the one obtained from Pile *1* for similar pile lateral displacements and same depths (Fig. 5.18).

A factor that may have contributed to the lower capacity of the first specimen is that the pile behaved as a rigid body with consequent tip rotation. An upwards movement of about 2 in was also recorded at the end of Pile *1*'s test, and have contributed to a reduction in ultimate capacity as well.

Another reason that could have influenced such a drastic difference between the two sets of *p-y* curves is that *p-y* curves are not so independent from the structural boundary conditions as implied instead by traditional *p-y* methods, which are mainly based on the geotechnical properties of the surrounding soil.

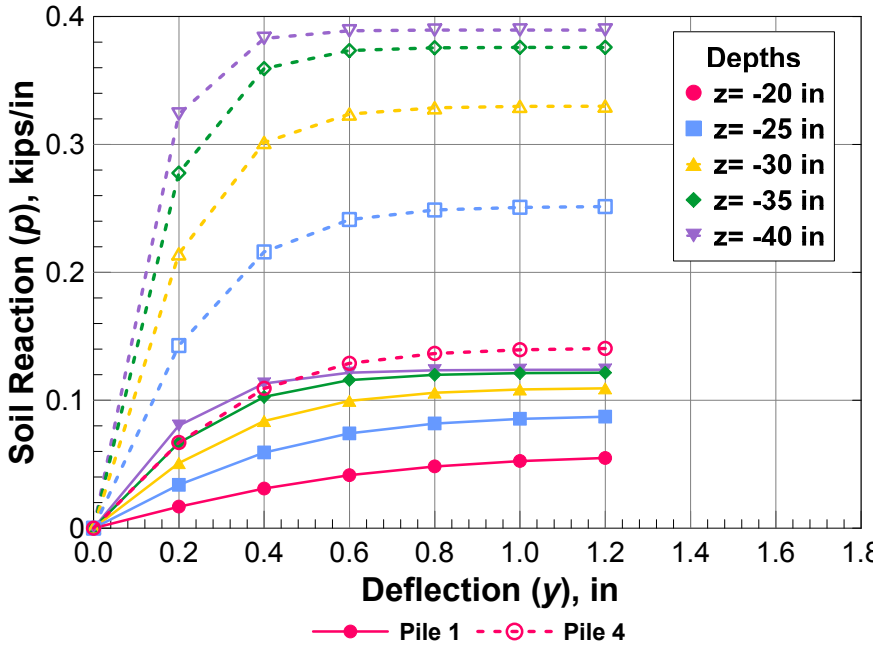

(a) Positive deflections

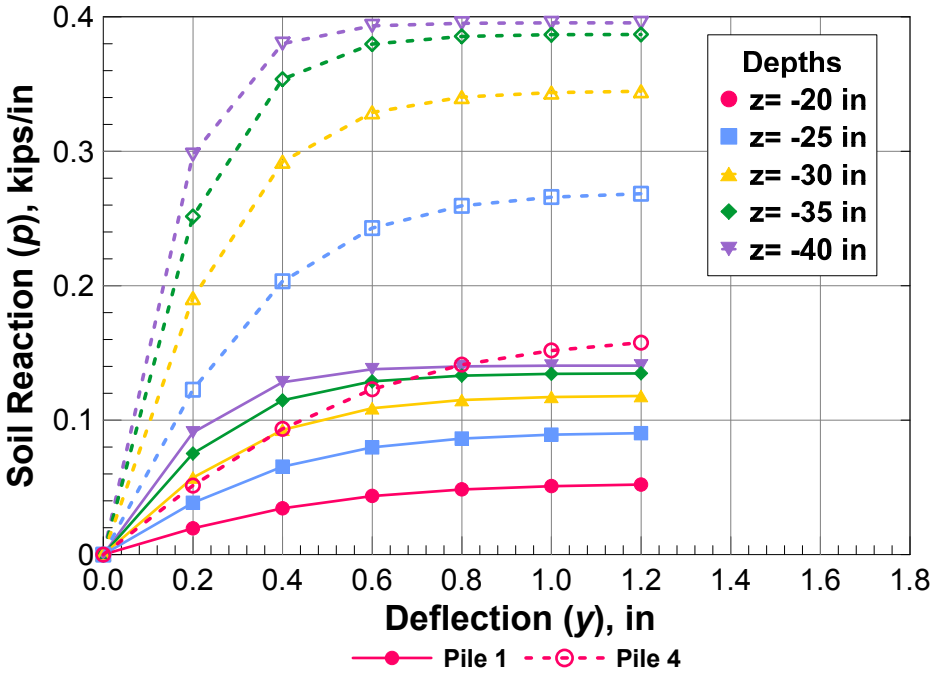

(b) Negative deflections

Figure 5.18: Experimental *p-y* curves obtained from the GA at various depths of Piles *1* and *4*.

5.7 Comparisons with Traditional Analytical Solutions

The derived *p-y* curves were compared to traditional analytical solutions for sand, such as Reese et al. [86]. This method is explained in detail in Chapter 1.5.2, and was obtained through LPILE [91]. The input mechanical and geometric properties of each piles can be found in Chapter 4.5.1.

The *p-y* curves at the depths ranging from -20 in to -40 in are compared in Figs. 5.19 and 5.20 for Pile *1* and *4*, respectively. The results show that traditional analytical methods do not perform well in predicting the soil behavior for both specimens.

The *p-y* curves generated between the depths of -20 in and -40 in, were also compared to traditional analytical solutions, and the comparison is presented in Figs. 5.19 and 5.20 for Pile *1* and *4*, respectively.

The results show that traditional analytical methods (e.g. Reese et al. [86]) do not perform well in predicting the soil behavior for both specimens. In Pile *1*, most of the experimental *p-y* curves exhibited smaller ultimate soil reaction if compared with Reese et al. [86]' s relationships, which are also significantly stiffer in both positive and negative deflections (Fig. 5.19). In Pile *4*, Reese et al. [86] was able to capture the SSIs only at shallower depths (z=-20 in). However, as the depth increases the experimental *p-y* curves become stronger and stiffer. A possible reason for this behavior is that Reese et al. [86]' s *p-y* relationship was based on a series of large scale tests on 2ft diameter piles, and then extrapolated to all other structural boundary conditions. It is possible that the downscaling of the pile diameter does not appropriately reflect the behavior of small diameter piles.

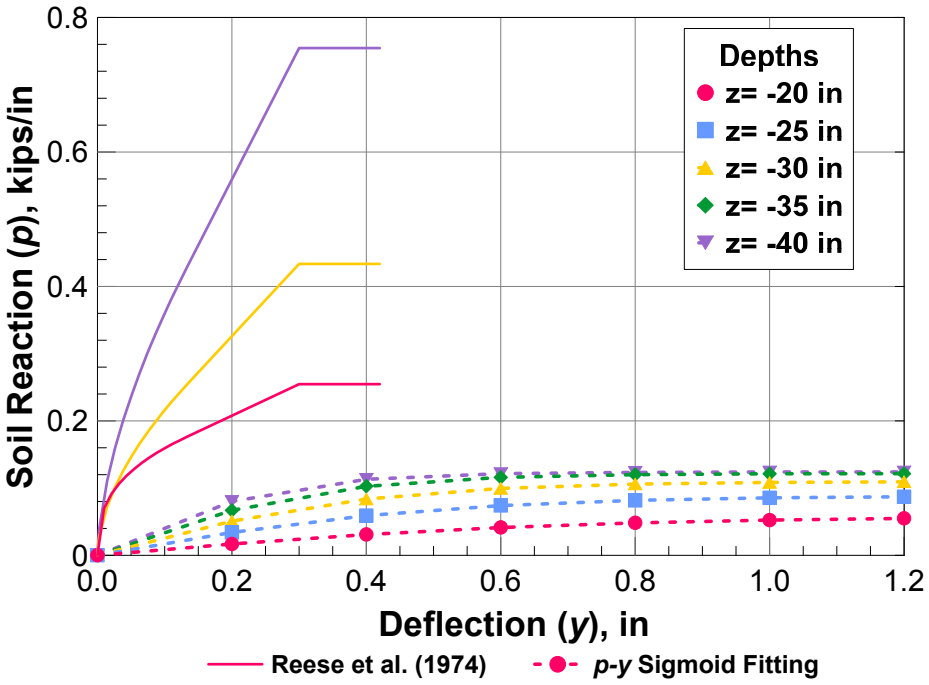

(a) Pile *1*: positive deflections

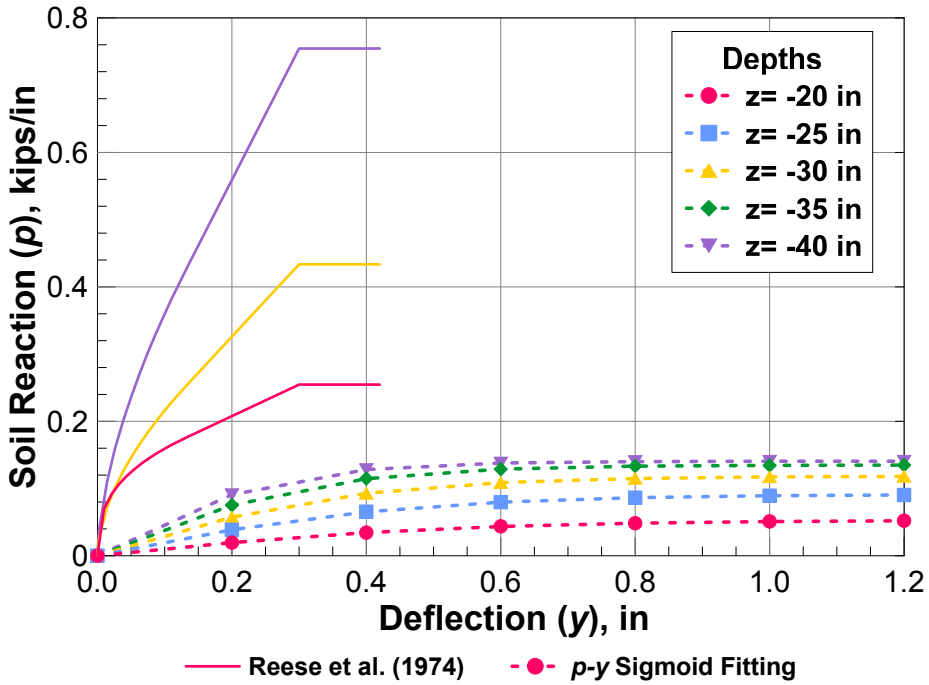

(b) Pile *1*: negative deflections

Figure 5.19: Comparison of *p*-*y* curves obtained experimentally from Pile *1* and various analytical methods.

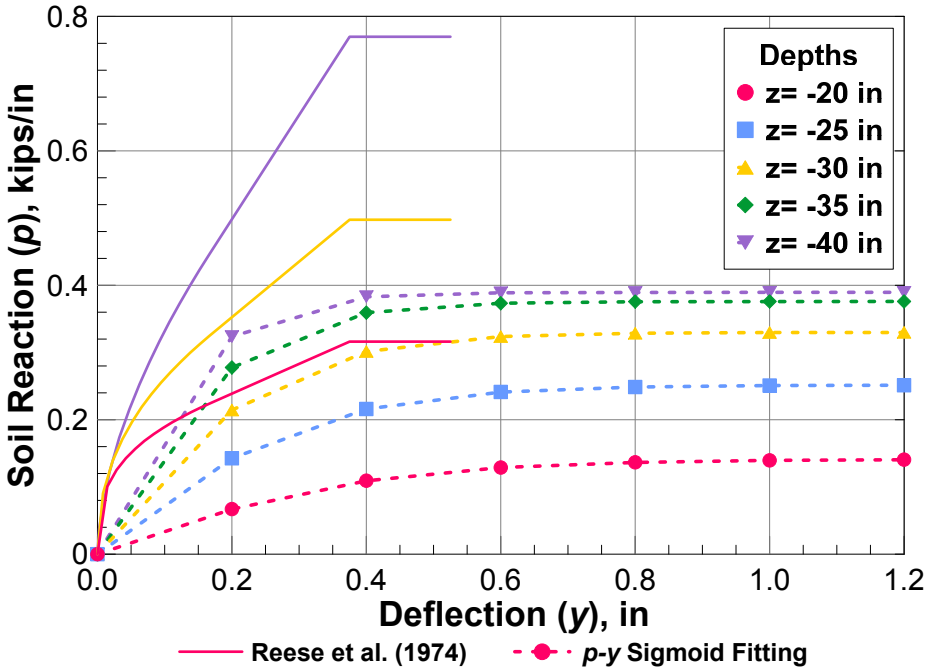

(a) Pile *4*: positive deflections

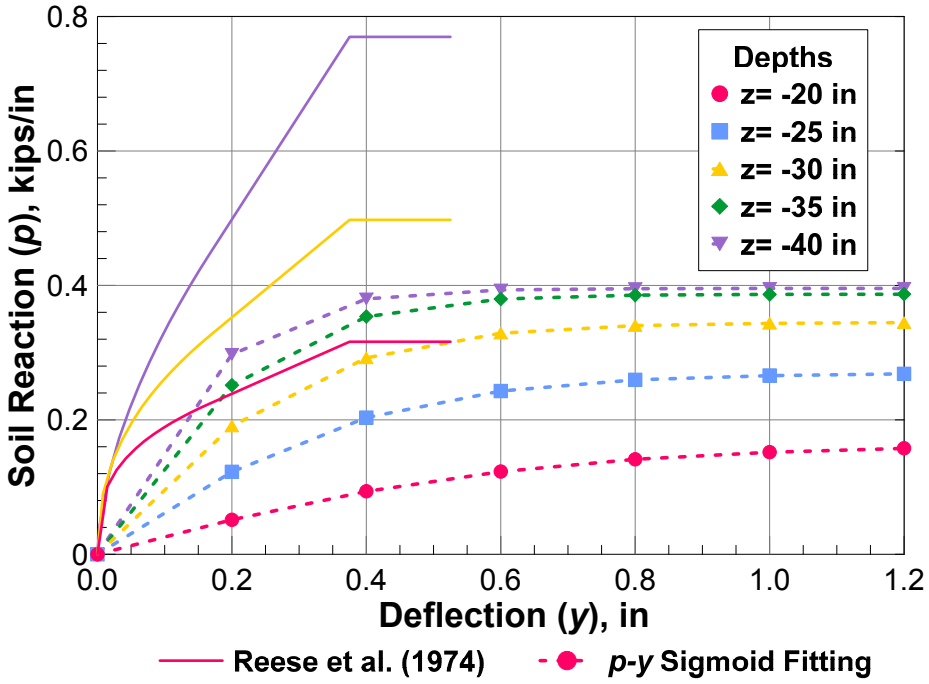

(b) Pile *4*: negative deflections

Figure 5.20: Comparison of *p*-*y* curves obtained experimentally from Pile *4* and various analytical methods.

5.8 Formulation of the Experimental *p-y* Relationship

Equation 5.13 represents a general sigmoid function chosen by the GA to fit the raw *p-y* curves values. That equation can be generalized as function of the geotechnical and structural test characteristics in the following way:

$$p(y) = \frac{A(2p_u)}{1 + e^{-ky}} - \frac{A(2p_u)}{2} \tag{5.14}$$

where A is the nondimensional coefficient for the ultimate soil resistance p_u, k is the slope function, and y is the pile deflection.

According to API [8], the theoretical ultimate soil resistance is given by:

$$p_{u,t} = {K_p}^2 \gamma D z \tag{5.15}$$

where K_p is the coefficient of soil passive pressure, which can be expressed as function of the soil friction angle φ ($tan^2(45° + \varphi/2)$), γ is the soil unit weight, D is the pile diameter, and z is the depth.

By comparing the theoretical ultimate resistance (Eq. 5.15) with the small-scale tests performed on Piles *1* and *4*, a poor agreement was found. Therefore, a coefficient A was introduced when calculating the actual ultimate resistance, p_u:

$$A = \frac{p_u}{p_{u,t}} \tag{5.16}$$

Average values of A were found to be 1.4 and 3.2, for Pile *1* and Pile *4*, respectively.

The slope function k represents the slope at each point of the fitted *p-y* curves (Eq. 5.13) and it is function of the initial slope, k_0, and depth, z. The experimental function is shown

in Fig. 5.21 and it is expressed by the following second order polynomial:

$$k = 9.6k_0^2 \tag{5.17}$$

The initial stiffness, k_0, is function of the modulus of subgrade reaction, n_h, and the depth. The value of n_h was 25 lb/^{3} for Pile *1* and 30 lb/in^3 for Pile *4*, based on the recommendation given by Terzaghi [111]. The values suggested by Reese et al. [86] produced too stiff curves and did not capture well the initial stiffness of the experimental p-y curves.

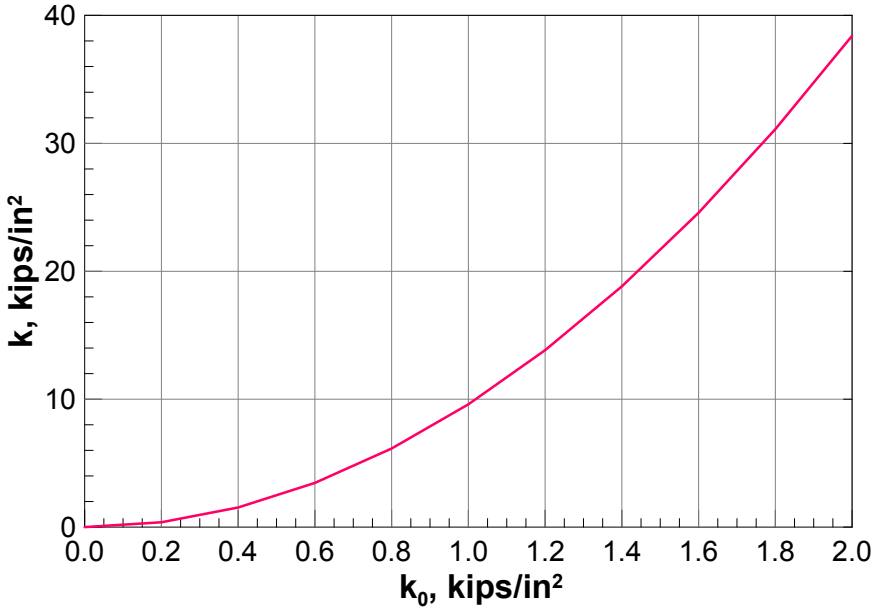

Figure 5.21: Slope function k vs. .

The experimental p-y points fit the curves obtained from Eq. 5.14 well, as shown in Figs. 5.22 and 5.23, respectively for Piles *1* and *4*.

Figure 5.24 shows the proposed hyperbolic relationship extended at various pile depths for the test conditions of both Piles *1* and *4*.

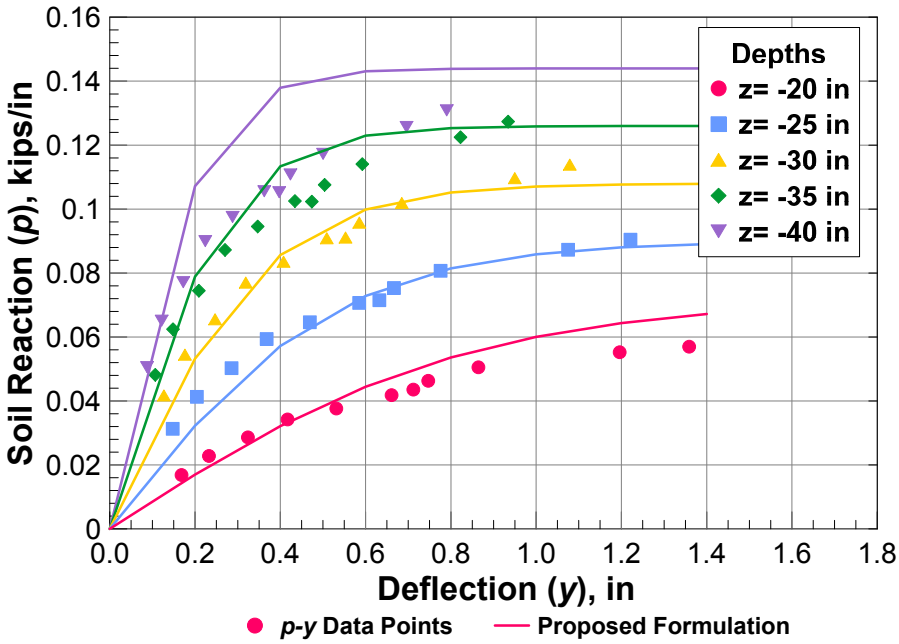

(a) Pile *1*: positive deflections

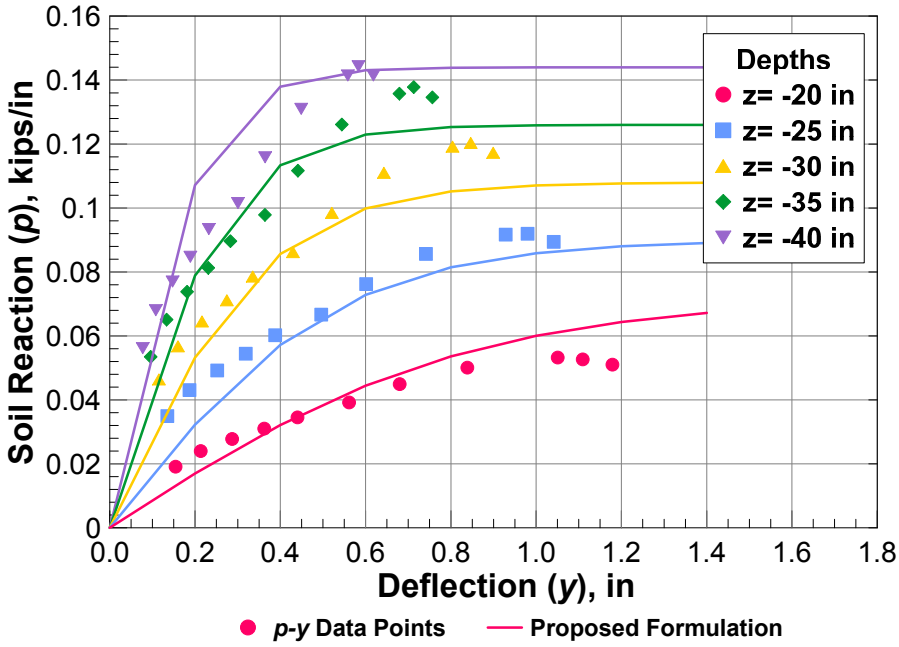

(b) Pile *1*: negative deflections

Figure 5.22: Pile *1*' s experimental data at various depths and proposed hyperbolic *p-y* relationship.

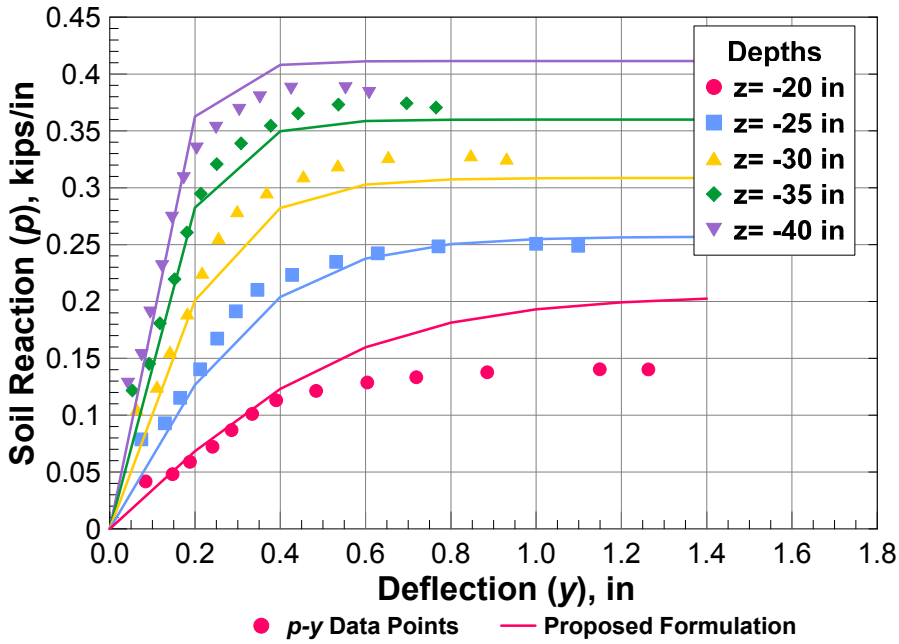

(a) Pile *4*: positive deflections

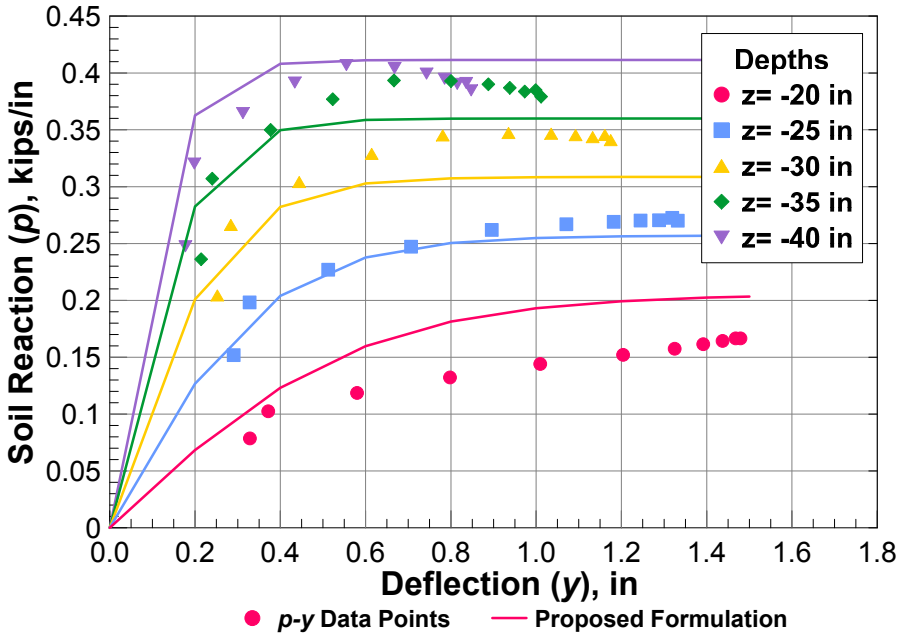

(b) Pile *4*: negative deflections

Figure 5.23: Pile *4*' s experimental data at various depths and proposed hyperbolic *p-y* relationship.

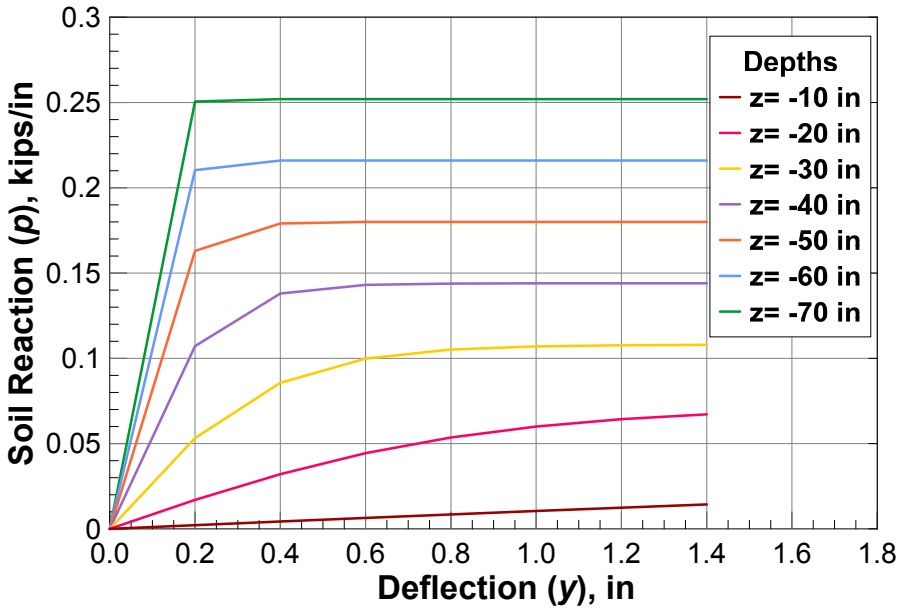

(a) Pile *1*

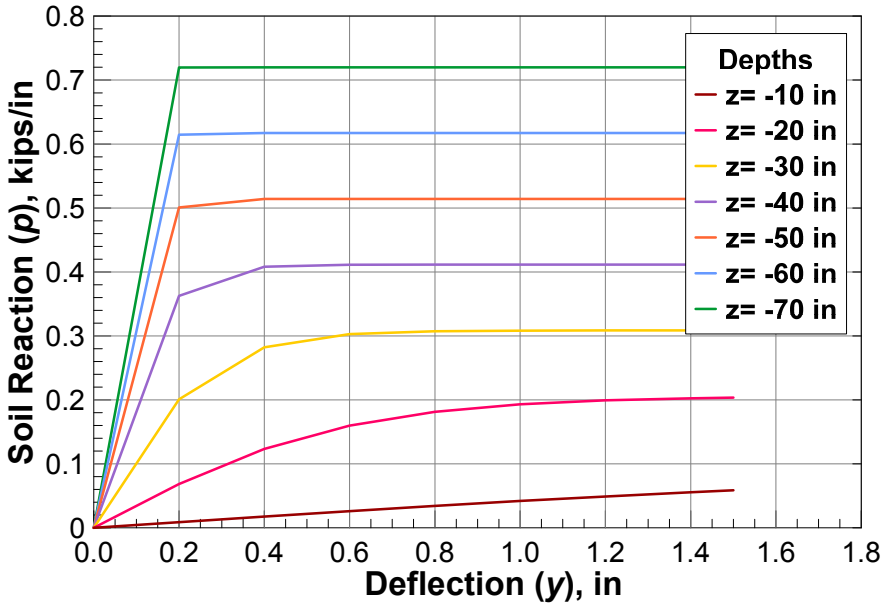

(b) Pile *4*

Figure 5.24: Proposed hyperbolic p-y relationship at various depths.

Chapter 6

Summary

This thesis research seeks to advance our fundamental understanding in analyzing and designing laterally loaded pile foundations through experimental studies and the derivation of new soil resistance formulations (i.e., p-y curves). Four reinforced concrete piles were installed in a laminar soil box, whose movements were restrained by external bracing. The lateral pile response was compared for specimens with various geometric configurations (e.g. pile diameter, tip boundary conditions), and mechanical properties (e.g. type of reinforcement and concrete). The pile specimens had diameters of 8 in and 10 in and a general length of approximately 120 inches. Three out of four pile specimens were constructed with high-strength polymer concrete ($f'_c \geq 8$ ksi); one specimen was fabricated with 4 ksi concrete. The sand consisted of loosely pluviated industrial sand with a relative density of 50%. The pile installation technique replicated the drilled shaft construction procedure in the field. Lateral loading was applied at the pile head through a hydraulic actuator until structural failure was reached. Each specimen was excavated after test completions and damage patters were recorded. Plastic hinging was observed for both pile specimens reinforced with traditional steel rebar at a location of approximately 2-3 pile diameters below ground surface. Pile Specimens reinforced with geotextile materials failed due to spontaneous cracking at similar

locations.

The main observations are summarized below:

1. **Evaluation of reinforcement type**: A new stiff polymer reinforcement was implemented for the first time in a laterally loaded pile (Pile *2*). Test results indicate that strengthening of the pile cross-section can be obtained and displacement ductility can be modestly increased. This application might be suitable for structural elements with minor bending demands, however, for laterally loaded piles with high horizontal or moment loading, the ConForce Grid TE-SCR100/150 needs to be modified and strengthened. Geotextile reinforcement, even though frequently implemented in structural pavement applications, might not be suitable for deep foundations' applications yet. However, it can be used for confinement purposes or for sign and traffic piles that are not supposed to resist to high lateral loads. Further pile testing are recommended to better study the ultimate flexural capacity of the pile - geogrid unit, and make a better assessment of the reinforcement usability.

2. **Observations with respect to tip boundary conditions**: The tip restraint in Pile *4* resulted in an increase of 20% in the specimen' s overall lateral force capacity when compared to Pile *1*. Pile *1* was not embedded in a stiff base layer at the pile tip and had a 20% smaller pile diameter. Internal shear measurements and external damage observations following pile excavation indicated that the pile did not fail in shear as predicted by the *p-y* type analysis. Pile failure was observed through plastic hinging at 2.5 pile diameters below ground surface.

3. **Evaluation of shear data obtained through tetrahedron instrumentation**: A strain gauge based instrumentation carrier with tetrahedral configuration was introduced to extract volumetric measurements in deep foundation systems near the pile surface. Based on preliminary results, the tetrahedra' s readings were generally re-

sponsive to the different loading cycles (push vs. pull) with strain readings increasing with the increase of pile lateral deflection. Moreover, in some cases the tetrahedra were able to capture strains and stresses at their centroid within an acceptable range of values predicted by LPILE. However, the shear stresses did not follow a consistent pattern and only few tetrahedra were able to capture realistic shear values. This limitation could be associated with constructibility issues such as damage of the tetrahedra during concrete pouring, and loss of connection rigidity during lateral displacements. Hence the tetrahedral carriers might not have bent as a rigid system as anticipated. Therefore, recommendations for second prototype of tetrahedral carriers consist of alternative manufacturing methodologies (e.g. 3D printing) and the use of stronger vertex connections.

4. **Genetic Algorithm implementation in *p-y* curves analysis**: A genetic algorithm (GA) framework has been used in the *p-y* analysis of Piles *1* and *4* with the intent of facilitating data interpretation even in presence of disturbed data readings and pile nonlinearity. This new approach overcomes the current challenges in experimental *p-y* curves derivation, related to the choice of fitting technique and input model parameters. A GA approach allows generating *p-y* curves from an ensemble of different statistical methods, and ensures the best solution across many variables and methods. The genetic algorithm is versatile and applicable to any experimental data set. The selection of independent model parameters is based on an objective fitness function (e.g. explained variance between *p-y* raw and fitted values) and not on empirical user choice. Traditionally, there is not a universally accepted method for the derivation of *p-y* curves from instrumented field data. The most common process implemented in previous research studies involves the double integration and double differentiation of curvature and moment profiles, respectively. In particular, the double differentiation process can result in serious errors if the appropriate fitting method is not considered. In this thesis research, the GA was set to consider three different interpolation

techniques (i.e., two least square fit (LSQ) methods and one B-spline method). Results indicated that the preferred choice for this specific data set was the UNIvariate method, where the knots location was dictated by the smoothing factor. This ensured curvature and moment data to be fitted with profiles without many local extrema. The results showed that a fourth order polynomial provided a satisfactory description of the moment and curvature profiles.

5. **Generation of a set of new soil resistance functions (i.e., *p-y* relationships)**: A set of *p-y* curves was derived for depths between -20 in and -40 in below ground surface. A formulation of the experimental *p-y* relationship was extrapolated for all the other depths (Eq. 5.14). Although the proposed formulation includes general geotechnical and structural characteristics (e.g. soil unit weight, soil friction angle, pile diameter), its application is only recommended for use in similar soil-structure configurations, given the highly peculiarity of the *p-y* curves. A comparison of *p-y* curves generated from Pile *1* and Pile *4* reveals that the back-calculated soil capacity obtained from Pile *4* is significant higher than the one obtained from Pile *1* for similar pile lateral displacements and depths. This difference emphasizes the strong dependence of *p-y* curves on structural boundary conditions, which are not properly captured in current analytical models. A sole association of *p-y* relationships with soil-type and soil properties may lead to erroneous results, particularly for reinforced concrete piles for which *p-y* relationships have been derived from highly non-linear pile response data. Comparison of test data with analytical formulations proposed in literature, e.g., Reese et al. [86]' s *p-y* model for sand, indicated a clear misfit between experimental and theoretical *p-y* resistance functions. While literature most commonly addresses pile diameter effects with respect to larger pile diameters and discusses errors introduced due to extrapolating analytical formulations to large diameter piles, the results of the current study indicate that the analytical *p-y* models do not well capture the behavior of the two small diameter piles either. Hence the applicability of the API sand

p-y curve to pile diameters similar to MicroPile configurations might yield erroneous results and scaling laws need to be revisited.

Hereafter a list of recommendations learned over the course of this research is provided to guide and benefit future studies that focus on the experimental derivation of p-y relationships:

- The spacing of the longitudinal strain gauges in this experimental program was 12 in for a total of eleven data points per pile. Even though this number exceeded the minimum number of gauges, indicated by Yang and Liang [119], who suggest the use of the degree of the curvature fitting function plus one; more data points would have been helpful in order to increase the reliability of data fitting with respect to experimental curvature and moment. Moreover, the estimation of the curvature in reinforced concrete piles is more difficult than in steel pipes because the strain measured along the pile is not uniform. The strain is high in the vicinity of the crack and lower at the locations away from the crack. In conclusion, more strain gauges are desirable at each depth in order to ensure data redundancy. A minimum gauge spacing of 6 in is therefore suggested for future testing.

- The use of other types of instrumentation is also suggested to supplement and validate the strain readings. Inclinometers and fiber braggs are just an example of valid additions to the pile instrumentation plan that can help to improve the accuracy of the derived p-y. This alternative instrumentation could not be implemented in the current study due to the small pile diameter.

- In order to mitigate the errors in the double differentiation process, it is suggested to introduce direct measurements of the normal soil pressure (e.g. tactile pressure sheets) to use as validation of the obtained soil reaction profile.

- Alternative fitting procedures such as the use of genetic algorithms and machine learning processes are recommended for data profiles with high variability.

Bibliography

[1] FEA Abaqus. "Dassault Systèmes Simulia Corporation". In: *Providence, Rhode Island, USA* (2010).

[2] K Abdel-Rahman and M Achmus. "Finite element modelling of horizontally loaded monopile foundations for offshore wind energy converters in Germany". In: *Proceedings of the International Symposium on Frontiers in Off-shore Geotechnics (ISFOG). Edited by S. Gourvenec and M. Cassidy. Taylor and Francis, Perth.* 2005, pp. 391–396.

[3] A Ahangar-Asr et al. "Lateral load bearing capacity modelling of piles in cohesive soils in undrained conditions: An intelligent evolutionary approach". In: *Applied Soft Computing* 24 (2014), pp. 822–828.

[4] Eric Reid Ahlberg. *Interaction between soil and full scale drilled shafts under cyclic lateral loads*. University of California, Los Angeles, 2008.

[5] M Alizadeh. "Lateral load tests on instrumented timber piles". In: *Performance of Deep Foundations*. ASTM International, 1969.

[6] Iyad Alkroosh and Hamid Nikraz. "Correlation of pile axial capacity and CPT data using gene expression programming". In: *Geotechnical and Geological Engineering* 29.5 (2011), pp. 725–748.

[7] JB Anderson, FC Townsend, and B Grajales. “Case history evaluation of laterally loaded piles”. In: *Journal of geotechnical and geoenvironmental engineering* 129.3 (2003), pp. 187–196.

[8] RP API. “2A-WSD”. In: *Recommended Practice for Planning, Designing and Constructing Fixed Offshore Platforms-Working Stress Design* 21 (2000).

[9] Prasanta Kumar Banerjee and Roy Butterfield. *Boundary element methods in engineering science*. Vol. 17. McGraw-Hill London, 1981.

[10] Evan C Bentz. *Sectional analysis of reinforced concrete members*. University of Toronto Toronto, 2000.

[11] M Asghar Bhatti. “Fundamental finite element analysis and applications”. In: *Hoboken, New Jersey: John Wiley & Sons* (2005).

[12] H Blum. “Wirtschaftliche dalbenformen und deren berechnung”. In: *Bautechnik* 10.5 (1932), pp. 122–135.

[13] Ross W Boulanger et al. “Seismic soil-pile-structure interaction experiments and analyses”. In: *Journal of Geotechnical and Geoenvironmental Engineering* 125.9 (1999), pp. 750–759.

[14] Scott J Brandenberg, Daniel W Wilson, and Mark M Rashid. “Weighted residual numerical differentiation algorithm applied to experimental bending moment data”. In: *Journal of Geotechnical and Geoenvironmental Engineering* 136.6 (2010), pp. 854–863.

[15] Scott J Brandenberg et al. “Behavior of pile foundations in laterally spreading ground during centrifuge tests”. In: *Journal of Geotechnical and Geoenvironmental Engineering* 131.11 (2005), pp. 1378–1391.

[16] JL Briaud, TD Smith, and LM Tucker. "A pressuremeter method for laterally loaded piles. Proceedings of the Eleventh International Conference on Soil Mechanics and Foundation Engineering, San Francisco, 12-16 August 1985". In: *Publication of: Balkema (AA)* (1985).

[17] Ronald Bastiaan Johan Brinkgreve and Wout Broere. *Plaxis: 3D Foundation-Version 1*. AA Balkema, 2004.

[18] Bengt B Broms. "Lateral resistance of piles in cohesionless soils". In: *Journal of the Soil Mechanics and Foundations Division* 90.3 (1964), pp. 123–158.

[19] Bengt B Broms. "Lateral resistance of piles in cohesive soils". In: *Journal of the Soil Mechanics and Foundations Division* 90.2 (1964), pp. 27–64.

[20] Dan A Brown, Clark Morrison, and Lymon C Reese. "Lateral load behavior of pile group in sand". In: *Journal of Geotechnical Engineering* 114.11 (1988), pp. 1261–1276.

[21] Dan A Brown, Lymon C Reese, and Michael W O'Neill. "Cyclic lateral loading of a large-scale pile group". In: *Journal of Geotechnical Engineering* 113.11 (1987), pp. 1326–1343.

[22] Yuk Hon Chai and Tara C Hutchinson. *Flexural strength and ductility of reinforced concrete bridge piles*. Dept. of Civil and Environmental Engineering, University of California, Davis, 1999.

[23] Jung In Choi, Myoung Mo Kim, and Scott J Brandenberg. "Cyclic p-y Plasticity Model Applied to Pile Foundations in Sand". In: *Journal of Geotechnical and Geoenvironmental Engineering* 141.5 (2015), p. 04015013.

[24] William R Cox, Lyman C Reese, Berry R Grubbs, et al. "Field testing of laterally loaded piles in sand". In: *Offshore Technology Conference*. Offshore Technology Conference. 1974.

[25] Sarat Kumar Das and Prabir Kumar Basudhar. "Undrained lateral load capacity of piles in clay using artificial neural network". In: *Computers and Geotechnics* 33.8 (2006), pp. 454–459.

[26] Huaren Dou and Peter M Byrne. "Dynamic response of single piles and soil pile interaction". In: *Canadian Geotechnical Journal* 33.1 (1996), pp. 80–96.

[27] J Michael Duncan, Leonard T Evans Jr, and Phillip SK Ooi. "Lateral load analysis of single piles and drilled shafts". In: *Journal of geotechnical engineering* 120.6 (1994), pp. 1018–1033.

[28] Todd Wayne Dunnavant and Michael W O'Neill. *Performance, Analysis, and Interpretation of a Lateral Load Test of a 72-inch-diameter Bored Pile in Overconsolidated Clay*. University of Houston, Department of Civil Engineering, 1985.

[29] GJ Dyson and MF Randolph. "Installation effects on lateral load-transfer curves in calcareous sands". In: *Proceedings of the international conference centrifuge*. Vol. 98. 1998, pp. 545–550.

[30] A Elshorbagy et al. "Experimental investigation of the predictive capabilities of data driven modeling techniques in hydrology-Part 1: Concepts and methodology". In: *Hydrology and Earth System Sciences* 14.10 (2010), pp. 1931–1941.

[31] Lawrence B Feagin. "Lateral pile-loading tests". In: *Transactions of the American Society of Civil Engineers* 102.1 (1937), pp. 236–254.

[32] MM Filonenko-Borodich. "Some approximate theories of elastic foundation". In: *Uchenyie Zapiski Moskovkogo Gosudarstuennogo Universiteta Mekhanika, Moscow* 46 (1940), pp. 3–18.

[33] Anthony TC Goh, Fred H Kulhawy, and CG Chua. "Bayesian neural network analysis of undrained side resistance of drilled shafts". In: *Journal of Geotechnical and Geoenvironmental Engineering* 131.1 (2005), pp. 84–93.

[34] ATC Goh. "Nonlinear modelling in geotechnical engineering using neural networks". In: *Transactions of the Institution of Engineers, Australia. Civil engineering* 36.4 (1994), pp. 293–297.

[35] David Goldberg. "Genetic algorithms in optimization, search and machine learning". In: *Reading: Addison-Wesley* (1989).

[36] J Brinch Hansen and NH Christensen. *The Ultimate Resistance of Rigid Piles Against Transversal Forces; Model Tests with Tranversally Loaded Rigid Piles in Sand*. Geoteknisk Institut, 1961.

[37] M Hetényi. *Beams on elastic foundation, 1946*.

[38] AS Hokmabadi, A Fakher, and B Fatahi. "Full scale lateral behaviour of monopiles in granular marine soils". In: *Marine Structures* 29.1 (2012), pp. 198–210.

[39] DM Holloway et al. "Response of a pile group to combined axial and lateral loading". In: *Proc., 10th Int. Conf. on Soil Mech. and Found. Engrg.* Vol. 2. 1981, pp. 731–734.

[40] Jin-wei Huang. "Development of modified py curves for Winkler Analysis to characterize the lateral load behavior of a single pile embedded in improved soft clay". In: (2011).

[41] Nabil F Ismael. "Lateral load tests on bored piles and pile groups in sand". In: *7th FMGM 2007: Field Measurements in Geomechanics*. 2007, pp. 1–11.

[42] Abdussamad Ismail and Dong-Sheng Jeng. "Modelling load–settlement behaviour of piles using high-order neural network (HON-PILE model)". In: *Engineering Applications of Artificial Intelligence* 24.5 (2011), pp. 813–821.

[43] FLAC Itasca. "Fast Lagrangian analysis of continua". In: *Itasca Consulting Group Inc., Minneapolis, Minn* (2000).

[44] K Janoyan, Jonathan P Stewart, and John W Wallace. "Analysis of py curves from lateral load test of large diameter drilled shaft in stiff clay". In: *Proceedings of the 6th Caltrans workshop on seismic research, Sacramento, CA*. 2001.

[45] Kerop D Janoyan, John W Wallace, and Jonathan P Stewart. "Full-scale cyclic lateral load test of reinforced concrete pier-column". In: *ACI structural journal* 103.2 (2006).

[46] H John. "Holland. 1975. Adaptation in Natural and Artificial Systems". In: *Ann Arbor: University of Michigan Press* ().

[47] Payman Khalili-Tehrani et al. "Nonlinear load-deflection behavior of reinforced concrete drilled piles in stiff clay". In: *Journal of Geotechnical and Geoenvironmental Engineering* (2013).

[48] M Kimura et al. "3-D finite element analyses of the ultimate behavior of laterally loaded cast-in-place concrete piles". In: *Proceedings of the Fifth International Symposium on Numerical Models in Geomechanics, NUMOG V*. AA Balkema. 1995, pp. 589–594.

[49] SL Kramer. *BEHAVIOR OF PILES IN FULL-SCALE, FIELD LATERAL LOADING TESTS. FINAL REPORT*. Tech. rep. 1991.

[50] PY Lee, LW Gilbert, et al. "Behavior of laterally loaded pile in very soft clay". In: *Offshore Technology Conference*. Offshore Technology Conference. 1979.

[51] Anne Lemnitzer. *Personal Communication*. Tech. rep. 2018.

[52] Anne Lemnitzer et al. "Nonlinear efficiency of bored pile group under lateral loading". In: *Journal of geotechnical and geoenvironmental engineering* 136.12 (2010), pp. 1673–1685.

[53] Weichao Li, David Igoe, and Kenneth Gavin. "Evaluation of CPT-based P–y models for laterally loaded piles in siliceous sand". In: *Geotechnique Letters* 4.2 (2014), pp. 110–117.

[54] Robert L Little and Jean-Louis Briaud. *Full scale cyclic lateral load tests on six single piles in sand*. Tech. rep. TEXAS A and M UNIV COLLEGE STATION DEPT OF CIVIL ENGINEERING, 1988.

[55] JH Long and Geert Vanneste. "Effects of cyclic lateral loads on piles in sand". In: *Journal of Geotechnical Engineering* 120.1 (1994), pp. 225–244.

[56] D Loukidis and V Vavourakis. "Limit lateral resistance of vertical piles in plane strain". In: *Numerical Methods in Geotechnical Engineering-Proceedings of the 8th European Conference on Numerical Methods in Geotechnical Engineering, NUMGE 2014*. Vol. 1. 2014, pp. 681–685.

[57] Nicos Makris. "Soil–pile interaction during the passage of Rayleigh waves: an analytical solution". In: *Earthquake engineering & structural dynamics* 23.2 (1994), pp. 153–167.

[58] S Marchetti et al. "The flat dilatometer test (DMT) in soil investigations-A report by the ISSMGE committee TC16". In: *International Conference on Insitu Measurement of Soil Properties and Case Histories (Insitu 2001)*. Parahyangan Catholic University. 2001, pp. 95–131.

[59] Leonardo Massone and Anne Lemnitzer. "The Influence of RC Nonlinearity on py Curves for CIDH Bridge Piers". In: *DFI Journal: The Journal of the Deep Foundations Institute* 6.1 (2012), pp. 33–40.

[60] Hudson Matlock. "Correlations for design of laterally loaded piles in soft clay". In: *Offshore technology in civil engineering's hall of fame papers from the early years* (1970), pp. 77–94.

[61] Hudson Matlock and EA Ripperger. "Procedures and instrumentation for tests on a laterally loaded pile". In: *Proceedings, Eighth Texas Conference on Soil Mechanics and Foundation Engineering*. 1956.

[62] Bramlette McClelland and John A Focht. “Soil modulus for laterally loaded piles”. In: *Transactions of the American Society of Civil Engineers* 123.1 (1958), pp. 1049–1063.

[63] M McVay et al. “Centrifuge modeling of laterally loaded pile groups in sands”. In: *Geotechnical Testing Journal* 17.2 (1994).

[64] Y Meimon, F Baguelin, and JF Jezequel. “Pile group behaviour under long time lateral monotonic and cyclic loading”. In: *Proceedings, Third International Conference on Numerical Methods in Offshore Piling, Inst. Francais du Petrole, Nantes, France.* 1986, pp. 285–302.

[65] Barry Joseph Meyer and Lymon C Reese. *Analysis of single piles under lateral loading.* Tech. rep. Center for Highway Research, University of Texas at Austin TX, 1979.

[66] Robert L Mokwa. “Investigation of the resistance of pile caps to lateral loading”. PhD thesis. Virginia Tech, 1999.

[67] Liam Moore and John Barrett. “A miniature 3D stress measurement module for in-situ stress analysis of heterogeneous system in package devices”. In: *Prognostics and Health Management Conference, 2010. PHM’10.* IEEE. 2010, pp. 1–9.

[68] Yasser E Mostafa and M Hesham El Naggar. “Dynamic analysis of laterally loaded pile groups in sand and clay”. In: *Canadian Geotechnical Journal* 39.6 (2002), pp. 1358–1383.

[69] David Muir Wood. “Experimental inspiration for kinematic hardening soil models”. In: *Journal of engineering mechanics* 130.6 (2004), pp. 656–664.

[70] Jack M Murchison and Michael W O’Neill. “Evaluation of py relationships in cohesionless soils”. In: *Analysis and design of pile foundations.* ASCE. 1984, pp. 174–191.

[71] George Mylonakis. “Simplified model for seismic pile bending at soil layer interfaces”. In: *Soils and Foundations* 41.4 (2001), pp. 47–58.

[72] SA Naramore and FY Feng. *FIELD TESTS OF LARGE DIAMETER DRILLED SHAFTS. PART I-LATERAL LOADS. FINAL REPORT*. Tech. rep. 1990.

[73] NO Nawari, R Liang, and J Nusairat. "Artificial intelligence techniques for the design and analysis of deep foundations". In: *Electronic Journal of Geotechnical Engineering* 4 (1999), pp. 1–21.

[74] F Pooya Nejad et al. "Prediction of pile settlement using artificial neural networks based on standard penetration test data". In: *Computers and Geotechnics* 36.7 (2009), pp. 1125–1133.

[75] Charles WW Ng, Limin Zhang, and Dora CN Nip. "Response of laterally loaded large-diameter bored pile groups". In: *Journal of Geotechnical and Geoenvironmental Engineering* 127.8 (2001), pp. 658–669.

[76] Milos Novak, Fakhry Aboul-Ella, and Toyoaki Nogami. "Dynamic soil reactions for plane strain case". In: *Journal of the Engineering Mechanics Division* 104.4 (1978), pp. 953–959.

[77] EA Novello. "From static to cyclic py data in calcareous sediments". In: *Proc. 2nd Int. Conf. on Engineering for Calcareous Sediments*. 1999, pp. 17–27.

[78] Michael W O'Neill and Sal Michael Gazioglu. *An evaluation of py relationships in clays*. University of Houston, Department of Civil Engineering, 1984.

[79] Michael W O'Neill and Jack M Murchison. *An evaluation of py relationships in sands*. University of Houston, 1983.

[80] PL Pasternak. "On a new method of an elastic foundation by means of two foundation constants". In: *Gosudarstvennoe Izdatelstvo Literaturi po Stroitelstuve i Arkhitekture* (1954).

[81] Harry G Poulos. "Behavior of laterally loaded piles I. Single Piles." In: *Journal of Soil Mechanics & Foundations Div* (1971).

[82] Harry G Poulos. “Behavior of laterally loaded piles II. Pile groups”. In: *Journal of Soil Mechanics & Foundations Div* (1971).

[83] HG Poulos et al. “Comparisons between theoretical and observed behaviour of pile foundations”. In: (1980).

[84] Mark Felton Randolph and GT Houlsby. “The limiting pressure on a circular pile loaded laterally in cohesive soil”. In: *Geotechnique* 34.4 (1984), pp. 613–623.

[85] Lymon C Reese. “Analysis of laterally loaded piles in weak rock”. In: *Journal of Geotechnical and Geoenvironmental engineering* 123.11 (1997), pp. 1010–1017.

[86] Lymon C Reese, William R Cox, and Francis D Koop. “Analysis of laterally loaded piles in sand”. In: *Offshore Technology in Civil Engineering Hall of Fame Papers from the Early Years* (1974), pp. 95–105.

[87] Lymon C Reese and Hudson Matlock. *Non-dimensional solutions for laterally-loaded piles with soil modulus assumed proportional to depth*. Association of Drilled Shaft Contractors, 1956.

[88] Lymon C Reese and W Randall Sullivan. *Documentation of computer program COM624*. Geotechnical engineering center, Department of civil engineering, University of Texas., 1980.

[89] Lymon C Reese and William F Van Impe. *Single piles and pile groups under lateral loading*. CRC Press, 2010.

[90] Lymon C Reese and Robert C Welch. “Lateral loading of deep foundations in stiff clay”. In: *Journal of the Geotechnical engineering division* 101.7 (1975), pp. 633–649.

[91] Lymon C Reese et al. “Computer program Lpile plus version 5.0 technical manual”. In: *Ensoft, Inc., Austin, Texas* (2000).

[92] E Reissner. “A note on deflections of plates on a viscoelastic foundation”. In: *J. Appl. Mech., ASME* 25 (1958), pp. 144–145.

[93] Peter Kay Robertson, Michael Paul Davies, and Richard G Campanella. "Design of laterally loaded driven piles using the flat dilatometer". In: *Geotechnical Testing Journal* 12.1 (1989), pp. 30–38.

[94] Peter K Robertson et al. "Design of laterally loaded displacement piles using a driven pressuremeter". In: *Laterally Loaded Deep Foundations: Analysis and Performance*. ASTM International, 1984.

[95] PK Robertson et al. "Design of axially and laterally loaded piles using in situ tests: A case history". In: *Canadian Geotechnical Journal* 22.4 (1985), pp. 518–527.

[96] Kyle M Rollins, J Dusty Lane, and Travis M Gerber. "Measured and computed lateral response of a pile group in sand". In: *Journal of Geotechnical and Geoenvironmental Engineering* 131.1 (2005), pp. 103–114.

[97] Kyle M Rollins, Kris T Peterson, and Thomas J Weaver. "Lateral load behavior of full-scale pile group in clay". In: *Journal of geotechnical and geoenvironmental engineering* 124.6 (1998), pp. 468–478.

[98] Kyle M Rollins and Andrew Sparks. "Lateral resistance of full-scale pile cap with gravel backfill". In: *Journal of Geotechnical and Geoenvironmental Engineering* 128.9 (2002), pp. 711–723.

[99] Kyle M Rollins et al. "Pile spacing effects on lateral pile group behavior: load tests". In: *Journal of Geotechnical and Geoenvironmental Engineering* 132.10 (2006), pp. 1262–1271.

[100] Pedro F Ruesta and Frank C Townsend. "Evaluation of laterally loaded pile group at Roosevelt Bridge". In: *Journal of Geotechnical and Geoenvironmental Engineering* 123.12 (1997), pp. 1153–1161.

[101] JOHN WATT SANDEMAN. "Experiments on the resistance to horizontal stress of timber piling". In: *Van Nostrand's Engineering Magazine (1879-1886)* 23.144 (1880), p. 493.

[102] JH Schmertmann. *Guidelines for using the CPT, CPTU and Marchetti DMT for geotechnical design, Rep. No.* Tech. rep. FHWA-PA-87-022+ 84-24 to PennDOT, Office of Research and Special Studies, Harrisburg, PA, 1988.

[103] Ronald F Scott. "Analysis of centrifuge pile tests; simulation of pile-driving". In: (1980).

[104] Mohamed A Shahin. "Intelligent computing for modeling axial capacity of pile foundations". In: *Canadian Geotechnical Journal* 47.2 (2010), pp. 230–243.

[105] Mohamed A Shahin. "Load–settlement modeling of axially loaded steel driven piles using CPT-based recurrent neural networks". In: *Soils and Foundations* 54.3 (2014), pp. 515–522.

[106] AW Skempton. "The bearing capacity of clays". In: (1951).

[107] Volker Slowik, Evelyn Schlattner, and Thomas Klink. "Fibre Bragg grating sensors in concrete technology". In: *p109-120, Leipzig Annual Civil Engineering Report* 3-1998 (1998).

[108] António G de Sousa Coutinho. "Data reduction of horizontal load full-scale tests on bored concrete piles and pile groups". In: *Journal of Geotechnical and Geoenvironmental Engineering* 132.6 (2006), pp. 752–769.

[109] Jonathan P Stewart et al. "Full scale cyclic testing of foundation support systems for highway bridges. Part II: Abutment backwalls". In: *UCLA Structural and Geotechnical Engineering Laboratory* UCLA-SGEL 2007/02 (2007).

[110] Juirnarongrit. Teerawut and Scott A Ashford. "SSRP–2001/22 Effect of pile diameter on the modulus of sub-grade reaction". In: (2005).

[111] Karl Terzaghi. "Evalution of conefficients of subgrade reaction". In: *Geotechnique* 5.4 (1955), pp. 297–326.

[112] John P Turner. *Rock-socketed shafts for highway structure foundations*. Vol. 360. Transportation Research Board, 2006.

[113] John P Turner, Fred H Kulhawy, and Wayne A Charlie. *Review of load tests on deep foundations subjected to repeated loading*. Tech. rep. Cornell Univ., Ithaca, NY (USA). Geotechnial Engineering Group; Electric Power Research Inst., Palo Alto, CA (USA), 1987.

[114] John W Wallace et al. "Cyclic large deflection testing of shaft bridges: Part I-Background and field test results". In: *Report to California Department of Transportation, December* (2001).

[115] James Matthew Walsh. "Full-scale lateral load test of a 3x5 pile group in sand". In: (2005).

[116] Daniel Wayne Wilson. "Soil-pile-superstructure interaction in liquefying sand and soft clay". PhD thesis. Citeseer, 1998.

[117] E Winkler. "Theory of elasticity and strength". In: *Dominicus Prague, Czechoslovakia* (1867).

[118] Jianfeng Xue et al. "Optimization Technique to Determine the py Curves of Laterally Loaded Stiff Piles in Dense Sand". In: *Geotechnical Testing Journal* 39.5 (2016), pp. 842–854.

[119] Ke Yang and Robert Liang. "Methods for deriving py curves from instrumented lateral load tests". In: (2006).

[120] Ke Yang, Robert Liang, Shuyu Liu, et al. "Analysis and test of rock-socketed drilled shafts under lateral loads". In: *Alaska Rocks 2005, The 40th US Symposium on Rock Mechanics (USRMS)*. American Rock Mechanics Association. 2005.

Appendix A

Small-Scale Conceptual Testing of 3D Strain Gauge Carriers

A.1 Introduction

Two suitable measurement techniques for internal 3D strain measurements have been identified upon extensive literature review, and are evaluated using small-scale laboratory testing on cubical and cylindrical test specimens made of epoxy resin and regular strength concrete. This chapter describes the selection of the carrier structures, their fabrication, material properties and test results under compressive loading.

A.1.1 Tetrahedral Skeleton Concept

Based on the fundamental principle proposed by Slowik [107], the first gauge carrier consists of three equilateral triangles assembled in a tetrahedral configuration. The tetrahedron is fabricated using flat copper bars of equal length and width. The individual components are

glued or welded at the nodes to form a rigid construction joint. The selection of copper was guided by the objective to minimize potential stiffness contrasts between the host and carrier material and to reduce the influence of the sensor instrumentation on the surrounding strain field. Copper's modulus of elasticity (E= $1.7 * 10^7$ psi) is closest to the elastic modulus of concrete (E= $2 * 10^6$ psi to $6 * 10^6$ psi). Other materials under consideration for this application were brass, steel and aluminum. Brass (E= $1.6 * 10^7$ psi) would have been an alternative option, while steel and aluminum were found to be unsuitable. Steel's stiff material properties (E= $2.9 * 10^7$ psi) are incompatible with the much more brittle host materials (i.e. resin or concrete material). The use of aluminum, whose chemical reaction with the cement would have led to expansion and damage of the surrounding cementitious matrix, was eliminated early in the selection process.

Instrumentation Each of the six tetrahedron sides accommodates one strain gauge as shown in Fig. A.1. The strain gauges selected were Micro-Measurement model EA-06-240LZ-120/E gauges. The EA gauges are 0.27 in in length and 0.12 in in width. The gauges were affixed to the carrier bars using M-BOND 200 adhesive and coated with M-Coat A and M- Coat B per manufacturers instructions. The strain gauges have temperature resistance from -100 to 350 °F and sensitivity of 0.5 micro-strain (0.5 ppm).

Figures A.1b - A.1d show the manufacturing process of a tetrahedron composed of 1 inch long, and 0.20 inch wide bars. Fig. A.2 shows the finished product before the attachment of the sensor wires. Bigger tetrahedra, composed of 2 inch long bars, have also been manufactured. Both types of tetrahedra have been installed in the cubical and cylindrical specimens to study the influence of their size on the surrounding strain field.

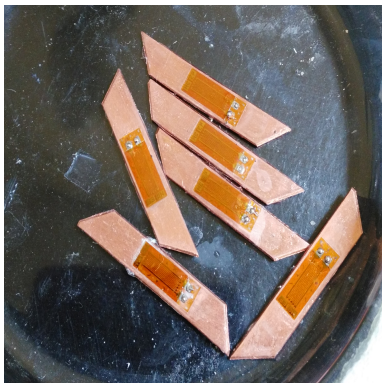

(a)

(b)

(c)

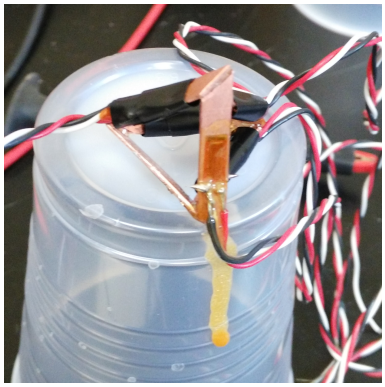

(d)

Figure A.1: Manifacture procedure of a 1-in tetrahedron.

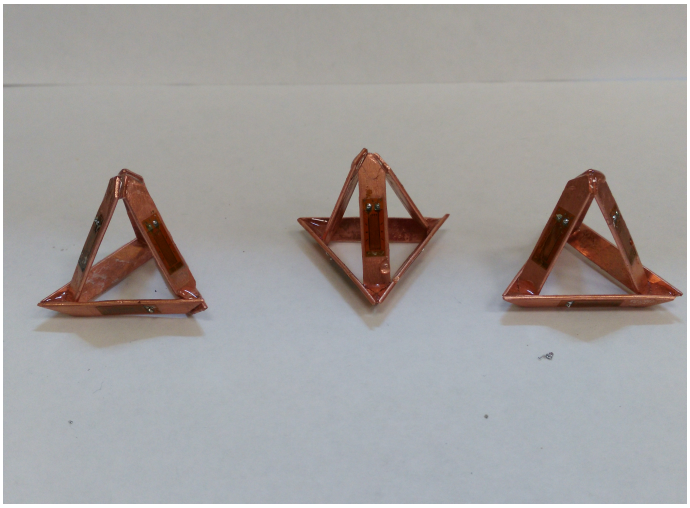

Figure A.2: Completed 1 in tetrahedra.

A.1.2 Solid Cube Concept

In addition to the skeletal tetrahedron described above, a solid cube, made of the host material, was evaluated as potential strain gauges carrier. This method is based on the research work by Moore and Barrett [67] and proposes to attach three strain gauges in a rosette-type configuration. The angle between gauges was selected as 45° from each other. Three faces of a 1-in cube made of aluminum filled castable epoxy were instrumented as shown in Fig. A.3. The strain gauges attached to the cube are the same as used for the tetrahedron.

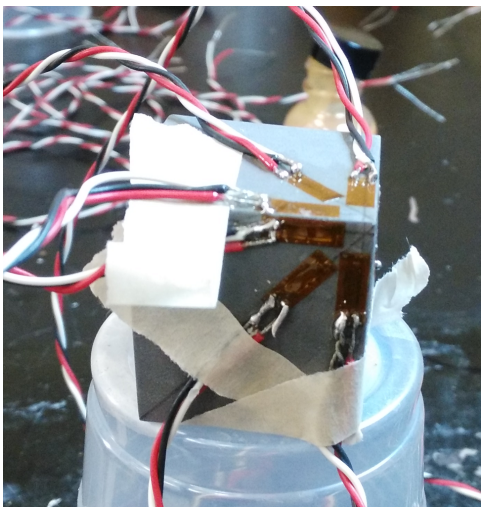

Figure A.3: Sample of a 1-in cube made of epoxy that hosts nine strain gauges in rosette configuration.

A.2 Casting Materials

The test specimens were fabricated using an aluminum-filled castable epoxy resin and a regular cement-based, 4ksi-design-strength concrete. The choice of materials has been based primarily on the material's ability to serve as flexible filler. In addition to this fillability, epoxy resin provides a flexible alternative to the brittle concrete material and will allow for

an assessment of the proposed instrumentation over a larger range of strains while delaying early cracking.

A.2.1 Aluminum Filled Castable Epoxy

The EpoxACast 655 material (manufacturer: *Smooth on*) is an aluminum filled castable epoxy, with Hardener 103 Slow, mixed in a ratio of 100A:12B by weight, where A is the base and B is the hardener. The modulus of elasticity is 2040 ksi. Table A.1 presents the material properties, published by the manufacturer. It can be noted that the resin's flexural strength is approximately ten times larger than the concrete flexural strength.

Table A.1: EpoxACast655 physical properties (from: *Smooth on*).

Mixed Viscosity-cps. (ASTM D2393)	23000
Specific Gravity- Mixed; g/c.c. (ASTM D1475)	1.66
Specific Volume- Mixed; in^3/lb (ASTM D792)	16.7
Shore D Hardness (ASTM D2240)	90
Ultimate Tensile - psi (ASTM D638)	4810
Tensile Modulus - ksi (ASTM D638)	2040
Ultimate Elongation - % (ASTM D638)	0.54
Flexural Strength - ksi (ASTM D790)	7.7
Flexural Modulus - ksi (ASTM D790)	1403
Compressive Strength - ksi (ASTM D695)	12.5
Compressive Modulus - psi (ASTM D695)	125500
Shrinkage - in/in (ASTM D-2566)	0.0006
Heat Deflection Temp. (ASTM D648)	135° F/ 57°C

A.2.2 Concrete

In addition to the resin specimen, and to better replicate the future model scale testing, additional proof of concept testing was executed using regular concrete as casting material. The selected concrete was a commercially available, premade concrete mix (manufacturer: *Quikrete*), consisting of a mixture of gravel, sand, and Portland cement. The design concrete compression strength was 4000 psi.

A.3 Specimen Construction

A total of 15 small scale test specimens were prepared. Table A.2 summarizes the specimen dimensions and type of instrumentation carriers embedded in the test specimens.

Table A.2: Compression tests list.

# Test	**Dimensions**	**Material**	**# Samples**	**Instrumentation**	
				# Tetrahedra	**# Cubes**
Cube	3 in. × 3 in.	Epoxy	11	1	0
Cube	8 in. × 8 in.	Epoxy	1	4	3
Cylinder	6 in. × 12 in.	Concrete	3	3	0

The following subchapters will describe the fabrication of the 3 types of test specimens listed in Table A.2.

A.3.1 3 inch and 8 inch Resin Cubes

The epoxy mixture presented in Chapter A.2.1 was used for all 12 resin cubes listed in Table A.2. The fabrication of the test specimen followed similar procedures: specimen mold

construction, placement of the internal instrumentation carriers (tetrahedra and cubes), and mold filling with the host material. The mold for the small (3x3x3 inch) specimens was created using five modular metallic plates, as shown in Fig. A.4a. A wax-based non-silicone liquid (Ease Release 2831, *Smooth-on*) was applied to the inside of the mold in order to enable an easy detachment of the specimen after curing. The small (3 in) specimens were instrumented with a 2 in. tetrahedron placed in the center of the mold and immersed in metal-filled castable epoxy resin. The tetrahedron was secured with wooden and epoxy sticks during the filling process. Figure A.4 describes the construction process of the 3 inch test specimens.

The 8 in test specimen was fabricated in an identical manner. The larger cube was furnished with a variety of sensor instrumentation to assess and compare the ability of the instrumentation to capture strains across the cross-section of the cube, and verify the strain measurements through sensor redundancy. The 8-in cube hosts three 1 inch cubes carriers, three 1 inch tetrahedral carriers, and one 2 in. tetrahedral carriers. Each gauge carrier was positioned on tiny epoxy columns with varying length, in order to reach a preselected height. Figure A.5 shows the internal disposition of the strain gauge carriers for the 8 inch epoxy cube. Figure A.6 shows the construction procedure for the 8 inch specimen.

A.3.2 Concrete Cylinder Specimens

Figure A.7 shows the fabrication process of the three concrete cylinder specimens. A standard concrete cylinder mold, used for compressive strength testing according to ASTM C39 was used to ease the specimen construction process. Hence, each specimen had a diameter of 6 inch and a height of 12 inch. Each concrete cylinder accommodated three 2-inch tetrahedral carriers. The tetrahedrons were vertically aligned and spaced with the aid of wood sticks as shown in Fig. A.7a. The cement based concrete described in Chapter A.2.2 was poured

around the gauge carriers until the mold was filled. The strain gauge wires were guided to the outside of the specimen using pre-drilled holes which were sealed with hot glued during concrete pouring (Figs. A.7b, A.7c).

Figure A.8 shows a schematic of the cylinder specimens with the internal arrangement of the tetrahedrons.

A.4 Test Setup and Loading Protocols

Figure A.9 shows a schematic layout of the compressive load testing on the instrumented test specimens. Testing was executed in a Tinus Olsen compression testing machine and data readings were recorded with a National Instrument Data acquisition system. The specimen (1) with internal strain gauge carriers (2) was mounted on a Tinius Olsen compression testing machine in the Structural Engineering Testing Hall (SETH) Laboratory at UC Irvine. The cube-shaped test specimen were subjected to compressive loading in two directions as shown in Fig. A.10a. The cylinder specimens were subject to uniaxial loading in z-direction only (Fig. A.10b). The specimen-specific loading protocols are explained in further detail below:

Loading Protocol 3 inch x 3 inch Cubes

The 3 inch cubical specimens were subjected to loading in y direction (Load I) and x direction (Load II), as shown in presented in Fig. A.11 and in Table A.3. Loading was increased as long as the specimen was not damaged during the previous loading cycle.

Table A.3: 3 in. cubes test summary.

Test	Cube	Load Direction	Max Load	Step Loads
1	T1	-y	3 kips	1, 2, 3 kips
2	T1	+x	3 kips	1, 2, 3 kips
3	T1	-y	93 kips	3, 5, 20, 50, 100 kips
4	T2	-y	3 kips	1, 2, 3 kips
5	T2	+x	3 kips	1, 2, 3 kips
6	T3	-y	20 kips	3, 5, 10, 15, 20 kips
7	T3	+x	20 kips	3, 5, 10, 15, 20 kips
8	T3	-y	127 kips	3, 5, 20, 50, 100, 200 kips
9	T4	-y	3 kips	1, 2, 3 kips
10	T4	+x	3 kips	1, 2, 3 kips
11	T5	-y	20 kips	5, 10, 15, 20 kips
12	T5	+x	20 kips	3, 5, 10, 15, 20 kips
13	T5	-y	130 kips	3, 5, 20, 50, 100, 200 kips

Loading Protocol 8 in. Cube

The loading direction of the 8 in. cube is shown in Fig. A.5. The step load was applied in -y direction. Table A.4 presents the loading protocol used for the three concrete cylinders.

Table A.4: 8 in. cube test summary.

Test	Max Load	Step Loads
1	50 kips	3, 5, 20, 50 kips
2	122 kips	3, 5, 20, 50, 100, 122 kips
3	100 kips	3, 5, 20, 50, 100 kips

Loading Protocol for Concrete Cylinders

The loading protocol for the three concrete cylinders is presented in Fig. A.8 and Table A.5. The compressive load was applied with a -z direction on the cylinders' top.

Table A.5: Cylinders test summary.

Test	**Cylinder**	**Max Load**	**Step Loads**
1	C1	30 kips	5, 15, 30 kips
2	C2	30 kips	5, 15, 30 kips
3	C3	50 kips	5, 15, 30, 50 kips

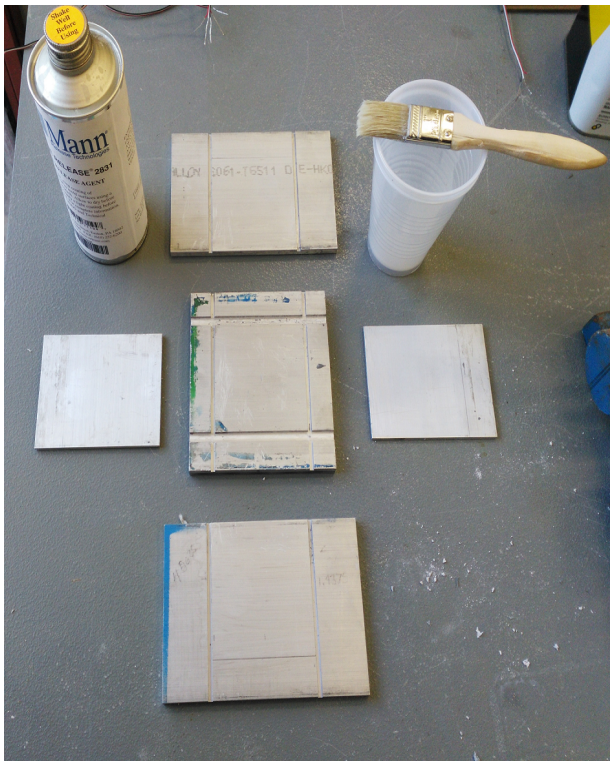

(a)

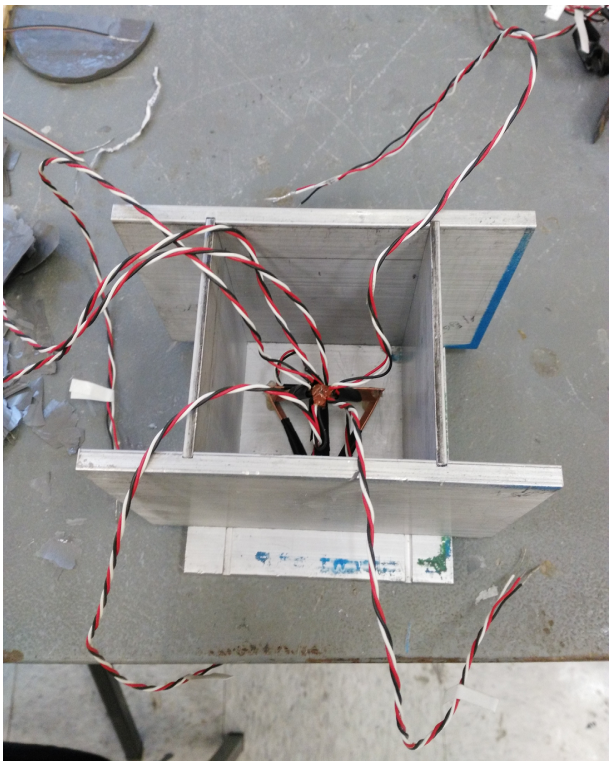

(b)

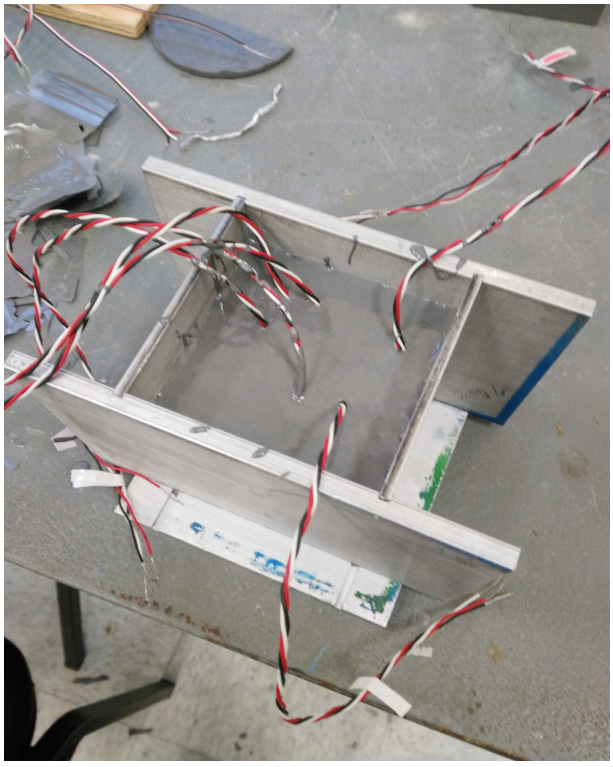

(c)

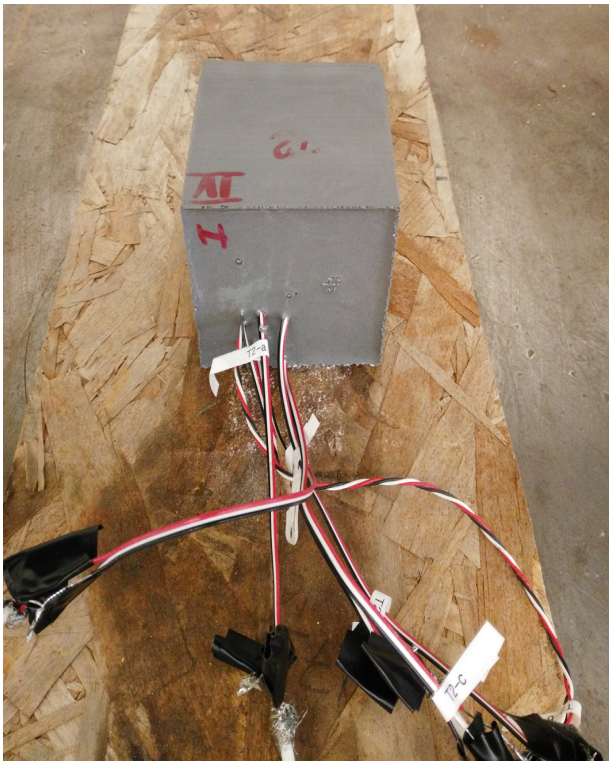

(d)

Figure A.4: Construction phases of a 3-in cube made of epoxy resin.

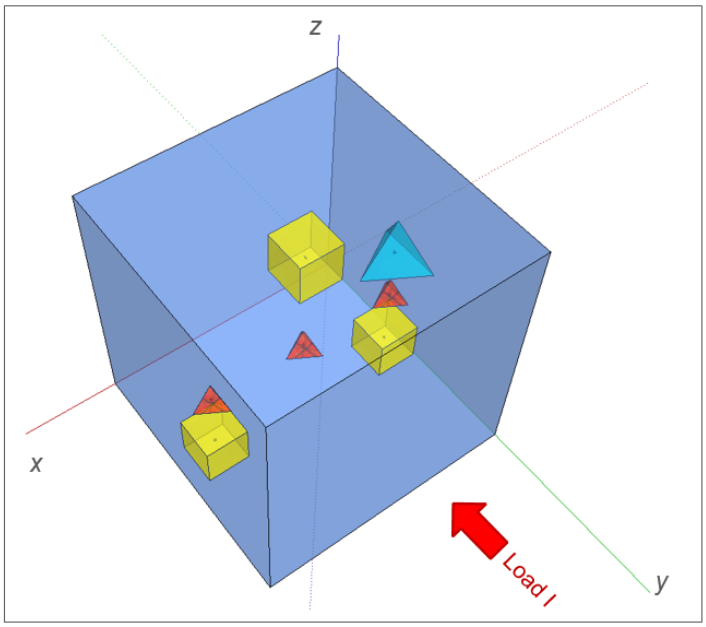

Figure A.5: 8-in cube setup and loading direction.

(a)

(b)

(c)

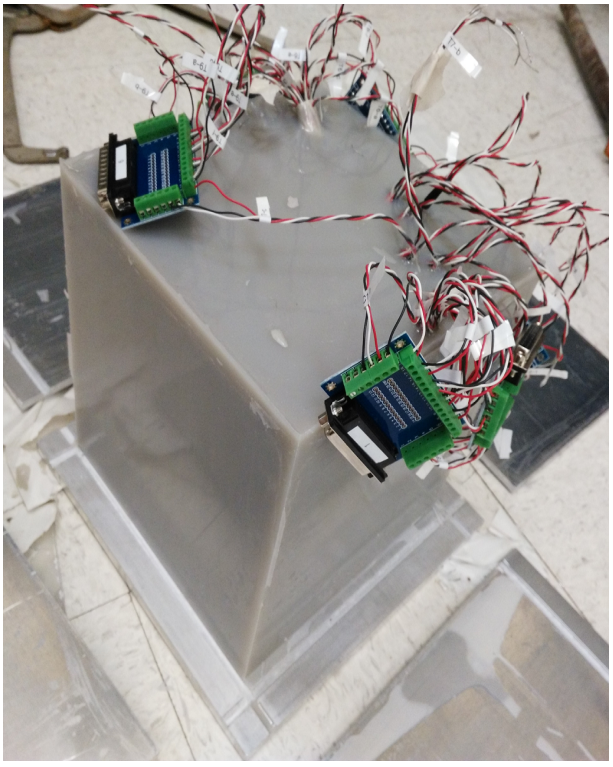

(d)

Figure A.6: Construction phases of a 8-in cube made of epoxy resin.

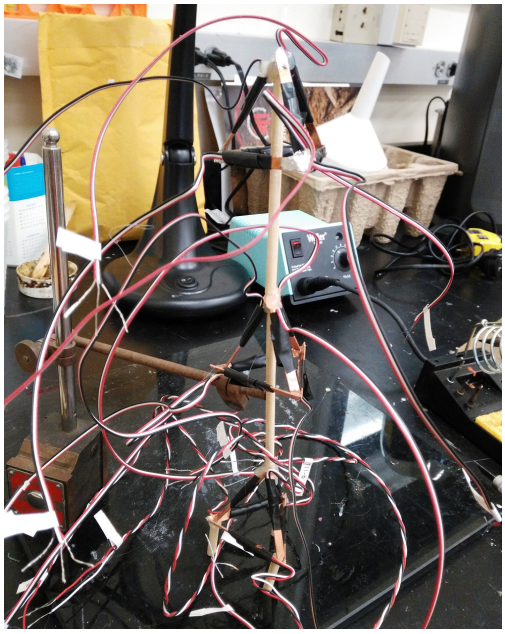

(a)

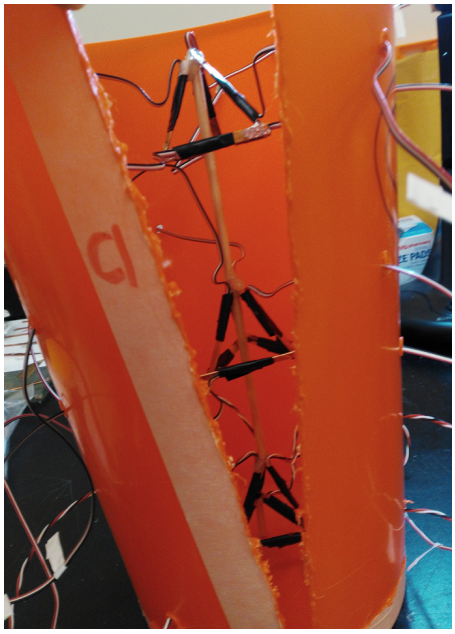

(b)

(c)

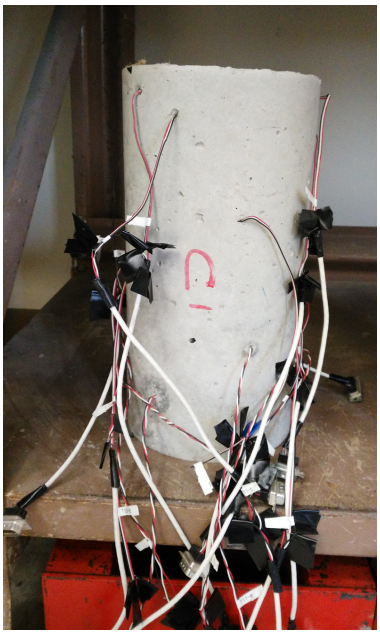

(d)

Figure A.7: Construction phases of a concrete cylinder.

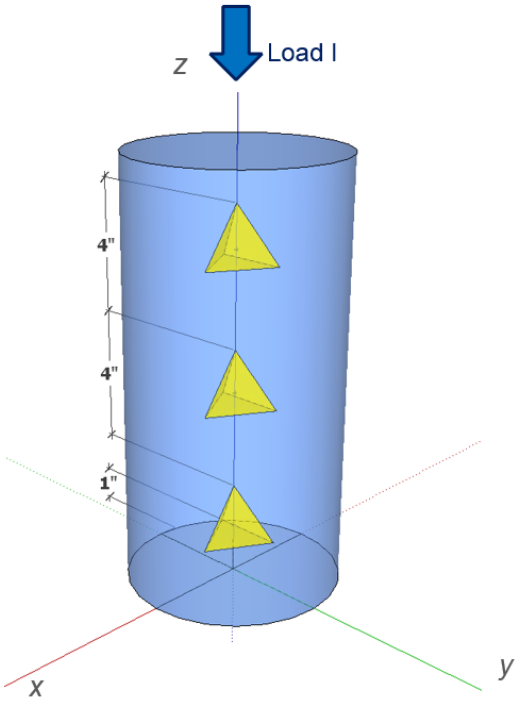

Figure A.8: Concrete cylinders setup and loading direction.

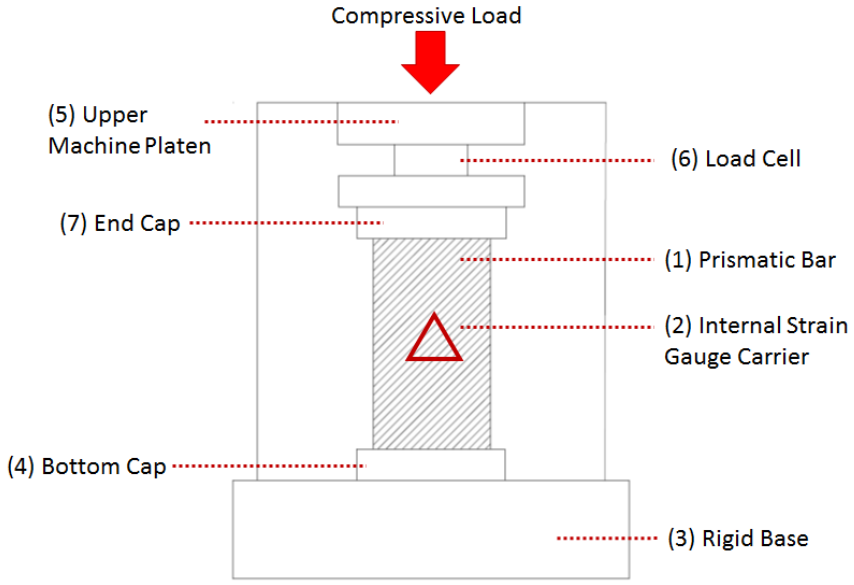

Figure A.9: Schematic of the compression machine layout.

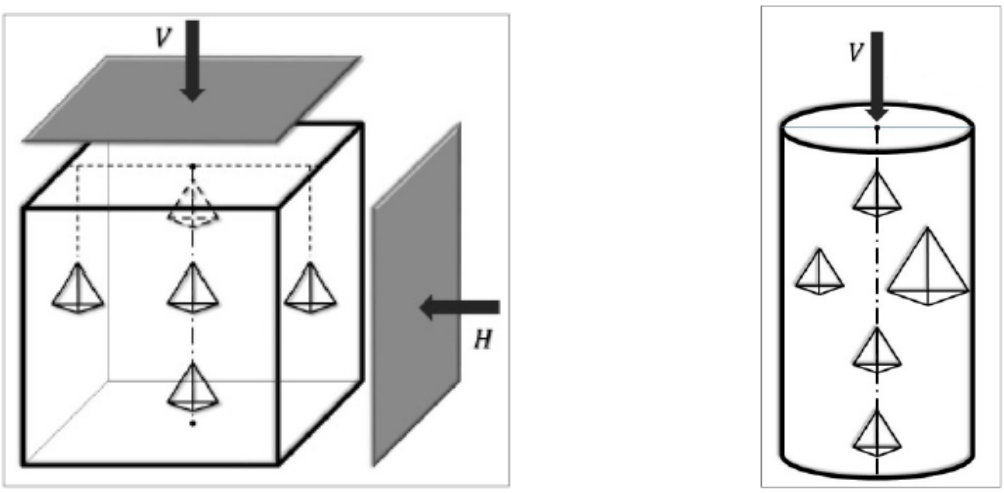

(a) Cubic specimen (b) Cylindrical specimen

Figure A.10: Schematic representation of specimen loading during proof of concept testing.

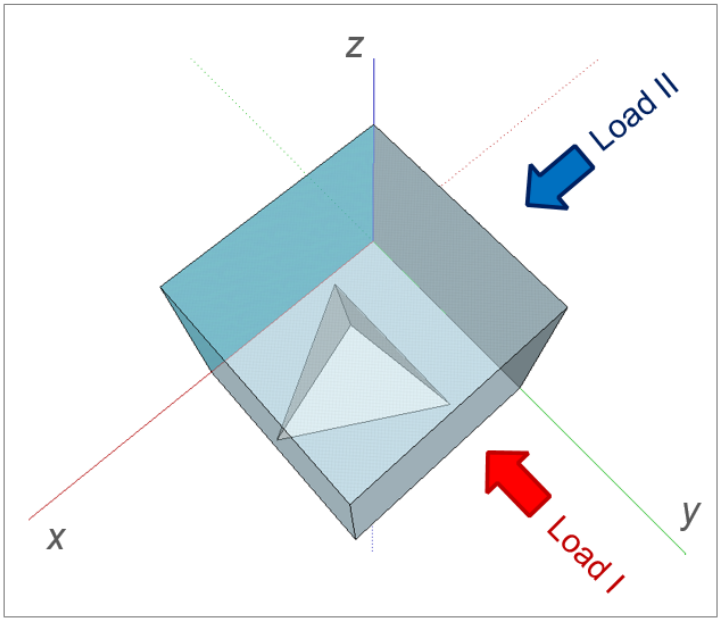

Figure A.11: 3 in cubes setup and loading direction.

A.5 Experimental Results: Strain Readings

A.5.1 3 in. Cubes

Specimen testing began in March, 2016, and was completed in October, 2016. A total of 13 compression tests were performed on all 5 specimen as outlined in Table A.3. The load and the strain readings of specimen *T5* are presented for reference. Figures A.12 and A.13 show the load vs. time histories for specimen *T5* in $+x$ and $-y$ directions, respectively. Loading was applied as step function with load steps shown in Table A.3. This loading protocol was followed for all cubical specimens. After reaching a target load level, the loading was held to allow sufficient time for strain stabilization and recording through the data acquisition system. Figures A.14 and A.15 present the strain time histories for specimen *T5* in $+x$ and $-y$ directions, respectively. Strain gauges were found to respond generally well, and showed response trends consistent with the applied load levels.

Table A.6 presents an overview of the state of strain registered in each strain gauge during the different compression tests. Positive readings represent a state of tension, while negative readings mean that the copper bar was in compression. The strains of interest were those developed at the compressive loads of 3, 5, 20, and 50 kips. Each strain reading refers to a different position in the tetrahedron, as explained in Fig. 3.20b. The results labeled as *NA* are the strain readings that did not yield good results, because the gauges were damaged during the construction process or they did not behave as expected since they register almost no change in strain during the test.

Table A.6: State of strain registered in strain gauges installed in 3 in cubes.

Test	**Load**	**a**	**b**	**c**	**d**	**e**	**f**
T1	+x	Compression	Tension	Compression	NA	Tension	Tension
T2	+x	Tension	Compression	Compression	Tension	NA	Tension
T4	+x	Tension	Compression	Compression	Tension	Tension	Tension
T3	+x	Tension	Compression	Compression	Tension	Tension	NA
T5	+x	Tension	Compression	Compression	Tension	Tension	Compression
T1	-y	NA	Compression	NA	Tension	NA	Tension
T2	-y	Compression	NA	Tension	Tension	Tension	Tension
T4	-y	Compression	NA	NA	Tension	Tension	Tension
T3	-y	Compression	Tension	Compression	NA	Tension	NA
T5	-y	Compression	Tension	Compression	Tension	Tension	Tension
T4	-y	Compression	Tension	Compression	Tension	Tension	Tension
T1	-y	Compression	Compression	Compression	Tension	Tension	Tension
T3	-y	Compression	Tension	Compression	NA	NA	NA
T5	-y	Compression	Tension	Compression	Tension	Tension	Tension

A.5.2 8 in. Cube

Fig. A.16 shows the step loading curve vs. time in the *-y* direction for a maximum compressive load of 100 kips. The data readings presented correspond to a stepwise loading

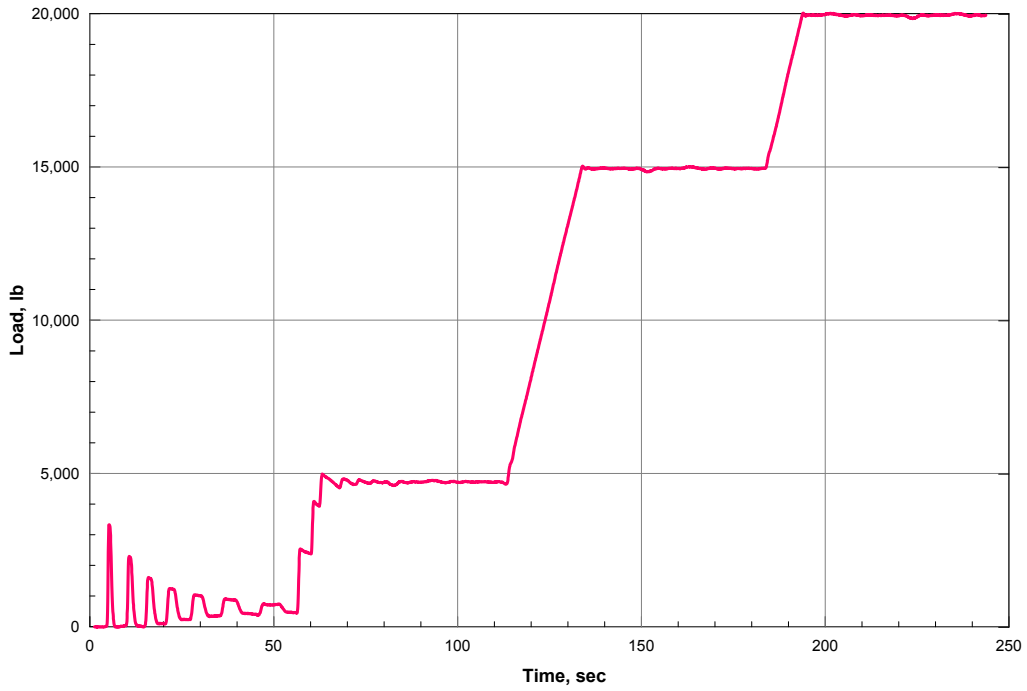

Figure A.12: Loading curve vs. time for cubical specimen T5 in $+x$ direction.

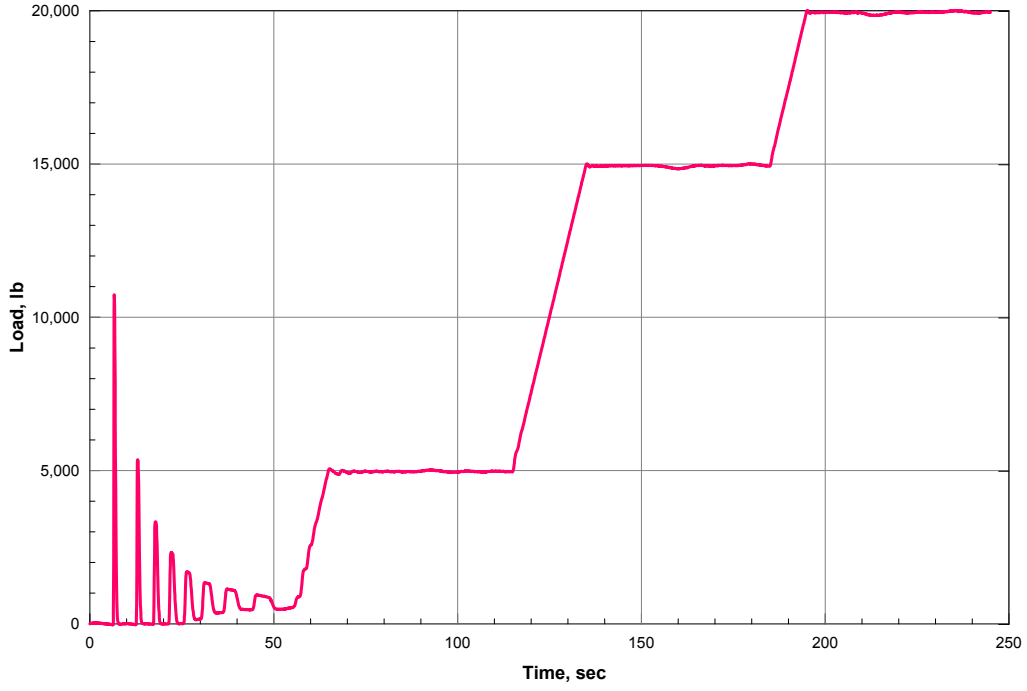

Figure A.13: Loading curve vs. time for cubical specimen T5 in $-y$ direction.

ranging from of 3, 5, 20, 50, up to 100 kips. Figures A.17 and A.18 depict the load-time and strain-time histories recorded from the embedded cube carrier C1 and the tetrahedron

carrier T9 during the test of the 8-inch cube specimen for reference.

Each strain reading refers to a different position within the strain gauge carriers. It can been noted that results obtained from the epoxy cubes generally gave better results than the tetrahedron. The cubes' strain gauges responded well to the increasing compressive loading and their readings were generally less noisy. This might have been caused by a better compatibility between the strain carriers' materials and the hosting epoxy. Another advantage in using the epoxy cube as strain carrier is the redundancy of its readings.

Table A.7: State of strain registered in strain gauges installed in 8 in cube.

Test	**Load**	**a**	**b**	**c**	**d**	**e**	**f**
T6	-y	Compression	Compression	Compression	NA	NA	Tension
T6	-y	Compression	Compression	Compression	NA	NA	Tension
T7	-y	Compression	NA	Compression	Compression	NA	NA
T7	-y	Compression	NA	Compression	Compression	NA	NA
T8	-y	Compression	Tension	Compression	Tension	Tension	NA
T8	-y	Compression	NA	Compression	Tension	Tension	NA
T9	-y	Compression	Tension	Compression	Compression	Tension	Tension
T9	-y	Compression	Tension	Compression	Compression	Tension	Tension

A.5.3 Cylinders

Construction of the concrete cylinders started in May, 2016. Testing began in October, 2016, and was completed in December, 2016. A total of three tests were performed on the three

specimens as outlined in Table A.5. The load and the strain readings of specimen *C1* are presented.Fig. A.19 shows the load vs. time histories for the specimen *C1* in the -*z* direction. The same loading protocol was applied to the other cylindrical specimens. The strains of interest were those developed at the compressive loads 5, 15, 20, and 30 kips. Figs. A.20, A.21 and A.22 present the strain readings for the concrete cylinder *C1* in the -*z* direction for the top, middle, and bottom tetrahedron, respectively. Each strain reading refers to a different position in the tetrahedron, as explained in Fig. 3.20b. The strain gauge *T10-e* broke in the construction process.

A step loading behavior can be observed in the strain time histories as well as the compressive/tensile behavior of the copper bars. However, this set of tests presented a repeatability concern that was not present in the previous tests, involving epoxy specimens. The compression tests were performed three times on the concrete cylinders.

The results presented hereafter belonged to the second round of tests. Unexpected strain readings were obtained during the first and third tests. The experimental results didn' t follow the usual step loading behavior, and in some cases the strains presented a sort of cyclic behavior that is difficult to explain given the unidirectional nature of the applied load. This might be explained with the lack of adhesion between the copper and surrounding concrete, which allows the copper to slide within the concrete.

Table A.8: Strain gauges state of stress in the concrete cylinders.

Test	**Load**	**a**	**b**	**c**	**d**	**e**	**f**
T15	+z	Tension	Tension	Tension	Compression	Compression	Compression
T10	+z	Tension	Tension	Tension	Compression	NA	Compression
T11	+z	Tension	Tension	Tension	Compression	Compression	Compression
T17	+z	Tension	Tension	Tension	Compression	Compression	NA
T13	+z	Tension	Tension	Tension	NA	NA	Compression
T9	+z	Tension	NA	Tension	NA	Compression	Compression
T16	+z	Tension	Tension	Tension	NA	Compression	Compression
T14	+z	Tension	Tension	NA	Compression	Compression	NA
T12	+z	NA	Tension	NA	Compression	Compression	Compression

A.6 Analyses of Test Results

The numerical simulations provided in this chapter pertain to the 3 in. epoxy cubes, the 8 in. epoxy cube, and the concrete cylinders tests. These simulations are used for assessing the expected response of the test specimens prior to the actual tests. The simulation predictions are then compared to the test results. The numerical simulations are carried out via three-dimensional Finite Element Method (FEM) and the compute program used is a finite element analysis package ABAQUS.

The epoxy cubes and the concrete cylinders consist of solid and truss element. The solid and the truss elements are used for modeling the casting materials (e.g. epoxy and concrete),

and the embedded copper, respectively. For every simulation, two ABAQUS models were developed. The first one included the copper tetrahedron inside the cubical or cylindrical specimen. The second one is identical to the first model in geometry and mechanical properties, but it does not host any tetrahedron. These simulations were ran with the purpose of understanding whether the tetrahedron was interfering with the state of stress of the specimen it was embedded in.

Hereby, the comparisons between experimental computed data with ABAQUS are presented. A particular focus was given to the three-dimensional state of strain and stress derived from the strain gauges readings.

A.6.1 3 in. Cubes

Figures A.23 and A.24 present 3D strains derived from strain gauge readings at the loading levels of 3 kips and 20 kips, respectively. Figures A.25 and A.26 present 3D stresses for the same loading levels.

It can be noted that the 3D strains and stresses obtained from different tests are generally consistent with each other, especially in terms of state of compression (negative strain/stress) and tension (positive strain/stress). Moreover, the increase of load from 3 kips to 20 kips was properly captured, as well as the 3D state of strain and stress at the tetrahedron' s centroid, if compared to the ABAQUS results for the $+x$ and $-y$ direction, respectively.

A.6.2 Cylinders

Figures A.27 and A.28 present 3D strains and 3D stresses derived from strain gauge readings at the loading levels of 20 kips. Each figure includes the results for the top, middle, and bottom tetrahedra installed in the concrete cylinders as shown in Fig. A.8.

The results were generally satisfactory. Different cylinder tests yielded similar 3D state of strain and stress at the centroid of the three tetrahedra. It can be noted that the the stresses are higher in the top tetrahedron, which is closer to the load application, and that they progressively decrease as the distance from the top increases.

The validity of the experimental results is confirmed by the ABAQUS strains and stresses, which are in general agreement with them.

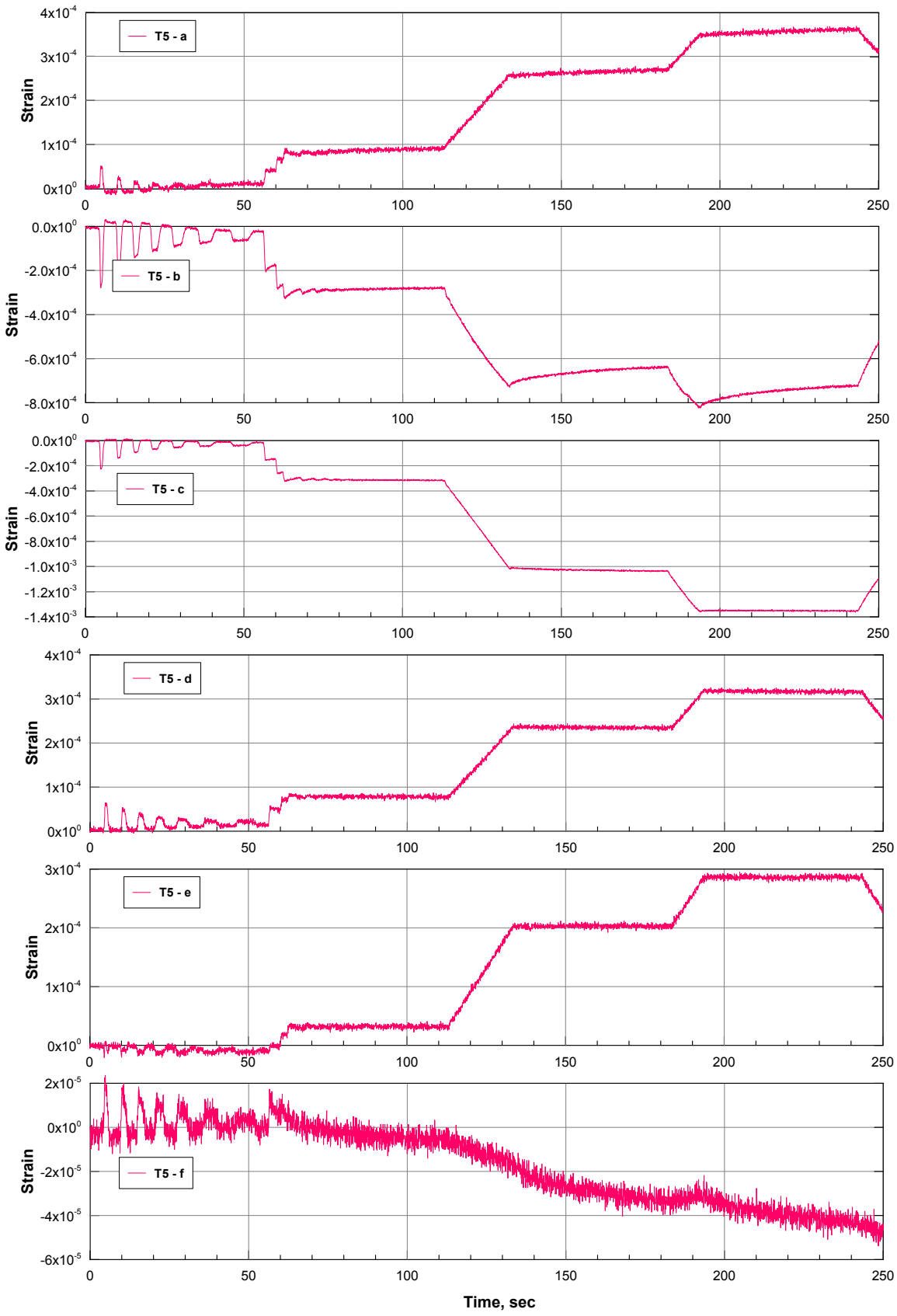

Figure A.14: Time histories cube specimen T5 in $+x$ direction.

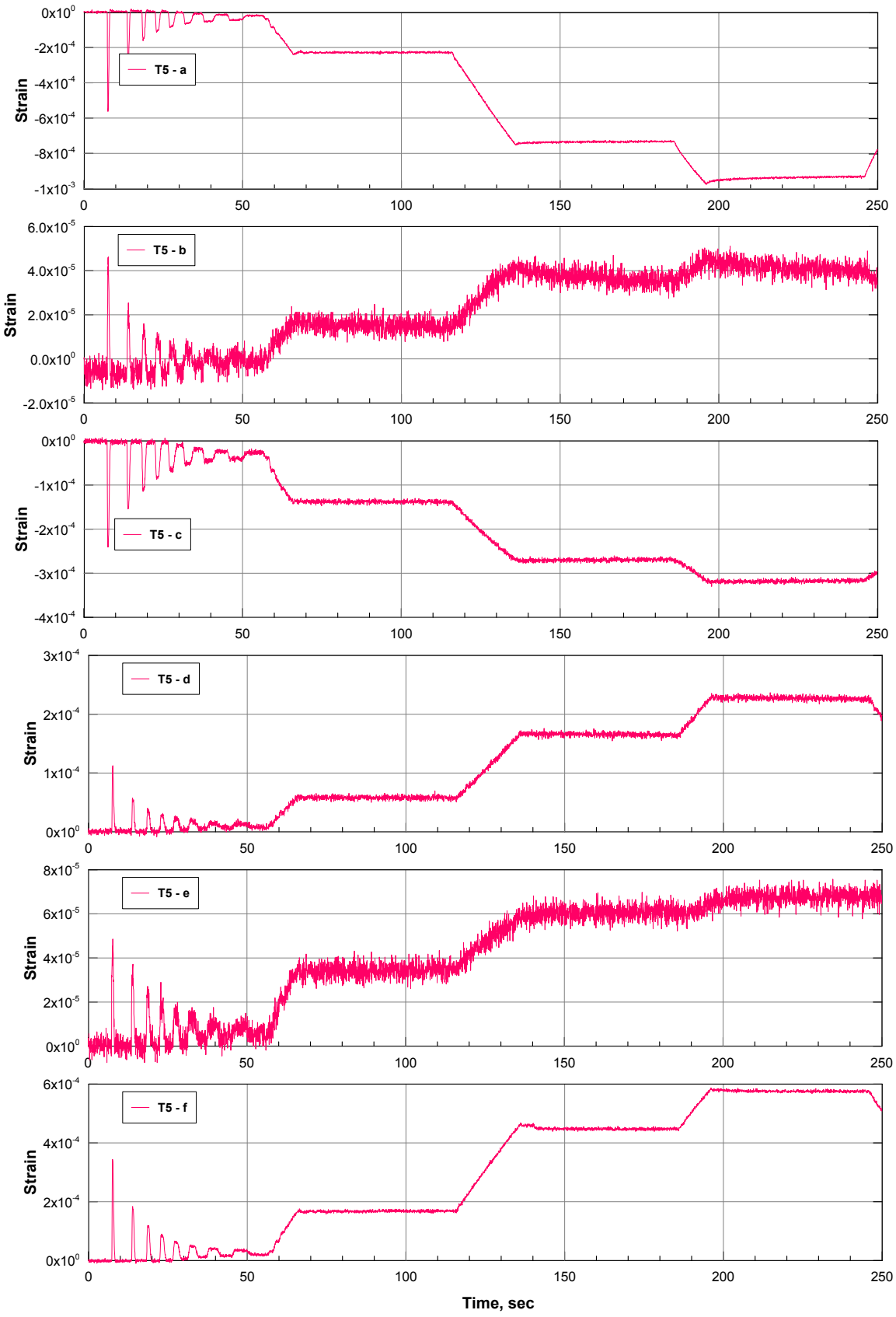

Figure A.15: Time histories cube specimen T5 in -y direction.

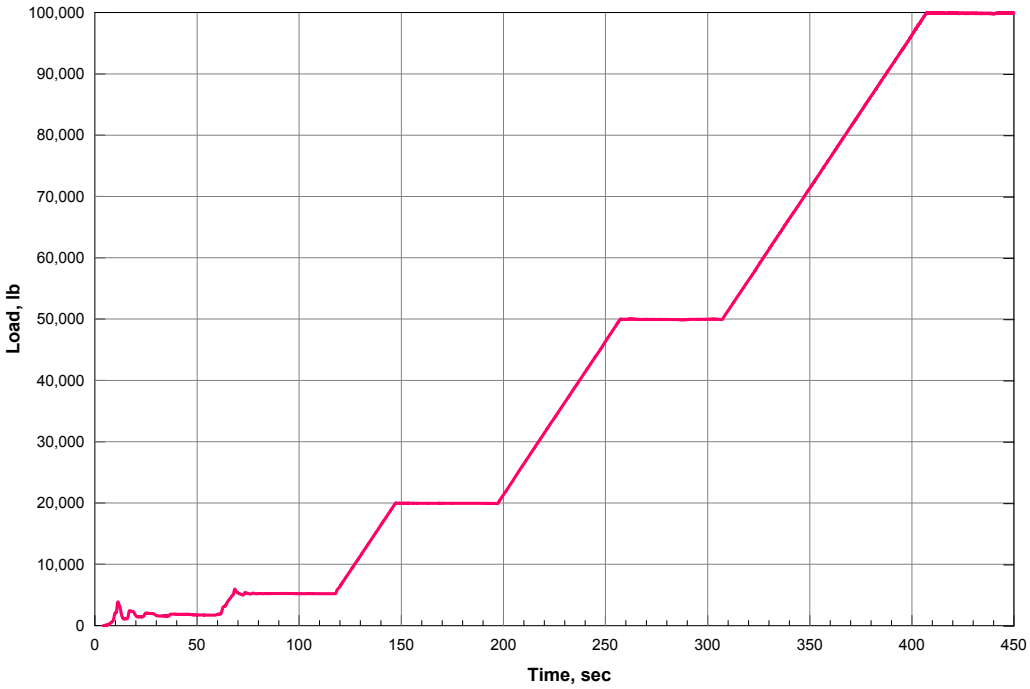

Figure A.16: Loading curve vs. time for the 8 in. cube in -y direction.

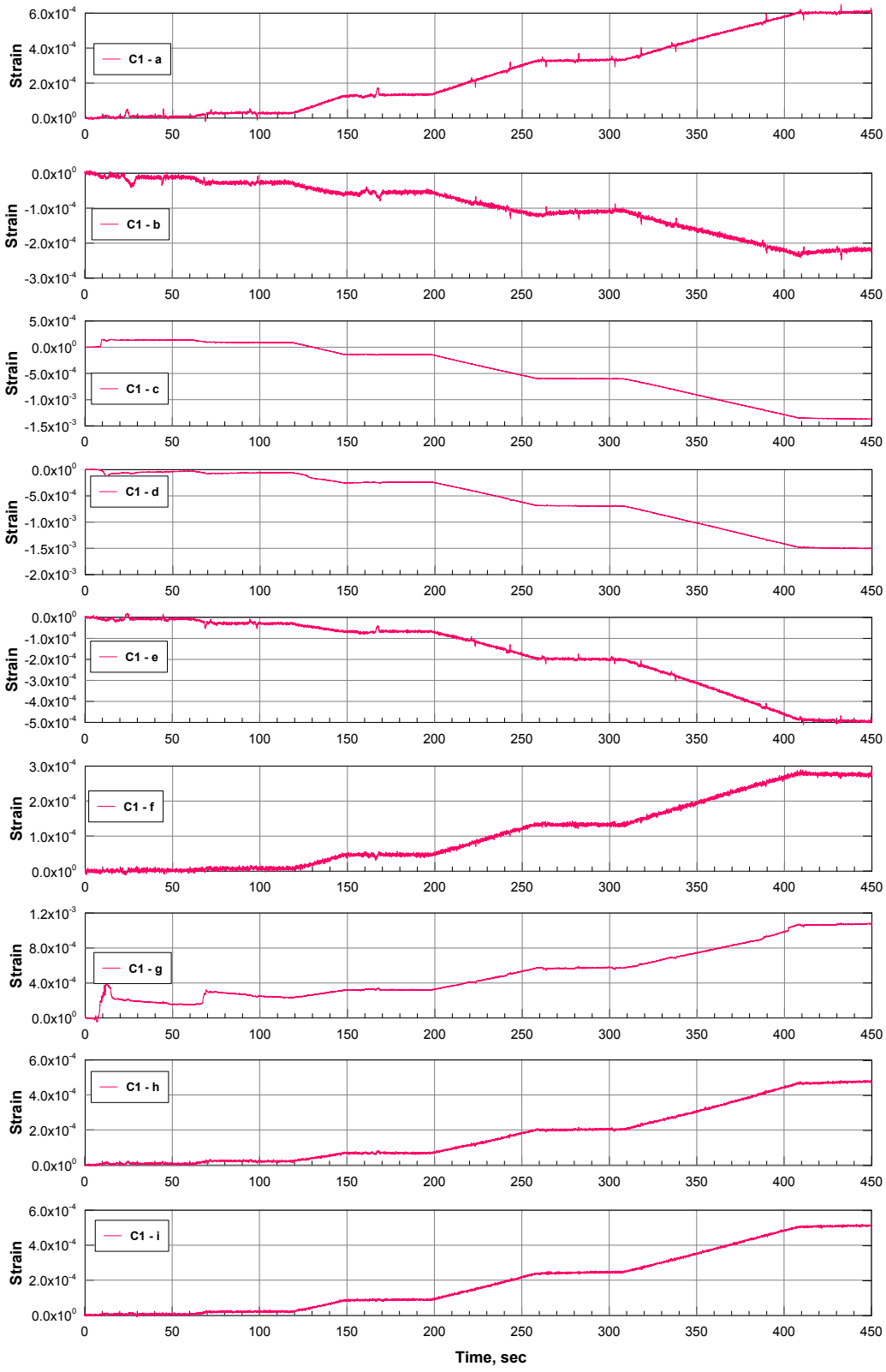

Figure A.17: Strain readings for embedded cube C1 in -y direction.

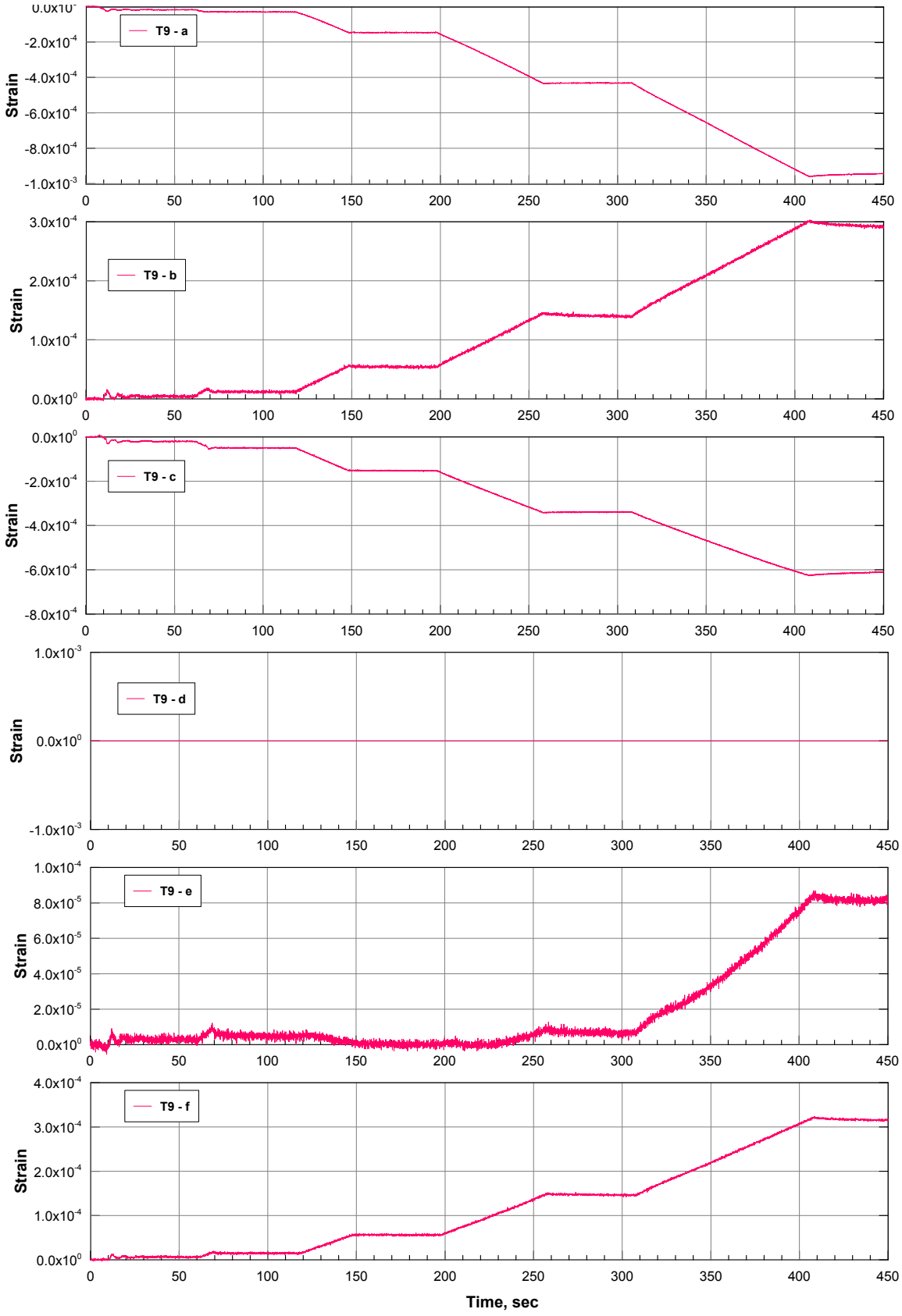

Figure A.18: Strain readings for tetrahedron T9 in -y direction.

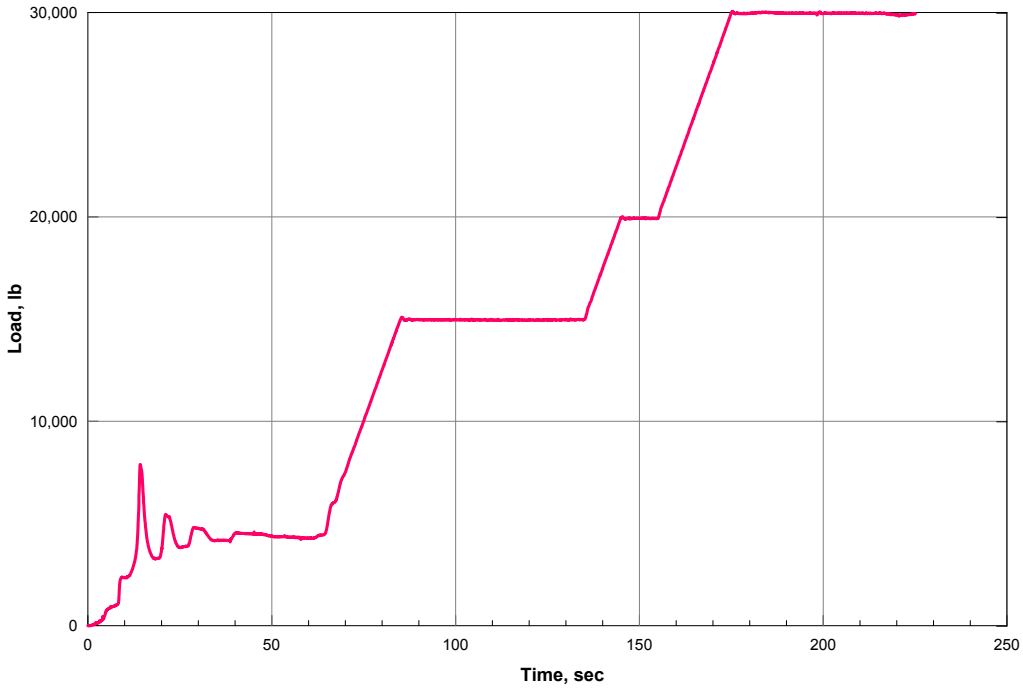

Figure A.19: Loading curve vs. time for cylindrical specimen C1 in -z direction.

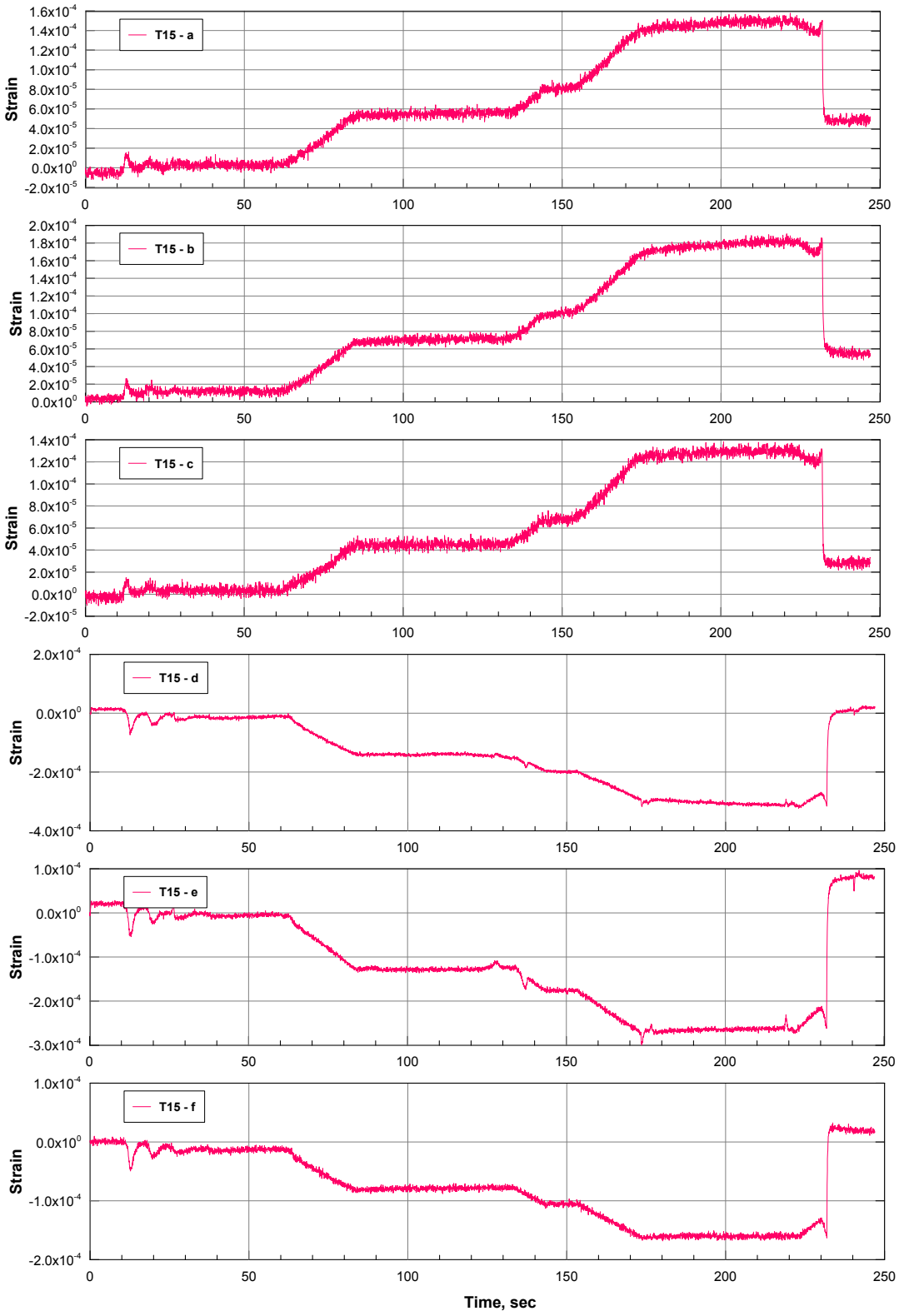

Figure A.20: Strain readings for the top tetrahedron in the cylindrical specimen C1.

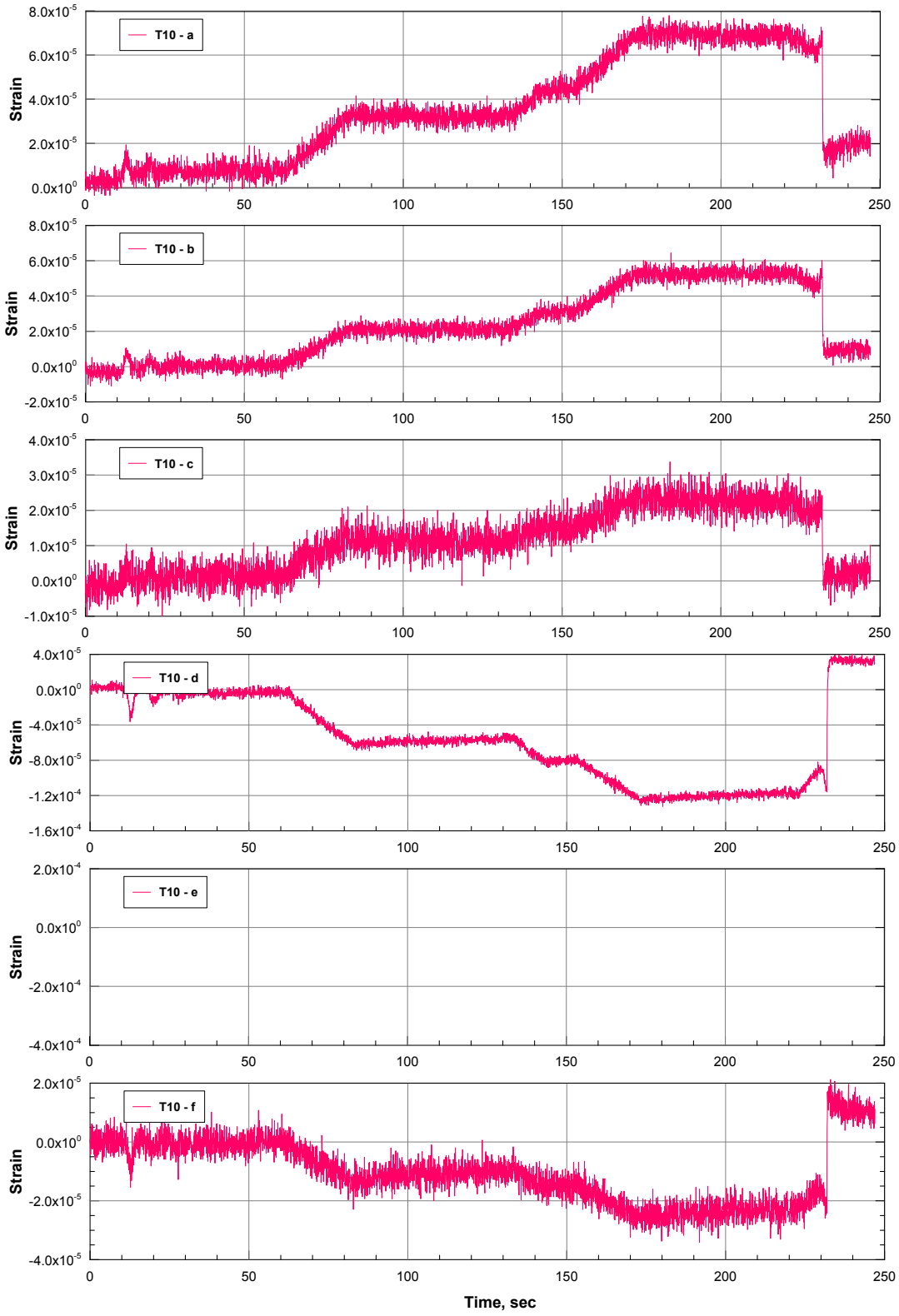

Figure A.21: Strain readings for the middle tetrahedron in the cylindrical specimen C1.

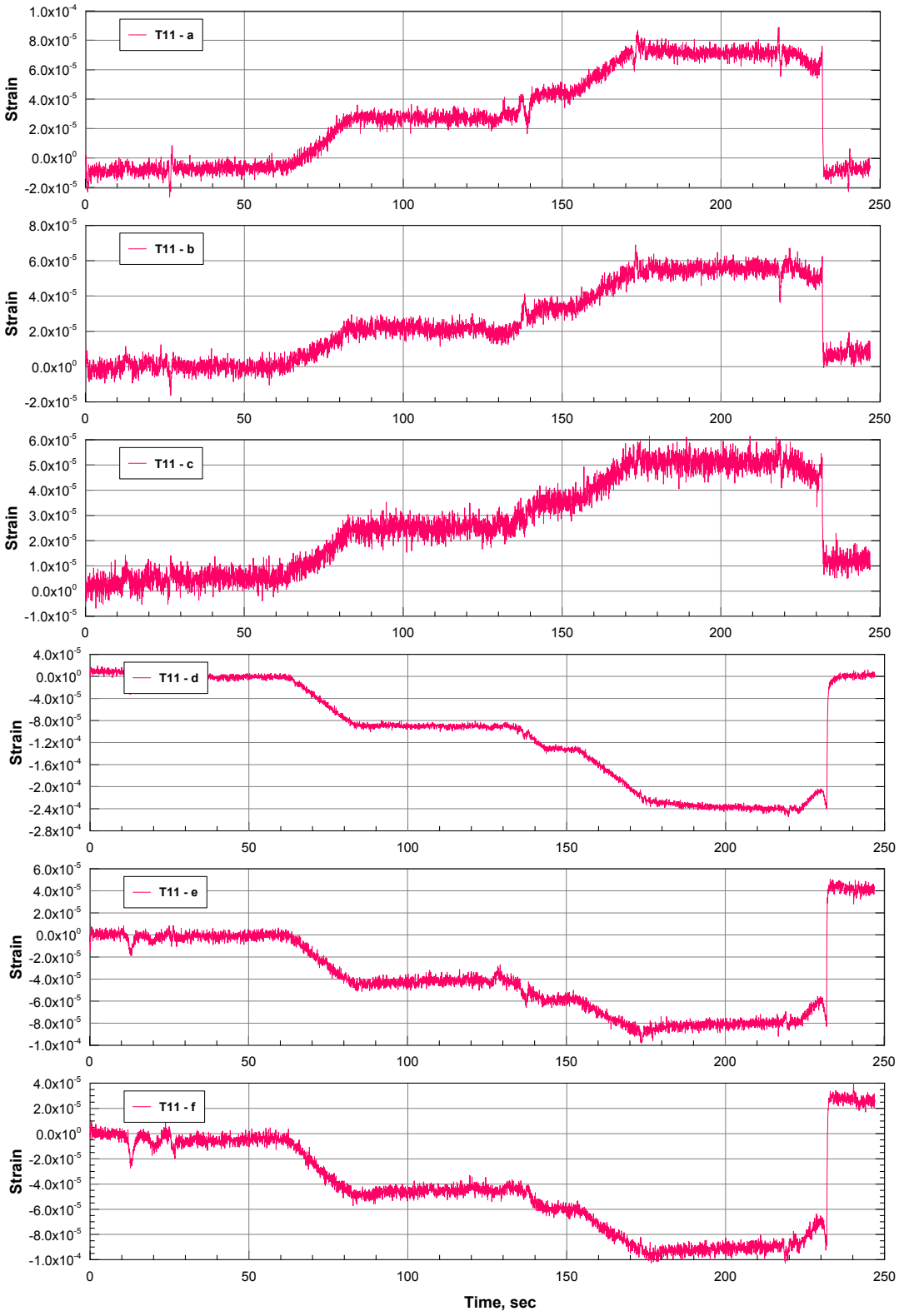

Figure A.22: Strain readings for the bottom tetrahedron in the cylindrical specimen C1.

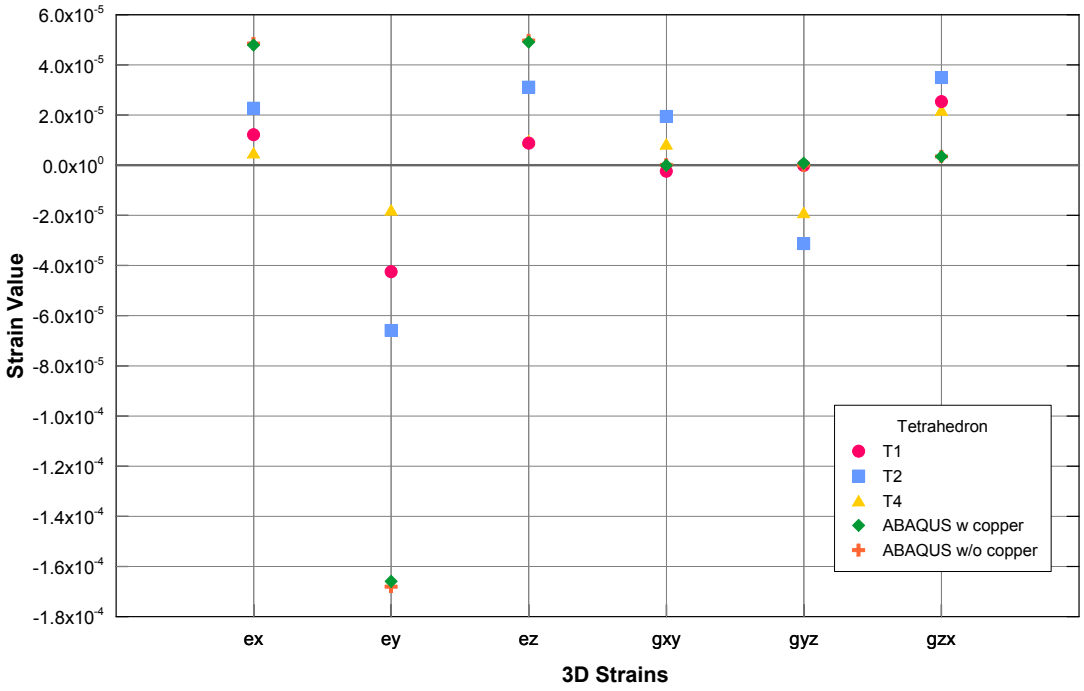

(a) -y direction

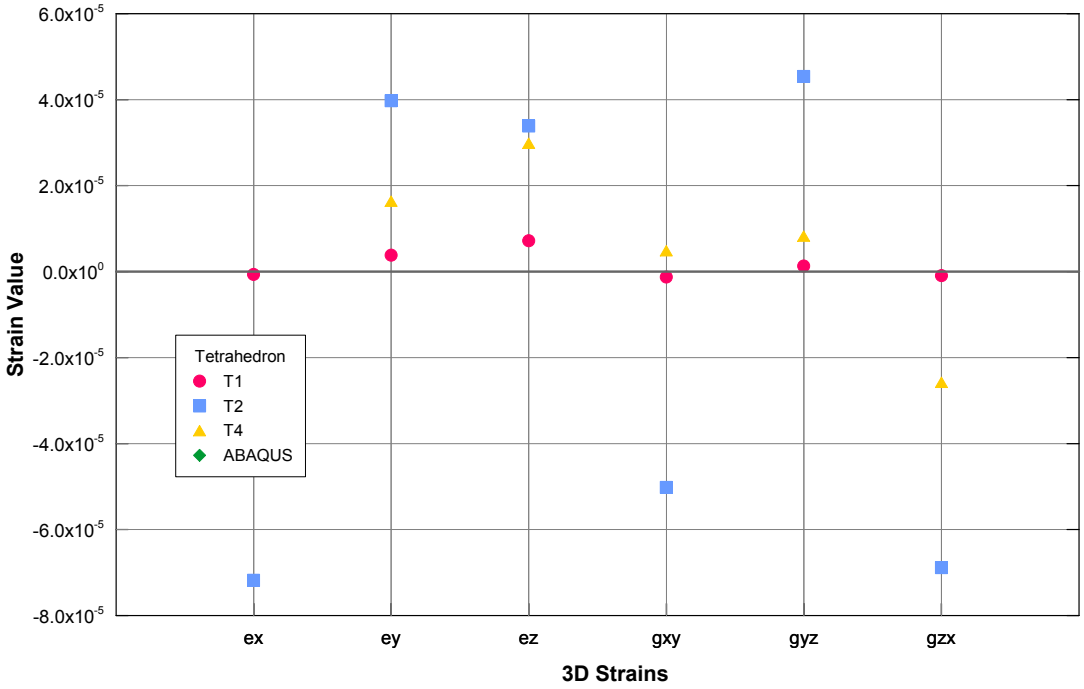

(b) $+x$ direction

Figure A.23: Experimental and computed 3D strains for five 3 in. cubes at a 3 kips load.

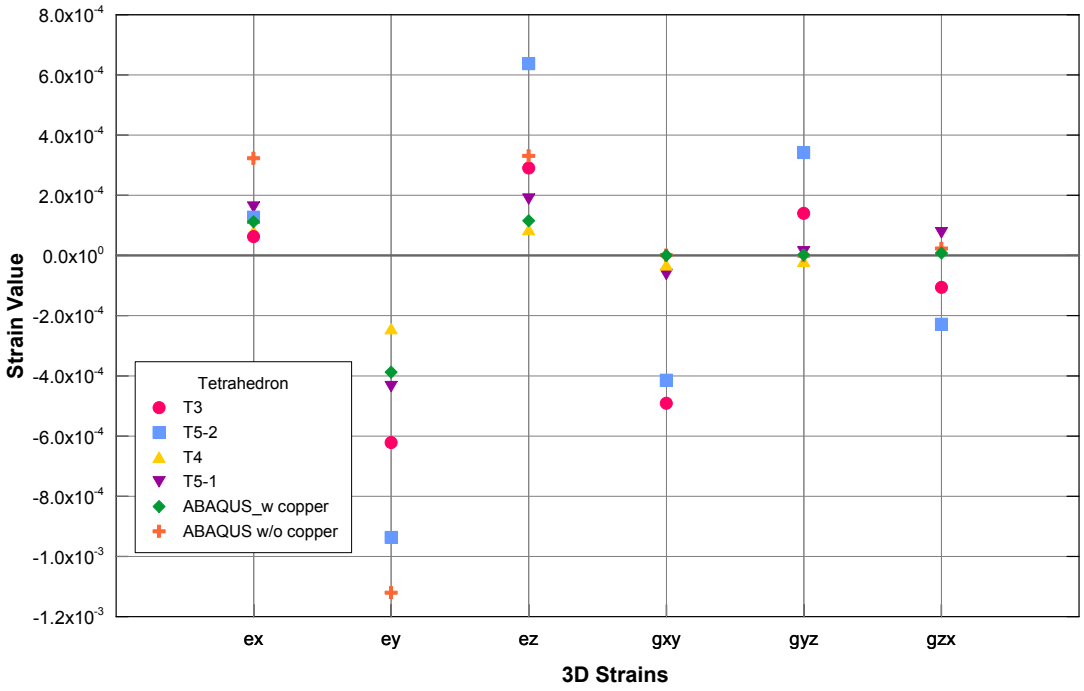

(a) $-y$ direction

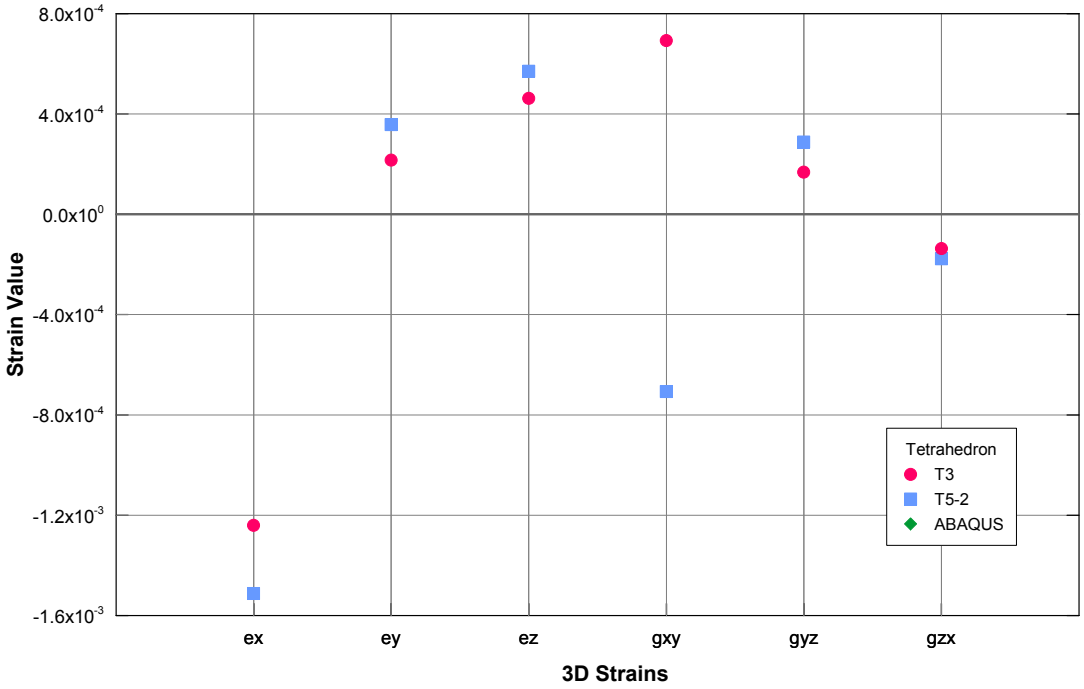

(b) $+x$ direction

Figure A.24: Experimental and computed 3D strains for five 3 in. cubes at a 20 kips load.

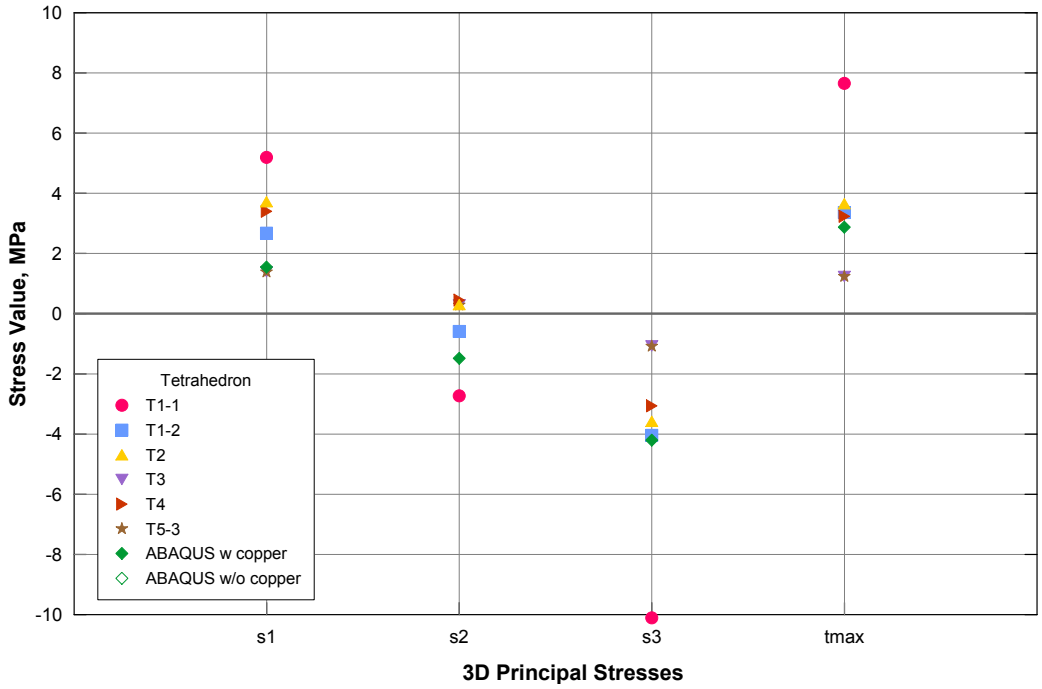

(a) -y direction

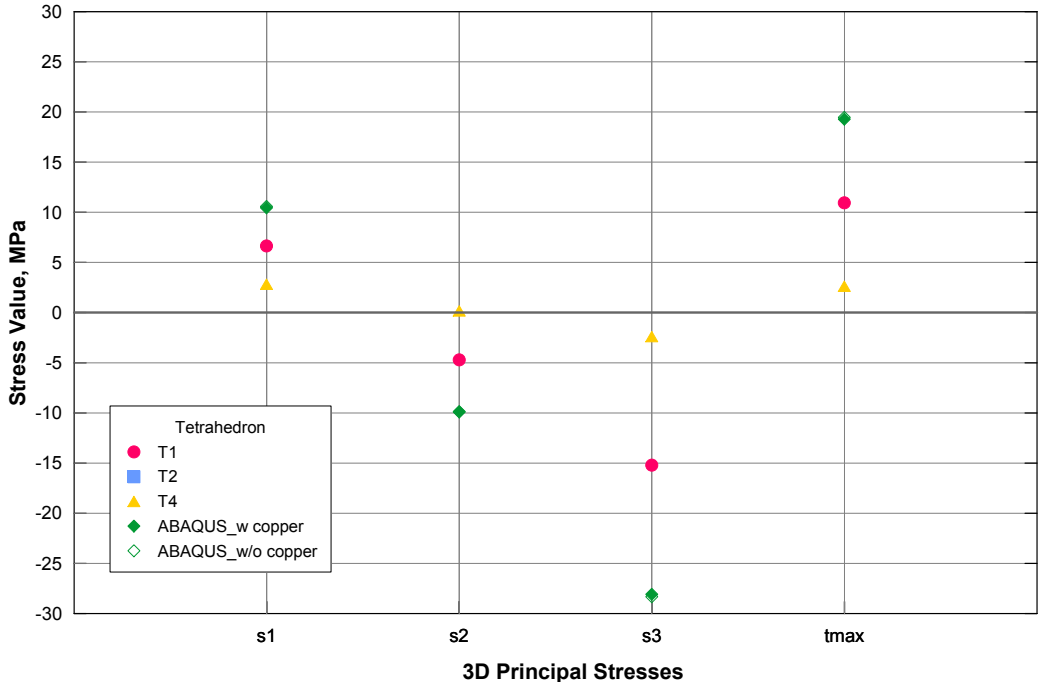

(b) $+x$ direction

Figure A.25: Experimental and computed 3D stresses for five 3 in. cubes at a 3 kips load.

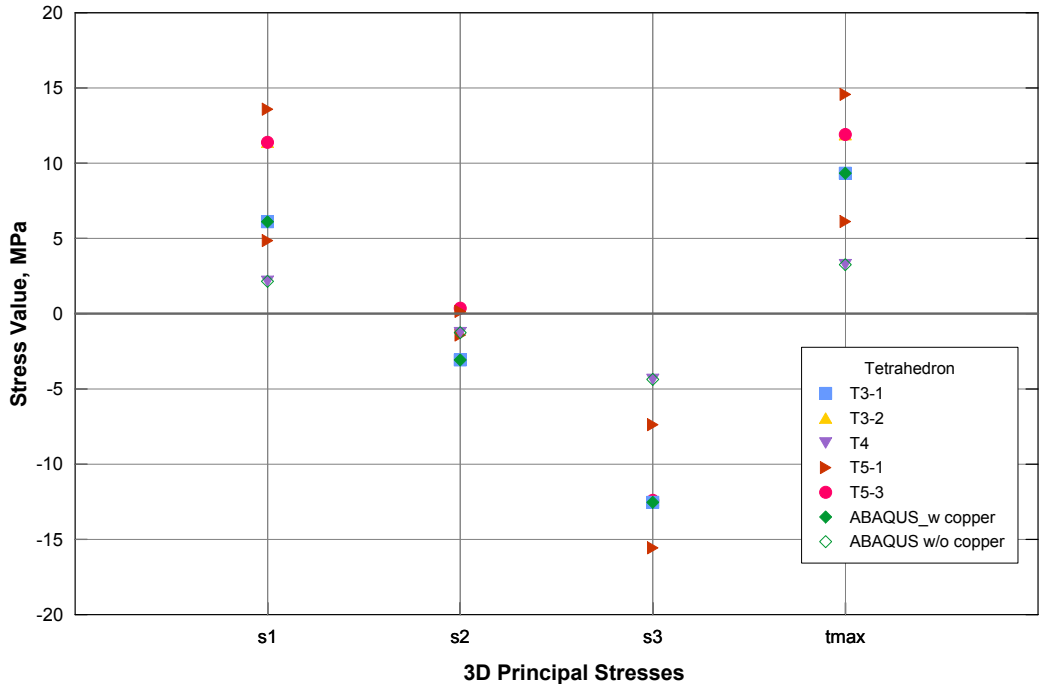

(a) -y direction

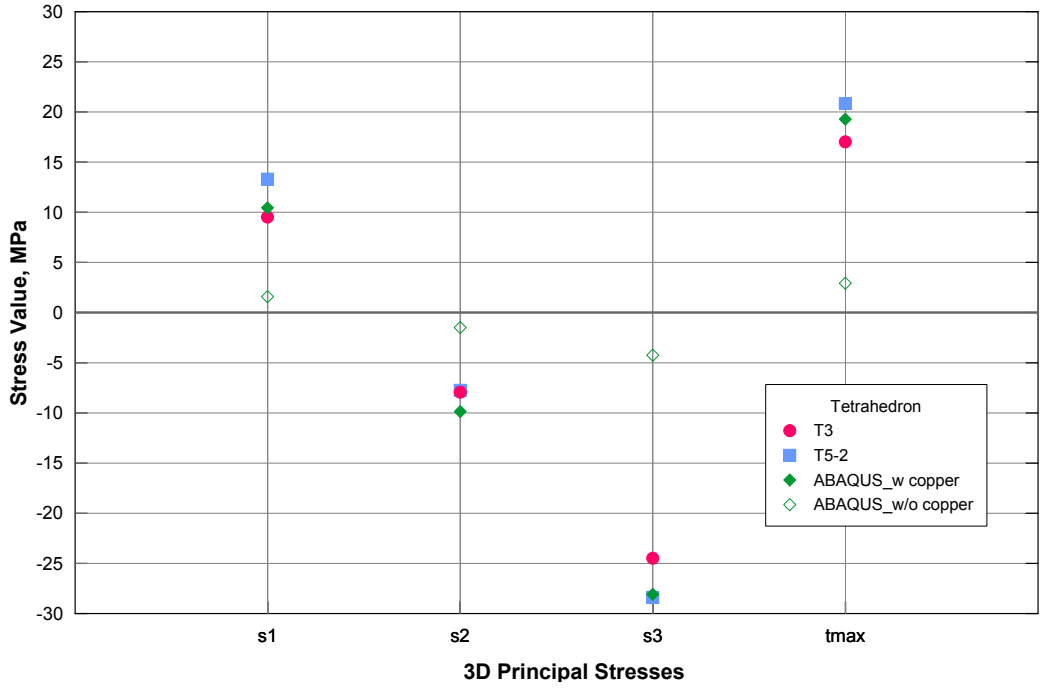

(b) $+x$ direction

Figure A.26: Experimental and computed 3D stresses for five 3 in. cubes at a 20 kips load.

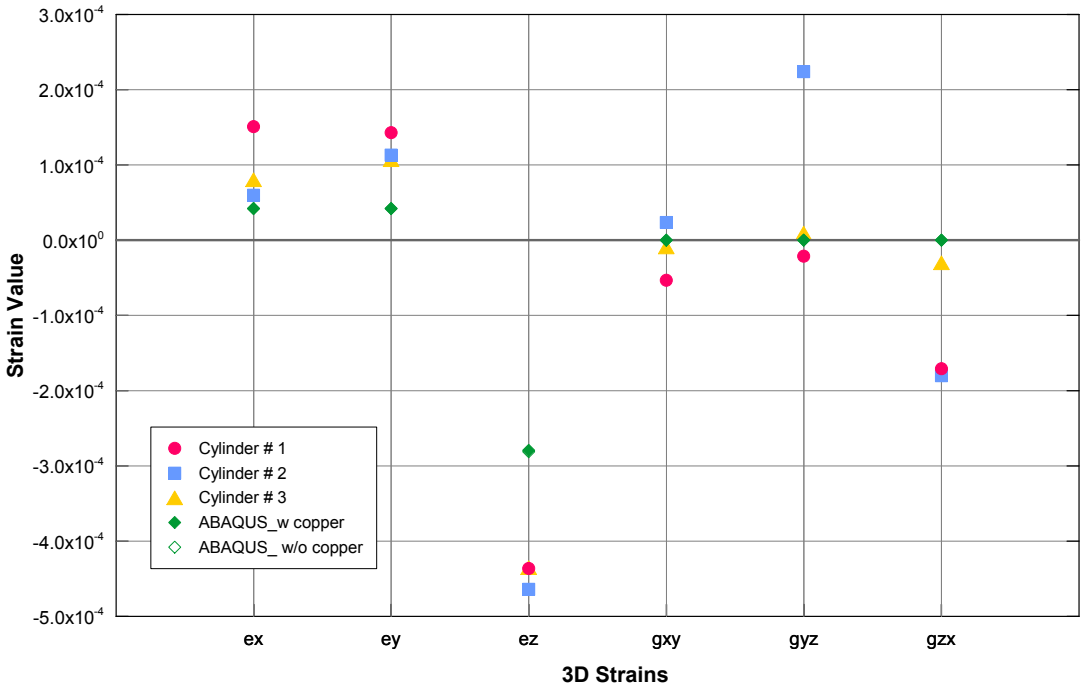

(a) Top Tetrahedron

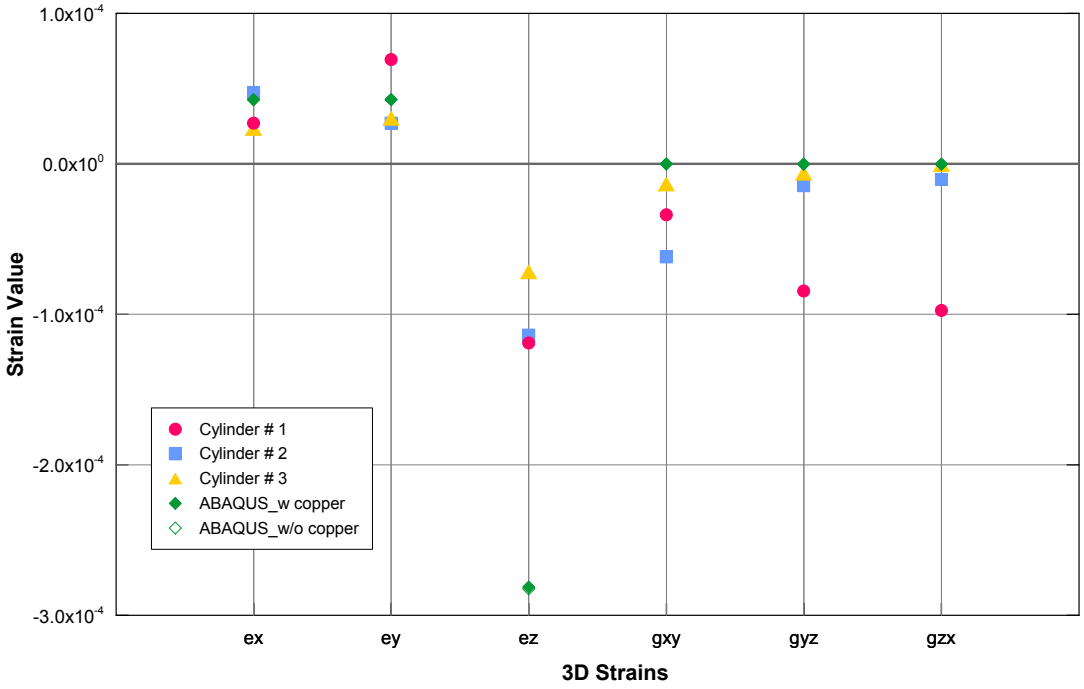

(b) Middle Tetrahedron

Figure A.27: Experimental and computed 3D strains for three concrete cylinders at the centroid of the three tetrahedra.

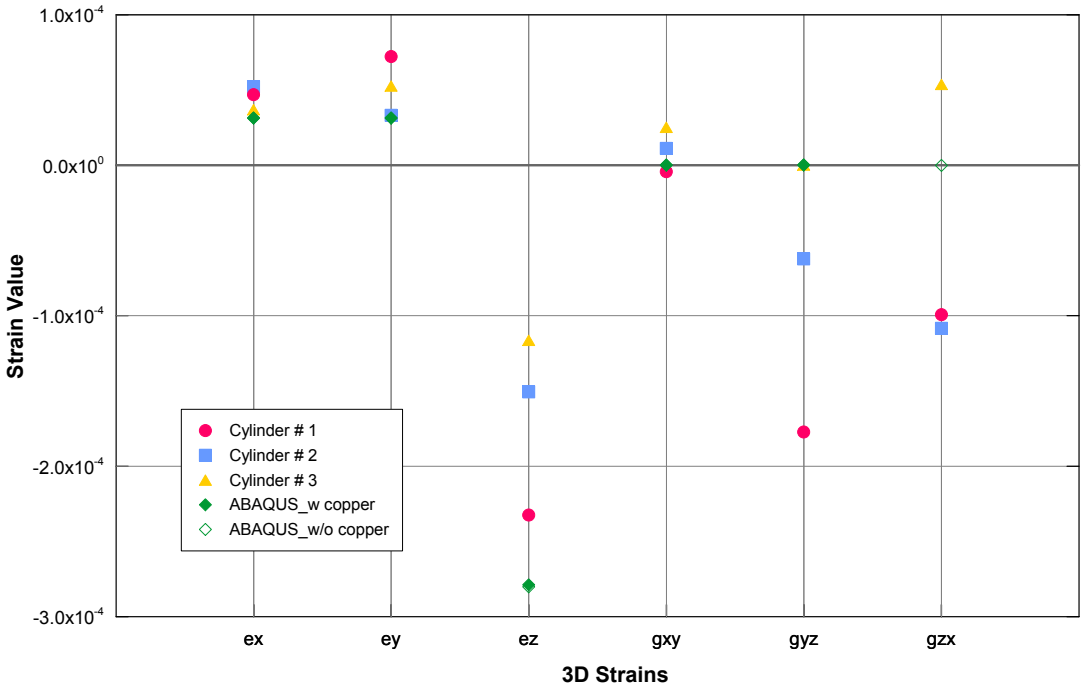

(c) Bottom Tetrahedron

Figure A.27: Experimental and computed 3D strains for three concrete cylinders at the centroid of the three tetrahedra (cont.).

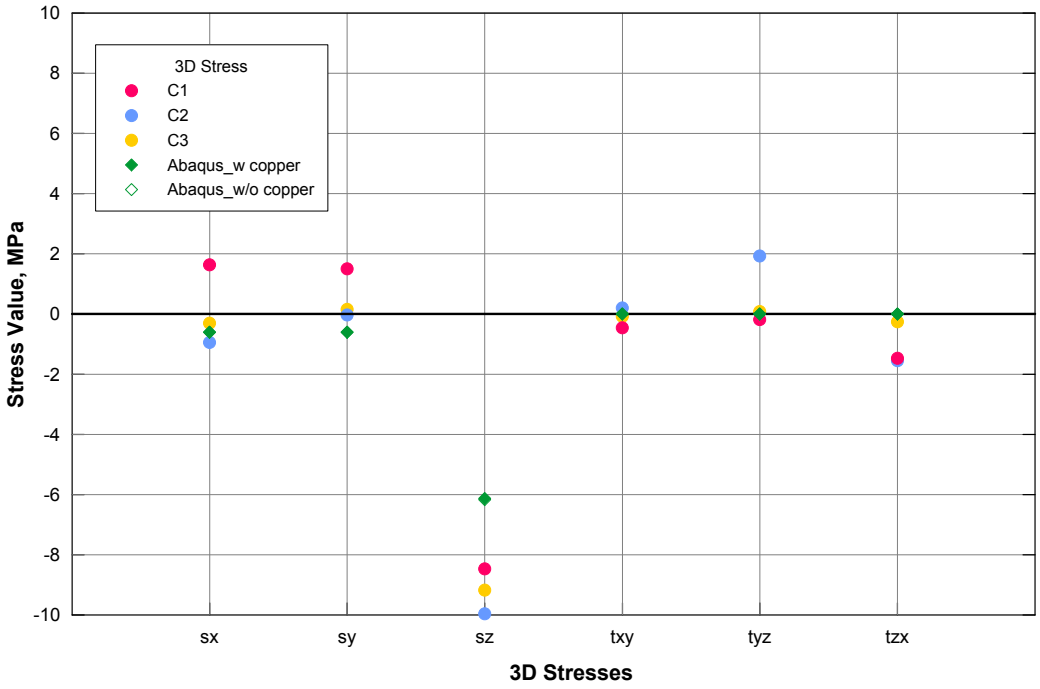

(a) Top Tetrahedron

Figure A.28: Experimental and computed 3D stresses for three concrete cylinders at the centroid of the three tetrahedra.

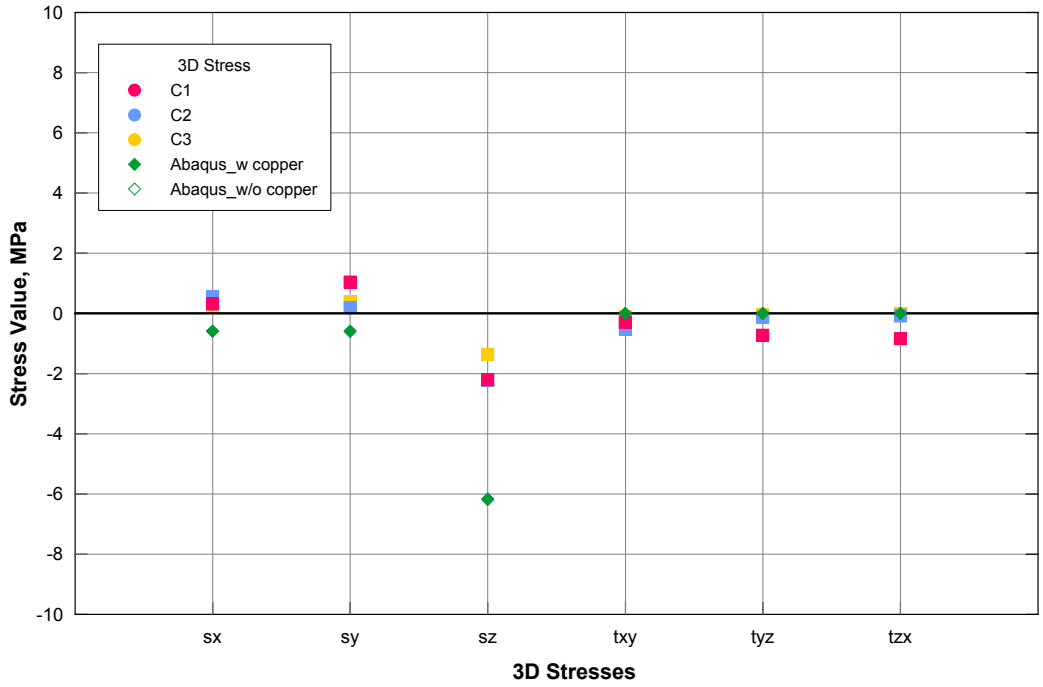

(b) Middle Tetrahedron

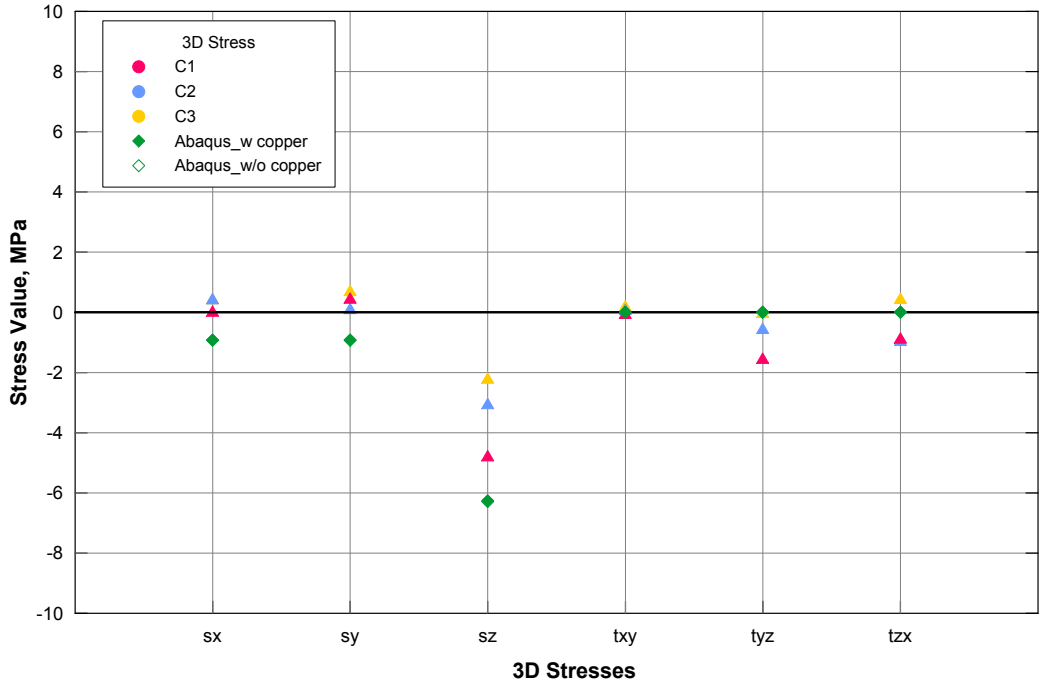

(c) Bottom Tetrahedron

Figure A.28: Experimental and computed 3D stresses for three concrete cylinders at the centroid of the three tetrahedra (cont.).